University of London
Imperial College of Science, Technology and Medicine
Department of Mechanical Engineering

Turbomachinery Aeroelasticity Using a Time-Linearised Multi Blade-row Approach

Gabriel Saiz

A thesis submitted to the University of London for the degree of
Doctor of Philosophy and the Diploma of Imperial College, January 2008

Statement of Originality

The work presented in the thesis is, to the best of the candidate's knowledge and belief, original and the candidate's own work, except as acknowledged in the text. The material has not been submitted, either in whole or in part, for a degree or comparable award of Imperial College or any other university or institution.

Gabriel Saiz
January 2008

Dedicated to Nicky

for all her love and understanding

Abstract

In turbomachinery, the continuous drive towards low weight and improved efficiency has led to the design of slender and lighter blades, resulting in higher stress levels and aeroelasticity interactions on blades. Consequently, fast and accurate predictions of turbomachinery aeroelasticity phenomena are essential to modern aero-engine design. Current prediction methods can be divided into three main categories: classical, nonlinear time-accurate, and harmonic. Classical methods work with simplified geometries and simplified flow conditions, and are therefore not reliable for design. Nonlinear time-accurate methods are usually accurate, but they demand too much computational effort to be used for design in the foreseeable future. Harmonic methods currently meet design efficiency requirements, but they can still lack accuracy in real turbomachinery applications. Several research works suggest that one of the reasons for this is that most current methods ignore potentially important multi blade-row effects.

In this thesis, a harmonic linearised solver for the computation of multi-stage unsteady turbomachinery flows was developed. Blade-row interactions were represented using the theory of spinning modes. The new method uses either the 3-D Euler or Navier-Stokes equations and is well suited to the computation of flutter and forced response. Efficient solutions were obtained thanks to the use of state-of-the-art acceleration techniques, such as local Jacobi preconditioner, multigrid, and GMRES. The method uses modern 3-D non-reflective boundary conditions, which use a wave-splitting method to minimise numerical reflections at the far-field boundaries. It also uses a novel inter-row boundary condition, based on the same wave-splitting method, to transfer waves between blade-rows.

The new method was first tested for stator-rotor interaction and flutter on both simplified geometries and flow conditions; results showed excellent agreement with the reference solutions. The method was then validated on industrial turbine configurations. Results were compared with nonlinear time-accurate unsteady solutions and experimental data and showed good agreement. It was demonstrated that multi-blade-row effects on the aerodynamic damping and the modal force of the vibrating

blade-row are significant. The new method is also very efficient; large gains in computing time were obtained compared to fully nonlinear time-accurate methods.

Acknowledgements

First of all, I would like to express my gratitude to Dr Jeff Green who encouraged me towards a PhD in the first place when I was a trainee at Rolls-Royce. I am convinced that this has been an invaluable experience from which I have learned a lot about CFD, computing, turbomachinery, and about myself.

I would also like to thank my supervisor Prof Mehmet Imregun for giving me the chance to complete my PhD in a world-class institute such as Imperial College. He has been a constant source of good ideas and motivation. He has always been very kind and understanding at every stage of my PhD. I am also grateful to him for providing the material that I needed and the freedom of travelling. I would also like to thank Prof Abdulnaser Sayma who also supervised my work from Imperial College during the first half of my PhD, and who generously offered to continue supervising my work from Brunel University, and then the University of Sussex where he continued his career. I also thank Dr Luca di Mare for making time in his busy schedule to assist me with technical issues.

I would also like to thank many Rolls-Royce 's employees for their contributions to my PhD. I wish I could write a line for all of them here, but that would require a huge amount of text. I have not missed to thank them all personally, and I am sure that they can recognize themselves. Amongst these people, I would like to especially thank John Coupland again for his useful advice, for his technical help, for his invaluable tutorials to the physics of acoustics and noise, and to the use of several Rolls-Royce in-house codes. I would also like to thank Richard Bailey for assisting me in the coding of pre- and post- processing tools to the work carried on in this thesis.

I am also extremely grateful to Rolls-Royce plc. and to Imperial College (EPSRC) for jointly sponsoring my thesis and supporting me until the end of my project.

Finally, many thanks to Andrea Bocelli for his peaceful songs which helped me to concentrate on my work. Thanks to the ice pack which helped to maintain my laptop running during the whole writing up process despite its overheating battery. And lastly, many thanks to the IT teams which helped me to retrieve (at least partially)

some of my data during the four hard disk failures that I came across during my PhD.

Contents

List of Tables

List of Figures

Nomenclature

Latin

B	number of blades
c	speed of sound and blade chord
c_v	specific heat at constant volume
c_p	specific heat at constant pressure
$C^{n\times m}$	complex matrix with n lines and m columns
$\mathcal{D}$	column vector of artificial dissipation
E	total internal energy per unit mass
$\mathcal{F}$	numerical flux function
$\mathbf{F}$	vector of convective and viscous fluid fluxes
$\bar{\mathbf{F}}$	vector of time-mean convective and viscous fluid fluxes
H	total enthalpy per unit mass
i	$\sqrt{-1}$
k_T	coefficient of thermal conductivity
k	wave number
k_x	axial wave number
k_θ	circumferential wave number
k_r	radial wave number
$\mathcal{L}$	pseudo-Laplacian operation for 4th order artificial dissipation
M	Mach number
M_x	axial Mach number
M_θ	circumferential Mach number
$\mathbf{n}$	unit normal vector
p	static pressure
P	blade pitch (rad)
Pr	Prandtl number
$\mathcal{R}$	numerical flow residual
$\mathbf{R}$	column vector of flow residual
r	radial coordinate (cylindrical coordinate system x, r, θ)
Re	Reynolds number
$\mathbf{S}$	column vector of centrifugal and Coriolis sources
$\bar{\mathbf{S}}$	column vector of time-mean centrifugal and Coriolis source terms
t	physical time
T	static temperature
$\mathbf{U}$	vector of conservative flow variables
$\bar{\mathbf{U}}$	vector of time-mean conservative flow variables

x, y, z	cartesian coordinates
x, r, θ	cylindrical coordinates
u, v, w	cartesian velocities
u_x, u_θ, u_r	cylindrical velocities
$\mathbf{v}$	vector of cartesian velocities
$\mathbf{X}$	vector of instantaneous Cartesian grid node coordinates
$\bar{\mathbf{X}}$	vector of time-mean Cartesian grid node coordinates
$\dot{\mathbf{X}}$	vector of grid node velocities

Greek

δ	delta
γ	ratio of specific heat
∞	infinity
λ	bulk viscosity
μ	molecular viscosity
ν	kinematic viscosity
τ_w	shear stress at the wall surface
ω	frequency (rad)
$\overline{\omega}$	reduced frequency
Ω	rotational speed
ρ	density
π	pi number
ψ	limiter function for inviscid fluxes
$\mathcal{R}(.)$	real part
$\Im(.)$	imaginary part
σ	inter-blade phase angle
τ	pseudo time
$\mathcal{V}$	controle volume
ξ	aerodynamic damping

Subscripts

∞	far-field
i	i-th blade-row
I	mesh point
J	mesh point connected to I by an edge
IJ	in the direction from node I to node J
K	boundary mesh point
w	quantity at the wall
l	laminar
ref	reference value of physical quantity
t	turbulent
0	steady-state value of physical quantity

Superscripts

I	inviscid
n	iteration number
T	transpose
V	viscous
$*$	normalised by reference values or complex conjugate

Abbreviations

AG	axial gap between the blade-rows
CAA	computational aero-acoustics
CFD	computational fluid dynamics
CFL	Courant Friedrichs Lewy number
CMM	coupled mode model
CND	current nodal diamter
CPU	central power unit
CT	computational time
dB	decibel
DNS	direct numerical simulation
EO	engine order
ESS	engine section stator
FE	finite element
GMRES	generalised minimal residual
GB	gigabyte
HCF	high cycle fatigue
HP	high pressure
IBPA	inter-blade phase angle
LCO	limit cycle oscillation
LE	leading edge
LEO	low engine-order
LES	large eddy simulation
LPT	low pressure turbine
MB	megabyte
ND	nodal diameter
NGV	nozzle guide vane
NPDES	number of partial differential equations
NSV	non-synchronous vibration
OGV	outlet guide vane
PWL	power watt level
SFV	separated flow vibration
SPL	sound pressure level
TE	trailing edge

TND	total nodal diameter
UTCs	university technology centres
VIGV	variable inlet guide vane
vs.	versus
1-D	one-dimensional
2-D	two-dimensional
3-D	three-dimensional

Operators

∇x	gradient of a scalar function x
$\nabla.\mathbf{x}$	divergence of a vector field $\mathbf{x}$
$\nabla \times \mathbf{x}$	curl of a vector field $\mathbf{x}$
$\nabla^2 x$	Laplacian of a scalar function x
$\frac{\partial x}{\partial a}$	partial derivative of a function x with respect to a variable a
$\frac{dx}{da}$	total derivative of a function x with respect to a variable a

Chapter 1

Introduction

1.1 Overview

The main purpose of a gas turbine is to produce work. This work is then used directly for energy production, or it is converted into thrust through a mechanical process. Turbomachineries produce work thanks to the rotation of several blade-rows, see Fig. 1.1. Unfortunately, the relative motion of the blade-rows also yields undesirable aeroelastic and aeroacoustic problems, which under certain circumstances can cause blade vibration and subsequent failure by high cycle fatigue (HCF). In this chapter, the most important aspects of gas flows in turbomachinery are presented. First, general features of gas flows in compressors and turbines are presented. Following this, the most common aeroelastic problems in turbomachineries are discussed. Finally, a brief description of the noise produced by turbomachineries is given.

1.2 General Flow Features in Turbomachinery

The different blade shapes and the relative motion of the blade-rows give rise to complex flows. Some of the most important flow features are depicted in Fig. 1.2. The blade-rows are shown between two end-walls, some of which are rotating. The end-wall at the outer radius is usually referred to as the casing, and the inner end-wall as the hub. Near the hub, the end-wall boundary layer is struck by a strong adverse pressure gradient at the junction between the blade and the hub. This causes a three dimensional flow separation on both sides of the blade, thus creating a horseshoe vortex, which is carried away downstream. As the flow passes through the blade-to-blade passage, the passage vortex on the pressure side of the blade is

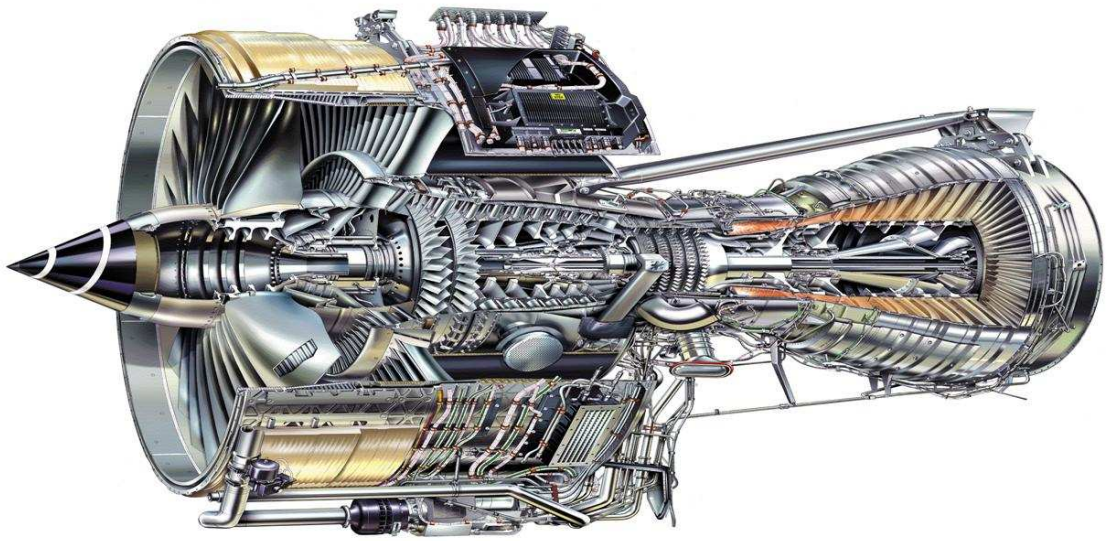

Figure 1.1: Typical civil aircraft engine - courtesy of Rolls-Royce plc

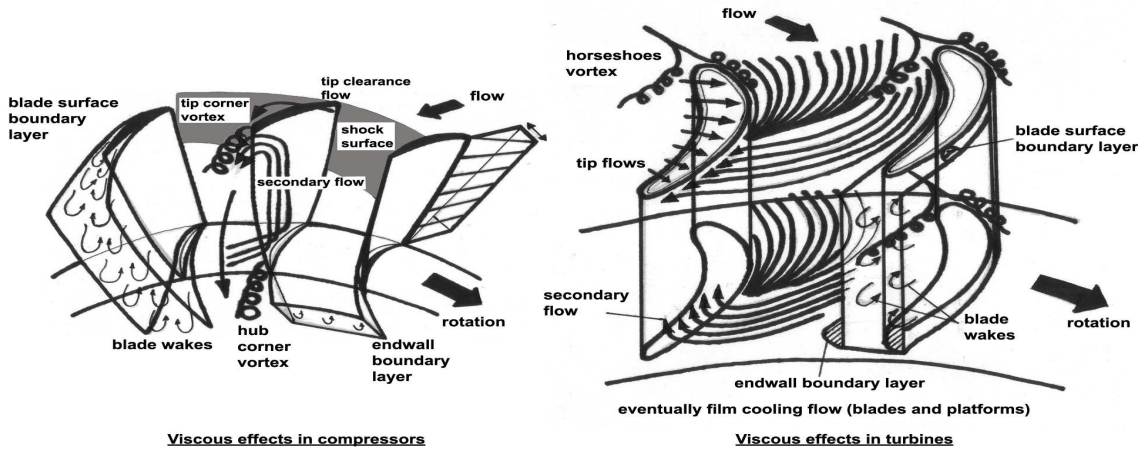

Figure 1.2: Typical flow features in compressors and turbines; taken from McNally [69]

carried by the adverse pressure gradient to the suction side of the adjacent blade. In some cases the horseshoe vortex later mixes with the passage vortex, giving rise to more complicated flows. In general, radial flow variations near the end-walls are referred to as secondary flows.

At the casing, the flow is somewhat more complicated due to the tip-leakage flow, which is present with both shrouded and unshrouded blades. The presence of this tip-leakage is obvious on unshrouded blades since there is a tip-clearance gap between the blade and the casing. With shrouded blades, there must also be a clearance between the rotating shroud and the stationary casing. Within the passage, the region

of maximum pressure is not attached to the pressure side of the blade, but located slightly away from it. The consequence of this is that the flow is divided in two zones. Some of the flow is sucked through the tip-gap from the blade pressure side to its suction side and forms the tip-leakage flow; the rest of the flow is accelerated towards the suction side of the adjacent blade, forming a cross passage flow, which is blocked partly by the tip-leakage flow and produces another passage vortex. The size of the tip gap on unshrouded blades is about 1% of the blade span for compressors and turbines. Although the size of the tip clearance is small, it can account for as much as one third of the losses in an axial turbine, and it has a major influence on the initiation of stall in transonic fans and compressors.

Shock waves occurring in transonic flows may also influence boundary layers and tip clearance vortices. Shocks are nonlinear pressure waves with an abrupt magnitude change in a very thin layer in the direction normal to the flow. They cause a sudden drop in velocity and a sudden increase in pressure. The flow through shocks is highly irreversible. In addition, when the shock configuration of a given blade row is expanding into neighbouring passages, shock waves may interact with each other.

Finally, near the blade midspan the flow is often considered 2-D, especially for blades with a high aspect ratio. In this region, the flow is mostly governed by the blade shape, the incoming flow conditions, and multi blade-row interaction effects.

1.3 Aeroelasticity

Unsteady flows give rise to several aeroelasticity problems which can affect the stability of the blades. Therefore, it is important to understand what the aeroelastic problems are. The following sections aim at answering this question. First, the word aeroelasticity is defined, then the most common aeroelastic problems encountered in turbomachinery applications are discussed briefly.

1.3.1 Definition

Aeroelasticity is the study of the interaction between mechanical and aerodynamic forces acting on a body. Tubomachinery designers are particularly concerned by aeroelasticity problems since blade-rows are continuously subjected to significant aerodynamic and centrifugal loads. Gravitational forces also contribute to the equilibrium of blade-rows, but these are generally negligible. Damping aside, the balance

of mechanical and aerodynamic forces acting on a solid body can be expressed as:

$$\underbrace{[M]\,\ddot{\mathbf{X}}}_{Inertial\ forces} + \underbrace{[K]\,\dot{\mathbf{X}}}_{Elastic\ forces} = \underbrace{\mathbf{f}}_{Aerodynamic\ forces} \tag{1.3.1}$$

where M and K represent the mechanical mass and stiffness matrices respectively, and $\mathbf{X}$ represents the dynamic response of the body.

Collar [20] defined a triangle of forces, shown in Fig. 1.3, in which inertia, elastic, and aerodynamic forces form a triangle, the vertices of which relate to various disciplines.

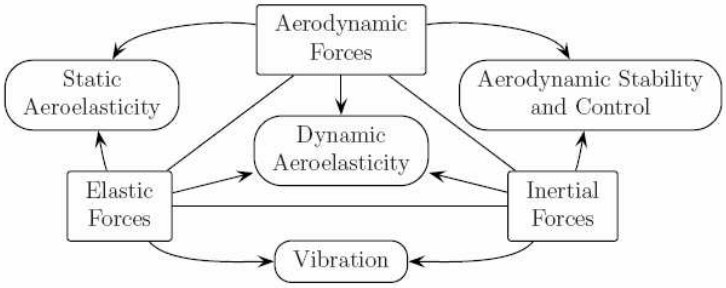

Figure 1.3: Collar diagram of aeroelasticity

1.3.2 Role of Aeroelasticity in Blade Design

Blade vibration is a major design concern as it may cause sudden destruction or longer-term fatigue of the structure. Blade design is achieved through an iterative process. First, a *geometric* and *aerodynamic* configuration of the blades is established from a performance standpoint. Secondly, it is verified whether the designed shapes will also be acceptable from an aeroelastic standpoint, based on mechanical strength and other operational conditions. If aeroelastic stability requires major modifications of a blade geometry, then the blade is re-designed for performance and re-verified for aeroelasticity.

1.3.3 Static Aeroelasticity

Turbomachinery blade-rows are subject to large variations of rotational speeds and flow conditions. For example, aircraft engines must endure take off, acceleration, cruise, descent, and landing conditions during their flight envelope. Flow conditions

Figure 1.4: Example of turbine blade failure from blade vibration

and rotational speed dictate the gas and centrifugal loads. As the centrifugal loads change, so does the stiffness of the blades, which deform elastically from their initial manufactured (or cold) shapes to their running shapes. The deformation usually occurs in a torsional mode, but a bending displacement also occurs for high aspect ratio blades. Static turbomachinery aeroelasticity is dedicated to the study of such deformations.

During design, the blade geometry is first built to obtain a peak aerodynamic efficiency at the design condition. Once this first step is achieved, the manufactured (or cold) shape of the blade must be retrieved by taking off the effects of centrifugal and pressure loads at the design conditions. This procedure is known as *unrunning*. During this process, designers may face the problem of *torsional divergence*. This corresponds to a condition in which the static aerodynamic forces become so large that the torsional stiffness of the blade cannot resist and collapses without any oscillation. This problem is avoided by using blades stiff enough to resist all gas loads encountered in flight conditions.

1.3.4 Dynamic Aeroelasticity

Dynamic aeroelasticity is the study of problems caused by the interaction of unsteady fluids with blade vibration. The main aeroelastic phenomena of interest are: forced response, flutter, non-synchronous vibrations (NSV), and acoustic resonance. These are explained below in more detail.

Forced response

Forced response belongs to the family of synchronous problems which occur when one of the engine order (EO) excitations - or multiples of the rotational speed -

coincides with one of the rotor assembly natural frequencies. The first significant piece of work on forced response was done by Campbell [7, 8]. He devised one of the most important aeroelastic tools, the *Campbell Diagram*, which is still in use today. An example is shown in Fig. 1.5. Note, when the shaft speed increases, the centrifugal stiffening causes the natural frequencies of the blade to increase, especially for the bending modes.

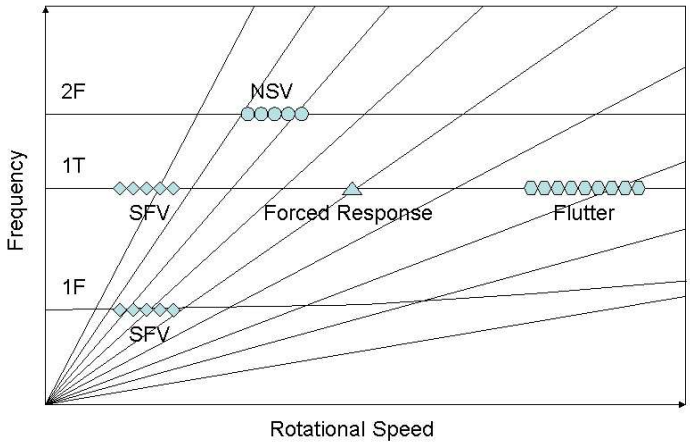

Figure 1.5: Compressor Campbell diagram where the possible occurrence of various aeroelastic phenomena is shown

From the outset, it is appropriate to distinguish between two types of forced response: classical forced response, and low engine-order (LEO) forced response. The first type of forced response originates from the rotation of a bladed-disk past a pressure field. This generates excitation forces, the strength of which varies periodically with the angular position of the blades around the whole annulus. Such excitation is mostly caused by stator blades. Stator blades create distortions, and the downstream rotor blades experience a periodic forcing with frequency based on the rotational speed. A Fourier decomposition of this periodic forcing provides the harmonics which excite the assembly modes. Typically, high nodal diameters (defined in Section 1.3.5) are excited, since they are related to the number of blades in the blade-rows. Classical forced response can further be divided into two categories: potential stator-rotor interaction, and wake-rotor interaction.

Potential Stator-Rotor Interaction The flow in the region between the blade-rows can be divided into three parts: (i) one which is steady and uniform in the stator frame; (ii) one which is steady but non-uniform in the stator frame; (iii) and one which is steady but non-uniform in the rotor frame. When the rotor blades rotate, both the stator and rotor blades experience an unsteady forcing which is

due to the non-uniform pressure components. This interaction is purely an inviscid process and can be modelled using the Euler equations [94]. Potential effects can be felt in both the upstream or downstream directions. Potential effects usually affect the flow in the regions near the blade's LE and TE, the reason being that the magnitude of the acoustic modes in such configurations often decay exponentially as they propagate.

Wake-rotor Interaction Stator wakes can generally be assumed to be steady in the absolute frame of reference. Nevertheless the rotor blades experience these wakes as periodic forces while they rotate around the annulus. The generation of stator wakes is a viscous phenomenon; however their subsequent interaction with the rotor blades is mostly an inviscid process. Two different approaches are commonly used to determine wake-rotor interaction. In the first one, one computes a viscous solution in the stator to obtain the stator wake, and an inviscid solution in the rotor to determine the effect of the wake on the rotor blades [30]. In the other approach, one computes a viscous solution in both blade-rows [83, 92], which is realistic but also more expensive.

Another type of forced response is low engine-order (LEO) excitation. This phenomenon is not well understood and there is no design procedure established for its avoidance. The engine order excitation is not a known function of the number of blades and low order nodal diameter assembly modes are excited because of a general loss of symmetry in the flow. Sources of excitation including changes in flow angle, stator/rotor axial gap, combustion effects and general unsteadiness are thought to influence LEO excitation [87, 14].

Flutter

Flutter is defined as a "sustained oscillation due to the interaction between aerodynamic forces, elastic response and inertia forces" (AGARD [2]). Flutter belongs to the family of asynchronous problems, thereby meaning that flutter is not caused by the interaction between upstream and downstream blade-rows. It is a self-excited phenomenon. Four main categories of flutter are encountered in turbomachinery, these are: classical flutter, stall flutter, acoustic flutter, and choke flutter. Some are presented in Fig. 1.6. This diagram is a compressor map in which the engine characteristic lines are plotted in a pressure ratio against flow mass rate.

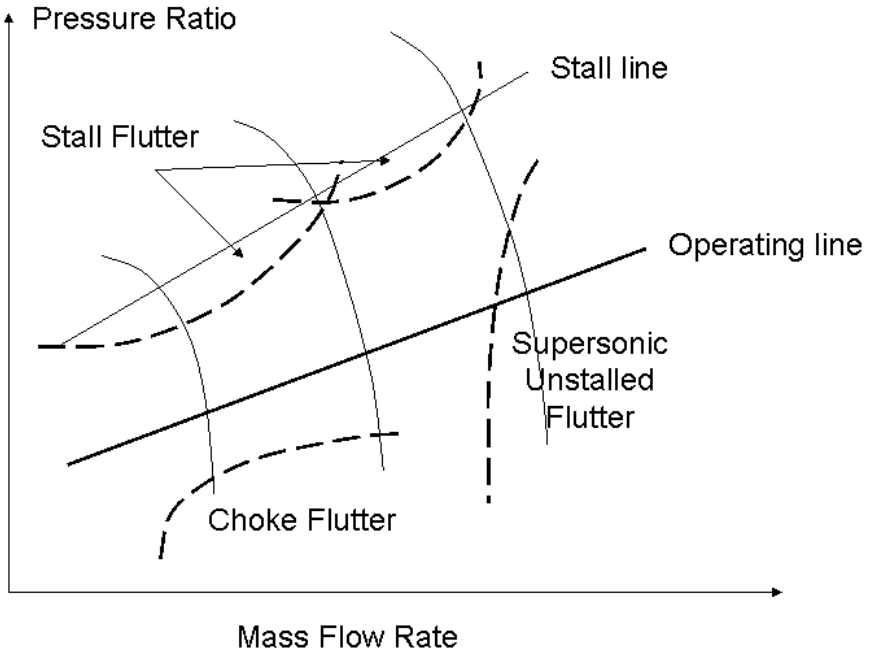

Figure 1.6: Typical compressor map showing various flutter regimes

Classical Flutter Classical flutter can occur when the flow is attached to the blade with no separation. A phase lag exists between the aerodynamic forces acting on the blade and the blade displacements. Depending on the value of the phase lag, the flow either: (i) feeds energy into the blade during its motion, this case represents an unstable vibration cycle; (ii) absorbs energy from the blade motion, this case represents a damped vibration; (iii) maintains its energy level without adding or subtracting energy to the blade, in this case the vibration is neutral.

Stall Flutter Stall flutter is given such a name because it occurs near the stall line on the compressor map. The incidence to the blade increases as the flow conditions approach the stall line, until the flow eventually stalls. High incidence provokes large flow separations, which seem to play an essential part of the blade flutter mechanism [116, 24].

Acoustic Flutter Acoustic flutter is encountered when acoustic waves, generated by the blade vibration, are reflected back onto the vibrating blade and feed the vibration. For this to happen, the temporal frequency of the acoustic wave must be equal to one of the natural frequencies of the blade, and must correspond to a resonant (or cut-on) mode of the annulus. For example, some acoustic flutter are known to occur due to the interaction between the fan blades and the engine intake

[89, 97].

Choke Flutter As the flow conditions approach the choke line, the incidence to the blade decreases - even becomes negative - and the flow gets choked. This happens because for a given mass flow rate the compressor does not accept any further decrease of pressure ratio. In this case, the flow includes flow separations with shock waves, and may excite a blade vibrational mode [22].

Non-synchronous vibration

Non-synchronous vibration occurs at a frequency which is not a multiple of the engine rotational speed. An excitation "locks" the blade vibration to a specific frequency and inter-blade phase angle, and may lead to large amplitude oscillations. Possible sources of excitations for non-synchronous vibration are numerous: vortex shedding (also known as Strouhal excitation), rotating stall, dynamic boundary layer separation, shock/boundary layer dynamics, tip flow/vortices, hub vortices, and combustion instabilities. Non-synchronous vibration belongs to the category of self-excited phenomena, like flutter. However, unlike flutter, vortex shedding occurs when the blade interacts with the wake that it generates [18]. Vorticities are shed away from the blade with a discrete number of frequencies and wave lengths, which are related to the shape of the blade and to the incident flow velocity. As a result, if the frequencies of the vorticities are close enough to a blade natural frequency, a vibration mode can be excited.

Acoustic Resonance

Acoustic resonance occurs when the fundamental flow perturbations (i.e. those associated with the original disturbance) travel a distance of exactly one or several wavelengths during one time period of oscillation. This corresponds to a resonance condition, which can lead to large amplitude blade oscillations, and sometimes failures. Acoustic resonance is still a poorly understood phenomenon. The linearised classical theory of Smith [104] which studies 2-D cascade of flat plates with inviscid, uniform, and subsonic flows, suggests that acoustic resonances occur at two different nodal diameters during flutter and forced response. However, in practice, flows are not uniform; they are sometimes transonic, sometimes strongly nonlinear. In addition, viscous effects may be dominant making acoustic resonance much more difficult to predict. However, vortex shedding from a usually stalled blade-row

has been identified as one possible source of excitation [81]. Further details about acoustic resonance can be found in Saymolovich [86] and Verdon [117, 118].

1.3.5 Characterisation of Turbomachinery Unsteady Flows

Unsteady flows in turbomachinery are complex, therefore it is necessary to isolate key parameters in order to characterise the nature of such flows. Although numerous parameters influence the aeroelastic behaviour of a bladed disk assembly, only a few parameters are considered to be crucial, and therefore receive specific attention during the design phase. Two parameters are known to be are particularly important, these are: the reduced frequency and the inter-blade phase angle.

Reduced Frequency

The reduced frequency is obtained from a simple dimensional analysis. Consider a local flow disturbance oscillating at frequency ω, then the time scale of the oscillation is given by $1/\omega$. While the flow perturbation is varying in time, the fluid particles also convect through the blade-row. If U is the fluid convection speed and L is the characteristic length of the blade, then a second time-scale is given by L/U. Usually L represents the blade chord [1], and thus this second time-scale represents the time taken by a fluid particle to pass the across the blade. The ratio of these two time-scales forms the reduced frequency, given by:

$$\bar{\omega} = \frac{\omega L}{U} = \frac{Convection\ time}{Disturbance\ period} \tag{1.3.2}$$

When the convection time is long, i.e. the reduced frequency is high ($\bar{\omega} \gg 1$), the flow varies locally very quickly and can be regarded as unsteady. On the other hand, when the convection time is short ($\bar{\omega} \ll 1$), then at each instant the flow appears to be changing very slowly. In such cases, the flow is quasi-steady. Therefore, the reduced frequency gives an indication of the nature of the flow.

The reduced frequency can also be interpreted differently. Consider the flow circulation around a blade. If the lift varies, this means that a variation of circulation was shed downstream of the blade, which, to a first approximation, convects at the flow speed U. Therefore when the blade vibrates at frequency ω, then the shed vortices

[1] In American literature L is taken as half-chord.

have travelled a distance equal to:

$$x = \frac{2\pi U}{\omega} \tag{1.3.3}$$

in one period of vibration. Inserting (1.3.3) into (1.3.2), the reduced frequency can be re-written as:

$$\bar{\omega} = \frac{2\pi L}{x} \tag{1.3.4}$$

From this equation, it is clear that a reduced frequency of one means that the vortices shed have propagated a distance of $2\pi L$ away from the blade. So these vortices are unlikely to interact with the blade, and the flow is likely to be steady. Similarly, a high reduced frequency means that the vortices move only a short distance away from the blade during on period of oscillation. Hence, the flow is likely to be unsteady. Note that the reduced frequency gives information about the nature of the flow, but not about the magnitude of unsteadiness.

The current drive towards low weight and high efficiency has forced turbomachinery designers to devise longer and thinner blades, causing their natural frequencies to decrease. Therefore, most self-excited aeroelastic problems occur at low reduced frequencies (or high reduced velocities - the inverse of reduced frequency). The design problems encountered at low and high reduced frequency are amusingly illustrated in Fig. 1.7.

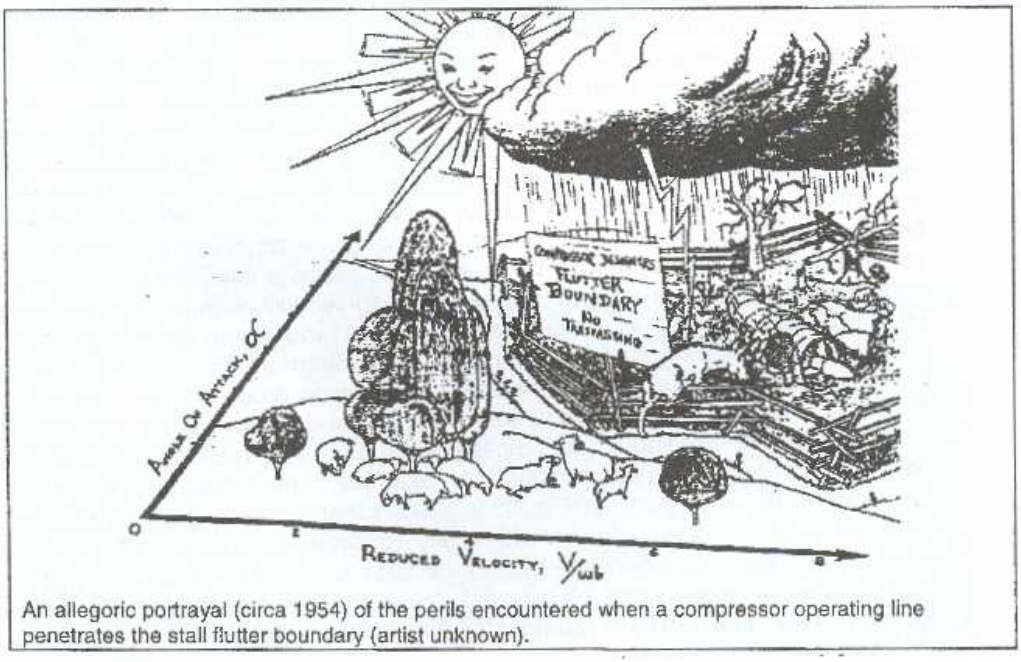

An allegoric portrayal (circa 1954) of the perils encountered when a compressor operating line penetrates the stall flutter boundary (artist unknown).

Figure 1.7: Reduced frequency issues; picture taken from Fransson [29]

Inter-blade Phase Angle

Lane [57] was the first researcher who introduced the inter-blade phase angle (IBPA). He used this parameter to analyse flutter on the assumption that all the blades from the same assembly were vibrating at the same frequency but with a phase shift between adjacent blades. The IBPA can be obtained from the knowledge of the assembly nodal diameter. The nodal diameter (ND) represents the number of diametrical lines at which the blades have zero plunging displacements. This is illustrated in Fig. 1.8. IBPA and ND are related by the following relationship:

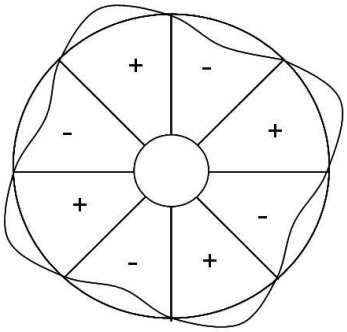

Figure 1.8: Four nodal diameter representation

$$\sigma = \frac{2\pi \times ND}{B} \tag{1.3.5}$$

where σ is the IBPA, and B is the number of blades in the current blade-row.

From an observer rotating with the blades, when the vibration mode is rotating in the same direction as the blades, it is said that the vibration mode is travelling forward, or that the nodal diameter number is positive. On the other hand, when the vibration mode is rotating in the direction opposite to the blades, it is said that the vibration mode is travelling backwards, or that the nodal diameter number is negative.

The IBPA is a parameter also used to analyse forced response. In such cases, the IBPA represents the unsteady flow field phase shift attached to adjacent blades in the same assembly resulting from the relative motion of the blade-rows. The IBPA is determined by the pitch ratio of neighbouring blade-rows as follows:

$$\sigma = \frac{2\pi n B_u}{B_c}, \tag{1.3.6}$$

where n is an integer, and B_u and B_c are the number of blades in the upstream and

current blade-rows respectively.

1.4 Noise

Although the generation of noise is not the major concern of this thesis, the propagation of acoustic waves, and thus of noise, will be discussed in following chapters as a convenient way to describe the origin of most unsteady phenomena in turbomachinery. This section gives a brief history of noise modelling in turbomachinery and it finishes with a brief description of traditional ways to measure noise.

1.4.1 A Brief History

The major problem due to turbomachinery noise is the nuisance that it causes to the environment. Roger [85] showed that aerodynamic noise produced by aircraft was recognised as the second most undesirable effect related to the traffic around urban areas, and maybe the first one in rural areas in 2000. All of the noise produced by aircraft does not come from the engines, the airframe also contributes significantly at low altitude, especially during take off and landing. In some cases, noise may also contribute to structural vibration, but fortunately, it does not usually lead to structural failure. Since the 1960s, the reduction of aeroplane noise has become a large area of research in order to meet the international standards around airports. The first significant piece of work on jet noise was done by Lighthill [63, 64], who introduced a technique called *acoustic analogy*. This formed the starting point to most analytical theories about aerodynamic noise. About ten years later, Ffowcs-Williams and Hawkings [28] applied the same theory to rotating machines. An important finding at the time was that the acoustic intensity radiated in jet noise was proportional to the eighth power of the jet velocity (the so-called Lighthill's eighth-power law), and only to the square of the diameter. Therefore, significant jet noise reduction from aircraft engines could be reached by decreasing the exhaust velocity, while keeping the thrust constant, i.e. by increasing the jet diameter. This result was the starting point of the progress made in the past 40 years, with the development of low- and then high- by-pass ratio engines. However, in modern turbofans, jet noise now is dominated by the noise of the fan itself. Rotor blades also produce noise. In most cases, the major part of the aerodynamic noise of a rotor is generated by blade loads. The noise spectrum of a rotor can be divided into two parts: (i) a broadband part due to random interaction with turbulence; (ii) a discrete-frequency part at the blade-passing frequency (i.e. number of blades

multiplied by the rotational speed) and its harmonics, due to all periodic interactions between the rotor and the flow. The latter is usually referred as rotational noise, and the use of frequency-domain time-linearised methods is suitable to study such phenomenon. The concerns with fan and rotor blades noise, together with the continuous restrictions with international standards, means that more work is still needed in this area.

1.4.2 Measures of Noise

The quantity of noise can be assessed by the determination of the frequencies and the magnitudes of acoustic waves. It is common practice to measure the sound pressure level (SPL) in decibel (dB) rather than in Pascal units. Since the noise level is very subjective to the nuisance it is causing, the acoustic pressure $\tilde{p}$ is normalised by a reference pressure $p_{ref} = 2 \times 10^{-5}$ (Pa), which is the rough limit of human hearing. The SPL is then given by:

$$SPL = 20 \times log_{10} \left(\frac{\tilde{p}}{p_{ref}} \right), \tag{1.4.7}$$

Another possible measure of sound is the acoustic power, or power watt level (PWL), in decibel (dB). It is defined as:

$$PWL = 20 \times log_{10} \left(\frac{\tilde{W}}{W_{ref}} \right), \tag{1.4.8}$$

where W_{ref} is the reference acoustic power usually equal to 10^{-12}. Depending on the study, the SPL and PWL may be integrated values over the whole range of frequencies covered by the signal, or else components of the spectrum at particular frequencies. Note that the non-integrated definition of the SPL will be used to measure the magnitude of acoustic waves in some blade-rows analysed in this thesis.

Chapter 2

Review of CFD Methods for Unsteady Flows in Turbomachinery

2.1 Introduction

A series of numerical methods for the computation of unsteady flows in turbomachinery are presented in this chapter. The chapter is divided in two parts. The first part gives a brief overview of the most popular methods of the past few decades for both analysis and design purposes. The second part presents a number of recent numerical methods which offer a compromise between computational accuracy and efficiency. The review is not exhaustive and other methods exist. The interested reader should refer to the references provided. The literature review was continued throughout the thesis and many of the later chapters have their own references.

2.2 Common CFD Methods

A very wide range of CFD methods have been developed since the first appearance of digital computers. A good assessment of unsteady flow modelling is given by Sharma *et al.* [101] and Verdon [120]. A review of these methods with emphasis on turbomachinery applications is given by Marshall and Imregun [67]. From the outset it is appropriate to divide these methods into three main categories: classical methods, frequency-domain time-linearised methods and fully nonlinear methods.

These methods have been widely used in the turbomachinery industry for many years.

2.2.1 Classical Methods

Classical methods first appeared in the 1970s. These methods have been designed to provide analytical or semi-analytical solutions to aerodynamic and aeroacoustic problems representative of turbomachinery applications. They are advantageous in the way that they are computationally very efficient and allow extensive parametric studies at low cost.

There are different types of classical methods but all are based on the same approximation which assumes that unsteady disturbances can be regarded as small compared to the mean flow. Each classical method uses one of the following theories: the linearised cascade theory, the singularity method, or the frequency panel methods (Marshall and Imregun [67]). Comprehensive reviews of 2-D and 3-D methods are given by Whitehead [124] and Namba [75] respectively. In the author 's opinion, the state of the art in classical methods in 2007 for aeroelasticity analysis is the 3-D multi blade-row method developed by Namba [77], which is based on the singularity method and the lifting surface theory. This method was designed to analyse multi blade-row flutter and forced response problems assuming axially uniform steady-state flows with zero steady-state blade loadings.

After years of extensive developments, classical methods cover a wide range of applications. However, their applicability is often under severe restrictions. They apply to flows inside or around configurations with simple geometries and, due to linearity, to phenomena where nonlinearity is not important. The mean flow is generally assumed to be inviscid, incompressible, uniform, either subsonic or supersonic, and the blades are often represented by flat plates which are not turning the flow. Such simplifications are acknowledged to be unrealistic to be representative of real turbomachinery, but they are certainly helpful to gain some insight into the physics.

Classical methods were initially used by researchers and designers as no other alternatives were available at the time. Nowadays, these methods are mostly used as to provide benchmark solutions for validating newly developed methods on simple test cases. A good example of such use is given in Chapter 6 where the classical method developed by Whitehead [124] is used to validate the unsteady flow solver developed in this thesis.

To finish the discussion on classical methods, it should be noted that despite the

development of more complicated theories, some of the unsteady aerodynamic analysis tools currently being used in preliminary aeroelastic and aeroacoustic design are still based on the classical linearised inviscid flow theory, essentially because of the speed of solution.

2.2.2 Frequency-domain Time-linearised Methods

Due to their complexity, real turbomachinery flows do not have any known analytical or semi-analytical solutions. Hence one should not exclusively rely on classical methods to determine unsteady flow integral parameters, which are needed to develop more efficient turbomachinery engines. With increasing computer capabilities, more advanced numerical methods were developed to include more physics. Two main methods became very popular: fully nonlinear, and frequency-domain (or harmonic) time-linearised methods. These two methods are based on some approximations of the flow governing equations, which are solved on a discretised domain using finite-difference, finite-element or finite-volume methods.

Historically, frequency-domain time-linearised methods appeared before nonlinear methods mostly because of the computational limitations. Like classical methods, harmonic linearised methods assume that unsteady perturbations can be regarded as small compared to the underlying steady-state flow. It is further assumed that perturbations are periodic in time, and thus they can be transformed into Fourier series. At every point of the discretised domain, this is mathematically expressed by:

$$\mathbf{U}(\mathbf{X},t) = \bar{\mathbf{U}}(\mathbf{X}) + \tilde{\mathbf{U}}(\mathbf{X},t) \tag{2.2.1}$$

where

$$\tilde{\mathbf{U}}(\mathbf{X},t) = \sum_{n=-\infty}^{+\infty} \hat{\mathbf{U}}_n(\mathbf{X}).e^{i\omega_n t} \tag{2.2.2}$$

and

$$\left|\tilde{\mathbf{U}}(\mathbf{X},t)\right| \ll \left|\bar{\mathbf{U}}(\mathbf{X})\right| \tag{2.2.3}$$

In these expressions, the vector $\mathbf{X}$ includes all the points of the computational domain at which the solution is computed, $\bar{\mathbf{U}}$ is the vector of steady-state primitive variables, and $\tilde{\mathbf{U}}$ is the corresponding vector of unsteady perturbation. By inserting these expressions into the flow governing equations, one can solve separately the unsteady perturbation for each Fourier harmonic n. In fact, for each harmonic the time derivative $\frac{\partial}{\partial t}$ is replaced by $i\omega_n$, and the unsteady equations become linear with variable coefficients depending only on the steady-state solution. Using a pseudo-time τ, the linearised equations become mathematically steady, and can be time-

marched in pseudo-time until a steady solution is reached. More details will be given in Chapter 4.

The linearisation of the flow governing equations offers many advantages. First, it enables the use of very efficient acceleration techniques, which were initially developed to compute steady-state solutions, such as preconditioning, local time-stepping, and multigrid. Second, by assuming that the unsteady solution is periodic around the whole annulus and by defining an inter-blade phase angle, the whole-annulus computational domain can be reduced to a single blade-passage. Lastly, the theory assumes an isolated blade-row in an infinitely long duct, thus ignoring potentially important multi blade-row effects. Such considerations allow significant computational saving to be made compared, for example, to fully nonlinear time-accurate unsteady methods which will be presented later. However, computational resources and computational time are still much higher than those required by classical methods. Harmonic linearised methods have greatly evolved along with time using successively the linearised potential, Euler, and Navier-Stokes equations.

Linearised Potential Methods

Potential methods are good examples for showing how significant simplifications to the flow equations can be made. In these methods, the flow is considered inviscid, and it is further assumed that the flow velocities can be derived from a scalar function ψ, so that $\mathbf{v} = \bigtriangledown\psi$. This also means that the flow is *irrotational*, since $\bigtriangledown \times \mathbf{v} = 0$. If the initial conditions are compatible with uniform entropy, then for continuous flows, the entropy is constant over the whole flow field. Therefore, potential methods assume *isentropic* flows which may be a serious limitation in some practical applications. For example, for cases where the flow is transonic, the flow solution may have shock waves. In reality, the entropy increases across shocks, as can be seen from the well-known Rankine-Hugoniot relations. However, it can easily be demonstrated that the isentropic assumption across a shock discontinuity satisfies the conservation of mass and energy but not of momentum. For low incoming supersonic Mach numbers, the isentropic assumption may still be acceptable, since the error on Mach number and pressure loss predictions is small. However, for higher Mach numbers, the isentropic assumption does not hold anymore, and may lead to inaccurate flow predictions. Potential methods have further shortcomings like, for example, the determination of the "true" shock position. Using the isentropic assumption, there is no mechanism which links the shock position to the outlet conditions. The same outlet value allows an infinite number of equally valid solutions, which are all different to the Euler solution. Some "fixes" have been developed by

several authors to tackle these problems. The interested reader can refer to the book by Hirsch [49]. The first significant works on linearised potential methods were done by Whitehead [125], and Verdon *et al.* [122, 121, 123, 119], who developed similar methods to solve the problems of blade motion (flutter) for bending or torsional mode. Later, linearised potential methods have been used, for example, by Hall and Verdon [43] and Caruthers and Dalton [15] to study the effect of incident vortical and entropic gust, and by Suddhoo *et al.* [107, 108] for the modelling of stator/rotor interaction. These methods have been used in the turbomachinery industry for many years due to their high computational efficiency. However, they are only applicable when the mean flow is irrotational, subsonic, and weakly transonic. Extensions to model accurately flows with strong shocks, three-dimensional rotational flows, and flows with unsteady wakes are extremely difficult. Therefore, these methods were later replaced by better approximations using either the Euler or Navier-Stokes equations.

Linearised Euler Methods

Time-linearised Euler methods are applicable to rotational, non-isentropic, transonic flows, in which unsteady disturbances are small compared to the steady-state flow. Unlike potential flow equations, the Euler equations account for the generation of vorticity and entropy at shocks. Hence, methods using the Euler equations are much more accurate than potential methods for simultating flows containing shocks. However, shocks still cause problems since flow perturbations cannot be considered as negligible compared to the steady-state flow across the shock (Fig. 2.1). Ni and Sisto [78] were amongst of the first to develop a time-linearised Euler solver. At the time, they applied their code to the study of two-dimensional flat plate cascades with homentropic flows. Later, Hall [38] introduced a two-dimensional time-linearised Euler solver using a shock fitting technique. In this work, unsteady flows produced by blade motion (the flutter problem) and incoming disturbances (the gust-response problem) were analysed. Shocks and wakes were modelled using shock fitting boundary conditions, which allowed a linear model to be valid, even across shocks. Importantly, this work demonstrated that the linearity assumption holds up to quite a substantial level of unsteadiness. However, a serious limitation with this method was that shocks had to be aligned with a computational grid line on a logically rectangular grid, allowing only the modelling of normal shocks on fairly unskewed grids. As a consequence, transonic flows through staggered cascades could not be analysed using this approach. An important subsequent work is the proof by Lindquist and Giles [65]: if correctly implemented, shock capturing methods can provide the same correct answer as shock fitting techniques. Lindquist and Giles [65],

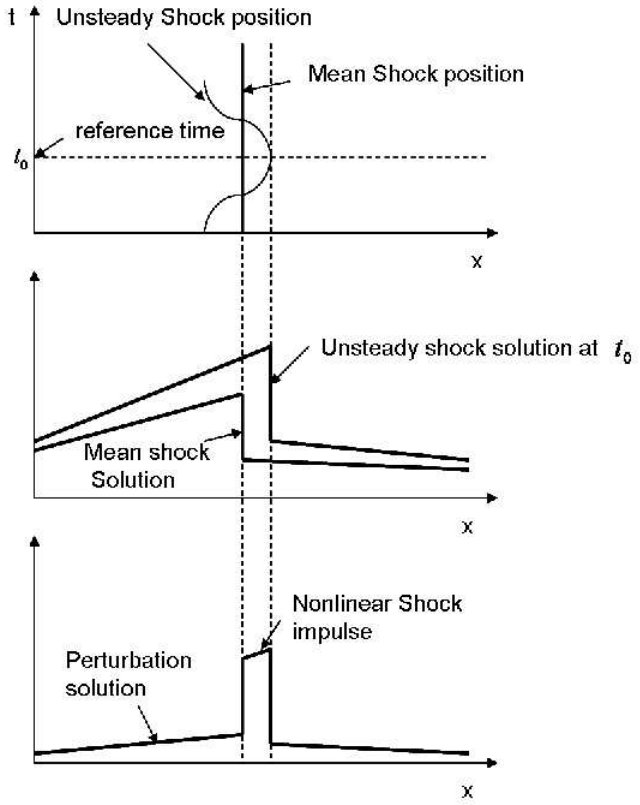

Figure 2.1: Shock impulse (pressure) representation

and later Hall *et al.* [37], demonstrated that, in order to obtain the correct shock impulse, three conditions should be respected: (i) a conservative discretisation of the Euler equation must be used; (ii) enough artificial viscosity must also be used so that the shape of the shock is better preserved and the magnitude of error is reduced; (iii) the shock must be smeared over several grid points. Another interesting finding from Giles was that when coarse meshes are used, predictions with low artificial viscosity are better represented, but when the mesh is fine, the results do not vary much. Hence, most subsequent works logically used shock capturing techniques because it is much easier to implement, and one does not have to know in advance the shock's position. Another important achievement was the development by Hall [36] of a two-dimensional time-linearised Euler solver with a harmonic mesh motion. It was found that harmonic mesh motion eliminates large error-producing mean flow gradient terms that appear in the unsteady flow tangency boundary conditions when a static mesh is used for the simulation of vibrating blades. This method had already been used for nonlinear methods, but Hall [36] was one of the first to use it for linear methods. It was demonstrated that the deformable grid technique significantly improves the accuracy of the time-linearised Euler solution for flutter. His solver was used to treat incident gust and vibratory blade motion problems.

From there, a large number of papers have been dedicated to the development of two-dimensional [50], quasi three-dimensional [80], and then three-dimensional time-linearised Euler solvers [40, 37]

Linearised Navier-Stokes Methods

Many researchers have now successfully incorporated the Reynolds-Averaged Navier-Stokes equations with a turbulence model into their time-linearised code [19, 51, 9, 11, 12, 79, 80]. As seen in Chapter 1, flow fields in real turbomachines are often driven by viscous effects that cannot be captured by the Euler equations. The wake that is produced at the blade's trailing edge is one such effect. Hence, the Navier-Stokes equations offer the possibility to study wake-interaction problems. A noteworthy remark is that although the wake generation is a phenomenon of viscous nature, there is a growing body of evidence that its subsequent interaction with the downstream blade-row is mostly an inviscid process. Other important features of the flow influenced by viscous effects can also be captured by the Navier-Stokes equations such as: boundary layer, secondary flow effects, correct mass flow in passage, tip-leakage flows, etc. The advantage of the Navier-Stokes equations over the Euler equations is that they offer more possibilities to study unsteady flows at off-design conditions, where viscous effects are not limited to the boundary layer. However, the major drawback is that potentially important nonlinear unsteady effects are not included in the model.

2.2.3 Nonlinear Time-marching Methods

In the category of computationally expensive but accurate methods, one can find fully nonlinear methods. Nonlinear methods aim to solve the flow governing equations without any restriction regarding the size of the unsteadiness. This way all types of nonlinear effects are included in the analysis. For most analyses, it is not affordable to solve directly the flow governing equations using Direct Numerical Simulation (DNS) or Large Eddy Simulation (LES). Therefore, a popular approach is to use a turbulence model to represent viscous effects. The same approach has also been used for harmonic linearised methods. In nonlinear methods, the flow governing equations are time-marched in "real" time and they are solved at several time intervals until a periodic solution is found. Typically, a *dual time-stepping* method can be used [92]; external Newton iterations are employed to ensure time accuracy, and within each Newton iteration, steady-state flow solution techniques are used

to drive the solution to convergence. Such methods provide more comprehensive modelling capabilities, but they also require substantial computational resources.

The first significant piece of work on nonlinear methods was done by Erdos [27], who presented a 2-D nonlinear inviscid solver to compute the unsteady flow in a fan stage by reducing the computational domain to one blade-passage per blade-row. What made his work remarkable was that it was the first time that a method enabling the reduction of the computational domain to one blade-passage was presented. The main problem at the time was the poor computational resources. It was primordial to find a way to reduce the computational domain from whole-annulus multi-blade-row to only a few blade-passage. In order to achieve this, Erdos used a specific algorithm, the *direct store* method, to treat the problem of unequal pitches. He introduced the new concept of phase-shifted boundary conditions at the periodic boundaries. The upper periodic boundary condition was expressed by:

$$\bar{\mathbf{U}}(x,\theta,t) = \mathbf{U}(x,\theta-\delta\theta,t-\delta t) \tag{2.2.4}$$

where $\delta\theta$ represents the computational pitch and δt is a time lag determined by:

$$\delta t = \frac{\delta\theta_s - \delta\theta_r}{\Omega} \tag{2.2.5}$$

with $\delta\theta_s$ and $\delta\theta_r$ respectively representing the stator and rotor pitches, and Ω is the rotor rotational speed. The boundary condition at the lower periodic boundary assumed that the flow was periodic in time, the period being equal to the blade passing one:

$$T = \frac{\delta\theta}{\Omega} \tag{2.2.6}$$

This work was later pursued by Koya [56], who extended the method to 3-D and used it for the computation of a wake/rotor problem in a low speed turbine. Almost at the same time, Rai [83, 84] developed a 2-D and then a 3-D Navier-Stokes solver to compute stator/rotor problems using one blade-passage domain per blade-row and a direct periodicity boundary condition. In this work, the direct periodicity boundary condition could be used at the periodic boundaries by artificially modifying the rotor blade-passage pitch so as to equalize the stator blade pitch. In this process, Rai always ensured that the rotor pitch-to-chord ratio remained unchanged. A large number of papers dedicated to these methods can be found in the literature and a fairly comprehensive list of them is given by Giles [33]. A widespread technique that was used in the industry for years to reduce the computational effort was to adjust the real number of blades in each blade-row, so that the pitch ratio of each blade-row would become simple, such as 1:1, 2:3 or 3:4. This implies that

only the corresponding number of blade-passages per blade-row need to be included in the computational domain using a direct periodicity boundary condition. For example, consider a stator/rotor problem where the exact number of blades are 36:73 respectively. The modification consists in reducing the number of rotor blades to 72, so that the pitch ratio stator/rotor becomes 1:2. Only one blade-passage in the stator and two blade-passages in the rotor are now necessary in the computational domain, instead of 36 and 73 given initially. This technique had the non-negligible advantage to reduce considerably the computational effort and to fit with the computational capabilities of the time. However, it was soon discovered [83, 3] that even though the steady-state results could be reasonably good, unsteady results could be extremely inaccurate when modifying the real number of blades. In fact, the blade loading changes, and a large part of the unsteady blade-rows coupling, which is achieved through the propagation of acoustic waves, is largely dependent on the real number of blades.

In order to avoid this problem, Giles [30] created a new method using *time-tilted* computational planes to handle arbitrary stator/rotor pitch ratios thanks to a genuine time-space transformation. This method allowed the blade ratios to be reduced to 1:1 without any loss of physical representation. Giles coded his method into a program called UNSFLO, which has been successfully applied to many practical cases [26, 53, 66]. However, there are two important drawbacks with this method. The first one is that there is a limitation on the time-tilted parameter for stability. The number B of blade-passages to include in the analysed blade-row is determined such that the ratio of the number of blades in the current blade-row to the number of blades in the adjacent blade-row satisfies:

$$\frac{\mathbf{RATIO}}{B} < 1.5. \tag{2.2.7}$$

For example, if the first blade-row has 40 blades, and the second blade-row 92 blades, then $RATIO = 2.3$ and the number of blade-passages to be included in the computational domain for the downstream blade-row must be equal to 2. The second limitation is that this technique could not be extended to more than two blade-rows when limiting the calculation to one blade-passage per blade-row. To understand this further, consider a problem including three blade-rows, in which the number of blades in the first and second rows is different with no common factor. Then each blade-passage in the third row experiences a different unsteady aerodynamic forcing according to its position relative to the first row. There is no mathematically correct way to solve this problem except to include the whole three blade-rows in the computation.

Since the first appearance of Erdos' and Giles' techniques, computing resources have enormously increased. Because of this, modelling techniques have also evolved and computations that would not have been practically possible a few decades ago, are now routine for designers. The physical assumptions included in nonlinear methods have logically evolved from the 2-D Euler to the 3-D Navier-Stokes equations. Nowadays, most nonlinear solvers use the 3-D Navier-Stokes equations, but these are solved with various degrees of approximations. One can find in the literature three major nonlinear unsteady methods known as: the whole-annulus model, the sliding plane plus upstream/downstream blade-passage model, and the unsteady single-passage model. These three methods can theoretically be developed starting from the same baseline code, i.e. from the same discretisation scheme, but they generally differ in the boundary conditions they apply.

Whole-annulus Model

The whole-annulus model [91, 93], also known as *multi-passage* model, consists of whole-annulus multi blade-rows in the computational domain. An example for nine blade-rows is presented in Fig. 2.2. This method is the most straightforward and

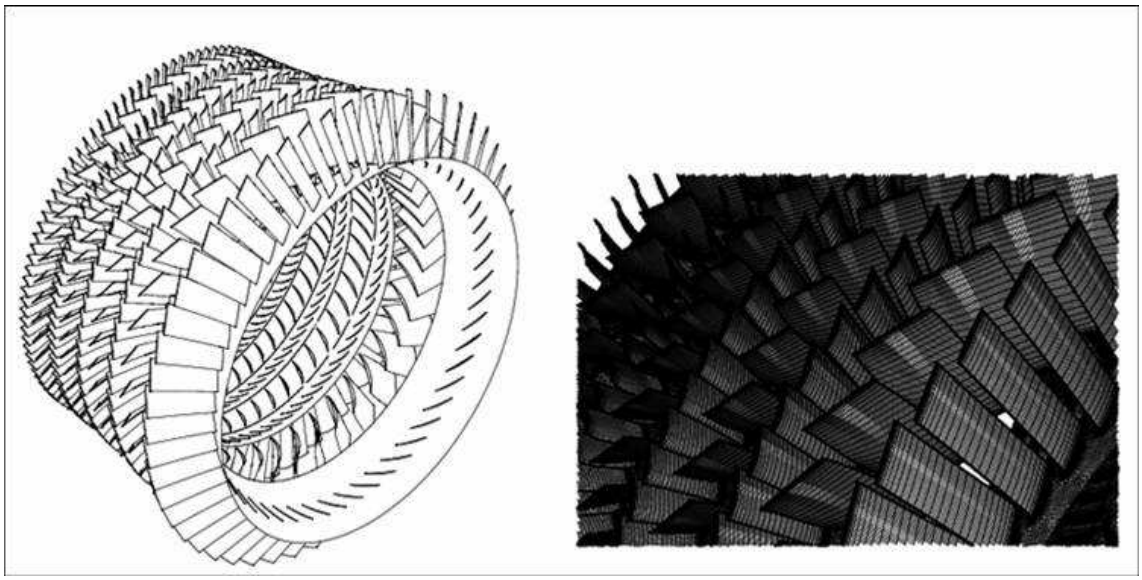

Figure 2.2: Core compressor whole-annulus model; from Vahdati [115]

accurate, but also the most expensive way to compute an unsteady solution. When the geometry allows it, i.e. when the number of blades in each blade-row have at least one common dividing factor, common practice is to truncate the computational domain by including only as many passages so that the computational sectors have the same circumferential length in each blade-row [94, 92, 95, 59]. This truncation

is possible thanks to what is called a *direct periodicity* boundary condition, applied between the first and the last passages of each blade-row. Note that the truncation of the number of blade-passages may lead to serious errors in some practical cases. In fact, the circumferential length covered by each blade-row must coincide between the blade-rows and it must include one or several periods of unsteadiness for the analysis to obtain accurate unsteady flow predictions. However, when a broadband signal, which includes a wide range of frequencies is created in one of the blade-rows, it may be extremely difficult, or even impossible, to find a location for the two periodic boundaries where the periods of the signal are all in phase. This situation is all the more problematic for multi-blade-row analysis, since it is likely that the periodic signals generated in one blade-row are not contained in another one.

Sliding Plane plus Upstream/Downstream Blade-passage Model

The sliding plane plus upstream/downstream blade-passage model was initially designed to reduce the effort required for the computation of forced response in any stator/rotor stage. The corresponding methodology is as follows. The stator and

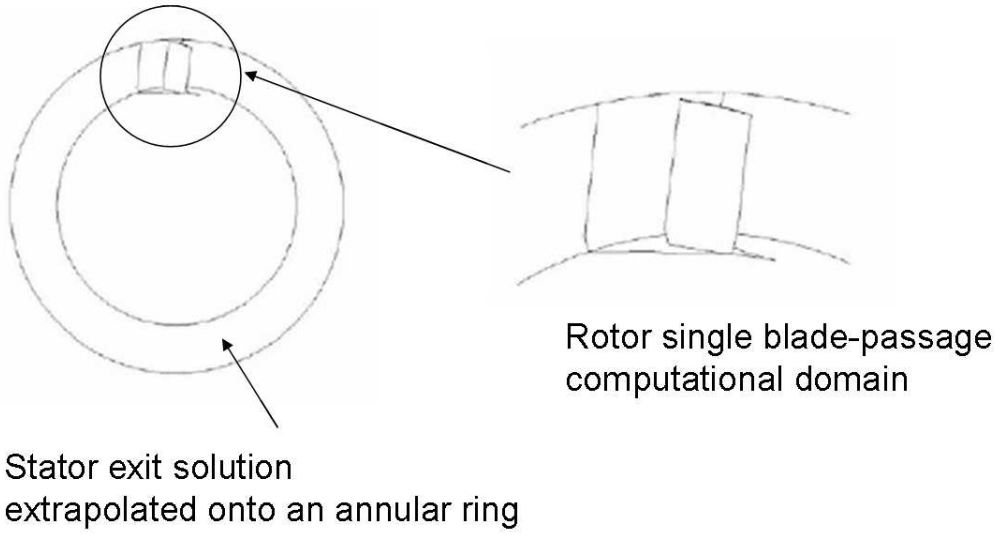

Figure 2.3: Sliding plane plus upstream/downstream blade-passage model representation

rotor steady-state solutions are first computed on a single blade-passage using a mixing-plane boundary condition between the blade-rows. Then, the stator outflow solution is extrapolated onto a ring covering the whole annulus (Fig. 2.3). Since the stator ring is rotating relatively to the rotor blade-row, it is used to impose the inflow boundary condition for the computation of the unsteady flow into the rotor.

The stator/rotor interaction is considered to be a periodic phenomenon with fundamental frequency in the rotor equal to the blades passing frequency. Therefore, the computation of the flow in the rotor can be reduced to a single-passage thanks to the use of a *phase-shifted boundary condition* at the periodic boundaries. This method was, for example, successfully used for the rapid assessment of forced response in a HP turbine stage [54]. The major drawback with this technique is that the computation of the unsteady flow in the rotor depends on the stator solution (wake), but no interaction is accounted for the other way around. This is only a one-way interaction method.

Unsteady Single-passage Model

The unsteady single-passage model has its roots into Erdos' *direct store* and Giles' *time-tilted* techniques which aimed at reducing the computational domain to single-passages. Even though Giles' technique did not assume any particular number of blades, it was limited by restrictions on the time-tilted parameter if used with single-passages. In order to avoid this problem, Li and He [58] created a new unsteady passage model, which uses a *phase-shifted* boundary condition in the form of *shape correction*. The novelty of this method is that it can compute unsteady flows under multiple perturbations.

Consider a general unsteady flow under a number N_{pt} of unsteady disturbances. The flow variables at the periodic boundaries can be expressed as:

$$U\left(x,y,z,t\right) = U_0\left(x,y,z\right) + \sum_{i=1}^{N_{pt}} U_i\left(x,y,z,t\right) \tag{2.2.8}$$

where U_0 represents the "time-averaged" and not the "steady-state" flow, and U_i is the i-th component of the unsteady flow induced by the i-th disturbance. The latter can be decomposed into Fourier series:

$$U_i\left(x,y,z,t\right) = \sum_{n=1}^{N_{Fou}} \left[A_{i,n}(x,y,z)sin\left(n\omega_i t\right) + B_{i,n}(x,y,z)cos\left(n\omega_i t\right)\right] \tag{2.2.9}$$

where N_{Fou} is the number of Fourier harmonics included in the analysis (typically equal to 5), and ω_i is the frequency of the i-th disturbance. Defining "pairs" of nodes at the periodic boundaries, the flow at the lower periodic boundary can be

expressed as:

$$U(x,y,z,t) = U_0(x,y,z) + \sum_{i=1}^{N_{pt}} \sum_{n=1}^{N_{Fou}} [A_{i,n}(x,y,z)sin(n\omega_i t) + B_{i,n}(x,y,z)cos(n\omega_i t)] \tag{2.2.10}$$

and the flow at the upper boundary as:

$$U(x,y,z,t) = U_0(x,y,z) + \sum_{i=1}^{N_{pt}} \sum_{n=1}^{N_{Fou}} [A_{i,n}(x,y,z)sin(n(\omega_i t + \sigma_i)) + B_{i,n}(x,y,z)cos(n(\omega_i t + \sigma_i))] \tag{2.2.11}$$

where σ_i is the inter-blade phase angle of the i-th disturbance. It should be emphasised that this method is not linear since the development into Fourier series does not include any linear assumption.

The method was first applied to the analysis of flutter [46] and flutter under inlet distortion [58], by modelling a blade-row in isolation. Note that for the latter analysis, the unsteady flow computations could include both perturbations at the same time despite the fact that they occurred at different frequencies and with different wavelengths.

Later, Li and He extended this methods to multi blade-row single-passage unsteady calculations, using two [60, 21] and then three [61] blade-rows. Due to the relative motion of the blade-rows, a temporal phase shift is required between the upstream and downstream blade-rows, which was expressed by:

$$\mathbf{U}_{DF}(t) = \mathbf{U}_{UA}(t + NP_F \frac{\sigma_U}{\omega_U}) \tag{2.2.12}$$

where the subscripts D, U, F, and A stand for downstream, upstream, fictitious and actual blade-passage respectively, σ_U and ω_U are the upstream disturbance inter-blade phase angle and frequency, and NP_F is an integer expressing which upstream fictitious blade-passage is adjacent to the downstream blade-passage at time t.

Importantly, this methodology offers great reductions in computing time and data storage compared to whole-annulus methods, and also compared to Erdos' technique. Indeed, in the *direct store* method the variables at the periodic boundaries were stored at each iteration for entire periods of the disturbance, whereas in Li and He 's technique, only Fourier coefficients are stored at the end of each time period. The CPU run-time represents typically between 10 % and 15 % of that of the whole-annulus model [21].

In the general context where each disturbance can be represented by an inter-blade phase angle and a frequency, the accuracy of the single-passage shape correction

method is comparable to that of whole-annulus method. However, it should be noted that the single-passage method is not completely accurate for unsteady analyses including more than two blade-rows. In fact, it is shown in the three blade-row analysis of [61] that the unsteady interactions between the first and the last blade-rows can generate aperiodicity in the downstream blade-row, which could not be represented by the single-passage shape-correction method, thus these effects had to be ignored in this analysis.

2.3 Conclusions on Common Methods

The most common CFD methods that were developed by researchers to solve aerodynamic, aeroelastic, and/or aeroacoustic problems in turbomachinery have been discussed in this section. These methods were divided into three main categories, namely: classical, harmonic linearised, and fully nonlinear time-accurate methods. Table (2.1) gives a brief overview based on two important criteria: (i) computational time; (ii) accuracy. The computational time (CT) for each method is given as an "estimated" percentage of what would be required if a nonlinear whole-annulus model were used. This percentage is based on information that were given in published articles for cases when the number of blades in adjacent blade-rows do not have any common factor. Where applicable, the analysis is assumed to be 3-D viscous. However, one should be aware that computational times heavily depend on the test case being studied and on the convergence quality of the numerical model being used. These two aspects could not be taken into account in these comparisons and results are given as reported.

From a designer's point of view, it is highly desirable to have a numerical method that is both accurate and efficient. This enables a rapid assessment of new geometries, so that they can be re-designed as quickly as possible if necessary. However, none of the above mentioned techniques meets, at least today, both requirements simultaneously. Having said that, fully nonlinear methods including the whole-annulus multi blade-rows are the most promising for the next few decades due to the expected exponential increase in computational resources. However, these nonlinear methods are not suitable for design use in the foreseeable future. Therefore, more efficient methods need to be developed, which is the subject of the next section.

Method Category	Advantages	Disadvantages	CT (%)
Classical	- Very fast	- Simple geometries - Simple flows	Insignificant
Harmonic linearised	- Fast	- Nonlinear effects ignored - Multi blade-row effects ignored	1 - 5
Nonlinear (Sliding plane)	- Fast - Nonlinear effects included	- One way only multi blade-row effects included	10 - 15
Nonlinear (Single passage)	- Fast - Nonlinear effects included - Multi blade-row effects included	- Issues with modelling more than two blade-rows	10 - 15
Nonlinear (whole model)	- All nonlinear effects included	- Slow	100

Table 2.1: Comparisons pros and cons of conventional CFD methods for turbomachinery applications

2.4 Review of Harmonic Methods

The need to obtain a compromise between computational accuracy and efficiency led researchers to create several novel numerical methods. However, the review that is given in this section focuses on one category only, **harmonic methods**, which have emerged in the past ten years. This decision was motivated by three important observations:

- There are three types of physical effects which are not accounted for in conventional harmonic time-linearised methods. To start with, the unsteady solution is decomposed into a steady-state solution and a small unsteady perturbation. Therefore, all nonlinear effects caused by large amplitude perturbations are not represented. Solutions are sought in the frequency domain, and the solution for each frequency is computed independently. Hence, nonlinear interactions between perturbations at different frequencies are not accounted for. Finally, the computational domain used for conventional harmonic methods is restricted to a single blade-passage in a single blade-row, hence ignoring potentially important multi blade-row effects. However, as it will be seen later, it is possible to include any of these physical effects in harmonic methods.

- Because a pseudo-time is usually introduced in these methods, the unsteady

flow equations become mathematically steady and can be time-marched in pseudo-time using very efficient acceleration techniques such as local time-stepping and multigrid methods. Therefore, these methods are usually very efficient.

- Unlike nonlinear methods, harmonic methods are well suited to adjoint sensitivity techniques, which are useful for design purposes. What makes nonlinear methods inappropriate for this is that adjoint methods require that the entire time history of the flow computation to be stored, which could be prohibitively expensive.

In the following, four harmonic methods are described: the SLIQ approach, the nonlinear harmonic method, the harmonic balance method, and the harmonic time-linearised multi blade-row method.

2.4.1 SLIQ Approach

The SLIQ approach was created by Giles [34, 32]. This method is based on the observation that the unsteadiness may change the mean flow parameters, such as mass flow rate and efficiency. Using traditional time-linearised methods, the flow solution is divided into a steady-state value plus a small (first-order) unsteady perturbation. The steady-state solution is first determined using a steady-state solver, then a harmonic linearised solution is computed, which is based on the steady-state solution. Since the time-average of the first order linear term is zero, and the steady-state solution does not depend on the linearised unsteady solution, the effects of unsteadiness on the steady-state flow are completely neglected.

Based on this observation, Giles [34] decided to include the *quadratic* terms in the series expansion of the conservation variables. This is where the SLIQ name comes from: Steady/LInear/Quadratic. Giles' idea originated from the earlier work of Adamczyk [1], who formulated a system of passage-averaged equations, in which the effect of unsteadiness was included to the mean flow through terms similar in nature to the Reynolds averaged stress terms.

The SLIQ equations are detailed below for the case of the two-dimensional Euler equations. The conservative form of the 2-D Euler equations are recalled here for completeness:

$$\frac{\partial \mathbf{U}}{\partial t} + \frac{\partial \mathbf{F}}{\partial x} + \frac{\partial \mathbf{G}}{\partial y} = 0 \tag{2.4.13}$$

where $\mathbf{U}$ is the vector of conservative variables, $\mathbf{F}$ and $\mathbf{G}$ represent the fluxes in the x and y directions, given by:

$$\mathbf{U} = \begin{pmatrix} \rho \\ \rho u \\ \rho v \\ \rho E \end{pmatrix}, \mathbf{F} = \begin{pmatrix} \rho u \\ \rho uu + p \\ \rho uv \\ (\rho E + p)u \end{pmatrix}, \mathbf{G} = \begin{pmatrix} \rho v \\ \rho uv \\ \rho vv + p \\ (\rho E + p)v \end{pmatrix} \tag{2.4.14}$$

The asymptotic expansion of the conservation variables is written as follows:

$$\mathbf{U}(\mathbf{X}, t) = \mathbf{U}^{(0)}(\mathbf{X}) + \epsilon \mathbf{U}^{(1)}(\mathbf{X}, t) + \epsilon^2 \mathbf{U}^{(2)}(\mathbf{X}, t) + .. \tag{2.4.15}$$

where ϵ represents some level of unsteadiness. In this form, one recognises the first two right hand side terms used in conventional linearised methods. The first term $\mathbf{U}^{(0)}$ represents the steady-state solution, and the second term $\mathbf{U}^{(1)}$ represents the conventional time-linearised frequency-domain solution. An additional quadratic term $\mathbf{U}^{(2)}$ is also introduced in (2.4.15), for which the time-average is not equal to zero. By neglecting the higher order terms, the time-average of the conservation variables can be approximated by:

$$\bar{\mathbf{U}}(\mathbf{X}, t) = \mathbf{U}^{(0)}(\mathbf{X}) + \epsilon^2 \bar{\mathbf{U}}^{(2)}(\mathbf{X}, t) \tag{2.4.16}$$

In the same manner, it is also possible to obtain approximations for the asymptotic expressions for the fluxes $\mathbf{F}(\mathbf{U})$ and $\mathbf{G}(\mathbf{U})$:

$$\begin{aligned} \mathbf{F}_i(\mathbf{U}^{(0)} + \epsilon \mathbf{U}^{(1)} + \epsilon^2 \mathbf{U}^{(2)}) &= \mathbf{F}_i(\mathbf{U}^{(0)}) + \epsilon \left(\frac{\partial \mathbf{F}_i^{(0)}}{\partial \mathbf{U}_j} \mathbf{U}_j^{(1)} \right) \\ &\quad + \epsilon^2 \left(\frac{\partial \mathbf{F}_i^{(0)}}{\partial \mathbf{U}_j} \mathbf{U}_j^{(2)} + \frac{1}{2} \frac{\partial^2 \mathbf{F}_i^{(0)}}{\partial \mathbf{U}_j \partial \mathbf{U}_k} \mathbf{U}_j^{(1)} \mathbf{U}_k^{(1)} \right) \end{aligned} \tag{2.4.17}$$

and

$$\begin{aligned} \mathbf{G}_i(\mathbf{U}^{(0)} + \epsilon \mathbf{U}^{(1)} + \epsilon^2 \mathbf{U}^{(2)}) &= \mathbf{G}_i(\mathbf{U}^{(0)}) + \epsilon \left(\frac{\partial \mathbf{G}_i^{(0)}}{\partial \mathbf{U}_j} \mathbf{U}_j^{(1)} \right) \\ &\quad + \epsilon^2 \left(\frac{\partial \mathbf{G}_i^{(0)}}{\partial \mathbf{U}_j} \mathbf{U}_j^{(2)} + \frac{1}{2} \frac{\partial^2 \mathbf{G}_i^{(0)}}{\partial \mathbf{U}_j \partial \mathbf{U}_k} \mathbf{U}_j^{(1)} \mathbf{U}_k^{(1)} \right) \end{aligned} \tag{2.4.18}$$

Matching together the terms of equal power of ϵ gives:

$$\frac{\partial \mathbf{F}(\mathbf{U}^{(0)})}{\partial x} + \frac{\partial \mathbf{G}(\mathbf{U}^{(0)})}{\partial y} = 0 \tag{2.4.19}$$

$$\frac{\partial \mathbf{U}_i^{(1)}}{\partial t} + \frac{\partial}{\partial x}\left(\frac{\partial \mathbf{F}_i^{(0)}}{\partial \mathbf{U}_j}\mathbf{U}_j^{(1)}\right) + \frac{\partial}{\partial y}\left(\frac{\partial \mathbf{G}_i^{(0)}}{\partial \mathbf{U}_j}\mathbf{U}_j^{(1)}\right) = 0 \tag{2.4.20}$$

$$\begin{aligned}\frac{\partial \mathbf{U}_i^{(2)}}{\partial t} + \frac{\partial}{\partial x}\left(\frac{\partial \mathbf{F}_i^{(0)}}{\partial \mathbf{U}_j}\mathbf{U}_j^{(2)}\right) + \frac{\partial}{\partial y}\left(\frac{\partial \mathbf{G}_i^{(0)}}{\partial \mathbf{U}_j}\mathbf{U}_j^{(2)}\right) &= -\frac{1}{2}\frac{\partial}{\partial x}\left(\frac{\partial^2 \mathbf{F}_i^{(0)}}{\partial \mathbf{U}_j \partial \mathbf{U}_k}\mathbf{U}_j^{(1)}\mathbf{U}_k^{(1)}\right) \\ &\quad -\frac{1}{2}\frac{\partial}{\partial y}\left(\frac{\partial^2 \mathbf{G}_i^{(0)}}{\partial \mathbf{U}_j \partial \mathbf{U}_k}\mathbf{U}_j^{(1)}\mathbf{U}_k^{(1)}\right)\end{aligned} \tag{2.4.21}$$

Equation (2.4.19) represents the well-known steady-state equations, while (2.4.20) represents the time-linearised equations. In harmonic methods, it is further assumed that the first-order linear solution is periodic in time at frequency ω. As a consequence, the solution $\mathbf{U}^{(1)}$ can be represented as a sum of components of the form $\hat{\mathbf{U}}(\mathbf{X})e^{i\omega t}$, which can be computed separately. Therefore, (2.4.20) can be re-written as follows:

$$i\omega \hat{\mathbf{U}}_i + \frac{\partial}{\partial x}\left(\frac{\partial \mathbf{F}_i^{(0)}}{\partial \mathbf{U}_j}\hat{\mathbf{U}}_j\right) + \frac{\partial}{\partial y}\left(\frac{\partial \mathbf{G}_i^{(0)}}{\partial \mathbf{U}_j}\hat{\mathbf{U}}_j\right) = 0 \tag{2.4.22}$$

Taking the time-average of (2.4.21) gives:

$$\begin{aligned}\frac{\partial}{\partial x}\left(\frac{\partial \mathbf{F}_i^{(0)}}{\partial \mathbf{U}_j}\overline{\mathbf{U}_j^{(2)}}\right) + \frac{\partial}{\partial y}\left(\frac{\partial \mathbf{G}_i^{(0)}}{\partial \mathbf{U}_j}\overline{\mathbf{U}_j^{(2)}}\right) &= -\frac{1}{2}\frac{\partial}{\partial x}\left(\frac{\partial^2 \mathbf{F}_i^{(0)}}{\partial \mathbf{U}_j \partial \mathbf{U}_k}\overline{\mathbf{U}_j^{(1)}\mathbf{U}_k^{(1)}}\right) \\ &\quad -\frac{1}{2}\frac{\partial}{\partial y}\left(\frac{\partial^2 \mathbf{G}_i^{(0)}}{\partial \mathbf{U}_j \partial \mathbf{U}_k}\overline{\mathbf{U}_j^{(1)}\mathbf{U}_k^{(1)}}\right)\end{aligned} \tag{2.4.23}$$

Finally, adding together the steady-state equations assembled in (2.4.19) to (2.4.23) gives the equation for the time-averaged variables:

$$\begin{aligned}\frac{\partial \mathbf{F}_i(\bar{\mathbf{U}})}{\partial x} + \frac{\partial \mathbf{G}_i(\bar{\mathbf{U}})}{\partial y} &= -\frac{\epsilon^2}{2}\frac{\partial}{\partial x}\left(\frac{\partial^2 \mathbf{F}_i^{(0)}}{\partial \mathbf{U}_j \partial \mathbf{U}_k}\overline{\mathbf{U}_j^{(1)}\mathbf{U}_k^{(1)}}\right) \\ &\quad -\frac{\epsilon^2}{2}\frac{\partial}{\partial y}\left(\frac{\partial^2 \mathbf{G}_i^{(0)}}{\partial \mathbf{U}_j \partial \mathbf{U}_\mathbf{k}}\overline{\mathbf{U}_j^{(1)}\mathbf{U}_k^{(1)}}\right)\end{aligned} \tag{2.4.24}$$

The strategy that SLIQ uses to obtain the solution of (2.4.24) is as follows. First, the steady-state solution is computed using (2.4.19). Secondly, the harmonic linearised solution is computed using (2.4.20). Finally, the solution of (2.4.24) can be computed since the steady-state and the linear solutions are already known. These three procedures are summarised in Fig. 2.4.

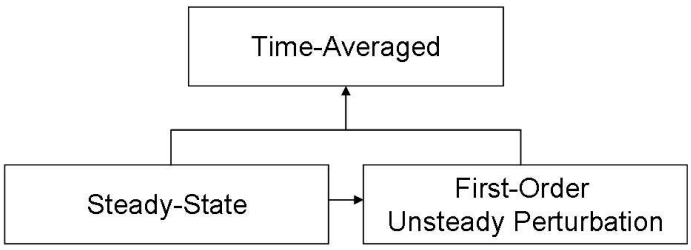

Figure 2.4: SLIQ strategy

There are several issues with the SLIQ approach. First, in terms of computational requirements, three calculations are required to obtain a mean (or time-averaged) flow solution, instead of one for a conventional steady-state solution. Second, the time-averaged corrections to the steady-state solution are exclusively based on the previously computed steady-state and harmonic linearised solutions. However, as already discussed, harmonic linearised solutions are not always reliable, especially when nonlinear effects (such as interaction between several temporal harmonics), or multi blade-row effects are dominant. Third, the harmonic linearised analysis of flutter or forced response is not influenced (or modified) in SLIQ. There is no influence back from the time-averaged corrections onto the linearised solution. Therefore, from an aeroelasticity analyst standpoint, SLIQ does not offer any advantage over any other harmonic linearised methods.

Finally, SLIQ can be used for applications other than aeroelasticity analysis, as discussed in [34]. For example, SLIQ can be used as an approach for multistage calculations, in which the quadratic terms provide corrections to the multistage steady-state flow. For that, an inter-row boundary conditions is used, which stipulates that the second-order flow perturbations is such that the averaged fluxes do match.

2.4.2 Nonlinear Harmonic Method

One of the major drawbacks with Giles' SLIQ method is that the unsteady analysis of flutter and forced response relies exclusively on conventional harmonic linearised results. What is gained by computing the time-averaged solution is not gained back on the harmonic linearised results. This problem was later overcome by He and Ning [48, 16, 47], who created a genuine *Nonlinear Harmonic* method, in which the harmonic linearised solution is based on the underlying time-averaged (mean) solution instead of the traditional steady-state solution. In this method, the time-averaged and time-linearised solutions are interdependent and must be computed interactively, and there is no restriction regarding the size of the unsteadiness.

For ease of comparison with the SLIQ method, the theory behind the nonlinear harmonic methodology is explained below by using the 2-D Euler equations given by (2.4.13) and (2.4.14). First, let the unsteady flow be decomposed into two parts, a "time-averaged" part and an unsteady perturbation:

$$\mathbf{U} = \bar{\mathbf{U}} + \mathbf{U}' \tag{2.4.25}$$

The flux vectors can also be decomposed into time-averaged and unsteady parts:

$$\mathbf{F} = \bar{\mathbf{F}} + \mathbf{F}' \tag{2.4.26}$$

and,

$$\mathbf{G} = \bar{\mathbf{G}} + \mathbf{G}' \tag{2.4.27}$$

Substitute the above expressions for the flux vectors and conservative variables into the 2-D Euler equations. The time-average version of the resulting equations is given by:

$$\frac{\partial \bar{\mathbf{F}}}{\partial x} + \frac{\partial \bar{\mathbf{G}}}{\partial y} = 0 \tag{2.4.28}$$

which represents the time-averaged Euler equations. Subtracting (2.4.28) from (2.4.13) and collecting together the first order terms only gives the unsteady perturbation equations:

$$\frac{\partial \mathbf{U}'}{\partial t} + \frac{\partial \mathbf{F}'}{\partial x} + \frac{\partial \mathbf{G}'}{\partial y} = 0 \tag{2.4.29}$$

By assuming that unsteady disturbances are periodic in time at frequency ω, the perturbation variables can be written in the form $\mathbf{U}' = \hat{\mathbf{U}}.e^{i\omega t}$, and the first-order unsteady perturbation equations become:

$$i\omega\hat{\mathbf{U}} + \frac{\partial \hat{\mathbf{F}}}{\partial x} + \frac{\partial \hat{\mathbf{G}}}{\partial y} = 0 \tag{2.4.30}$$

Equations (2.4.28), (2.4.29), and (2.4.30) look very similar to the ones found in conventional frequency-domain time-linearised methods, except that since we have considered the time-averaged variables rather than their steady-states counterparts, the time-averaged fluxes are given by:

$$\bar{\mathbf{F}} = \begin{pmatrix} \overline{\rho u} \\ \bar{u}\overline{\rho u} + \bar{p} + \overline{(\rho u)'u'} \\ \bar{v}\overline{\rho u} + \overline{(\rho u)'v'} \\ \bar{H}\overline{\rho u} + \overline{H'(\rho u)'} \end{pmatrix}, \bar{\mathbf{G}} = \begin{pmatrix} \overline{\rho v} \\ \bar{u}\overline{\rho v} + \overline{(\rho v)'u'} \\ \bar{v}\overline{\rho v} + \overline{(\rho v)'v'} \\ \bar{H}\overline{\rho v} + \overline{H'(\rho v)'} \end{pmatrix} \tag{2.4.31}$$

and the unsteady fluxes are given by:

$$\mathbf{F}' = \begin{pmatrix} (\rho u)' \\ u'\overline{\rho u} + p' + \bar{u}(\rho u)' \\ u'\overline{\rho v} + (\rho v)'\bar{u} \\ H'\overline{\rho u} + \bar{H}(\rho u)' \end{pmatrix}, \mathbf{G}' = \begin{pmatrix} (\rho v)' \\ u'\overline{\rho v} + \bar{u}(\rho v)' \\ v'\overline{\rho v} + (\rho v)'\bar{v} \\ H'\overline{\rho v} + \bar{H}(\rho v)' \end{pmatrix} \tag{2.4.32}$$

Note that the same type of decomposition is easily extendable to the Navier-Stokes equations. Using these equations, the time-averaging generates extra terms in the momentum and energy equations due to the nonlinearity. These extra terms are similar to the turbulence (Reynolds) stress terms, and thus are referred as unsteady (or deterministic) stress terms.

From the new expressions of the time-averaged and unsteady fluxes, one can see that the time-averaged and the unsteady Euler equations are now inter-dependent, and thus the problem is no longer linear. Equations (2.4.28) and (2.4.30) have to be solved in a coupled manner to model nonlinear interactions between the two parts. By introducing a pseudo-time τ, (2.4.28) and (2.4.30) become:

$$\frac{\partial \bar{\mathbf{U}}}{\partial \tau} + \frac{\partial \bar{\mathbf{F}}}{\partial x} + \frac{\partial \bar{\mathbf{G}}}{\partial y} = 0 \tag{2.4.33}$$

and

$$\frac{\partial \tilde{\mathbf{U}}}{\partial \tau} + \frac{\partial \tilde{\mathbf{F}}}{\partial x} + \frac{\partial \tilde{\mathbf{G}}}{\partial y} = -i\omega\tilde{\mathbf{U}} \tag{2.4.34}$$

Several important remarks can be made about these two equations: (i) they are mathematically steady, and can be time-marched (in pseudo-time) until a "steady-state" solution is reached. Hence, traditional acceleration techniques such as local time-stepping and multigrid techniques can be used to converge their solutions; (ii) the use of complex periodic boundary conditions allows the computation to include one blade-passage only rather than the whole annulus; (iii) owing to the physi-

cal nature of the coupling between the time-averaged and the unsteady flow, it is preferable that the coupling between these two sets of equations is achieved through a simultaneous time-marching procedure (strong coupling method), i.e. the entire coupled system, consisting of the two sets of equations, is integrated simultaneously in time. This is illustrated in Fig. 2.5.

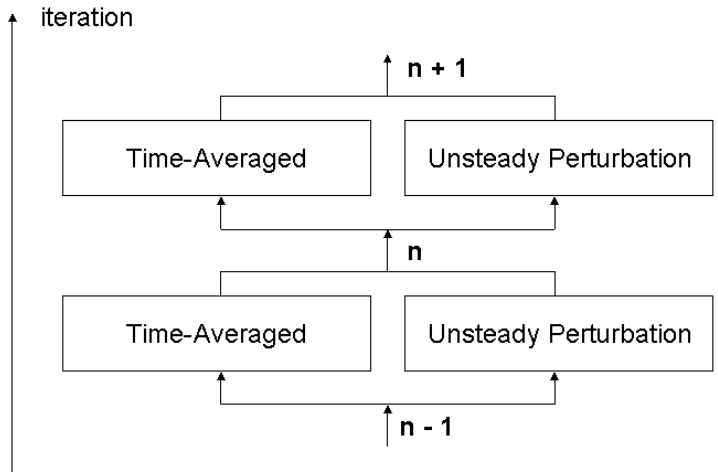

Figure 2.5: Coupling between time-averaged and unsteady perturbation equations for the nonlinear harmonic method

The main advantage of the nonlinear harmonic method over conventional harmonic linearised methods is that the former method includes the nonlinear interactions between the mean flow and the first-order unsteady perturbations in the model. This can be very beneficial in situations where the effects of those interaction are strong. This can seen, for example, in the regions of the flow where there is a shock wave. Steady-state and conventional linearised solutions tend to predict sharp peaks of pressures at the shock location, even when these peaks are much more smeared in reality due to nonlinear effects. These nonlinear effects are better represented using the nonlinear harmonic approach, but unfortunately not entirely. In fact, with this method the nonlinear interactions between disturbances with different frequencies are included only by communicating with the time-averaged flow. Nonlinear interactions between disturbances with different frequencies are not represented.

In terms of computational requirement, He and Ning [48] specified that the nonlinear harmonic method requires typically 60 % more CPU time that conventional time-linearised methods, and about the same computing time as full nonlinear methods when the computational domain is reduced to one blade-passage. This also means that the nonlinear harmonic method is one or two-orders of magnitude faster than full nonlinear methods where full annulus must be included. An important remark

is that, unlike fully nonlinear methods, the computational domain required by the nonlinear harmonic method can always be reduced to a single blade-passage, which always guarantees computational efficiency.

The nonlinear harmonic method discussed above was initially developed to model a blade-row in isolation. However, the method was later extended to deal with multi blade-row calculations. In such cases, the inter-row boundary condition treatment is based on a flux-averaged characteristic-based mixing-plane approach, which includes the deterministic stress terms due to upstream going potential disturbances and downstream going wakes. The complete description of this boundary condition is beyond the scope of this thesis, but more information can be found in [17, 80].

Chen *et al* [17] used the nonlinear harmonic method to study the time-averaged flow of a stator/rotor compressor stage. They found that the time-averaged solution transfered better the mixing loss through the inter-row interface compared to a conventional steady-state solution.

He *et al* [45] used the nonlinear harmonic method to study stage interaction effects on the performance of a two-and-a-half compressor. The authors defined a passage-averaged solution in adjacent stages to deal with the flow aperiodicity generated by the different blade counts between rotor-rotor and stator-stator. Their analysis showed stronger rotor-rotor interaction than stator-stator interaction, and clocking effects were qualitatively shown in terms of loss variation.

Moffatt and He [70] later coupled the nonlinear harmonic method whith a modal reduction technique, to create a fully-coupled method for the efficient prediction of forced response. The aerodynamic forcing and damping calculations were regrouped into a single analysis, which is approximately twice as fast as conventional decoupled methods. In this work, the coupled method predicted a significant reduction in vibration amplitude due to the resonant frequency shift, caused by aerodynamic added mass effects.

2.4.3 Harmonic Balance Method

Following the works from Giles [34], and He and Ning [48], which have been described above, Hall [35] introduced a new method, the so-called *harmonic balance*, for the computation of unsteady flows in turbomachinery. Instead of including uniquely the nonlinear interaction between the steady-state (or mean) flow solution and the first temporal Fourier harmonic, the nonlinear interaction between several harmonics at the same time is included. More importantly, like He's nonlinear harmonic method,

there is no restriction regarding the size of the unsteadiness. The basic equations of the harmonic balance method are explained below, by basing the description on the 2-D Euler equations given by (2.4.13).

For most applications, flows in turbomachinery can be regarded as periodic in time. Under such approximation, it is possible to decompose the conservative variables into Fourier series with spatially varying coefficients. Hence, the conservative variables may be decomposed as:

$$\rho = \sum_n R_n.e^{i\omega nt} \quad \rho u = \sum_n U_n.e^{i\omega nt} \quad \rho v = \sum_n V_n.e^{i\omega nt} \quad \rho E = \sum_n E_n.e^{i\omega nt} \tag{2.4.35}$$

In theory, these series have an infinite number of terms. However, in practice, it is believed that enough engineering accuracy can be reached by truncating these series into a finite number of terms, so that $-N \leq n \leq N$. Substituting the obtained expressions for the conservation variables into the governing equations gives their harmonic balance form:

$$\frac{\partial \tilde{\mathbf{F}}(\tilde{\mathbf{U}})}{\partial x} + \frac{\partial \tilde{\mathbf{G}}(\tilde{\mathbf{U}})}{\partial y} + \tilde{\mathbf{S}}(\tilde{\mathbf{U}}) = 0 \tag{2.4.36}$$

where $\tilde{\mathbf{U}} = (R_0, \ldots, R_n, U_0, U_1, \ldots, U_n, \ldots, E_0, \ldots, E_n)^T$ represents the unknown vector of Fourier series coefficients of the conservative variables. Having used the above formulation, Hall realised that this harmonic balance form of the flow governing equations had two major problems: (i) this approach is not readily applicable to more complex flows such as viscous flows, because it is not always possible to decompose the turbulence models into simple algebraic forms; (ii) the computation of the harmonic fluxes is expensive and grows rapidly with the number of harmonics.

To avoid these problems, Hall re-wrote the previous equations into a more convenient form. The first key step was to note that the Fourier coefficients of the conservation variables $\tilde{\mathbf{U}}$ and the flux terms $\tilde{\mathbf{F}}$ and $\tilde{\mathbf{G}}$, could be determined from the knowledge of the temporal behaviour of $\mathbf{U}$, $\mathbf{F}$ and $\mathbf{G}$ over 2N + 1 equally spaced points on a temporal period. Mathematically, this gives:

$$\tilde{\mathbf{U}} = \mathbf{E}\mathbf{U}^* \quad \tilde{\mathbf{F}} = \mathbf{E}\mathbf{F}^* \quad \tilde{\mathbf{G}} = \mathbf{E}\mathbf{G}^* \tag{2.4.37}$$

in which $\mathbf{U}^*$, $\mathbf{F}^*$ et $\mathbf{G}^*$ are the vectors of conservative variables and flux terms at 2N + 1 points which are equally-spaced on one temporal period. $\mathbf{E}$ is the discrete Fourier transform operator matrix. Plugging (2.4.37) into (2.4.36), and pre-multiplying the

obtained equation by $\mathbf{E^{-1}}$ gives:

$$\frac{\partial \mathbf{F}^*}{\partial x} + \frac{\partial \mathbf{G}^*}{\partial y} + \mathbf{S}^* = 0 \tag{2.4.38}$$

where

$$\mathbf{S}^* = j\omega \mathbf{E^{-1}} \mathbf{N} \mathbf{E} \mathbf{U}^* \tag{2.4.39}$$

Here, $\mathbf{N}$ is a diagonal matrix with n in the entries, the i-th entry corresponding to the i-th harmonic. In practice, $\mathbf{S}^*$ is a spectral operator, which approximates the time derivative $\frac{\partial \mathbf{U}^*}{\partial t}$. Using this approach the computation of the fluxes, which are those requiring the most computational time, is scaled only by the number of Fourier harmonics retained in the solution. Therefore, the harmonic balance form of the governing equations, given by (2.4.38), is a great improvement over the original version given by (2.4.36).

The numerical strategy used to solve (2.4.38) is as follows:

(i) *2N+1* grids are generated, one for each time level.

(ii) On each of these grids (2.4.38) is solved by introducing a pseudo time term to drive the equations to steady-state.

(iii) The fluxes are computed in the usual way using standard nonlinear formulation.

(iv) The solutions at each time level are only coupled through the spectral time derivative term in (2.4.39) and the periodic boundary conditions. For further discussions about the boundary conditions, see [35].

One of the main advantages of the harmonic balance method over dual time-stepping nonlinear methods is that the latter, in general, require very small time steps and thus a large number of time levels per time period. This is a necessary condition for nonlinear schemes to be both stable and accurate. However, in the harmonic balance method, the solutions must be stored at only *2N+1* time levels over a single time period, which means significantly fewer time levels are required than for nonlinear methods.

Compared to conventional harmonic linearised methods, the harmonic balance method also offers many advantages: (i) there is no assumption regarding the size of the unsteadiness; (ii) the nonlinear interactions between several temporal harmonics are

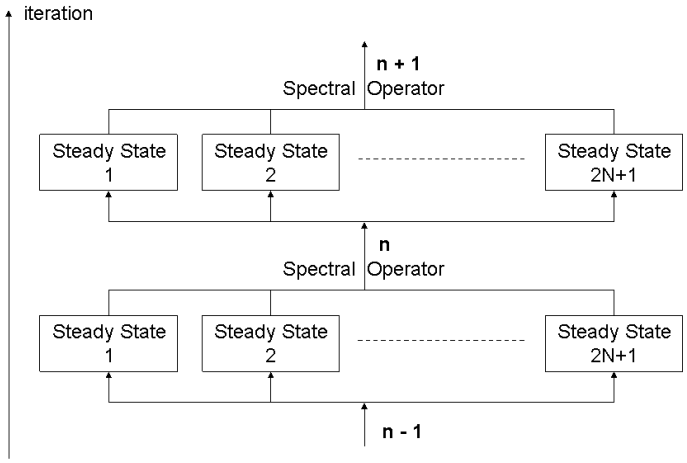

Figure 2.6: Harmonic Balance Strategy

represented and these interactions are essential, for example, for an accurate treatment of large unsteady shocks wave excursion. In this work, Hall demonstrated that five harmonics are usually enough to obtain converged solutions for the zeroth and first harmonic components of the unsteady flow. In terms of the computational requirements, the CPU time per iteration of the harmonic balance method including one, three, five and seven harmonics (and one blade-row) is about 2.15, 4.62, 7.45, and 10.29 times respectively of the cost per iteration of the steady flow solver. Above this number of harmonics, however, the harmonic balance method fails to converge for the reasons discussed in [35].

The harmonic balance method was successfully tested on many flutter applications, such as the front stage transonic rotor of a modern high-pressure compressor [35], a transonic wing configuration [113], the flutter onset and LCO response of a F-16 fighter [111, 112], the modelling of the flow vortex shedding from a cylinder with enforced motion [106], for the study of how nonlinear aerodynamics can affect the divergence, flutter, and limit-cycle oscillation (LCO) characteristics of a transonic airfoil configuration [110]. The results presented in these studies show remarkable improvements compared to conventional harmonic linearised methods when nonlinear effects are dominant, for example for large amplitude vibrating blades. In recent publications, the harmonic balance method has also been extended and applied to the calculation of both flutter and forced response problems in multistage turbomachines [25].

Despite the advantages offered by the harmonic balance method, there are also some important issues which should be emphasised. First, since $2N+1$ steady-state solutions must be computed at the same time, this increases significantly the CPU effort

over one steady-state solution and one linearised solution requirement for conventional harmonic linearised methods. The retention of 5 harmonics roughly multiplies the computational time by 10 compared to conventional harmonic linearised methods, thus making the computational time significantly closer to that needed by fully nonlinear methods. This general remark is all the more true for multi blade-row calculations, since Hall later extended the harmonic balance method to multi blade-row problems [25]. For this type of calculation, the computational time also scales with the number of blade-rows and of spinning modes included in the analysis (the definition of a spinning will be given in Section 2.5). In this context, the author of the present thesis believes that the harmonic balance method is too expensive for design use; however, it may be considered as an analysis tool until computational capabilities have improved enough to make this type of calculation more affordable.

2.5 Harmonic Linearised Methods Including Multirow Effects

As well as developing the harmonic balance method, Hall and his co-researchers also worked on a different type of method, which aims to include nonlinear effects due to the presence of neighbouring blade-rows, instead of those originating *from* the flow induced by the analysed blade-row. This work was initially motivated by the observation that nearly all existing unsteady aerodynamic theories model a single blade-row in an infinitely long duct, ignoring potentially important multistage effects. This situation was thought to cause inaccuracies since unsteady flows are fundamentally made up of acoustic, vortical and entropic waves, which provide a mechanism of communication between the blade-rows.

Before Hall 's work, there had been a number of investigators studying multistage problems [5, 44]. In multi blade-row methods, the coupling between the blade-rows is usually modelled using a subset of "spinning modes", which represent a group of waves travelling across the blade-rows with pre-determined circumferential wave numbers. The mathematical description of a spinning mode is given in Chapter 4. In theory, there is an infinite number of these spinning modes but, in practice, it is believed that only a small number of modes have a significant impact on the aerodynamics of the blade-rows.

Silkowski [103, 102] developed an interesting Coupled Mode Model (CMM), which includes efficiently multirow effects into the solution of harmonic linearised methods using the theory of spinning modes. Hall and Silkowski used a 2-D linearised full

potential flow model with rapid distortion theory to account for incident vortical waves, and the effects of neighbouring blade-rows were represented by transmission and reflection coefficients, which depended on the spinning modes considered. The reflection and transmission coefficients $w_{n_1,\ldots,n_N}$ (where N is the number of blade-rows) had to be determined before the main computation by pre-computing the aerodynamic response of the neighbouring blade-rows to incident forcing. The determination of such coefficients could either be achieved by the pre-computation of an harmonic linearised solution for each blade-row and for each different mode, or when the geometry allowed it, by the use of a "classical method" such as LINSUB.

The method of determination of reflection and transmission coefficients is illustrated here by a simple example. Consider an analysis of two blade-rows, Row1 and Row2. The notations L and R are used to represent respectively the left hand side (upstream) and right hand side (downstream), and $+$ and - mean upstream and downstream travelling waves. Then, the matrix of transmission and reflection coefficients $w_{n_1n_2,n_1n_{2'}}$ describing how an incident mode $(n_1, n_{2'})$ scatters into a different mode (n_1, n_2) has the form:

$$\begin{pmatrix} P_L^+ \\ P_R^- \\ \xi_R \end{pmatrix}_{n_1n_2} = \sum_{j=} \begin{bmatrix} w_{11} & w_{12} & w_{13} \\ w_{21} & w_{22} & w_{23} \\ w_{31} & w_{32} & w_{33} \end{bmatrix}_{n_1n_2,n_1n_{2'}} \begin{pmatrix} P_R^+ \\ P_L^- \\ \xi_L \end{pmatrix}_{n_1n_{2'}} + \begin{pmatrix} b_1 \\ b_2 \\ b_3 \end{pmatrix}_{n_1n_2} \tag{2.5.40}$$

where the symbol P refers to an acoustic wave, and ξ to a vortical wave. The vector $\mathbf{b}_{n_1n_2}$ is an inhomogeneous term arising from the imposition of external disturbances. For example, $\mathbf{b}_{n_1n_2}$ could describe travelling waves due to fluttering blades at frequency ω_0 and nodal diameter k_0.

The coupled mode model solves the harmonic linearised equations in the studied blade-row, in which the blade-row reflection, transmission coefficients, inter-row coupling relationships, and appropriate boundary conditions form a small sparse linear system of equations which describes the unsteady multistage flow. Such a linear system is not explicitly given here for conciseness but the interested reader can refer to [102]. The method was very efficient. Importantly, the results obtained with this method demonstrated that the multi blade-row effects on the aerodynamic of the blade-rows are often significant and should not be ignored. However, the major drawback with this work was that it did not work well in three-dimensions where many radial mode shapes must be modelled. Hence the method was not suitable for real turbomachinery applications.

To avoid this problem, Hall [39] further proposed an improved harmonic linearised multistage approach, which uses the three-dimensional Euler equations. In this

approach, neighbouring blade rows are no longer modelled by transmission and reflection coefficients. Instead, the solutions in all the blade rows are computed simultaneously using conventional harmonic linearised methods. A specific boundary condition treatment is required at the inter-row boundaries, which couples the solutions in all blade-rows in such a way that three-dimensional entropic, vortical and acoustic waves are allowed to travel across the multirow domain. This methodology had been successfully tested on a three dimensional modern front stage compressor in [39]. It was shown that the harmonic linearised multi blade-row method was very efficient, typically several orders of magnitude faster than most nonlinear methods, which would make it affordable for design use.

2.6 Conclusions on Harmonic Methods

Unlike nonlinear methods, harmonic methods are well suited to adjoint sensitivity techniques and they are aimed to be used for design purposes. They are also much more efficient than the conventional nonlinear method (with the notable exception of the nonlinear single-passage method). The pros and cons for each of the reviewed methods are summarised in Table 2.2. Once again, the numbers shown in this table are estimated values based on information collected from related publications.

Method's name	Advantages	Disadvantages	CT (%)
SLIQ approach	- Time-averaged effects included for the mean flow description	- No improvement in aeroelasticity predictions - Linear assumption	1 - 5
Nonlinear harmonic	- Nonlinear interactions between mean flow and 1 harmonic perturbation - No linear assumption	- Nonlinear interaction between harmonic perturbations ignored	8
Harmonic balance (isolated)	- Nonlinear interactions between mean flow and several harmonic perturbations - No linear assumption	- 2N+1 steady-state solutions stored	7 - 10
Harmonic linearised multi blade-row	- Multi blade-row effects included	- Linear assumption	% nb. of blade-rows

Table 2.2: Comparisons pros and cons of the reviewed harmonic CFD methods for turbomachinery applications

Importantly, all harmonic methods which were reviewed aim to include three different types of physical effects, which are normally ignored in conventional harmonic

linearised methods. A first physical effect is the nonlinear interaction between one or several temporal harmonics with the mean flow (SLIQ, nonlinear harmonic, harmonic balance). In some cases, the inclusion of such nonlinear effects improves unsteady flow predictions by 10-15% in terms of pressure distributions compared to what would have been obtained using other conventional linearised methods. A second physical effect is the nonlinearity related to the magnitude of the unsteadiness. Most harmonic theories assume that the unsteady perturbations are small compared to the mean flow (SLIQ, harmonic linearised multi blade-row). A great novelty comes from the nonlinear harmonic and the harmonic balance methods, which assume no restriction regarding the magnitude of the unsteadiness. In order to give an order of magnitude, such effects can be assessed to improve the accuracy of the numerical solution by 10-20% when nonlinear effects are not very strong. A third physical effect is produced by the interaction between the blade-rows. All methods which included such effects showed that multi blade-row effects are never small, and could completely change the isolated blade-row unsteady flow solution. In this context, the numerical results can change by as much as 100% or more, with and without the presence of neighbouring blade-rows. Therefore, it is the opinion of the author of the present thesis that it is highly preferable to seek to include the effects of the interactions between the blade-rows into a numerical method before other nonlinear effects.

Before the present PhD thesis was started, the state of the art for efficient multi blade-row methods was the harmonic linearised multi blade-row method by Hall based on 3-D Euler equations. This method was tested on simple geometries and real turbomachinery compressors, showing that multi blade-row effects were large for these applications. By the time the present PhD thesis finished, the same method was extended by Ekici & Hall [55] to Navier-Stokes equations with the study of a three-dimensional modern front stage compressor, and of a fan geometry.

2.7 Purposes of the Thesis

The purpose of the present thesis is to develop a harmonic linearised multi blade-row solver for the efficient and accurate predictions of flutter and forced response in turbomachinery. This model will be based on an existing and validated harmonic linearised isolated blade-row solver, which is an in-house code developed at Rolls-Royce plc. The present study follows previous work by Hall discussed in this Chapter. Importantly, the contributions of the present thesis include:

- The implementation of the multi blade-row methodology using either 3-D Euler or Navier-Stokes equations on a numerical scheme incorporating a finite-volume method, an edge-based discretisation scheme for structured and unstructured meshes, a 5-step Runge-Kutta solution method, a multigrid strategy, and a GMRES acceleration method for improved convergence of the residual. These details are described in Chapter 4.

- The development of an inter-row boundary condition which allows acoustic, vortical, and entropic waves to propagate appropriately across the blade-rows. This inter-row boundary condition will be based on a genuine combination of the "spinning modes" theory, and of one of the latest developments on 3-D non-reflecting boundary conditions. These are also described in Chapter 4.

- A series of numerical tests for wave-propagation analysis on simple geometries to compare solutions with known analytical solutions. This is done in Chapter 5.

- A series of numerical tests for flutter analysis on simple geometries by comparison of the solutions with known semi-analytical solutions, and reference multi blade-row solutions. This is done in Chapter 6.

- An assessment of multi blade-row effects for flutter and wake/rotor interaction on two real turbine geometries. This is done in Chapters 7 and 8.

- An analysis of both when multi blade-row effects are significant, and how many blade-rows must be included in the model to obtain enough accuracy.

- A study of which parameters are important to obtain both accurate harmonic linearised isolated blade-row and harmonic linearised multi blade-row results.

Chapter 3

Nonlinear Steady-State Analysis

3.1 Introduction

The purpose of this thesis is to develop a frequency-domain time-linearised multi blade-row model for the analysis of unsteady flows in turbomachinery. With this motivation, the corresponding multi blade-row code is developed from an existing nonlinear single-passage multi blade-row steady-state code that has been developed by Rolls-Royce and several UTCs for more than a decade. The starting point is a steady-state model from which linearisation takes place. This chapter presents the nonlinear steady-state code, which uses the Reynolds-Averaged Navier-Stokes equations coupled with the one-equation Spalart and Allmaras turbulence model. First, the most important aspects of the spatial discretisation are discussed, which include the edge-based data structure suitable for both structured and unstructured grids, the construction of the viscous and inviscid fluxes, and the application of the boundary conditions. Finally, the iterative solution procedure, which uses both a Runge-Kutta method to converge the solution to steady-state and a multigrid strategy to accelerate convergence, is presented. The full description of the nonlinear analysis is beyond the scope of this thesis and is comprehensively discussed in [71]. Nevertheless, the key elements required for understanding the time-linearised analysis presented in Chapter 4 are described here.

3.2 The Governing Equations

The nonlinear flow analysis uses the 3-D Navier-Stokes equations, which express the conservation of mass, momentum, and energy for viscous flows. In addition,

the fluid is assumed to be Newtonian. For clarity, the Navier-Stokes equations are first given in their most general form, i.e. for unsteady flows. Some aspects of the frequency-domain time-linearised analysis, presented in Chapter 4, will be derived from these equations. However, the formulation of the time-linearised equations, and its subsequent numerical scheme can be obtained for the most part from the steady-state analysis, which is the main concern of the present chapter.

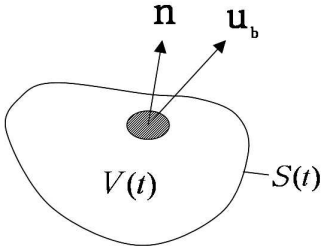

Figure 3.1: Moving control volume

Consider the control volume *V(t)* shown in Fig. 3.1. Let its local unit normal be $\mathbf{n}$, and its boundary surface *S(t)*. Assume that this control volume is rotating around the x axis at speed Ω (in *rad/s*) and, at the same time, that its boundaries are deforming at velocity $\mathbf{u}_b(\mathbf{x})$. The conservative form of the Navier-Stokes equations, integrated around this control volume, can regrouped into a single equation given in the relative frame by:

$$\int_{V(t)} \frac{\partial \mathbf{U}}{\partial t} dV + \oint_{S(t)} \mathbf{F}(\mathbf{U}, \nabla \mathbf{U}).\mathbf{n} dS = \int_{V(t)} \mathbf{S}(\mathbf{U}) dV \tag{3.2.1}$$

The Reynolds transport theorem allows the following decomposition:

$$\int_{V(t)} \frac{\partial \mathbf{U}}{\partial t} dV = \frac{d}{dt} \int_{V(t)} \mathbf{U} dV - \oint_{S(t)} (\mathbf{U}\mathbf{u}_b).\mathbf{n} dS \tag{3.2.2}$$

Therefore, combining (3.2.1) and (3.2.2) gives:

$$\frac{d}{dt} \int_{V(t)} \mathbf{U} dV + \oint_{S(t)} \mathbf{F}(\mathbf{U}, \nabla \mathbf{U}).\mathbf{n} dS = \int_{V(t)} \mathbf{S}(\mathbf{U}) dV + \oint_{S(t)} (\mathbf{U}\mathbf{u}_b).\mathbf{n} dS \tag{3.2.3}$$

the steady-state form of which is given by:

$$\mathbf{R}(\mathbf{U}) = \int_{V} \mathbf{S}(\mathbf{U}) dV - \oint_{S} \mathbf{F}(\mathbf{U}, \nabla \mathbf{U}).\mathbf{n} dS = 0 \tag{3.2.4}$$

In the above expressions, $\mathbf{U} = (\rho, \rho u, \rho v, \rho w, \rho E)^T$ represents the vector of conser-

vative flow variables, ρ is the density, u, v, w are the three cartesian components of the velocity in the relative frame, and E is the total internal energy per unit mass. $\mathbf{S}$ is the vector of centrifugal and Coriolis sources, given by:

$$\mathbf{S} = \left(0, 0, \rho\left(\Omega^2 y + 2\Omega w\right), \rho\left(\Omega^2 z - 2\Omega v\right), 0\right)^T, \tag{3.2.5}$$

Note that, by convention, the axial axis is coincident with the engine axis. $\mathbf{F}\left(\mathbf{U}, \nabla\mathbf{U}\right)$ is the vector of convective and viscous fluid fluxes that can be decomposed as follows:

$$\mathbf{F}\left(\mathbf{U}, \nabla\mathbf{U}\right) = \underbrace{\mathbf{F}^I\left(\mathbf{U}\right)}_{inviscid\ flux} + \underbrace{\mathbf{F}^V\left(\mathbf{U}, \nabla\mathbf{U}\right)}_{viscous\ flux} \tag{3.2.6}$$

In three dimensions, the total flux has contributions from the three cartesian directions x,y,z. Calling $\mathbf{i}, \mathbf{j}, \mathbf{k}$ the unit vectors in these three directions respectively, then the flux vectors can be decomposed as follows:

$$\mathbf{F}^I = \mathbf{F}^I_x\mathbf{i} + \mathbf{F}^I_y\mathbf{j} + \mathbf{F}^I_z\mathbf{k} \tag{3.2.7}$$

and

$$\mathbf{F}^V = \mathbf{F}^V_x\mathbf{i} + \mathbf{F}^V_y\mathbf{j} + \mathbf{F}^V_z\mathbf{k} \tag{3.2.8}$$

where

$$\mathbf{F}^I_x = \begin{pmatrix} \rho u \\ \rho u^2 + p \\ \rho uv \\ \rho uw \\ (\rho E + p)u \end{pmatrix} \tag{3.2.9}$$

$$\mathbf{F}^I_y = \begin{pmatrix} \rho v \\ \rho uv \\ \rho v^2 + p \\ \rho vw \\ (\rho E + p)v \end{pmatrix} \tag{3.2.10}$$

$$\mathbf{F}^I_z = \begin{pmatrix} \rho w \\ \rho uw \\ \rho vw \\ \rho w^2 + p \\ (\rho E + p)w \end{pmatrix} \tag{3.2.11}$$

and

$$\mathbf{F}_x^V = \begin{pmatrix} 0 \\ -\tau_{xx} \\ -\tau_{yx} \\ -\tau_{zx} \\ -u\tau_{xx} - v\tau_{yx} - w\tau_{zx} + q_x \end{pmatrix} \tag{3.2.12}$$

$$\mathbf{F}_y^V = \begin{pmatrix} 0 \\ -\tau_{xy} \\ -\tau_{yy} \\ -\tau_{zy} \\ -u\tau_{xy} - v\tau_{yy} - w\tau_{zy} + q_y \end{pmatrix} \tag{3.2.13}$$

$$\mathbf{F}_z^V = \begin{pmatrix} 0 \\ -\tau_{xz} \\ -\tau_{yz} \\ -\tau_{zz} \\ -u\tau_{xz} - v\tau_{yz} - w\tau_{zz} + q_z \end{pmatrix} \tag{3.2.14}$$

The viscous stress terms are given by:

$$\tau_{xx} = 2\mu\frac{\partial u}{\partial x} + \lambda\left(\frac{\partial u}{\partial x} + \frac{\partial v}{\partial y} + \frac{\partial w}{\partial z}\right) \tag{3.2.15}$$

$$\tau_{yy} = 2\mu\frac{\partial v}{\partial y} + \lambda\left(\frac{\partial u}{\partial x} + \frac{\partial v}{\partial y} + \frac{\partial w}{\partial z}\right) \tag{3.2.16}$$

$$\tau_{zz} = 2\mu\frac{\partial w}{\partial z} + \lambda\left(\frac{\partial u}{\partial x} + \frac{\partial v}{\partial y} + \frac{\partial w}{\partial z}\right) \tag{3.2.17}$$

$$\tau_{xy} = \tau_{yx} = \mu\left(\frac{\partial u}{\partial y} + \frac{\partial v}{\partial x}\right) \tag{3.2.18}$$

$$\tau_{xz} = \tau_{zx} = \mu\left(\frac{\partial u}{\partial z} + \frac{\partial w}{\partial x}\right) \tag{3.2.19}$$

$$\tau_{yz} = \tau_{zy} = \mu\left(\frac{\partial v}{\partial z} + \frac{\partial w}{\partial y}\right) \tag{3.2.20}$$

and the heat fluxes are:

$$q_x = -k_T\frac{\partial T}{\partial x}; q_y = -k_T\frac{\partial T}{\partial y}; q_z = -k_T\frac{\partial T}{\partial z} \tag{3.2.21}$$

In these expressions, $k_T = \frac{\mu c_p}{Pr}$ is the coefficient of thermal conductivity, where Pr is the Prandtl number ($Pr = 0.72$ for air), c_p is specific heat at constant pressure, μ is

the molecular viscosity modelled by Sutherland's law:

$$\mu = \frac{1.461 \times 10^{-6} T^{\frac{3}{2}}}{T + 110.3} \tag{3.2.22}$$

where T is the gas temperature in Kelvin (K), and λ is the bulk viscosity defined by Stokes' relationship:

$$\lambda = -\frac{2}{3}\mu \tag{3.2.23}$$

Looking at the expressions for the vector of conservative variables $\mathbf{U}$, the fluxes $\mathbf{F}$, and the source terms $\mathbf{S}$, it is clear that the system of five equations regrouped in (3.2.4) presents a total number of seven unknowns, which are ρ, u, v, w, p, T, E. Therefore, this system is under-determined and needs additional considerations in order to be closed. In this work, we consider the air as a perfect gas, which is generally acknowledged as being a good approximation of the gas behaviour at engine working conditions. The equation of state for a perfect gas is given by:

$$\frac{p}{\rho} = rT \tag{3.2.24}$$

where r is the gas constant per unit of mass and is equal to the universal gas constant ($R \approx 8.314\, kJ.kmol^{-1}.K^{-1}$) divided by the molecular mass of the fluid. For a perfect gas, the total internal energy E becomes a function of the flow quantities through the equation of state:

$$E = \frac{1}{\gamma - 1}\frac{p}{\rho} + \frac{1}{2}\left(u^2 + v^2 + w^2\right) \tag{3.2.25}$$

where γ is the ratio of the specific heat under constant pressure and constant volume. The flow equations are now completely defined, and could, in theory, be used as they are to solve unsteady flow problems. However, from the perspective of solving these equations using a numerical method, an important procedure still needs to be done.

It is preferable to normalise to flow quantities, i.e. density, velocity, and pressure, so that the flow field unknowns are all within the same range of magnitude. In the present work, the normalisation is achieved as follows:

$$\begin{gathered} x^* = \tfrac{x}{L_{ref}}, \qquad y^* = \tfrac{y}{L_{ref}}, \qquad z^* = \tfrac{z}{L_{ref}}, \qquad t^* = \tfrac{t \times U_{ref}}{L_{ref}}, \\ u^* = \tfrac{u}{U_{ref}}, \qquad v^* = \tfrac{v}{U_{ref}}, \qquad w^* = \tfrac{w}{U_{ref}}, \qquad \mu^* = \tfrac{\mu}{\rho_{ref} \times U_{ref} \times L_{ref}}, \\ \rho^* = \tfrac{\rho}{\rho_{ref}}, \qquad p^* = \tfrac{p}{p_{ref}}, \qquad T^* = \tfrac{T}{T_{ref}} \end{gathered} \tag{3.2.26}$$

where the superscript $*$ refers to the normalised quantity. The reference length scale L_{ref} is equal to one meter, the reference density ρ_{ref}, pressure p_{ref}, and temperature

T_{ref} are standard values at sea level, and the reference velocity is defined as $U_{ref} = \sqrt{p_{ref}/\rho_{ref}}$. For the rest of this chapter, the subscript $*$ will be omitted for clarity, but the reader should bear in mind that all subsequent equations are based on normalised flow quantities.

The flow governing equations are used to represent the gas fluid dynamics including turbulence. It is important to recall that the practical description of turbulence at every point in time and space of a given flow is extremely difficult to achieve. This is caused by the large range of length scales and time scales that constitute the turbulent flow perturbations. Typically, the perturbation dimensions can vary from several percents of the geometric dimensions, to micro-distances l_k (called *Kolmogorov* scale) given approximately by $l_k \approx l\,(Re_l)^{-3/4}$, where Re_l is the Reynolds number of the larger disturbances, and l represents a measure of the largest turbulent eddy scale (or integral scale), which is the distance over which the fluctuating component of the velocity remains correlated. In recent years, there have been several successful attempts to compute directly turbulent flows but these have been done using simple geometric configurations, and for low Reynolds numbers. The reason is that the computing times are extremely large due to the immense number of mesh points that are needed to capture the details of turbulence. However, computing time decreases with increasing computing power and it may be possible to use direct numerical simulation in the future to treat practical problems. For now, computing resources are such that current methods to represent turbulence are still based on a statistical approach. The statistical approach used in this work is expressed by the Reynolds-Averaged Navier-Stokes equations. These equations are obtained by averaging the flow quantities over a time interval T, so that only the averaged part of the turbulence is resolved. The time interval T must be chosen significantly larger than the characteristic time of the perturbations, while remaining small compared to the time-scale of other time-dependent effects. The new form of the Navier-Stokes equations known as the Reynolds-Averaged Navier-Stokes equations obtained after time-averaging is given, for example, by Hirsch [49]. In short, the time-averaging has the effect of adding new stress terms and heat flux terms comparable in nature to viscous stresses and heat fluxes, and hence are called turbulent (or Reynolds) stresses and turbulent heat fluxes respectively. Under Boussinesq's hypothesis, the turbulent stresses and heat fluxes can be re-expressed in terms of the averaged flow quantities in the form of (3.2.15) to (3.2.20) and (3.2.21), by replacing the thermal conductivity k_T, molecular viscosity μ, and bulk viscosity λ, by their turbulent counterparts, $k_{T,t}$, μ_t and λ_t, which need to be determined. The result is remarkable. Exactly the same set of equations forming (3.2.3) can be re-used to form the Reynolds-Averaged Navier-Stokes equations, by simply replacing the viscosities by

their total counterparts:

$$\mu_{tot} = \mu + \mu_t, \lambda_{tot} = -\frac{2}{3}\mu_{tot} \tag{3.2.27}$$

and the thermal conductivity, by the total thermal conductivity:

$$k_{T,tot} = \frac{\mu c_p}{Pr} + \frac{\mu_t c_p}{Pr_t} \tag{3.2.28}$$

where μ_t is called the turbulent eddy viscosity, and Pr_t ($= 0.9$ for air) is the turbulent Prandtl number.

Finally, the application of the Reynolds-averaged equations to the computation of turbulence flows requires the introduction of a turbulence model for the determination of the turbulent unknown μ_t, the turbulence model being based on theoretical considerations coupled with unavoidable empirical information.

3.3 Turbulence Model

In this work, the one-equation Spalart-Allmaras turbulence model is used [105]. This is a parabolic partial differential equation having the same form as (3.2.1) with convection, diffusion, and source terms given by

$$\frac{\partial \tilde{\nu}}{\partial t} + \underbrace{u\frac{\partial \tilde{\nu}}{\partial x} + v\frac{\partial \tilde{\nu}}{\partial y} + w\frac{\partial \tilde{\nu}}{\partial z}}_{Convection\ terms} = \underbrace{\frac{1}{\sigma}\left(\nabla.\left[\left(\nu + \tilde{\nu}\right)\nabla\tilde{\nu}\right] + c_{b2}\left(\nabla\tilde{\nu}\right)^2\right)}_{Diffusion\ terms} + \underbrace{S}_{Source\ term} \tag{3.3.29}$$

In this equation, $\tilde{\nu}$ is the Spalart unknown parameter related to the turbulence eddy viscosity by the relation $\mu_t = \tilde{\nu} f_{v1}$, where f_{v1} is defined below. ν is the molecular kinetic viscosity, and S is the source term, which, in turn, can be decomposed into the sum of a production, destruction, and trip terms, as follow

$$S = \underbrace{P\left(\tilde{\nu}\right)}_{Production\ term} - \underbrace{D\left(\tilde{\nu}\right)}_{Destruction\ term} + \underbrace{T}_{Trip\ term}, \tag{3.3.30}$$

where

$$\begin{aligned} P\left(\tilde{\nu}\right) &= c_{b1}\tilde{S}\tilde{\nu}, \\ D\left(\tilde{\nu}\right) &= \left(c_{\omega 1} f_\omega - \tfrac{c_{b1}}{\kappa^2} f_{t2}\right)\left(\tfrac{\tilde{\nu}}{d}\right)^2, \\ T &= f_{t1}\left(\Delta u\right)^2 \end{aligned}$$

The trip term provides a mechanism for triggering transition at a specified location of the geometry. However, this trip term is not used in this work for two reasons. The first one is that the flow is considered to be fully turbulent, as is the case in

most turbomachinery applications. The second reason is that, if this trip term was to be used, the transition zone must be known in advance, in which the source terms are then multiplied by an increasing factor varying from zero to one, and triggers turbulence. However, it is rarely the case that the transition zone can be known in advance.

The other terms in (3.3.29) and (3.3.30) are given by

$$f_{v1} = \frac{\chi^3}{\chi^3+c_{v1}^2}, \qquad f_{v2} = 1 - \frac{\chi}{1+\chi f_{v1}}, \qquad \chi = \frac{\tilde{\nu}}{\nu},$$
$$f_\omega = g\left(\frac{1+c_{\omega 3}^6}{g^6+c_{\omega 3}^6}\right)^{\frac{1}{6}}, \quad g = r + c_{\omega 2}\left(r^6 - r\right), \quad r = \frac{\tilde{\nu}}{\tilde{S}\kappa^2 d^2},$$

$$f_{t1} = c_{t1} g_t . e^{\left(-c_{t2}\frac{S_t^2}{(\Delta u)^2}\left[d^2 + g_t^2 d_t^2\right]\right)}, \quad f_{t2} = c_{t3} . e^{\left(-c_{t4}\chi^2\right)}, \quad g_t = min\left(0.1, \frac{\Delta u}{S_t \Delta x_t}\right),$$

$$\tilde{S} = S + \frac{\tilde{\nu}}{\kappa^2 d^2} f_{v2}, \quad S = \sqrt{\left(\frac{\partial w}{\partial y} - \frac{\partial v}{\partial z}\right)^2 + \left(\frac{\partial u}{\partial z} - \frac{\partial w}{\partial x}\right)^2 + \left(\frac{\partial u}{\partial y} - \frac{\partial v}{\partial x}\right)^2}$$

and the constants used in the above equations are given by

$$\begin{array}{llll} c_{b1} = 0.1355, & c_{b2} = 0.622, & \sigma = \frac{2}{3}, & c_{v1} = 7.1, \\ c_{\omega 1} = \frac{c_{b1}}{\kappa^2} + \frac{1+c_{b2}}{\sigma}, & c_{\omega 2} = 0.3, & c_{\omega 3} = 2, & \kappa = 0.41. \\ c_{t1} = 1, & c_{t2} = 2, & c_{t3} = 1.2, & c_{t4} = 0.5 \end{array}$$

In the above equations, d is the distance to the nearest wall, d_t is the distance to the trip point on the wall, S_t is the wall vorticity at the trip, Δu is the difference in velocity between the field cell and the trip point, and Δt is the grid spacing at the wall at the trip point.

Finally, in this work, (3.3.29) is normalised using the normalisation factors given in (3.2.26), and the Spalart parameter is normalised as follows:

$$\tilde{\nu}^* = \frac{\tilde{\nu}}{U_{ref} . L_{ref}} \tag{3.3.31}$$

3.4 Discretisation

A finite-volume method is used to obtain the solution of the Reynolds-averaged Navier-Stokes equations to imposed boundary conditions and on three-dimensional domains. Fundamentally, the finite volume method is based on sub-dividing the spatial domain into finite volumes, also called grid cells, while keeping track of an approximation of the integral of the conservative variables over each of these volumes.

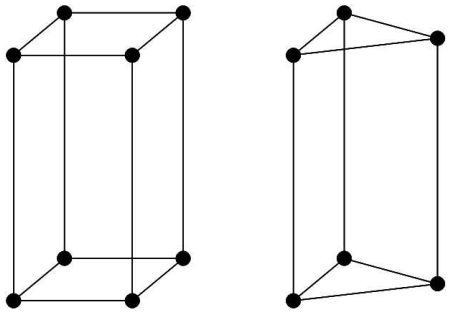

Figure 3.2: Hexahedron (left) and Prism (right)

In the application cases presented in this thesis, the three-dimensional domains are discretised using structured or unstructured hybrid grids, formed exclusively of hexahedra and/or prisms, as those shown in Fig. 3.2. The control volume associated to each node is the median-dual. It is constructed by joining the centroids of each cell surrounding the node with the midpoints of the edges connected to the node. A two-dimensional representation of the median-dual core volume is shown in Fig. 3.3. The unknowns variables are stored at the nodes.

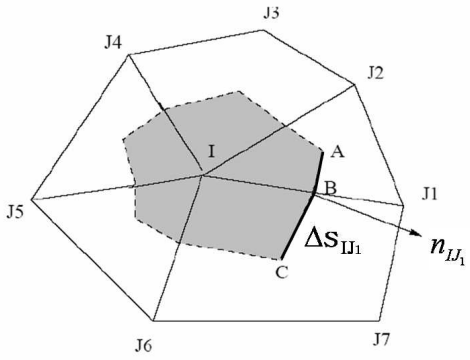

Figure 3.3: Medial-dual control volume representation for internal node.

The numerical scheme has an edge based data structure. The fluxes are evaluated at the middle of each edge $\mathbf{x} = \frac{1}{2}(\mathbf{x}_I + \mathbf{x}_J)$, and are approximated using pre-computed edge-weights $\Delta\mathbf{s}_{IJ}$. The edge-weights are determined for each edge, the weight being equal to the area associated with the edge, multiplied by its normal, so that:

$$\Delta\mathbf{s}_{IJ} = \mathbf{n}_{IJ}.\Delta s_{IJ}.$$

Coming back to the example shown in Fig. 3.3, the normal $\mathbf{n}_{IJ_1}$ of the surface AC between the nodes I and J_1, is obtained by taking the average of the normals between

the surfaces AB and BC. By construction, the edge-weights are anti-symmetric, i.e:

$$\Delta \mathbf{s}_{IJ} = -\Delta \mathbf{s}_{JI} \tag{3.4.32}$$

and they ensure conservation since

$$\sum_{J \in E_I} \Delta \mathbf{s}_{IJ} = 0 \tag{3.4.33}$$

where E_I represents the set of all nodes connected to node I.

Finally, using the edge-weights, the discretised form of the steady-state Navier-Stokes equations is given by:

$$\mathcal{R}_I = \frac{1}{\mathcal{V}_I} \left[\mathcal{V}_I \mathbf{S}_I - \sum_{J \in E_I} \left(\mathcal{F}^I_{IJ} + \mathcal{F}^V_{IJ} \right) \Delta \mathbf{s}_{IJ} \right] = 0 \tag{3.4.34}$$

in which $\mathcal{F}^I_{IJ}$ and $\mathcal{F}^V_{IJ}$ represent the discretised inviscid and viscous fluxes in the direction IJ, $\mathcal{R}_I$ is the residual, $\mathbf{S}_I$ is the source term, and $\mathcal{V}_I$ is the measure of the control volume associated to node I. At convergence, the flow residual should be zero or below a threshold value. The above formulation includes the discretisation of the turbulence model, the details of which are not presented here but are comprehensively discussed in [71].

3.4.1 Inviscid Flux

The discrete approximation of the inviscid flux $\mathcal{F}^I_I$ at each node is obtained by summing the contributions from each edge surrounding the node, as follows:

$$\mathcal{F}^I_I = \sum_{J \in E_I} \mathcal{F}^I_{IJ} \Delta \mathbf{s}_{IJ} \tag{3.4.35}$$

The flux across the edge IJ is obtained by combining a central differencing of the inviscid fluxes at both ends of the edge, and a numerical smoothing, as follows:

$$\mathcal{F}^I_{IJ} = \frac{1}{2} \left(\mathcal{F}^I_I + \mathcal{F}^I_J \right) - \mathcal{D}^I_{IJ} \tag{3.4.36}$$

where the central difference term is a second order approximation of the space derivative. D^I_{IJ} represents the numerical dissipation and is a blend of second order and fourth-order smoothing terms, which are included in order to damp the high frequency mode components of the flow solution. These higher order terms are also essential to improve the convergence to a steady-state solution for the multigrid

method that will be presented in Section 3.4.5. The formulation of the numerical dissipation is given by:

$$\mathcal{D}_{IJ}^{I} = \frac{1}{2}\left|A_{IJ}\right|\left[\psi_{IJ}\left(\mathbf{U}_J - \mathbf{U}_I\right) - \epsilon_2\left(1-\psi_{IJ}\right)\left(\mathcal{L}\left(\mathbf{U}_J\right) - \mathcal{L}\left(\mathbf{U}_I\right)\right)\right] \tag{3.4.37}$$

where A_{IJ} is the Roe matrix, $\epsilon_2 = 0.5$ is a smoothing parameter, and $\mathcal{L}$ is the pseudo-Laplacian operator given by:

$$\mathcal{L}\left(\mathbf{U}_I\right) = \left(\sum_{J\in E_I}\frac{1}{\left|\mathbf{X}_J - \mathbf{X}_I\right|}\right)^{-1}\left(\sum_{J\in E_I}\frac{\left(\mathbf{U}_J - \mathbf{U}_I\right)}{\left|\mathbf{X}_J - \mathbf{X}_I\right|}\right) \tag{3.4.38}$$

where $\mathbf{X}_I$ and $\mathbf{X}_J$ represent the coordinates of nodes I and J respectively. ψ_{IJ} is a limiter introduced so that the smoothing reverts to first order ($\psi_{IJ} = 1$) in the vicinity of discontinuities such as shocks to avoid oscillations. This limiter is given by:

$$\psi_{IJ} = min\left(\epsilon_3\left(\frac{\left|\mathcal{L}\left(p_j\right)\right|}{\left|\mathcal{L}\left(p_j\right) + 2p_j\right|} + \frac{\left|\mathcal{L}\left(p_i\right)\right|}{\left|\mathcal{L}\left(p_i\right) + 2p_i\right|}\right), 1\right) \tag{3.4.39}$$

where $\epsilon_3 = 8$.

3.4.2 Viscous Flux

Similarly to the inviscid flux, the discrete approximation of the viscous flux F_I^V at each node of the computational domain is given by:

$$\mathcal{F}_I^V = \sum_{J\in E_I}\mathcal{F}_{IJ}^V \Delta\mathbf{s}_{IJ} \tag{3.4.40}$$

However, unlike the inviscid flux, F_{IJ}^V is composed of spatial derivatives of the flow variables. Therefore, the discrete approximation of this term is completely defined by the discrete representation of the flow gradients. These gradients are determined at the mid-point of each edge. If $\mathbf{Q}$ denotes the vector of primitive variables, the gradient of $\mathbf{Q}$ is obtained by:

$$\nabla\mathbf{Q}_{IJ} = \overline{\nabla\mathbf{Q}}_{IJ} - \left(\overline{\nabla\mathbf{Q}}_{IJ}.\delta\mathbf{s}_{IJ} - \frac{\left(\mathbf{Q}_J - \mathbf{Q}_I\right)}{\left|\mathbf{X}_J - \mathbf{X}_I\right|}\right)\delta\mathbf{s}_{IJ} \tag{3.4.41}$$

with

$$\overline{\nabla\mathbf{Q}}_{IJ} = \frac{1}{2}\left(\nabla\mathbf{Q}_I + \nabla\mathbf{Q}_J\right) \tag{3.4.42}$$

and

$$\delta\mathbf{s}_{IJ} = \frac{\mathbf{X}_J - \mathbf{X}_I}{\left|\mathbf{X}_J - \mathbf{X}_I\right|} \tag{3.4.43}$$

and

$$\nabla \mathbf{Q}_I = \sum_{J \in E_I} \frac{1}{2} \left(\mathbf{Q}_I + \mathbf{Q}_J \right) \Delta \mathbf{s}_{IJ} \tag{3.4.44}$$

The above formulation can be regarded as a combination of central differences of the flow gradients at both ends of each edge, with a numerical dissipation term. The central difference is second order accurate, so the role of the numerical dissipation term is to damp the high-frequency modes from the flow solution.

From the code standpoint, note that the numerical smoothing term D_{IJ}^I in the inviscid flux is composed of second- and fourth-order terms, similar in nature to the viscous dissipation terms. So the strategy that has been adopted was to take off this term from the discrete approximation of the inviscid flux F_{IJ}^I, and to include it to the discrete representation of the viscous flux.

Now that the flux discretisation has been formulated for all interior nodes, it remains to describe how the boundary conditions are imposed.

3.4.3 Boundary Conditions

A typical blade-row computational domain can be represented by a single blade-passage as shown in Fig. 3.4. More complex geometries including several blade-passages or even the whole annulus can easily be obtained by assembling as many blade-passages as required. As far as the computation of steady-state flows in turbomachinery blade-rows is concerned, there are three main categories of boundary conditions that are needed: inlet/outlet, solid wall, and periodicity. These are illustrated in Fig. 3.4. In the present nonlinear analysis, the boundary conditions are applied directly to the evaluation of the flow residuals in (3.4.34). This is a necessary requirement for the correct implementation of a multigrid method since, as we will see in Section 3.4.5, residuals are transmitted from grid levels and must be consistent between each grid. The detailed implementation of the boundary conditions is presented below.

Far-field boundary conditions

The far-field boundary conditions are imposed at the inflow and outflow boundaries. They are directly applied to the evaluation of the inviscid flux term F_K^I at the boundary node K by solving the following one-dimensional characteristic problem:

$$\mathcal{F}_K^I = \frac{1}{2} \left(\mathbf{F}_K^I \left(\mathbf{U}_K \right) + \mathbf{F}_K^I \left(\mathbf{U}_\infty \right) - \left| \mathbf{A}_K \right| \left(\mathbf{U}_\infty - \mathbf{U}_K \right) \right) \tag{3.4.45}$$

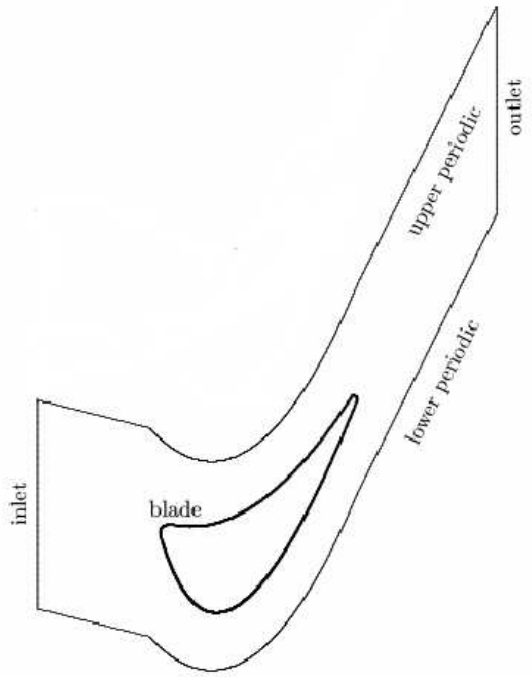

Figure 3.4: Computational domain with blade boundary conditions

where

$$\mathbf{A}_K = \frac{\partial \mathbf{F}_K^I}{\partial \mathbf{U}_K} \tag{3.4.46}$$

The term $\mathbf{U}_\infty$ in (3.4.45) is the prescribed far-field state that can be defined in many ways. Indeed, the correct definition of the boundary conditions depends upon the mathematical nature of the flow equations, whether these are elliptic, parabolic, or hyperbolic. The boundary conditions are determined using the method of characteristics. Since an unsteady time-marching solution procedure is used to ultimately obtain a steady-state flow result in the limit of large pseudo-time, the Euler equations are hyperbolic, no matter whether the flow is locally subsonic or supersonic, and no matter whether we have one, two, or three spatial dimensions, the marching direction is always the time direction. As a consequence of their hyperbolic nature, the three-dimensional Euler equations require four boundary conditions at the inflow for subsonic inlet velocities, and only one at the outflow also for a subsonic outlet boundary. Typically, total pressure, total temperature, and flow angles are imposed at the inlet, and static pressure at the outlet. For supersonic inflow and outflow, the number of boundary conditions are five and zero, respectively. Following the same logic, the three-dimensional unsteady Navier-Stokes equations form a hybrid system of mixed nature, being parabolic-hyperbolic in time and space, but becoming elliptic-hyperbolic in space for the steady formulation. Therefore, the three-dimensional Navier-Stokes equations require more boundary conditions than

the Euler equations. For example, for subsonic flows, five boundary conditions are required at the inlet, and one at the outlet. Usually, total pressure, total temperature, flow angles, and turbulence parameter are prescribed at the inlet, and static pressure at the outlet.

Solid Wall

The boundary conditions at the solid walls vary depending on the type of flow. As far as we are concerned, flows can either be considered as:

- Inviscid: In this case the fluid is allowed to slip on the solid wall, and thus its direction remains tangential to the wall surface. This is represented by the slip boundary condition.

- Viscous: In this case the fluid velocity is equal to wall velocity, which means that the fluid velocity in the frame relative to the wall is equal to zero. This is the no-slip boundary condition. In turbomachinery blade-row applications, these boundary conditions are typically applied to the hub, casing, and blade surfaces.

Slip Boundary Condition In the frame relative to the wall, the fluid velocity $\mathbf{u}_I$, in the direction $\mathbf{n}_K$ normal to the wall, is equal to zero. Mathematically, this is expressed by imposing the condition that:

$$\mathbf{u}_I^T.\mathbf{n}_K = 0 \tag{3.4.47}$$

at the nodes belonging to solid walls, where $\mathbf{u}_I = (u_{Ix}, u_{Iy}, u_{Iz})^T$, and $\mathbf{n}_K = (n_{Kx}, n_{Ky}, n_{Kz})^T$. In this work, the slip boundary condition is implemented by imposing a zero mass flux in the evaluation of the boundary flux. Additionally, the normal momentum components of the residual at the nodes on the wall are explicitly set to zero. Consequently, only the tangential component of the flow residuals is solved and the solution of the Navier-Stokes equations with solid wall boundary condition can algebraically be represented by:

$$(\mathbf{I} - \mathbf{B}_I)\,\mathbf{R}\,(\mathbf{U}_I) = 0 \tag{3.4.48}$$

where

$$\mathbf{B}_I = \begin{pmatrix} 0 & 0 & 0 & 0 & 0 \\ 0 & n_{Ix}n_{Ix} & n_{Ix}n_{Iy} & n_{Ix}n_{Iz} & 0 \\ 0 & n_{Iy}n_{Ix} & n_{Iy}n_{Iy} & n_{Iy}n_{Iz} & 0 \\ 0 & n_{Iz}n_{Ix} & n_{Iz}n_{Iy} & n_{Iz}n_{Iz} & 0 \\ 0 & 0 & 0 & 0 & 0 \end{pmatrix} \tag{3.4.49}$$

represents the product $\mathbf{n}_K.\mathbf{n}_K^T$ into a matrix of dimensions (5×5).

Finally, in order to avoid any spurious normal components of the velocity appearing during the multigrid transfers, all components of the velocity normal to the wall are also deleted before the multigrid transfer. Algebraically, this is given by:

$$\mathbf{B}_I\mathbf{U}_I = 0 \tag{3.4.50}$$

No-Slip Boundary Condition The no-slip boundary condition is obtained by imposing:

$$\mathbf{u}_I = 0 \tag{3.4.51}$$

at the nodes on the solid wall and in the frame relative to the blade. Similarly to the slip boundary condition, all the components of the momentum and turbulence equations of the residual are explicitly set to zero using (4.6.59). However in the present case $\mathbf{B}_I$ is given by:

$$\mathbf{B}_I = \begin{pmatrix} 0 & 0 & 0 & 0 & 0 & 0 \\ 0 & 1 & 1 & 1 & 0 & 0 \\ 0 & 1 & 1 & 1 & 0 & 0 \\ 0 & 1 & 1 & 1 & 0 & 0 \\ 0 & 0 & 0 & 0 & 0 & 0 \\ 0 & 0 & 0 & 0 & 0 & 1 \end{pmatrix} \tag{3.4.52}$$

In the present code, the no-slip boundary condition is accompanied by a wall function, the details of which are presented below.

Wall Function

The wall function is used to represent the boundary layer profiles near the viscous walls in order to avoid the generation of an extremely fine mesh, which would otherwise lead to prohibitively expensive computations. Instead, the wall function determines the boundary layers from fluid dynamic considerations. For example, in

the linear sub-layer (i.e. where the fluid layer is in contact with a smooth wall), the viscous shear stress is much higher than the Reynolds shear stress, thus the fluid dynamic is dominated by viscous effects. This layer is in practice extremely thin and is limited to a distance normal to wall y verifying:

$$y^+ = \frac{y}{\nu_l}\sqrt{\frac{\tau_w}{\rho}} < 5$$

where τ_w is the wall shear stress, and ν_l is the laminar kinematic viscosity.

Within the linear sub-layer, the shear stress is approximately constant and equal to the wall shear stress given by:

$$\tau\left(y\right) = \mu_l \frac{\partial u}{\partial y} \cong \tau_w, \quad for\ 0 < y^+ < 5 \tag{3.4.53}$$

where u is the fluid velocity in the linear sub-layer, and μ_l is the laminar molecular viscosity. Hence, in this region of the flow, velocity varies linearly in the direction normal to the wall. The discrete form of (3.4.53) can be represented by:

$$\tau_w = \mu_l \frac{\Delta u}{\Delta y}, \quad for\ 0 < y^+ < 5 \tag{3.4.54}$$

In practice, two main methods can used to obtain the correct value of the wall shear stress:

- In the first method, the turbulence model and the flow equations are solved up to the wall. This means that a very fine mesh must be produced, which includes a sufficient number of mesh points in the linear sub-layer. In this case, the stress at the wall can be determined by:

$$\tau_w = \mu_l \frac{\Delta u_p}{\Delta y_p}, \quad for\ 0 < y^+ < 5 \tag{3.4.55}$$

  where Δy_p is the distance between the wall node and the near-wall node, and Δu_p is the corresponding velocity difference.

- In the second method, a standard wall function is used, which estimates the characteristics of the boundary layer without resolving it in detail. This method is much cheaper computationally because it requires substantially less mesh points than the first method.

Using a wall function and (3.4.55), two options are possible for the computation of the wall shear stress:

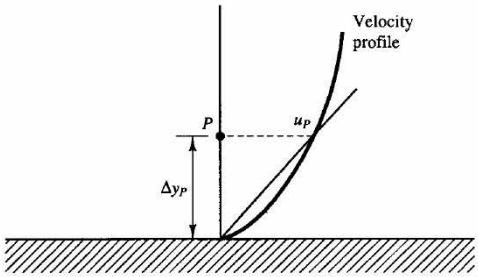

Figure 3.5: Wall function representation

- In the first option, one allows the fluid velocity on the wall to slip, so that the value of Δu_p gives the correct wall shear stress. This is the so called *slip-velocity* condition.

- In the second option, the molecular viscosity μ_l is replaced by an *effective* velocity μ_{eff}, which gives the correct wall shear stress. This is the method adopted in the present work.

In order to determine the correct value of μ_{eff}, one first needs to express the relationship that gives the wall shear stress in relation to the skin friction coefficient (c_f). Such relationship can be given by:

$$\tau_w = \frac{1}{2}\rho c_f \left(\Delta u_p\right)^2 \tag{3.4.56}$$

where c_f is determined by:

$$c_f = \frac{2}{\left(u_p^+\right)^2} \tag{3.4.57}$$

with

$$u_p^+ = u_p\sqrt{\frac{\rho}{\tau_w}} \tag{3.4.58}$$

We also define the near wall Reynolds number as:

$$Re = \frac{\Delta u_p \Delta y_p}{\nu_l} = u_p^+ y_p^+ \tag{3.4.59}$$

where

$$y_p^+ = \frac{\Delta y_p}{\nu_l}\sqrt{\frac{\tau_w}{\rho}} \tag{3.4.60}$$

so that the wall shear stress can be re-expressed by:

$$\tau_w = \frac{\rho \Delta u_p^2}{u_p^{+2}} \tag{3.4.61}$$

and finally, the effective viscosity is given by:

$$\mu_{eff} = \frac{Re}{\left(u_p^+\right)^2}\mu_l \tag{3.4.62}$$

Since the near wall Reynolds number is easily obtained, what remains to be done is to determine the value of u_p^+. For that, we use the Spalding's formulation given by

$$y^+ = u_p^+ + e^{-\kappa B}\left[e^{\kappa u_p^+} - 1 - \kappa u_p^+ - \frac{1}{2}\left(\kappa u_p^+\right)^2 - \frac{1}{6}\left(\kappa u_p^+\right)^3\right] \tag{3.4.63}$$

where

$$\kappa = 0.41, \quad B = 5.3, \quad e^{\kappa B} = 8.8 \tag{3.4.64}$$

Equation (3.4.63) is solved by iteration, using the Newton-Raphson method. In order to accelerate the convergence of the iterative scheme, two different cases are distinguished:

- If $Re \leq 140$:

$$0 = u_p^+ + e^{-\kappa B}\left[e^{\kappa u_p^+} - 1 - \kappa u_p^+ - \frac{1}{2}\left(\kappa u_p^+\right)^2 - \frac{1}{6}\left(\kappa u_p^+\right)^3\right] - \frac{Re}{u_p^+}$$

  for which the starting solution is set to $u_p^+ = \sqrt{Re}$, which corresponds to the laminar sub-layer solution $u_p^+ = y_p^+$

- If $Re > 140$:

$$0 = u_p^+ - B - \frac{1}{\kappa} ln\left(e^{-\kappa B}\left[e^{\kappa u_p^+} - 1 - \kappa u_p^+ - \frac{1}{2}\left(\kappa u_p^+\right)^2 - \frac{1}{6}\left(\kappa u_p^+\right)^3\right] + \frac{Re}{u_p^+} - u_p^+\right)$$

  for which the starting solution is set to $u_p^+ = B + ln\left(Re\right)/\kappa$, which corresponds to the log-layer solution.

Periodicity

In most cases, it can be assumed that there is no blade-to-blade variation of the mean flow in the same blade-row. When this is verified, it is correct to compute the mean flow solution for only one blade-passage in the assembly, and to repeat this solution to all the other blade-passages. This approach allows significant computational savings to be made.

The computation of the mean flow over one blade-passage requires the implementation of a periodic boundary condition. For that, two periodic boundaries are

typically inserted in the computational domain, which are super-imposable by an angular rotation around the engine given by:

$$P = \frac{2\pi}{B}$$

where B is the number of blades in the current blade-row. The boundary located at the minimum values of θ is called the lower periodic boundary, while the other one is called the upper periodic boundary. The two periodic boundaries must be meshed so that the periodic nodes form pairs of nodes, which are also super-imposable by an angular rotation P around the engine. The periodic boundary condition imposes that the flow solutions are identical at both periodic boundaries. Mathematically, this is expressed by:

$$\mathbf{U}(\theta + P) = \mathbf{U}(\theta) \tag{3.4.65}$$

In the present code, this boundary condition is imposed directly to the evaluation

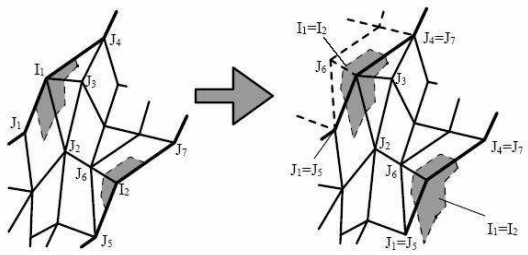

Figure 3.6: 2-D representation of discrete flux residual at the periodic boundaries

of the flow residual R_I in (3.4.34). This is done by sharing a common control volume between each periodic pair of nodes. This is illustrated in Fig. 3.6. The residual associated with the node on the lower periodic boundary contributes to the residual of its periodic pair on the upper boundary, *et vice-versa*.

3.4.4 Smoothing iteration

The iterative scheme used to converge the flow residuals to zero is the pseudo time-stepping 5-stage Runge-Kutta algorithm developed by Martinelli [68]. This is an explicit scheme in which the new iterate is determined as follows:

$$\begin{aligned} \mathbf{U}_I^{(0)} &= \mathbf{U}_I^n \\ \mathbf{U}_I^{(k)} &= \mathbf{U}_I^n - \alpha_k \Delta t_I \mathbf{R}_I^{(k-1)}, \quad k = 1,2,3,4,5 \\ \mathbf{U}_I^{(n+1)} &= \mathbf{U}_I^{(5)} \end{aligned} \tag{3.4.66}$$

where

$$\begin{aligned}\mathbf{R}_I^{(k-1)} &= \mathbf{C}_I\left(\mathbf{U}^{(k-1)}\right) - \mathbf{B}_I^{(k-1)} \\ \mathbf{B}_I^{(k-1)} &= \beta_k \mathbf{D}_I\left(\mathbf{U}^{(k-1)}\right) + (1-\beta_k)\,\mathbf{B}_I^{(k-2)}\end{aligned}$$

and

$$\begin{aligned}\alpha_1 = \tfrac{1}{4}, \alpha_2 = \tfrac{1}{6}, \alpha_3 = \tfrac{3}{8}, \alpha_4 = \tfrac{1}{2}, \alpha_5 = 1 \\ \beta_1 = 1, \beta_2 = 0, \beta_3 = \tfrac{14}{25}, \beta_4 = 0, \beta_4 = \tfrac{11}{25}\end{aligned}$$

In the above expressions, $\mathbf{C}_I$ represents the convective part of the flow residual R_I and $\mathbf{D}_I$ regroups all the other terms which contribute to evaluation of the flow residual, i.e. source term, viscous flux, and numerical smoothing. This iterative scheme combines adequately two important aspects of the solution method. First, it has a large stability region. And second, this method requires low memory storage, essentially because the terms $\mathbf{D}_I\left(\mathbf{U}^{(2)}\right)$ and $\mathbf{D}_I\left(\mathbf{U}^{(4)}\right)$ do not need to be computed, since $\beta_2 = 0$ and $\beta_4 = 0$. The term Δt_I in (3.4.66) represents the local time-step used to time-march the flow solution in pseudo-time. For the Navier-Stokes equations, this local time-step is determined as follows:

$$\frac{1}{\Delta t_I} = \frac{1}{CFL} \times max\left(\frac{1}{\Delta t_I^I}, \frac{\epsilon^V}{\Delta t_I^V}\right) \tag{3.4.67}$$

where CFL is the inviscid CFL number, $\epsilon^V = 0.5$, and Δt_I^I and Δt_I^V are the inviscid and viscous time-steps respectively, given by:

$$\frac{1}{\Delta t_I^I} = \frac{1}{\mathcal{V}_I}\left(\sum_{J\in E_I} \rho\left(\mathbf{A}_{IJ}\right)\Delta s_{IJ} + \sum_{K\in B_I} \rho\left(\mathbf{A}_k\right)\Delta s_K\right) \tag{3.4.68}$$

and

$$\frac{1}{\Delta t_I^V} = \frac{1}{\mathcal{V}_I}\sum_{J\in E_I} \rho\left(\mathbf{B}_{IJ}\right)\frac{1}{|\mathbf{x}_J - \mathbf{x}_I|}\Delta s_{IJ} \tag{3.4.69}$$

where $\mathbf{A}_{IJ} = \partial \mathbf{F}_{IJ}^I / \partial \mathbf{U}$, $\mathbf{B}_{IJ} = \partial \mathbf{F}_{IJ}^V / \partial \mathbf{U}$, and $\rho\left(\mathbf{A}\right)$ represents the spectral radius of the matrix $\mathbf{A} \in \Re^{n\times n}$, defined by $\rho\left(\mathbf{A}\right) = max\left|\lambda_i\right|$, $\forall 1 \leq i \leq n$, $\lambda_1, ..., \lambda_n$ being the eigenvalues of $\mathbf{A}$.

When local time-stepping is not used alone, a local Jacobi preconditioner, described in [71], is also added to relax the discrete stiffness of the turbulent Navier-Stokes equations and to improve the convergence rate of the mean flow solution without affecting it.

Finally, an optional multigrid strategy is used to accelerate the convergence properties of the Runge-Kutta operations. This is described below.

3.4.5 Multigrid Method

The fundamental concept of the multigrid method is the elimination of the high frequency modes from the flow solution in order to accelerate the flow residual convergence. For this, a number of successively coarser grids are used, and smoothing iterations are performed on these grids to eliminate the high frequency modes of the solution. Two transfer operations need to be defined to transfer the flow solution onto the next grid level, either coarser or finer. In the following description, the subscript f will be used for the flow quantities related to the fine mesh, and c for those on the coarse mesh. The transfer operations are:

• **Restriction**: This operator is used to transfer the flow quantities from a fine to coarse grid. The flow quantities that are transfered are the flow residual and the flow variables, so that

$$R_c = \mathbf{I}_f^c \left(R_f \right)$$

and

$$\mathbf{U}_c = \mathbf{I}_f^c \left(\mathbf{U}_f \right)$$

The detailed description of the transfer operation $\mathbf{I}_f^c$ for an arbitrary quantity Q is given by:

$$Q_{Ic} = \frac{\sum_{J \in K_I} \mathcal{V}_{Jf} Q_{Jf}}{max \left(\mathcal{V}_{Ic}, \sum_{J \in K_I} \mathcal{V}_{Jf} \right)}$$

where K_I represents the set of grid points on the fine grid related to node I on the coarse grid.

• **Prolongation**: The flow solution on the fine grid is corrected using the prolongation operator $\mathbf{I}_c^f$, from coarse to fine grid, defined by:

$$\Delta \mathbf{U}_f = \mathbf{I}_c^f \left(\Delta \mathbf{U}_c \right)$$

where

$$\Delta \mathbf{U}_{Jf} = \Delta \mathbf{U}_{Ic} + \left(\mathbf{x}_{Jf} - \mathbf{x}_{Ic} \right) . \nabla \left(\Delta \mathbf{U}_c \right)_I , \forall J \in K_I$$

in which, the gradients of the corrections are given by

$$\begin{aligned} \nabla \left(\Delta \mathbf{U}_c \right)_I &= \sum_{J \in E_I} \tfrac{1}{2} \left(\Delta \mathbf{U}_{Ic} + \Delta \mathbf{U}_{Jc} \right) \mathbf{n}_{IJ} \Delta s_{IJ} + \sum_{K \in B_I} \Delta \mathbf{U}_{Ic} \mathbf{n}_K \Delta s_K \\ &= \sum_{J \in E_I} \tfrac{1}{2} \left(\Delta \mathbf{U}_{Jc} - \Delta \mathbf{U}_{Ic} \right) \mathbf{n}_{IJ} \Delta s_{IJ} \end{aligned}$$

Knowing the details of these transfer operators, the Full Approximation Scheme [4] (FAS), which is used to obtain the iterative solution of the nonlinear steady-state flow problem, can now be presented. For clarity, the discrete Navier-Stokes equations are now expressed as a nonlinear system $N(\mathbf{U}) = f$, where N approximates the nonlinear set of partial differential equations, f is a forcing function, and $\mathbf{U}$ is the solution of this system of equations. Also for simplicity, the iterative scheme is presented for the case of two grids, one coarse and one fine. Then, the iterative procedure can be expressed as:

$$\mathbf{U}^{n+1} = \mathbf{U}^n + R\left(f - N\left(\mathbf{U}^n\right)\right), n = 1, 2, ... \tag{3.4.70}$$

where R represents the Runge-Kutta procedure. The Full Approximation Scheme is given by a succession of procedures that are described below:

• **Pre-smoothing (on fine grid)**: At each iteration, the flow solution on the fine grid is determined using the smoothing operation being the explicit 5-stage Runge-Kutta procedure, that can be represented as follows:

$$\mathbf{U}_f^{n+1} = \mathbf{U}_f^n + R\left(f_f - N_f\left(\mathbf{U}_f^n\right)\right), n = 1, 2, ... \tag{3.4.71}$$

• **Restriction (from fine to coarse grid)**: On the first step of the multigrid process, the flow solution obtained on the fine grid is transfered onto the coarse grid, and constitutes the coarse grid initialisation solution given by $\mathbf{U}_c^0 = \mathbf{I}_f^c\left(\mathbf{U}_f\right)$. The flow residual is also transfered from the fine to coarse grid $R_c^0 = \mathbf{I}_f^c\left(R_f\right)$.

Coarse grid smoothing: An extra source term is added to the smoothing operations on the coarse grid, by subtracting the flow residuals, which are transfered from the fine to coarse grid, to the coarse grid residual which is based on the coarse grid initial solution $\mathbf{U}_c^0$. In other words, the smoothing iterations on the coarse grid are expressed by:

$$\mathbf{U}_c^{n+1} = \mathbf{U}_c^n + R\left(f_c - N_c\left(\mathbf{U}_c^n\right)\right), n = 1, 2, ... \tag{3.4.72}$$

where the source term on the coarse mesh is now given by:

$$f_c = N_c\left(\mathbf{U}_c^0\right) - R_c^0 \tag{3.4.73}$$

• **Prolongation (from coarse to fine grid)**: Given the superscript *old* to the last iterative solution obtained on the fine grid before the

restriction operation, and *new* for the updated solution on the fine grid based on the correction from the coarse grid smoothing, the update on the fine grid solution is then given by

$$\mathbf{U}_f^{new} = \mathbf{U}_f^{old} + \Delta \mathbf{U}_f \tag{3.4.74}$$

- **Post-smoothing (on fine grid)**:

$$\mathbf{U}_f^{n+1} = \mathbf{U}_f^n + R\left(f_f - N_f\left(\mathbf{U}_f^n\right)\right), n = 1, 2, ... \tag{3.4.75}$$

The above description given for two grids, one coarse and the other one fine, is easily applicable to a greater number of grids by applying the same transfer operations between consecutive grid levels. From practical experience, it was found that four grid levels provides the most effective strategy for the vast majority of cases. There are theoretically many possible multigrid cycles strategies. The one adopted in this work is the *V* cycle shown in Fig. 3.7.

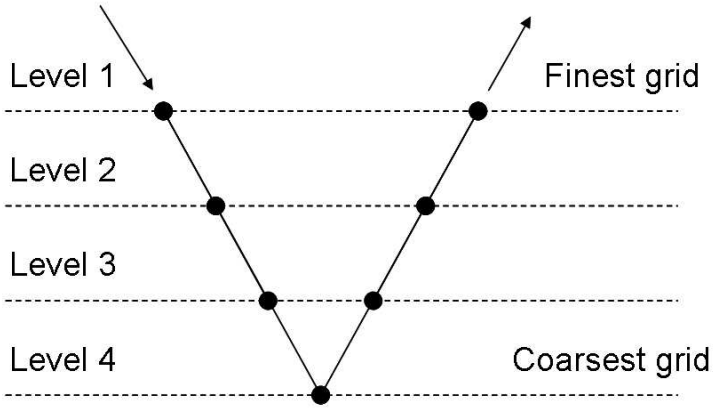

Figure 3.7: V-multigrid cycle representation

Chapter 4

Harmonic Linearised Multi Blade-Row Analysis

4.1 Introduction

This chapter is devoted to the presentation of the harmonic linearised multi blade-row analysis. The chapter is divided in two parts. The first part presents the multi blade-row coupling kinematics. The coupling is represented by the theory of *spinning modes*, which applies to flows with small amplitude perturbations that are decomposed in the frequency domain. The second part describes the numerical method used to solve the linearised multi blade-row equations. The linear code is based on the linearisation of the discretised steady-state equations presented in Chapter 3. Finally, the boundary conditions are discussed, followed by the iterative solution method used to converge the flow solution.

4.2 Multi Blade-row Coupling Kinematics

Most theories describing multi blade-row coupling use the time-linearised approach and are based on the same framework. That's to say, they describe how blade-rows interact via the so-called *spinning modes* [39, 77, 76]. The same theory is used in this thesis. Its formulation is extremely convenient as it fits well with two fundamental aspects of the harmonic time-linearised analysis: (i) the small amplitude perturbation assumption; (ii) the analysis in the frequency domain.

4.2.1 General Model Description

Consider an annular duct with its axis in the x coordinate direction. Let $r_2(x)$ and $r_1(x)$ be the outer and inner radius as a function of the axial distance x. Let N blade-rows be inserted into this duct, as represented in Fig. 4.1, where B_j is the

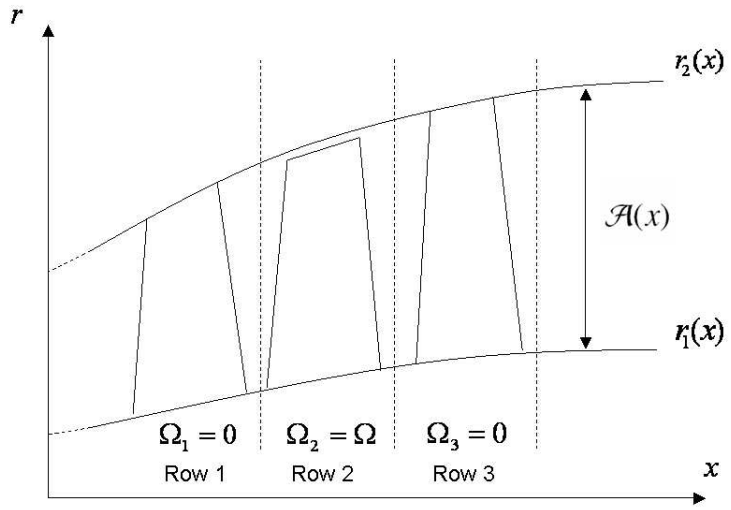

Figure 4.1: Two dimensional representation of several blade-row lining on the axial direction

number of blades of the j^{th} blade-row and Ω_j is the corresponding rotational speed. Let us assume that *even*-numbered blade-rows are rotors and *odd*-numbered blade-rows are stators. If all the rotors rotate with the same speed, then the rotational speeds of the blade-rows are given by:

$$\Omega_j = 0,\ j = 1, 3, 5, \cdots \tag{4.2.1}$$

and,

$$\Omega_j = \Omega,\ j = 2, 4, 6, \cdots \tag{4.2.2}$$

with $\Omega > 0$ in the positive θ direction. If we name (x_j, θ_j, r_j, t) the cylindrical coordinates relative to the j_{th} blade-row, and (x, θ, r, t) the absolute cylindrical coordinates fixed to the duct, then the coordinates transformations between frames of reference are given by:

$$x = x_j,\quad \theta = \theta_j + \Omega_j t,\quad r = r_j \tag{4.2.3}$$

where t represents time.

Finally, consider that we are studying an aeroelastic problem in turbomachinery such as flutter or forced response, for which the amplitudes of unsteady perturbations

associated with the original disturbance are small compared to the time mean flow. Under these conditions, the unsteady flow is governed by the linearised equations.

4.2.2 Multiplication Mechanism of Frequency and Circumferential Wave Number

Unsteady flows are made up of acoustic, entropic, and vortical waves (see Appendix A), which provide a mechanism of communication between the blade-rows. As waves propagate across the blade-rows, their frequencies vary in the relative frames of the blade-rows due to their relative motion. This phenomenon is known as the *Doppler* effect. The theory behind the multi blade-row coupling is based on the mathematical representation of this phenomenon. When the number of blade-rows and the wave numbers are large, the representation of the blade-row coupling can be very complicated. Hence, for simplicity, the theory is first illustrated for the simple two-blade-row flutter case of Fig. 4.2.

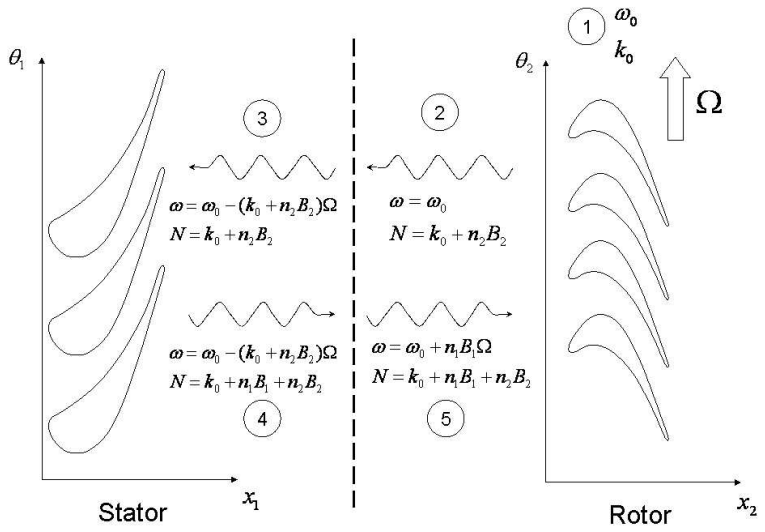

Figure 4.2: Shifting and scattering effect of frequency and circumferential wave number over one stage

The description of Fig. 4.2 is divided into several parts:

- First, consider a single stage (stator/rotor) for which the rotor blades are vibrating at frequency ω_0 and nodal diameter k_0, B_1 and B_2 representing the number of stator and rotor blades respectively. Subscript 1 refers to the quantities in the stator frame, while subscript 2 refers to the rotor. Ω is the rotor rotational speed, positive in the positive θ

direction. Using linear theory, the vibration amplitude of the m_{th} rotor blade is given by:

$$\tilde{h}_2(x_2, \theta_2, r_2, m, t) = \hat{h}_2(x_2, \theta_2, r_2) e^{j(\omega_0 t + m\sigma_0)} \tag{4.2.4}$$

where σ_0 is the inter-blade phase angle of the motion.

• When the rotor blades vibrate, the flow attached to them responds aerodynamically producing acoustic, vortical, and entropic waves. Some of these waves propagate upstream and others downstream away from the blades. In the rotor frame, these waves have the same time frequency ω_0 as the frequency of blade vibration, and they have an infinite number of circumferential wave numbers. Mathematically, this can be represented as follows:

$$\tilde{\mathbf{U}}\left(x_2, \theta_2, r_2, t\right) = \sum_{n_2=-\infty}^{+\infty} \hat{\mathbf{U}}_{n_2}\left(x_2, r_2\right) e^{j(\omega_0 t + (k_0 + n_2 B_2)\theta_2)} \tag{4.2.5}$$

where n_2 represents a circumferential Fourier mode, which has the complex amplitude $\hat{\mathbf{U}}_{n_2}(x_2, r_2)$.

• Some of the waves originating from the rotor blades vibration impinge on the neighbouring stator blades. The Doppler effect causes the frequency of the waves in the rotor to shift in the stator frame. However, the Doppler effect does not affect the circumferential wave number, which thus remains identical between one frame of reference and the next. Therefore, written in the stator frame, (4.2.5) becomes:

$$\tilde{\mathbf{U}}\left(x_1, \theta_1, r_1, t\right) = \sum_{n_2=-\infty}^{+\infty} \hat{\mathbf{U}}_{n_2}\left(x_1, r_1\right) e^{j((\omega_0 - (k_0 + n_2 B_2)\Omega)t + (k_0 + n_2 B_2)\theta_1)} \tag{4.2.6}$$

Note that the frequencies of the waves in the stator, given by $\omega_{n_2} = \omega_0 - (k_0 + n_2 B_2)\,\Omega$, depend on the circumferential mode n_2.

• When the waves emanating from the rotor impinge on the stator, the system in the stator responds aerodynamically producing in turn acoustic, vortical and entropic waves, which propagate away from the stator. The waves must satisfy the complex periodicity condition in the stator. This affects their circumferential wave numbers, which then

scatter as follows:

$$\tilde{\mathbf{U}}(x_1,\theta_1,r_1,t)=\sum_{n_1=-\infty}^{+\infty}\sum_{n_2=-\infty}^{+\infty}\hat{\mathbf{U}}_{n_1n_2}(x_1,r_1)e^{j((\omega_0-(k_0+n_2B_2)\Omega)t+(k_0+n_1B_1+n_2B_2)\theta_1)} \tag{4.2.7}$$

• Some of the waves travelling away from the stator later impinge on the rotor. The relative motion of the blade-rows and the subsequent Doppler effect again cause the frequencies of the waves in the stator to shift in the rotor frame. Therefore, written in the rotor frame, (4.2.7) has the form:

$$\tilde{\mathbf{U}}(x_2,\theta_2,r_2,t)=\sum_{n_1=-\infty}^{+\infty}\sum_{n_2=-\infty}^{+\infty}\hat{\mathbf{U}}_{n_1n_2}(x_2,r_2)e^{j((\omega_0+n_1B_1\Omega)t+(k_0+n_1B_1+n_2B_2)\theta_2)} \tag{4.2.8}$$

Note that the frequencies in the rotor are now given by $\omega_{n_1}=\omega_0+n_1B_1\Omega$, and thus depend on the circumferential mode n_1, but not on n_2. The system in the rotor then responds aerodynamically to the stator's wave excitation, and so on.

The above description for two blade-rows shows that the aerodynamic response of the system to an initial excitation in the rotor at frequency ω_0 and nodal diameter k_0, results in waves travelling across the two blade-rows with circumferential waves numbers k_θ given by:

$$k_\theta=k_0+n_1B_1+n_2B_2 \tag{4.2.9}$$

The waves frequencies in the stator are given by:

$$\omega_1=\omega_{n_2}=\omega_0-(k_0+n_2B_2)\Omega \tag{4.2.10}$$

and the waves frequencies in the rotor by:

$$\omega_2=\omega_{n_1}=\omega_0+n_1B_1\Omega \tag{4.2.11}$$

Equations (4.2.9), (4.2.10), and (4.2.11) are easily extendable to a system with more than two blade-rows. For that, reconsider the general model described in Section 4.2.1 to include N blade-rows. For ease of comparison with the case of two blade-rows, the rotors are represented by even-numbered blade-rows, and the stators by odd-numbered blade-rows. From these considerations, the unsteady flow response to an initial excitation in one of the rotors at frequency ω_0 and nodal diameter k_0

is composed of waves with circumferential wave numbers k_θ given by:

$$k_\theta = k_0 + \sum_{i=1}^{N} n_i B_i \tag{4.2.12}$$

The waves frequencies in the stators are given by:

$$\omega_{stators} = \omega_0 - (k_0 + \underbrace{\sum_{i=1}^{N} n_i B_i}_{\forall i \; even})\Omega \tag{4.2.13}$$

and the waves frequencies in the rotors by:

$$\omega_{rotors} = \omega_0 + (\underbrace{\sum_{i=1}^{N} n_i B_i}_{\forall i \; odd})\Omega \tag{4.2.14}$$

The circumferential modes n_i in (4.2.12), (4.2.13), and (4.2.14) characterise the so-called *spinning modes*. In theory, n_i can take an infinite number of values, and thus the number of combinations of n_i is also infinite. However, in practice, we believe that only a few combinations of *spinning modes* contribute significantly to the multi blade-row coupling. This assumption makes the above theory affordable using a numerical method, as will be seen later.

The above theory was explained for the case of vibrating blades at frequency ω_0 and nodal diameter k_0. However, the same theory can be applied to the study of wake/rotor and potential/rotor interaction, in which the frequency ω_0 is given by the stator wake passing frequency in the rotor, and σ_0 is its corresponding IBPA. In this case, the excited nodal diameter k_0 in the rotor is determined by the simple relationship: $k_0 = \frac{\sigma_0 B_2}{2\pi}$.

4.2.3 Computation of Aerodynamic Force

Looking at the above flutter example with two blade-rows, (4.2.8) indicates that the unsteady aerodynamic force on the m_2-th rotor blade should be the sum of multiple frequency components:

$$\tilde{\mathcal{F}}_2^{(m_2)} = \sum_{n_1=-\infty}^{+\infty} \Delta\hat{p}_{2,(n_1)}.e^{j[(\omega_0+n_1B_1\Omega)t+2\pi m_2(k_0+n_1B_1)/B_2]} \tag{4.2.15}$$

where $\Delta\hat{p}_{2,(n_1)}$ is the complex pressure perturbation associated with mode n_1 integrated on the rotor blade surface. Similarly, (4.2.6) shows that the unsteady aerodynamic force acting on the m_1-th stator blade which is caused by the rotor blades vibrations can be obtained from:

$$\tilde{\mathcal{F}}_1^{(m_1)} = \sum_{n_2=-\infty}^{+\infty} \Delta\hat{p}_{1,(n_2)}.e^{j[(\omega_0-(k_0+n_2B_2)\Omega)t+2\pi m_1(k_0+n_2B_2)/B_1]} \tag{4.2.16}$$

Generalising these results to a model with N blade-rows, if the j-th blade-row is a rotor, one can write that the aerodynamic force acting on the m-th blade is obtained from:

$$\tilde{\mathcal{F}}_j^{(m)} = \underbrace{\sum_{n_1=-\infty}^{+\infty} \cdots \sum_{n_N=-\infty}^{+\infty}}_{\forall n_i \neq n_j} \Delta\hat{p}_{j,\underbrace{(n_1,\cdots,n_N)}_{\forall n_i \neq n_j}}.e^{\left[j\left(\omega_0+\left(\underbrace{\sum_{i=1}^{N} n_iB_i}_{\forall i\ odd}\right)\Omega\right)t+j2\pi m\left(k_0+\underbrace{\sum_{i=1}^{N} n_iB_i}_{\forall i\neq j}\right)/B_j\right]} \tag{4.2.17}$$

And if the j-th blade-row is a stator, one can write:

$$\tilde{\mathcal{F}}_j^{(m)} = \underbrace{\sum_{n_1=-\infty}^{+\infty} \cdots \sum_{n_N=-\infty}^{+\infty}}_{\forall n_i \neq n_j} \Delta\hat{p}_{j,\underbrace{(n_1,\cdots,n_N)}_{\forall n_i \neq n_j}}.e^{\left[j\left(\omega_0-\left(k_0+\underbrace{\sum_{i=1}^{N} n_iB_i}_{\forall i\ even}\right)\Omega\right)t+j2\pi m\left(k_0+\underbrace{\sum_{i=1}^{N} n_iB_i}_{\forall i\neq j}\right)/B_j\right]} \tag{4.2.18}$$

where $\Delta\hat{p}_{1,(n_1\cdots n_N)}$ refers to the complex pressure perturbation associated with the modes n_i, for $i = 1,\cdots,N$ where $i \neq j$, integrated on the m-th blade surface of the j-th blade-row. It is important to emphasise that all frequency components are coupled with each other and thus cannot be determined independently.

4.2.4 The Concept of Worksum

Complex work coefficients are first defined to evaluate the aerodynamic work on the blades. This work is the product of pressure perturbations and blade vibration displacement integrated over the whole blade surface. Hence, for the above flutter case with two blade-rows, a work coefficient can be defined as:

$$CW_{j,(n)} = \int_{S_j} \Delta\hat{p}_{j,(n)}\left(x_j,\theta_j,r_j\right).\hat{h}_j^{\star}\left(x_j,\theta_j,r_j\right)dS \tag{4.2.19}$$

where S_j represents a blade surface in the j-th blade-row, $\hat{h}_j$ is the complex blade displacement in the j-th blade-row, and n is a circumferential mode solution from the neighbouring blade-row. Note that the $\star$ symbol is used to refer to the complex conjugate of the displacements in (4.2.19). Having defined a work coefficient, the aerodynamic work per cycle on a blade of the j-th blade-row is now given by:

$$\mathcal{W}_j = \Im\left[CW_{j,(0)}\right] \tag{4.2.20}$$

The reason for choosing $n = 0$ is that for such value of n the perturbation frequency coming back in the j-th blade-row is equal to the original blade vibration frequency in that blade-row, as seen in (4.2.8). Using (4.2.20), the aerodynamic work on a rotor blade for the above flutter case with two blade-rows, is then given by:

$$\mathcal{W}_2 = \Im\left[CW_{2,(0)}\right] \tag{4.2.21}$$

And the aerodynamic work on a stator blade is given by:

$$\mathcal{W}_1 = \Im\left[CW_{2,(0)}\right] = 0 \tag{4.2.22}$$

The fact that the stator blades are not vibrating causes this term to be zero.

Generalising these results to a model with N blade-rows, the work coefficient on a blade belonging to the j-th blade-row is given by:

$$CW_{j,\underbrace{(n_1,\cdots,n_N)}_{\forall n_i \neq n_j}} = \int_{S_j} \Delta\hat{p}_{j,\underbrace{(n_1,\cdots,n_N)}_{\forall n_i \neq n_j}}(x_j,\theta_j,r_j)\,.\hat{h}_j^{\star}(x_j,\theta_j,r_j)\,dS \tag{4.2.23}$$

And the aerodynamic work per cycle is given by:

$$\mathcal{W}_j = \Im\left[CW_{j,(0,\cdots,0)}\right] \tag{4.2.24}$$

From these results, it is now clear that the work coefficient, and thus the aerodynamic damping, is always influenced by the presence of neighbouring blade-rows.

4.2.5 Solution Method

Based on the above framework, a solution method needs to be defined to take into account the influence of the neighbouring blade-rows for the determination of aerodynamic work and force on the blades. As seen above, a spinning mode is completely determined by a frequency and an IBPA per blade-row. Hence, it

is possible to extend frequency-domain time-linearised methods to include multi blade-row effects.

In the present work, the infinite series of spinning modes is first truncated to a finite number of modes prior to the unsteady flow computation. The selection of which spinning modes is arbitrary, but these should be chosen wisely enough to represent all multi blade-row effects with enough engineering accuracy. We then must make sure that the unsteady flow solution remains unchanged (or quasi) by adding more spinning modes in the analysis. Secondly, we know that each spinning mode defines a frequency and an IBPA per blade-row. So these must be determined prior to the unsteady computation. When several spinning modes are included in the analysis, several frequencies and IBPAs are represented per blade-row. This means that several harmonic linearised solutions must be computed per blade-row. The harmonic linearised solutions in all the blade-rows are computed simultaneously and are coupled through appropriate boundary conditions.

Hall [42] used a similar approach for the computation of flutter problems. In his method, a computational grid spanning a single blade-passage per blade-row was first generated. Several harmonic linearised solutions were then computed simultaneously on each of these grids. In the present thesis, a different strategy is used. Several computational grids spanning a single blade-passage are generated for each blade-row, and the harmonic linearised solution for each set of frequency and IBPA is computed on a different grid. This approach allows different meshes to be used for different unsteady flow properties. This can be a considerable benefit in cases where the unsteady flow solution includes a wide range of wave-lengths, since coarser grids can be used to resolve the large wave-length parts of the solution, and finer grids can be used to resolve the short wave-length solutions.

Finally, the total number of grids (or sub-domains) required for the computation of an harmonic linearised multi blade-row solution scales with two parameters: (i) the number of blade-rows; (ii) the number of spinning modes retained in the analysis. An example for the set up of an harmonic linearised multi blade-row calculation is provided below.

Two-blade-row Example

Reconsider the previous flutter case with two blade-rows. We now give some guidelines on how to determine each set of frequency and IBPA per blade-row for a given set of spinning modes retained in the analysis of this problem. The frequency and IBPA results are summarised in Table 4.1 and Fig. 4.3.

		TND	Stator		Rotor	
Mode	(n_1, n_2)		ω_1	$\frac{\sigma_1}{2\pi}$	ω_2	$\frac{\sigma_2}{2\pi}$
1	$(0,0)$	k_0	$\omega_0 - k_0\Omega$	$\frac{k_0}{B_1}$	ω_0	$\frac{k_0}{B_2}$
2	$(0,-1)$	$k_0 - B_2$	$\omega_0 - (k_0 - B_2)\Omega$	$\frac{k_0 - B_2}{B_1}$	ω_0	$\frac{k_0}{B_2} - 1$
3	$(0,1)$	$k_0 + B_2$	$\omega_0 - (k_0 + B_2)\Omega$	$\frac{k_0 + B_2}{B_1}$	ω_0	$\frac{k_0}{B_2} + 1$
4	$(-1,0)$	$k_0 - B_1$	$\omega_0 - k_0\Omega$	$\frac{k_0}{B_1} - 1$	$\omega_0 - B_1\Omega$	$\frac{k_0 - B_1}{B_2}$
5	$(1,0)$	$k_0 + B_1$	$\omega_0 - k_0\Omega$	$\frac{k_0}{B_1} + 1$	$\omega_0 + B_1\Omega$	$\frac{k_0 + B_1}{B_2}$
6	$(1,-1)$	$k_0 + B_1 - B_2$	$\omega_0 - (k_0 - B_2)\Omega$	$\frac{k_0 - B_2}{B_1} + 1$	$\omega_0 + B_1\Omega$	$\frac{k_0 + B_1}{B_2} - 1$
7	$(-1,-1)$	$k_0 - B_1 - B_2$	$\omega_0 - (k_0 - B_2)\Omega$	$\frac{k_0 - B_2}{B_1} - 1$	$\omega_0 - B_1\Omega$	$\frac{k_0 - B_1}{B_2} - 1$
8	$(1,1)$	$k_0 + B_1 + B_2$	$\omega_0 - (k_0 + B_2)\Omega$	$\frac{k_0 + B_2}{B_1} + 1$	$\omega_0 + B_1\Omega$	$\frac{k_0 + B_1}{B_2} + 1$
9	$(-1,1)$	$k_0 - B_1 + B_2$	$\omega_0 - (k_0 + B_2)\Omega$	$\frac{k_0 + B_2}{B_1} - 1$	$\omega_0 - B_1\Omega$	$\frac{k_0 - B_1}{B_2} + 1$

Table 4.1: Example of spinning mode generation for one stage

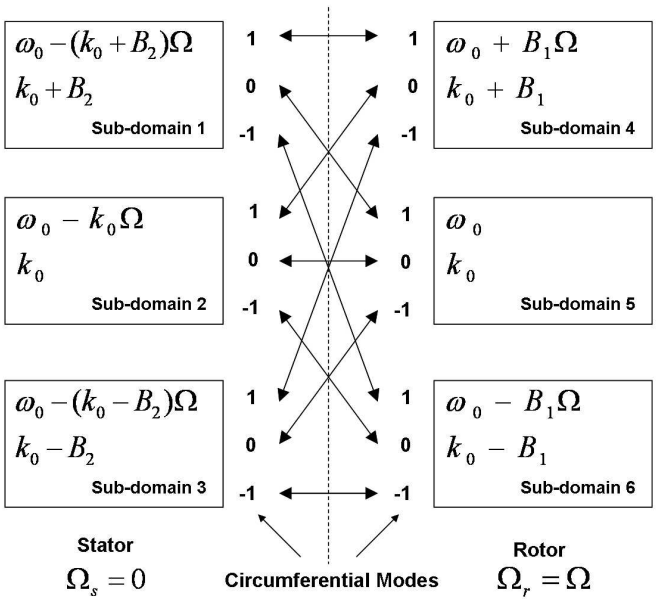

Figure 4.3: Frequency-domain multi blade-row solution including nine spinning modes obtained by the simultaneous computation of six harmonic linearised solution, each of these being computed in an individual computational sub-domain

Each line of the above table is now going to be explained but first, new notations are introduced. Let (ω_j, k_j, n_j) represent the $n_j - th$ circumferential Fourier mode component of the harmonic linearised solution in the j-th blade-row at frequency ω_j and nodal diameter k_j. Let the symbol $\leftrightarrow$ denote the interdependencies between harmonic linearised solutions. The quantities on the left hand side of this symbol are related to the stator, and the quantities on the right hand side to the rotor. Lastly, $\tilde{\mathbf{U}}_2$ is used to represent the harmonic linearised solution in the rotor at frequency ω_0 and IBPA $\sigma_0 = 2\pi k_0/B_2$.

Example 1 The unsteady flow solution $\tilde{\mathbf{U}}_2$ is composed only of outgoing waves at the inlet boundary of this domain. Consider that only the waves associated with the fundamental mode ($n_2 = 0$ in (4.2.5)) are allowed to propagate in the upstream direction. When these waves reach the stator, their frequency and circumferential wave number are determined from (4.2.6) by:

$$\omega_{1,(0)} = \omega_0 - k_0\Omega$$

and

$$k_{1,(0)} = k_0$$

Therefore, these waves' solution can be determined by computing an harmonic linearised solution in the stator at frequency $\omega_{1,(0)}$ and IBPA $\sigma_{1,(0)} = 2\pi k_{1,(0)}/B_1$. Following the same approach, now consider that only the waves reflected back in the stator, associated with the fundamental mode ($n_1 = 0$), are allowed to propagate in the downstream direction. When these waves reach the rotor, their frequency and circumferential wave number are determined by:

$$\omega_{2,(0)} = \omega_{1,(0)} + k_0\Omega = \omega_0$$

and

$$k_{2,(0)} = k_{1,(0)} = k_0$$

which corresponds to an IBPA:

$$\sigma_{2,(0)} = 2\pi k_0/B_2$$

It can be seen that the waves reflected back to the rotor have the same frequency as the frequency of the rotor blades vibration, and a circumferential wave number equal to the nodal diameter of the assembly vibration. Consequently, it can be concluded that the unsteady solutions in the stator and rotor are coupled by the following relationship:

$$(\omega_0 - k_0\Omega, k_0, 0) \quad \leftrightarrow \quad (\omega_0, k_0, 0) \quad Mode\,1$$

This is Mode 1 in Table 4.1. To recapitulate, the multi blade-row solution for this stage, which only includes the fundamental spinning mode ($(n_1 = 0, n_2 = 0)$), can be obtained by the computation of one harmonic linearised solution in the stator at frequency $\omega_{1,(0)}$ and IBPA $\sigma_{1,(0)}$, and one harmonic linearised solution in the rotor at frequency ω_0 and IBPA $\sigma_{2,(0)}$. In this example, only the waves associated with the fundamental spinning mode are allowed to be transmitted at the inter-row boundary.

Example 2 Consider that the waves associated with the first three circumferential modes ($n_2 = -1, 0, 1$) are now allowed to propagate in the upstream direction from the rotor. For each mode there corresponds one set of frequency and circumferential wave number in the stator given by:

$$\omega_{1,(n_2)} = \omega_0 - (k_0 + n_2 B_2)\,\Omega, \quad \forall n_2 = -1, 0, 1$$

and,

$$k_{1,(n_2)} = k_0 + n_2 B_2, \quad \forall n_2 = -1, 0, 1$$

Therefore, these waves' solutions can be obtained by computing three harmonic linearised solutions in the stator, each at frequency $\omega_{1,(n_2)}$ and IBPA $\sigma_{1,(n_2)} = 2\pi k_{1,(n_2)/B_1}$, for $n_2 = -1, 0, 1$. It was seen in (4.2.8) that the frequencies and circumferential wave numbers of the waves reflected back to the rotor do not depend on the circumferential mode n_2, but only on n_1. Therefore, whatever the value for n_2, all downstream going waves associated with the fundamental mode ($n_1 = 0$) in the stator reach the rotor with the same frequency and circumferential wave number, namely the ones associated with the original excitation. Consequently, it can be concluded that the unsteady solutions in the stator and rotor are coupled by the following relationships:

$$\begin{array}{lcll} (\omega_0 - (k_0 - B_2)\,\Omega, k_0 - B_2, 0) & \leftrightarrow & (\omega_0, k_0, -1) & Mode\,2 \\ (\omega_0 - k_0\Omega, k_0, 0) & \leftrightarrow & (\omega_0, k_0, 0) & Mode\,1 \\ (\omega_0 - (k_0 - B_2)\,\Omega, k_0 + B_2, 0) & \leftrightarrow & (\omega_0, k_0, 1) & Mode\,3 \end{array}$$

These correspond to Modes 1, 2, and 3 in Table 4.1. To recapitulate, the multi blade-row solution for this stage, which includes three spinning modes ($n_1 = 0, n_2 = -1$), ($n_1 = 0, n_2 = 0$), and ($n_1 = 0, n_2 = 1$), can be obtained by the computation of four harmonic linearised solutions; three in the stator at frequencies $\omega_{1,(n_2)}$ and IBPA $\sigma_{1,(n_2)}$, and one in the rotor at frequency ω_0 and IBPA σ_0.

Example 3 It was shown in Example 1 that the waves associated with the fundamental mode ($n_2 = 0$) in the rotor, reach the stator with a frequency and circumferential wave number given by:

$$\omega_{1,(0)} = \omega_0 - k_0\Omega$$

and,

$$k_{1,(0)} = k_0$$

and that these waves' solution could be obtained by computing an harmonic linearised solution in the stator at frequency $\omega_{1,(0)}$ and IBPA $\sigma_{1,(0)}$. Now consider that the reflected waves in the stator associated with the first three circumferential modes $n_1 = -1, 0, 1$ are allowed to propagate in the direction of the rotor. For each of these modes corresponds one set of frequency and circumferential wave number in the rotor given by:

$$\omega_{2,(n_1)} = \omega_0 + n_1 B_1 \Omega, \quad for \;\; n_1 = -1, 0, 1$$

and,

$$k_{2,(n_1)} = k_0 + n_1 B_1, \quad for \;\; n_1 = -1, 0, 1$$

Therefore, these waves' solutions can be obtained by computing three harmonic linearised solutions in the rotor, each at frequency $\omega_{2,(n_1)}$ and IBPA $\sigma_{2,(n_1)} = 2\pi k_{2,(n_1)/B_2}$, for $n_1 = -1, 0, 1$. As explained above, no matter the value of n_1, all the waves associated with the fundamental mode ($n_2 = 0$) in the rotor are reflected back to the stator with the same frequency and circumferential wave number as they left it, i.e. $\omega_{1,(0)}$, and $k_{1,(0)}$. Consequently, it can be concluded that the unsteady solutions in the stator and the rotor are coupled by the following relationships:

$$\begin{array}{lcll} (\omega_{1,(0)}, k_{1,(0)}, -1) & \leftrightarrow & (\omega_{2,(-1)}, k_{2,(-1)}, 0) & Mode\,4 \\ (\omega_{1,(0)}, k_{1,(0)}, 0) & \leftrightarrow & (\omega_{2,(0)}, k_{2,(0)}, 0) & Mode\,1 \\ (\omega_{1,(0)}, k_{1,(0)}, 1) & \leftrightarrow & (\omega_{2,(1)}, k_{2,(1)}, 0)) & Mode\,5 \end{array}$$

These correspond to Modes 1, 4, and 5 in Table 4.1. To recapitulate, the multi blade-row solution for this stage, which includes three spinning modes ($n_1 = -1, n_2 = 0$), ($n_1 = 0, n_2 = 0$), and ($n_1 = 1, n_2 = 0$), can be obtained by the computation of four harmonic linearised solutions: one in the stator at frequency $\omega_{1,(0)}$ and IBPA $\sigma_{1,(0)}$, and three in the rotor at frequencies $\omega_{2,(n_1)}$ and IBPAs $\sigma_{2,(n_1)}$.

Example 4 Collect together the three spinning modes shown in Example 2, and add the three spinning modes shown in Example 3, one obtains a total number of five spinning modes, since the fundamental spinning mode is repeated twice. Consequently, it can be concluded that the unsteady solutions in the stator and

rotor can be coupled by the following relationships:

$$\begin{array}{lcll}
(\omega_0 - k_0\Omega, k_0, 0) & \leftrightarrow & (\omega_0, k_0, 0) & Mode\,1 \\
(\omega_0 - (k_0 - B_2)\,\Omega, k_0 - B_2, 0) & \leftrightarrow & (\omega_0, k_0, -1) & Mode\,2 \\
(\omega_0 - (k_0 - B_2)\,\Omega, k_0 + B_2, 0) & \leftrightarrow & (\omega_0, k_0, 1) & Mode\,3 \\
(\omega_0 - k_0\Omega, k_0, -1) & \leftrightarrow & (\omega_0 - B_1\Omega, k_0 - B_1, 0) & Mode\,4 \\
(\omega_0 - k_0\Omega, k_0, 1) & \leftrightarrow & (\omega_0 + B_1\Omega, k_0 + B_1, 0)) & Mode\,5
\end{array}$$

These correspond to Modes 1, 2, 3, 4, and 5 in Table 4.1. To recapitulate, the multi blade-row solution, which includes five spinning modes ($n_1 = -1, n_2 = 0$), ($n_1 = 0, n_2 = 0$), ($n_1 = 1, n_2 = 0$), ($n_1 = 0, n_2 = -1$), and ($n_1 = 0, n_2 = 1$), can be obtained by the computation of six harmonic linearised solutions: three in the stator at frequencies $\omega_{1,(n_2)}$ and IBPA $\sigma_{1,(n_2)}$, and three in the rotor at frequencies $\omega_{2,(n_1)}$ and IBPAs $\sigma_{2,(n_1)}$.

Example 5 The six harmonic linearised computations that have been defined in Example 4 can be re-used wisely to include more spinning modes. This approach starts by noticing that two harmonic linearised solutions in the rotor in Example 4 were unrelated to two other harmonic linearised solutions in the stator. Theoretically, it is possible to relate each harmonic linearised solution in the stator to each harmonic linearised solution in the rotor. For example, consider the harmonic linearised solution in the stator at frequency $\omega_{1,(-1)}$ and IBPA $\sigma_{1,(-1)}$. The waves associated with the circumferential mode $n_1 = 1$ from this solution reach the rotor at frequency:

$$\omega_{2,(1)} = \omega_0 - (k_0 - B_2)\,\Omega + (k_0 + B_1 - B_2)\,\Omega = \omega_0 + B_1\Omega$$

and are characterised by a circumferential wave number:

$$k_2 = k_0 + B_1 - B_2$$

Now consider the harmonic linearised solution in the rotor at frequency $\omega_{2,(1)}$ and IBPA $\sigma_{2,(1)}$. The waves associated with the circumferential mode $n_2 = -1$ from this solution have a circumferential wave number $k_0 + B_1 - B_2$ and reach the stator at frequency $\omega_0 - (k_0 - B_2)\,\Omega$. Hence, it can be concluded that both harmonic linearised solutions just mentioned in the stator and the rotor can be related by the following relationship:

$$(\omega_0 - (k_0 - B_2)\,\Omega, k_0 - B_2, 1) \;\leftrightarrow\; \omega_0 + B_1\Omega, k_0 + B_1, -1) \quad Mode\,6$$

This corresponds to Mode 6 in Table 4.1. Similarly, it is possible to relate each harmonic linearised solution in the stator to each harmonic linearised solution in the rotor that were unrelated in Example 4, as follows:

$$\begin{array}{rcll} (\omega_0 - (k_0 - B_2)\,\Omega, k_0 - B_2, -1) & \leftrightarrow & \omega_0 - B_1\Omega, k_0 - B_1, -1) & Mode\,7 \\ (\omega_0 - (k_0 + B_2)\,\Omega, k_0 + B_2, 1) & \leftrightarrow & \omega_0 + B_1\Omega, k_0 + B_1, 1) & Mode\,8 \\ (\omega_0 - (k_0 + B_2)\,\Omega, k_0 + B_2, -1) & \leftrightarrow & \omega_0 - B_1\Omega, k_0 - B_1, 1) & Mode\,9 \end{array}$$

These correspond to Modes 7, 8, 9 in Table 4.1. Therefore, the multi blade-row solution, which includes the nine spinning modes indicated in Table 4.1, can be obtained by the computation of the six harmonic linearised solutions specified in Example 4. Only the boundary conditions at the inter-row boundary differ between Example 4 and Example 5.

To conclude on these five examples, it was shown that the number of harmonic linearised solutions that must be coupled to obtain a multi blade-row solution depend on both the spinning modes that are retained, and the number of blade-rows. The next section aims to explain how each harmonic linearised solution is computed, and what the boundary conditions are.

4.3 Harmonic Linearised Unsteady Flow Equations

Reconsider the nonlinear unsteady Navier-Stokes equations shown in Chapter 3:

$$\frac{\partial}{\partial t}\int_{V(t)} \mathbf{U} dV + \oint_{S(t)} \left(\mathbf{F}^I(\mathbf{U}) + \mathbf{F}^V(\nabla\mathbf{U})\right).\mathbf{n} dS = \int_{V(t)} \mathbf{S}(\mathbf{U}) dV + \oint_{S(t)} (\mathbf{U}\,\mathbf{u}_b).\mathbf{n} dS \tag{4.3.25}$$

All terms in (4.3.25) were discussed in Chapter 3, except the last term on the right hand side. This term vanishes in the nonlinear steady-state analysis since the computational domain is static in the frame relative to the blades. An important feature of the harmonic linearised analysis is that the computational domain can be moving in the relative frame, and thus the integral $\oint_{S(t)} (\mathbf{U}\,\mathbf{u}_b).\mathbf{n} dS$ appears as a new flux term contributing to the balance of the control volume $V(t)$. For convenience, we start the description of the harmonic linearised equations for the analysis of flutter, in which the computational domain is moving. The harmonic linearised equations for the analysis of forced response will then easily be deducted from the flutter harmonic equations, the process being done by setting the grid motion to zero and by imposing appropriate boundary conditions.

Unsteady flow quantities can be decomposed into a steady-state value and an unsteady perturbation. Linear theory further assumes that the unsteady perturbation is small compared to the steady-state flow. The vector of conservative variables can then be decomposed as follows:

$$\mathbf{U}(\mathbf{X},t) = \bar{\mathbf{U}}(\mathbf{X}) + \tilde{\mathbf{U}}(\mathbf{X},t) \tag{4.3.26}$$

where $\bar{\mathbf{U}}(\mathbf{X})$ is the vector of steady-state conservative variables, and $\tilde{\mathbf{U}}(\mathbf{X})$ is the vector perturbation of the conservative variables. In the case of moving boundaries, the grid coordinates can also be decomposed into the sum of a steady-state (or time-mean) position, and a small oscillation around that steady-state position, so that:

$$\mathbf{X} = \bar{\mathbf{X}} + \tilde{\mathbf{X}}\,(t) \tag{4.3.27}$$

Based on the above decomposition, the boundary velocity $\mathbf{u}_b$ of an internal mesh element can be expressed in the relative frame by:

$$\mathbf{u}_b = \frac{d\tilde{\mathbf{X}}_b}{dt} \tag{4.3.28}$$

It is clear from this expression that the boundary velocity $\mathbf{u}_b$ is a first-order term.

Following the same approach, the flux and source terms in (4.3.25) can be decomposed into steady-state terms, and perturbation terms. Keeping the only zeroth- and first-order terms, the fluxes are now given by:

$$\mathbf{F}^I = \bar{\mathbf{F}}^I + \tilde{\mathbf{F}}^I \tag{4.3.29}$$

$$\mathbf{F}^V = \bar{\mathbf{F}}^V + \tilde{\mathbf{F}}^V \tag{4.3.30}$$

$$\mathbf{S} = \bar{\mathbf{S}} + \tilde{\mathbf{S}} \tag{4.3.31}$$

The steady-state fluxes and source terms, $\bar{\mathbf{F}}^I$, $\bar{\mathbf{F}}^V$, and $\bar{\mathbf{S}}$ were described in Chapter 3. $\tilde{\mathbf{F}}^I$ and $\tilde{\mathbf{F}}^V$ represent the fluxes sensitivity to perturbations of the steady-state flow. The first-order inviscid fluxes can be decomposed as follows:

$$\tilde{\mathbf{F}}^I = \tilde{\mathbf{F}}^I_x\mathbf{i} + \tilde{\mathbf{F}}^I_y\mathbf{j} + \tilde{\mathbf{F}}^I_z\mathbf{k} \tag{4.3.32}$$

where

$$\tilde{\mathbf{F}}_x^I = \begin{pmatrix} \bar{\rho}\tilde{u} + \tilde{\rho}\bar{u} \\ \left(\tilde{\rho}\bar{u} + \bar{\rho}\tilde{u}\right)\bar{u} + \left(\bar{\rho}\bar{u}\right)\tilde{u} + \tilde{p} \\ \left(\tilde{\rho}\bar{v} + \bar{\rho}\tilde{v}\right)\bar{u} + \left(\bar{\rho}\bar{v}\right)\tilde{u} \\ \left(\tilde{\rho}\bar{w} + \bar{\rho}\tilde{w}\right)\bar{u} + \left(\bar{\rho}\bar{w}\right)\tilde{u} \\ \left(\left(\tilde{\rho}\bar{E} + \bar{\rho}\tilde{E}\right) + \tilde{p}\right)\bar{u} + \left(\left(\bar{\rho}\bar{E}\right) + \bar{p}\right)\tilde{u} \end{pmatrix} \tag{4.3.33}$$

$$\tilde{\mathbf{F}}_y^I = \begin{pmatrix} \bar{\rho}\tilde{u} + \tilde{\rho}\bar{u} \\ \left(\tilde{\rho}\bar{u} + \bar{\rho}\tilde{u}\right)\bar{v} + \left(\bar{\rho}\bar{u}\right)\tilde{v} \\ \left(\tilde{\rho}\bar{v} + \bar{\rho}\tilde{v}\right)\bar{v} + \left(\bar{\rho}\bar{v}\right)\tilde{v} + \tilde{p} \\ \left(\tilde{\rho}\bar{w} + \bar{\rho}\tilde{w}\right)\bar{v} + \left(\bar{\rho}\bar{w}\right)\tilde{v} \\ \left(\left(\tilde{\rho}\bar{E} + \bar{\rho}\tilde{E}\right) + \tilde{p}\right)\bar{v} + \left(\left(\bar{\rho}\bar{E}\right) + \bar{p}\right)\tilde{v} \end{pmatrix} \tag{4.3.34}$$

$$\tilde{\mathbf{F}}_z^I = \begin{pmatrix} \bar{\rho}\tilde{u} + \tilde{\rho}\bar{u} \\ \left(\tilde{\rho}\bar{u} + \bar{\rho}\tilde{u}\right)\bar{w} + \left(\bar{\rho}\bar{u}\right)\tilde{w} \\ \left(\tilde{\rho}\bar{v} + \bar{\rho}\tilde{v}\right)\bar{w} + \left(\bar{\rho}\bar{v}\right)\tilde{w} \\ \left(\tilde{\rho}\bar{w} + \bar{\rho}\tilde{w}\right)\bar{w} + \left(\bar{\rho}\bar{w}\right)\tilde{w} + \tilde{p} \\ \left(\left(\tilde{\rho}\bar{E} + \bar{\rho}\tilde{E}\right) + \tilde{p}\right)\bar{w} + \left(\left(\bar{\rho}\bar{E}\right) + \bar{p}\right)\tilde{w} \end{pmatrix} \tag{4.3.35}$$

And the first-order viscous fluxes by:

$$\tilde{\mathbf{F}}^V = \tilde{\mathbf{F}}_x^V\mathbf{i} + \tilde{\mathbf{F}}_y^V\mathbf{j} + \tilde{\mathbf{F}}_z^V\mathbf{k} \tag{4.3.36}$$

where

$$\tilde{\mathbf{F}}_x^V = \begin{pmatrix} 0 \\ -\tilde{\tau}_{xx} \\ -\tilde{\tau}_{yx} \\ -\tilde{\tau}_{zx} \\ -\bar{u}\tilde{\tau}_{xx} - \bar{v}\tilde{\tau}_{yx} - \bar{w}\tilde{\tau}_{zx} + \tilde{q}_x \; - \tilde{u}\bar{\tau}_{xx} - \tilde{v}\bar{\tau}_{yx} - \tilde{w}\bar{\tau}_{zx} \end{pmatrix} \tag{4.3.37}$$

$$\tilde{\mathbf{F}}_y^V = \begin{pmatrix} 0 \\ -\tilde{\tau}_{xy} \\ -\tilde{\tau}_{yy} \\ -\tilde{\tau}_{zy} \\ -\bar{u}\tilde{\tau}_{xy} - \bar{v}\tilde{\tau}_{yy} - \bar{w}\tilde{\tau}_{zy} + \tilde{q}_y \; - \tilde{u}\bar{\tau}_{xy} - \tilde{v}\bar{\tau}_{yy} - \tilde{w}\bar{\tau}_{zy} \end{pmatrix} \tag{4.3.38}$$

$$\tilde{\mathbf{F}}_z^V = \begin{pmatrix} 0 \\ -\tilde{\tau}_{xz} \\ -\tilde{\tau}_{yz} \\ -\tilde{\tau}_{zz} \\ -\bar{u}\tilde{\tau}_{xz} - \bar{v}\tilde{\tau}_{yz} - \bar{w}\tilde{\tau}_{zz} + \tilde{q}_z \; - \tilde{u}\bar{\tau}_{xz} - \tilde{v}\bar{\tau}_{yz} - \tilde{w}\bar{\tau}_{zz} \end{pmatrix} \tag{4.3.39}$$

All the terms that make up (4.3.37), (4.3.38), and (4.3.39) are first-order. As an example, the shear stress term on the third line of (4.3.38) is given by:

$$\tilde{\tau}_{xy} = \tilde{\tau}_{yx} = \tilde{\mu}\left(\frac{\partial \bar{u}}{\partial y} + \frac{\partial \bar{v}}{\partial x}\right) + \bar{\mu}\left(\frac{\partial \tilde{u}}{\partial y} + \frac{\partial \tilde{v}}{\partial x}\right) \tag{4.3.40}$$

where the perturbation molecular viscosity $\tilde{\mu}$ is obtained through the linearisation of the turbulence model. Note that, in general, the full linearisation of the viscous terms yields better results than freezing the turbulence model in areas of flow re-circulation, but the two approaches are equivalent elsewhere [98]. The other stress and flux components are built in the same manner.

Inserting (4.3.26), (4.3.28) ,(4.3.29), (4.3.30), and (4.3.31), into (4.3.25) gives:

$$\begin{aligned} &\tfrac{\partial}{\partial t}\int_{V(t)}\left(\bar{\mathbf{U}}+\tilde{\mathbf{U}}\right)\left(\overline{dV}+\widetilde{dV}\right) + \oint_{S(t)}\left(\bar{\mathbf{F}}^I+\bar{\mathbf{F}}^V+\tilde{\mathbf{F}}^I+\tilde{\mathbf{F}}^V\right).\left(\overline{\mathbf{n}dS}+\widetilde{\mathbf{n}dS}\right) \\ &\quad = \int_{V(t)}\left(\bar{\mathbf{S}}+\tilde{\mathbf{S}}\right)\left(\overline{dV}+\widetilde{dV}\right) + \oint_{S(t)}\left(\bar{\mathbf{U}}+\tilde{\mathbf{U}}\right)\left(\tfrac{d\tilde{\mathbf{X}}}{dt}\right).\left(\overline{\mathbf{n}dS}+\widetilde{\mathbf{n}dS}\right) \end{aligned} \tag{4.3.41}$$

Gathering all zeroth-order terms from (4.3.41) gives the nonlinear steady-state equations, already obtained in Chapter 3:

$$\oint_{\bar{S}}\left(\bar{\mathbf{F}}^I+\bar{\mathbf{F}}^V\right).\overline{\mathbf{n}dS} = \int_{\bar{V}}\bar{\mathbf{S}}\,\overline{dV} \tag{4.3.42}$$

Gathering together the first-order terms provides the linearised equations of the unsteady perturbation:

$$\begin{aligned} &\tfrac{\partial}{\partial t}\int_{\bar{V}}\tilde{\mathbf{U}}\,\overline{dV} + \tfrac{\partial}{\partial t}\int_{\bar{V}}\bar{\mathbf{U}}\,\widetilde{dV} + \oint_{\bar{S}}\left(\tilde{\mathbf{F}}^I+\tilde{\mathbf{F}}^V\right).\overline{\mathbf{n}dS} + \oint_{\bar{S}}\left(\bar{\mathbf{F}}^I+\bar{\mathbf{F}}^V\right).\widetilde{\mathbf{n}dS} \\ &\quad = \int_{\bar{V}}\tilde{\mathbf{S}}\,\overline{dV} + \int_{\bar{V}}\bar{\mathbf{S}}\widetilde{dV} + \oint_{\bar{S}}\left(\bar{\mathbf{U}}\tfrac{d\tilde{\mathbf{X}}}{dt}\right).\overline{\mathbf{n}dS} \end{aligned} \tag{4.3.43}$$

Equation (4.3.43) is linear in the sense that all terms pre-multiplying the unknown $\tilde{\mathbf{U}}$ are dependent on the steady-state solution and geometric properties, but not on time. Therefore, a Fourier series solution is of the form:

$$\tilde{\mathbf{U}}(\mathbf{X},t) = \sum_{n=-\infty}^{+\infty}\hat{\mathbf{U}}_n(\mathbf{X}).e^{i\omega_n t}$$

Similarly, the grid displacements can also be decomposed into Fourier series:

$$\tilde{\mathbf{X}}(t) = \sum_{n=-\infty}^{+\infty}\hat{\mathbf{X}}_n.e^{i\omega_n t}$$

Equation (4.3.43) can be written for each Fourier harmonic:

$$\begin{array}{c} \int_{\bar{V}} \left(i\omega\hat{\mathbf{U}} - \hat{\mathbf{S}}\right) \overline{dV} + \oint_{\bar{S}} \left(\hat{\mathbf{F}}^I + \hat{\mathbf{F}}^V\right) .\overline{\mathbf{n}dS} \\ = \int_{\bar{V}} \left(\bar{\mathbf{S}} - i\omega\bar{\mathbf{U}}\right) \widehat{dV} - \oint_{\bar{S}} \left(\bar{\mathbf{F}}^I + \bar{\mathbf{F}}^V\right) .\widehat{\mathbf{n}dS} + \oint_{\bar{V}} \left(\bar{\mathbf{U}} \left(i\omega\hat{\mathbf{X}}\right)\right) .\overline{\mathbf{n}dS} \end{array} \tag{4.3.44}$$

where the subscript n has been omitted for clarity. Introducing a pseudo-time to time-march the solution, (4.3.44) finally becomes:

$$\begin{array}{c} \frac{\partial}{\partial\tau} \int_{\bar{V}} \hat{\mathbf{U}}\, \overline{dV} + \int_{\bar{V}} \left(i\omega\hat{\mathbf{U}} - \hat{\mathbf{S}}\right) \overline{dV} + \oint_{\bar{S}} \left(\hat{\mathbf{F}}^I + \hat{\mathbf{F}}^V\right) .\overline{\mathbf{n}dS} \\ = \int_{\bar{V}} \left(\bar{\mathbf{S}} - i\omega\bar{\mathbf{U}}\right) \widehat{dV} - \oint_{\bar{S}} \left(\bar{\mathbf{F}}^I + \bar{\mathbf{F}}^V\right) .\widehat{\mathbf{n}dS} + \oint_{\bar{V}} \left(\bar{\mathbf{U}} \left(i\omega\hat{\mathbf{X}}\right)\right) .\overline{\mathbf{n}dS} \end{array} \tag{4.3.45}$$

The left hand side of this equation contains homogeneous terms, while the right-hand side contains the non-homogeneous terms that depend on the steady-state solution and the grid motion. These equations are solved subject to appropriate boundary conditions that will be described later in this chapter.

4.4 Deforming Computational Grid

Aeroelastic problems such as flutter are characterised by the vibration of blades, which is induced by gas flow passing around them. The vibration of the blades needs to be represented numerically, a feature which can cause numerical difficulties when not handled properly. To illustrate the numerical difficulty about flutter, imagine an observer located on a vibrating blade surface while the fluid computational mesh remains static. To first order, this observer faces two types of flow unsteadiness. The first type is the natural unsteadiness created by the blade vibration, which perturbs the steady flow field around it. The second type of unsteadiness results from the fact that the blade vibration causes the local observer to pass periodically across a non-uniform steady flow. When harmonic time-linearised methods were first developed, researchers used an upwash boundary condition to treat the problem of blade vibration at the blade surface [38]. However, the flow gradients around the blade can be very large, or even singular around the leading and trailing edges of the blades. This, accompanied with the potentially large truncation errors of the numerical scheme that may appear in this region of the flow, leads to difficulties in the accurate evaluations of the gradients.

In order to avoid this problem, the computational grid can be allowed to move along with the blade displacements, thereby eliminating the aforementioned numerical difficulty. The grid motion is expressed mathematically by the evaluation of the vector position $\mathbf{X}(t)$ in (4.3.27). This vector is not determined by the harmonic

linearised analysis, but is an input parameter for these equations. From (4.3.27), it is seen that the vector position $\mathbf{X}(t)$ has two components. A time-mean value $\bar{\mathbf{X}}$, and an unsteady perturbation $\tilde{\mathbf{X}}(t)$. The time-mean grid node coordinates $\bar{\mathbf{X}}$ are determined using a mesh generator, which defines the structure of the grid together with the topology of its elements. This is what is conventionally done in most CFD applications. On the other hand, the grid node displacements $\tilde{\mathbf{X}}(t)$ are determined by solving an elliptic equation with Dirichlet boundary conditions. These boundary conditions must satisfy several criteria. First, the displacements of the nodes on the blade surface must follow the motion of the blade exactly. For this, a finite element analysis of the mechanical model is used to determine the modeshapes and the natural frequencies of the blades. The obtained modeshapes are then interpolated onto the CFD mesh at the blade's boundary. Note that, for consistency, the natural frequency of the assembly, determined by the mechanical FE model, must also be equal to the harmonic frequency imposed for the aerodynamic analysis. This means that from the perspective of solving a multi blade-row harmonic problem for flutter, which includes several harmonic solutions per blade-row, only the computational grid associated with the harmonic solution at frequency equal to the natural frequency of the blade, is allowed to deform. Secondly, the grid nodes at the far field boundaries must remain static, hence $\tilde{\mathbf{X}}(t) = 0$ for these nodes. Thirdly, the matching pair of nodes at the periodic boundaries, introduced in Chapter 3, must have the same displacements after rotation by a pitch angle, and after a phase-shift equal to the IBPA of the blade vibration. Mathematically, this is expressed as:

$$\hat{\mathbf{X}}_u = \mathbf{I}_l^u \hat{\mathbf{X}}_l . e^{i\sigma}$$

in which $\mathbf{I}_l^u$ represents the rotational matrix of the nodes coordinates from the lower to the upper boundary, and the subscripts u and l refer to the upper and lower boundaries respectively. Finally, the motion of all interior nodes is determined so that the variation of the displacements between adjacent nodes is smooth, thereby minimising truncation errors associated with linearisation. Enough smoothness is achieved using the spring analogy, in which the stiffness of the edges is inversely proportional to the square root of the initial edge lengths.

4.5 Discretisation

In the present thesis, the discretised form of the harmonic linearised equations is obtained from the linearisation of the discretised nonlinear equations shown in Chapter

3. The discretised-linearised form of the Navier-Stokes equations is given by:

$$\frac{\left(\partial \mathcal{V}_I \hat{\mathbf{U}}_I\right)}{\partial \tau} + \sum_{J \in E_I} \left[\hat{\mathcal{F}}^I_{IJ} + \hat{\mathcal{F}}^V_{IJ}\right] \Delta \mathbf{s}_{IJ} = \mathcal{V}_I \left(-i\omega \hat{\mathbf{U}}_I + \hat{\mathbf{S}}_I + \hat{\mathbf{H}}_I\right) \tag{4.5.46}$$

where $\hat{\mathbf{H}}_I$ regroups all the non-homogeneous terms that form the right hand side of (4.3.45), which depend on the grid motion and the steady-state solution, so this term can be determined once for all prior to the harmonic linearised unsteady flow computation.

4.5.1 Inviscid Flux

The discretised linearised approximation of the inviscid flux $\hat{\mathcal{F}}^I_I$ is evaluated at the nodes:

$$\hat{\mathcal{F}}^I_I = \sum_{J \in E_I} \hat{\mathcal{F}}^I_{IJ} \Delta \mathbf{s}_{IJ} \tag{4.5.47}$$

where the inviscid flux $\hat{\mathcal{F}}^I_{IJ}$ in the direction IJ, is given by a central (or Galerkin) differencing of the inviscid fluxes with added numerical dissipation term:

$$\hat{\mathcal{F}}^I_{IJ} = \frac{1}{2}\left(\hat{\mathcal{F}}^I_I + \hat{\mathcal{F}}^I_J\right) - \hat{\mathcal{D}}^I_{IJ} \tag{4.5.48}$$

where

$$\begin{array}{rcl} \hat{\mathcal{D}}^I_{IJ} & = & \frac{1}{2}\left|\bar{A}_{IJ}\right| \left[\bar{\psi}_{IJ}\left(\hat{\mathbf{U}}_J - \hat{\mathbf{U}}_I\right) - \epsilon_2\left(1 - \bar{\psi}_{IJ}\right)\left(\mathcal{L}\left(\hat{\mathbf{U}}_J\right) - \mathcal{L}\left(\hat{\mathbf{U}}_I\right)\right)\right] \\ & + & \frac{1}{2}\left|\hat{A}_{IJ}\right| \left[\bar{\psi}_{IJ}\left(\bar{\mathbf{U}}_J - \bar{\mathbf{U}}_I\right) - \epsilon_2\left(1 - \bar{\psi}_{IJ}\right)\left(\mathcal{L}\left(\bar{\mathbf{U}}_J\right) - \mathcal{L}\left(\bar{\mathbf{U}}_I\right)\right)\right] \end{array} \tag{4.5.49}$$

$\bar{A}_{IJ}$ and $\hat{A}_{IJ}$ are the time-averaged and first-order perturbation Roe matrices respectively, $\bar{\psi}_{IJ}$ is a limiter, $\epsilon_2 = 0.5$ is a smoothing parameter, and $\mathcal{L}$ is the pseudo-Laplacian operator defined in Chapter 3.

4.5.2 Viscous Flux

The discretised linearised approximation of the viscous flux $\hat{\mathcal{F}}^V_I$ is given by:

$$\hat{\mathcal{F}}^V_I = \sum_{J \in E_I} \hat{\mathcal{F}}^V_{IJ} \Delta \mathbf{s}_{IJ} \tag{4.5.50}$$

In order to understand how the discretised viscous flux $\hat{\mathcal{F}}^V_{IJ}$ is constructed along the edges, consider the shear stress term τ_{xy}, which appears in the nonlinear viscous

flux:

$$\tau_{xy} = \mu \left(\frac{\partial u}{\partial y} + \frac{\partial v}{\partial x} \right)$$

Separating the flow variables into a steady-state and a small perturbation, the first-order unsteady stress term is given by:

$$\hat{\tau}_{xy} = \bar{\mu} \left(\frac{\partial \hat{u}}{\partial y} + \frac{\partial \hat{v}}{\partial x} \right) + \hat{\mu} \left(\frac{\partial \bar{u}}{\partial y} + \frac{\partial \bar{v}}{\partial x} \right)$$

Looking at the above expression, it is clear that the linearisation of the discrete viscous flux $\hat{\mathcal{F}}^V_{IJ}$ requires the determination of both the time-averaged and the unsteady flow gradients. The way the gradients of the steady-state variables are computed is detailed in Chapter 3. Using a similar approach, the gradients of the perturbations are also evaluated at the mid-point of the edges and are determined by:

$$\nabla \hat{\mathbf{Q}}_{IJ} = \overline{\nabla \hat{\mathbf{Q}}}_{IJ} - \left(\overline{\nabla \hat{\mathbf{Q}}}_{IJ} . \delta \mathbf{s}_{IJ} - \frac{\left(\hat{\mathbf{Q}}_J - \hat{\mathbf{Q}}_I \right)}{\left| \bar{\mathbf{X}}_J - \bar{\mathbf{X}}_I \right|} \right) \delta \mathbf{s}_{IJ} \tag{4.5.51}$$

where $\hat{\mathbf{Q}}$ represents the perturbation primitive variables.

4.5.3 Time Integration

The time integration procedure can be summarised as follows:

$$\frac{\partial \left(\mathcal{V}_I \hat{\mathbf{U}}_I \right)}{\partial \tau} = \mathcal{R}_I \left(\hat{\mathbf{U}} \right) \tag{4.5.52}$$

where the residual $\mathcal{R}_I$ is formed through the fluxes and right hand side terms from (4.5.46). The correct evaluation of the residual requires the inclusion of the boundary conditions. These are presented below.

4.6 Boundary Conditions

As far as we are concerned, the evaluation of the linearised flow residual involves four types of boundary conditions, namely: solid wall, periodicity, inlet/outlet, and inter-row. In the present code, these boundary conditions are directly applied to the evaluation of the flow residual. As will be seen later, this implementation of the boundary conditions is mandatory as the overall time integration scheme is inserted into a multigrid strategy.

4.6.1 Solid Wall

The solid wall boundary condition requires that the fluid velocities must remain tangential to the wall surfaces for inviscid flows, this is represented by the slip boundary condition, or be attached to the wall surfaces for viscous flow, this is the no-slip boundary condition.

Slip Boundary Condition Let us call $\mathbf{u}_{I,wall}$ the wall relative velocity of any node I on a solid wall. Relatively to the steady nodes positions, $\mathbf{u}_{I,wall}$ is given by:

$$\mathbf{u}_{I,wall} = \frac{d\mathbf{X}_I}{dt} = i\omega\tilde{\mathbf{X}}_I \tag{4.6.53}$$

Thus, the wall velocity is a first-order term. The wall normal vector can be decomposed into a steady vector and a small amplitude perturbation:

$$\mathbf{n}_I = \bar{\mathbf{n}}_I + \tilde{\mathbf{n}}_I \tag{4.6.54}$$

Consequently, the wall boundary condition, which imposes that the fluid velocity vector normal to the wall is zero, can be expressed by:

$$\left(\mathbf{u}_I - \mathbf{u}_{I,wall}\right).\mathbf{n}_I = 0 \tag{4.6.55}$$

where $\mathbf{u}_I$ is the fluid velocity at node I. Developing this expression yields:

$$\left(\bar{\mathbf{u}}_I + \tilde{\mathbf{u}}_I - \mathbf{u}_{I,wall}\right).\left(\bar{\mathbf{n}}_I + \tilde{\mathbf{n}}_I\right) = 0 \tag{4.6.56}$$

Collecting together the first-order terms gives the linearised slip boundary condition:

$$\bar{\mathbf{u}}_I.\hat{\mathbf{n}}_I + \left(\hat{\mathbf{u}}_I - \mathbf{u}_{I,wall}\right).\bar{\mathbf{n}}_I = 0 \tag{4.6.57}$$

which can be re-arranged as:

$$\hat{\mathbf{u}}_I.\bar{\mathbf{n}}_I = i\omega\hat{\mathbf{X}}_I.\bar{\mathbf{n}}_I - \bar{\mathbf{u}}_I.\hat{\mathbf{n}}_I \tag{4.6.58}$$

The slip boundary condition is imposed at two levels in the present numerical scheme. Once for the evaluation of the vector of flow variables, and another time for the evaluation of the linearised flow residual. To achieve this, the components of the residual in the direction normal to the wall are explicitly set to zero when the mesh does not move. Using the 3-D Euler equations, this operation is algebraically

represented by:

$$\mathcal{R}_I(\hat{\mathbf{U}}) := \mathcal{R}_I(\hat{\mathbf{U}}) - \mathbf{B}_I \mathcal{R}_I(\hat{\mathbf{U}}) \tag{4.6.59}$$

where

$$\mathbf{B}_I = \begin{pmatrix} 0 & 0 & 0 & 0 & 0 \\ 0 & n_{Ix}n_{Ix} & n_{Ix}n_{Iy} & n_{Ix}n_{Iz} & 0 \\ 0 & n_{Iy}n_{Ix} & n_{Iy}n_{Iy} & n_{Iy}n_{Iz} & 0 \\ 0 & n_{Iz}n_{Ix} & n_{Iz}n_{Iy} & n_{Iz}n_{Iz} & 0 \\ 0 & 0 & 0 & 0 & 0 \end{pmatrix} \tag{4.6.60}$$

No-Slip Boundary Condition For viscous flow, the solid wall boundary condition imposes that the fluid relative velocity at the wall is zero. In the relative frame, this is equivalent to as the fluid velocity at the wall equals to the wall velocity. Mathematically, the no-slip boundary condition is expressed as:

$$\mathbf{u}_I - \mathbf{u}_{I,wall} = 0 \tag{4.6.61}$$

Gathering together the first-order terms gives:

$$\hat{\mathbf{u}}_I = i\omega \hat{\mathbf{X}}_I \tag{4.6.62}$$

In the present code, the no-slip boundary condition is implemented in a similar fashion as the slip boundary condition, i.e. is directly applied to the evaluation of the vector of flow variables and to the evaluation of the linearised flow residual. To achieve this, the components of the residual at the walls are explicitly set to zero when the mesh does not move. Using the 3-D Navier-Stokes equations, this operation is achieved by using (4.6.59), but the $\mathbf{B}_I$ matrix becomes:

$$\mathbf{B}_I = \begin{pmatrix} 0 & 0 & 0 & 0 & 0 & 0 \\ 0 & 1 & 1 & 1 & 0 & 0 \\ 0 & 1 & 1 & 1 & 0 & 0 \\ 0 & 1 & 1 & 1 & 0 & 0 \\ 0 & 0 & 0 & 0 & 0 & 0 \\ 0 & 0 & 0 & 0 & 0 & 1 \end{pmatrix} \tag{4.6.63}$$

4.6.2 Periodicity

The periodicity boundary condition imposes that:

$$\hat{\mathbf{U}}\left(x, \theta + P\right) = \hat{\mathbf{U}}\left(x, \theta\right).e^{i\sigma} \tag{4.6.64}$$

where P is the circumferential pitch between the periodic boundaries and σ is the corresponding IBPA. The periodicity condition is imposed at two levels, directly at the periodic nodes as well as to the evaluation of the flow residuals $\mathcal{R}_I$. The residuals associated with the nodes on the lower periodic boundary contribute to the evaluation of the residual of their periodic pairs on the upper boundary, et vice-versa. Let us call R_{I1}^{I2} the operation which rotates the velocities from the lower periodic boundary to the upper periodic boundary, and R_{I1}^{I2} the same operation but in the opposite direction. If $\mathcal{R}_{I2,(0)}$ is the residual evaluated via the edges connected to the node *I2* on the upper boundary, and $\mathcal{R}_{I1,(0)}$ is the residual of its associated (pair) node *I1* on the lower boundary, then the complete residuals for each of these nodes are given by:

$$\mathcal{R}_{I2}(\hat{\mathbf{U}}) = \mathcal{R}_{I2,(0)}(\hat{\mathbf{U}}) + R_{I1}^{I2}\mathcal{R}_{I1,(0)}(\hat{\mathbf{U}}).e^{i\sigma} \tag{4.6.65}$$

$$\mathcal{R}_{I1}(\hat{\mathbf{U}}) = \mathcal{R}_{I1,(0)}(\hat{\mathbf{U}}) + R_{I2}^{I1}\mathcal{R}_{I2,(0)}(\hat{\mathbf{U}}).e^{-i\sigma} \tag{4.6.66}$$

4.6.3 Far-field Boundary Conditions

In turbomachinery applications, the far-field boundaries are often close to the blades since the axial gap between the blade-rows can be quite small. The use of efficient non-reflecting boundary conditions is therefore crucial in order to prevent harmonic linearised solutions being corrupted by spurious numerical reflections at the far-field boundaries. The standard approach is to impose a prescribed unsteady perturbation at the far-field boundaries; this affects the flux balance at the boundaries, and thus in the rest of the field. One of the first developed far-field boundary conditions is known as the 1-D non-reflecting boundary condition, which is based on the standard one dimensional characteristic variable. Using this technique, only waves reflected in the direction normal to the boundary nodes are deleted. This is illustrated in Fig. 4.4. In the past few decades, many different approaches have been developed to create efficient non-reflecting boundary conditions in the fields of CFD and CAA. A review of the methods used in CAA is presented in [109]. Giles [31] produced a work of significant importance in CFD, when he developed non-reflecting boundary conditions for the 2-D Euler equations. This work was later generalised by Hall *et al* [41] to the 3-D Euler equations using a mixed analytical and numerical approach to approximate the inviscid radial eigenmodes. Later, Moinier and Giles [72] extended Hall et al's technique to the 3-D Navier-Stokes equations for the determination of viscous radial eigenmodes. Moinier and Giles used this theory for the post-processing of harmonic linearised solutions from the 3-D Euler or Navier-Stokes equations, and also for the definition of 3-D non-reflecting boundary conditions [73], which are

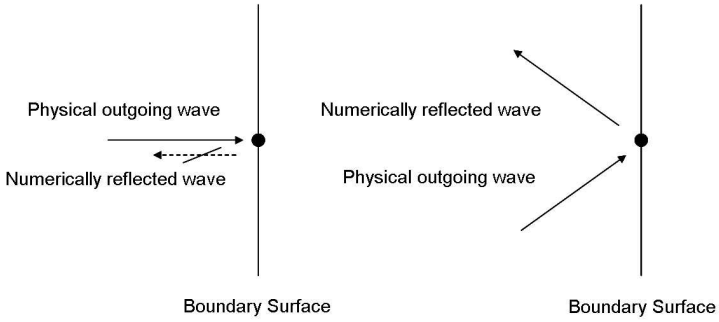

Figure 4.4: 1-D non-reflecting boundary conditions representation: (left) incoming wave normal in the direction normal to the node; (right) incoming wave with a non-zero angle from the normal direction to the node

valid for turbomachinery applications. This latter work probably constitutes the most general boundary condition treatment currently available. The present thesis uses Moinier and Giles boundary condition treatment at the far-field boundaries.

Inviscid Right Eigenmodes

Consider the 3-D Euler equations in primitive form and in cylindrical coordinates. Linearise these equations about an axisymmetric steady-state flow independent of x and θ. The harmonic linearised solution of these equations on a computational domain spanning a single blade-passage can be decomposed into the sum of circumferential and radial eigenmodes, as follows:

$$\tilde{\mathbf{U}}\left(x,\theta,r,t\right)=\sum_{n}\sum_{m}a_{mn}\times\hat{\mathbf{U}}_{mn}^{R}(r).e^{i\left(k_{x,mn}x+k_{\theta,n}\theta+\omega t\right)} \tag{4.6.67}$$

In more compact form, (4.6.67) can be written as:

$$\tilde{\mathbf{U}}\left(x,\theta,r,t\right)=\sum_{n}\tilde{\mathbf{U}}_{n}(x,r,t).e^{ik_{\theta,n}\theta} \tag{4.6.68}$$

where

$$\tilde{\mathbf{U}}_{n}(x,r,t)=\frac{1}{P}\int_{P}\tilde{\mathbf{U}}\left(x,\theta,r,t\right)e^{-ik_{\theta,n}\theta}d\theta \tag{4.6.69}$$

Using (4.6.67) and (4.6.68), it can also be concluded that:

$$\tilde{\mathbf{U}}_{n}(x,r,t)=\sum_{m}a_{mn}\times\hat{\mathbf{U}}_{mn}^{R}.e^{i(k_{x,mn}x+\omega t)} \tag{4.6.70}$$

where $\tilde{\mathbf{U}}$ is the vector of primitive variables, n and m are the circumferential and radial mode numbers respectively. a_{nm} is a measure of the "amplitude" of the mode and $k_{x,mn}$ the axial wave number, both of which being dependent on the values of n and m. The circumferential wave number is given by:

$$k_{\theta,n} = \frac{\sigma + 2\pi n}{P} \tag{4.6.71}$$

where $P = 2\pi/B$, B being the number of blades in the blade-row of interest. Assuming a solution of the form shown in (4.6.67), the harmonic linearised Euler equations, discretised on a radial grid with fourth-difference numerical smoothing, yield an algebraic equation of the form:

$$\left(i\omega\widehat{M} + \widehat{A_r} + ik_{\theta,n}\widehat{A_\theta} + ik_{x,mn}\widehat{A_x} - \widehat{S}\right)\hat{\mathbf{U}}^R_{mn} = 0, \quad \forall n, m \tag{4.6.72}$$

where the matrices $\widehat{M}, \widehat{A_x}, \widehat{A_\theta}, \widehat{A_r}$, and $\widehat{S}$ depend solely on the steady-state flow quantities.

For each circumferential mode number n, (4.6.72) can be viewed as a generalised eigenvalue problem (GEP), in which the axial wave numbers $k_{x,mn}$ are the eigenvalues, and $\hat{\mathbf{U}}^R_{mn}$ are the right eigenvectors. Thus, the number of eigenvalues and eigenvectors depends on the number of radial levels. If Nr represents the number of radial levels, then the number of eigenvalues and radial eigenmodes solutions to (4.6.72) is equal to $5 \times N_r$.

From this it is clear that for each mode number n and m, both $\hat{\mathbf{U}}_{mn}$ and $k_{x,mn}$ can be determined prior to the harmonic time-linearised computation. Given these quantities, the harmonic time-linearised solution $\tilde{\mathbf{U}}$ can be decomposed into Fourier series using (4.6.68) and (4.6.69), and the amplitude a_{mn} of each mode can be determined using (4.6.70), at each iteration of the numerical scheme.

Viscous Right Eigenmodes

The determination of viscous eigenmodes and their eigenvalues is done in a similar fashion as for inviscid flows. In addition, extra viscous flux terms are added to the eigenmode analysis in order to take into account the boundary layer profiles near the end walls exhibited by the steady-state flow. These flux terms are given by:

$$\tau_{rr} = \mu_{tot}\frac{\partial u_r}{\partial r}, \quad \tau_{xr} = \mu_{tot}\frac{\partial u_x}{\partial r}, \quad \tau_{\theta r} = \mu_{tot} r\frac{\partial}{\partial r}\left(\frac{u_\theta}{r}\right), \quad q_r = -k_{T,tot}\frac{\partial T}{\partial r} \tag{4.6.73}$$

where $\mu_{tot} = \mu_l + \mu_t$ is the total viscosity, $k_{T,tot} = c_p\left(\mu_l/Pr_l + \mu_t/Pr_t\right)$ is the thermal conductivity, Pr is the Prandtl number, and the subscripts l and t refer to laminar and turbulence quantities respectively. This formulation is valid for large Reynolds numbers. It also assumes that the mean flow varies only in the radial direction, and that the unsteady flow gradients are predominantly in the radial direction. Numerically, it is possible to obtain a steady flow which varies only in the radial direction by averaging the flow quantities in the circumferential direction. Using the viscous terms described in (4.6.73), the viscous equivalent of (4.6.72) is given by:

$$\left(i\omega\widehat{M} + \widehat{A_r} + ik_{\theta,n}\widehat{A_\theta} + ik_{x,mn}\widehat{A_x} - \widehat{S} - \widehat{V}\right)\hat{\mathbf{U}}^R_{mn} = 0, \quad \forall n, m \tag{4.6.74}$$

where the viscous terms are included in the matrix $\widehat{V}$.

Eigenvalue Identification

The definition of non-reflecting boundary conditions requires the identification of the eigenmodes. It has long been known that each eigenmode must belong to one of the following categories: acoustic upstream, acoustic downstream, vortical, or entropic modes. Hence, it is possible to differentiate between these modes by using a treatment based on their physical behaviour. For this, consider a wave of the form $e^{i(k_x x + k_\theta \theta + \omega t)}$, where $k_x = k_{r,x} + ik_{i,x}$ is the complex axial number. If the frequency ω is a real number, then it is clear that $k_{i,x} > 0$ corresponds to an evanescent mode in the positive x direction, which therefore is an acoustic downstream mode. Following the same logic, $k_{i,x} < 0$ is associated with an acoustic upstream mode. However, when $k_i = 0$, the group velocity $-\partial\omega/\partial k$ needs to be computed in order to find out in which direction the acoustic wave is going. To avoid the practical difficulty of computing the group velocity, a small imaginary part $\omega_i = -10^{-5}\omega_r$, is added to the frequency of the waves, with $\omega_r = \omega$. Having done that, $k_i > 0$ corresponds to a downstream propagating mode, while $k_i < 0$ is an upstream propagating mode. Having introduced an imaginary part to the frequency, the acoustic upstream modes are easily identified as those for which $k_i < 0$. However, the separation of the remaining downstream modes into acoustic, entropic and vortical modes is now a difficult task. The modes identification process which is adopted in the present work is as follows. The modes with the largest values of $||\hat{p}||^2$ are defined as the acoustic downstream modes, the number of which is equal to the number of acoustic upstream modes. The modes with the largest values of $||\hat{p} - c^2\hat{\rho}||^2$ are defined as the entropic modes, their number being equal to half the number of the remaining modes. The remaining are thus defined as vortical modes.

Deletion of Reflected Modes

The reflected modes at the far-field boundaries can be identified as those modes having no physical origin. When the unsteadiness is caused by the blades' vibration, the reflected modes at the outlet boundaries must be acoustic upstream modes, while at the inlet boundaries the reflected modes can be acoustic downstream, vortical or entropic modes. Each reflected mode is deleted using the orthogonality properties of the left and right eigenvectors. In fact, when the eigenvalues are distinct, each left eigenvector is orthogonal to all the right eigenvectors except the one corresponding to the same eigenvalue. This can be proved by considering the following GEP. Consider that $\hat{\mathbf{U}}_j^R$ is the right eigenvector associated with the eigenvalue k_j, and $\hat{\mathbf{U}}_i^L$ is the left eigenvector associated with the eigenvalue k_i. Then, the following relationships are verified:

$$\hat{\mathbf{U}}_i^L \left(A - Bk_i\right) \hat{\mathbf{U}}_j^R = 0 \tag{4.6.75}$$

and

$$\hat{\mathbf{U}}_i^L \left(A - Bk_j\right) \hat{\mathbf{U}}_j^R = 0 \tag{4.6.76}$$

Therefore, the combination of (4.6.75) and (4.6.76) gives:

$$\left(k_j - k_i\right) \hat{\mathbf{U}}_i^L B \hat{\mathbf{U}}_j^R = 0 \tag{4.6.77}$$

Update of boundary data

An external flow state called $\hat{\mathbf{U}}_{ext}^n \in C^{5\times N}$ is introduced for the application of the non-reflecting boundary conditions at the far-field boundaries. The role of this exterior state is to modify the far field boundary fluxes so as to reach the state of no-reflection. For the following description, let $\hat{\mathbf{U}}_{inc}$ be the vector of incoming waves representing the flow forcing coming from adjacent blade-rows. This vector is usually non-zero for forced response, but is equal to zero for the single blade-row analysis of flutter. At each iteration of the numerical scheme, the update of the flow data at the far field boundaries is achieved through a relaxation technique. First, the vector of incoming wave is subtracted from the external state:

$$\mathit{Step}\,1: \quad \hat{\mathbf{U}}_{ext}^n := \hat{\mathbf{U}}_{ext}^n - \hat{\mathbf{U}}_{inc} \tag{4.6.78}$$

Then, the external state is updated:

$$\mathit{Step}\,2: \quad \hat{\mathbf{U}}_{ext}^{n+1} = \hat{\mathbf{U}}_{ext}^n + \sigma_{nrbc} F^{-1} \left(\left(\mathbf{U}^L F \hat{\mathbf{U}}^n \right) \mathbf{U}^R - F \hat{\mathbf{U}}_{ext}^n \right) \tag{4.6.79}$$

where σ_{nrbc} is a relaxation factor between 0 and 1. And finally, the vector of incoming wave is added from the external state:

$$Step\,3: \quad \hat{\mathbf{U}}_{ext}^{n+1} := \hat{\mathbf{U}}_{ext}^{n+1} + \hat{\mathbf{U}}_{inc} \tag{4.6.80}$$

In these expressions, the matrix F represents the Fourier operator, and F^{-1} its inverse. The product $F^{-1}\left(\mathbf{U}^L F \hat{\mathbf{U}}^n\right)\mathbf{U}^R$ corresponds to the desired flow state, i.e. the state which includes only the waves that are leaving the computational domain. Finally, note that for harmonic linearised isolated blade-row analyses, the vector $\hat{\mathbf{U}}_{inc}$ is never updated.

4.6.4 Inter-row Boundary Condition

At the interface between the blade-rows, the boundary condition must have at least two functionalities. It must delete numerically reflected waves as well as allow physical outgoing waves to propagate across the blade-rows. In this thesis, an inter-row boundary condition associating these two functionalities has been created. For the most part, this boundary condition uses the eigenmode and the eigenvalue decomposition of Section 4.6.3, plus the kinematic theory of the blade-row coupling detailed in Section 4.2.

The application of the inter-row boundary condition is first illustrated over a simple example with two blade-rows. Consider that the harmonic linearised solution of only one set of frequency and IBPA needs to be computed per blade-row, and that these solutions are coupled at the inter-row boundary. To help the following description, let subscript 1 be used to refer to the flow quantities in the first (upstream) domain, and subscript 2 for the second (downstream) domain.

Deletion of Reflected Modes at the Inter-row Boundary

In the process of coupling boundary conditions between domains, the 3-D non-reflecting boundary conditions are first applied on both sides of the inter-row boundary to delete spurious numerical reflections. After application of 3-D non-reflecting boundary conditions, the harmonic linearised solution at outlet boundary of the first domain can be written as follows:

$$\tilde{\mathbf{U}}_1(x,\theta,r,t) = \sum_{n_1} \tilde{\mathbf{U}}_{1,(n_1)}(x,r,t).e^{ik_{1\theta,(n_1)}\times\theta} \tag{4.6.81}$$

with,

$$\tilde{\mathbf{U}}_{1,(n_1)}(x,r,t) = \underbrace{\sum_{m_1} a_{1,(m_1 n_1)} \hat{\mathbf{U}}^R_{1,(m_1 n_1)} . e^{i\left(k_{1x,(m_1 n_1)} \times x + \omega_{n_1} \times t\right)}}_{Outgoing \quad eigenmodes} \tag{4.6.82}$$

where ω_{n_1} represents the frequency of the waves in the absolute frame, which depends on the circumferential mode n_1:

$$\omega_{n_1} = \omega_1 - \Omega_1 \times k_{1\theta,(n_1)} \tag{4.6.83}$$

and,

$$k_{1\theta,(n_1)} = \frac{\sigma_1 + 2\pi n_1}{P_1} \tag{4.6.84}$$

In these expressions, Ω_1 is the blade-row rotational speed, $P_1 = 2\pi/B_1$ where B_1 is the number of blades in the current row. n_1 and m_1 are integers denoting the circumferential harmonic and the radial mode numbers respectively. $\hat{\mathbf{U}}^R_{1,(m_1 n_1)}$ represents the set of right eigenmodes corresponding to outgoing waves for modes n_1 and m_1. The harmonic linearised solution at the inlet boundary of the second domain can also be written in the same manner, by substituting subscript 1 by 2.

Transmission of Outgoing Modes at the Inter-row Boundary

The harmonic linearised solutions in domain 1 and 2 can only be coupled if one can find at least one set circumferential modes (n_1, n_2) for which the associated waves in both domains have the same circumferential wave numbers, and the same frequency in the absolute frame:

$$Condition\,1 : \omega_{n_1} = \omega_{n_2} \tag{4.6.85}$$

and

$$Condition\,2 : k_{1\theta,(n_1)} = k_{2\theta,(n_2)} \tag{4.6.86}$$

In theory, if the set-up of the multi blade-row calculation is correct, there must be at least one pair of harmonic solutions in adjacent blade-rows, which satisfies (4.6.85) and (4.6.86). In fact, this is precisely by using these two equations that the frequencies and IBPAs must be determined in each domain prior to the harmonic linearised multi blade-row computation.

Once the outgoing modes which satisfy (4.6.85) and (4.6.86) are transfered between adjacent domains, the new coupled solution at the inter-row boundary in domain 1

is then given in the absolute frame by:

$$\begin{aligned}\tilde{\mathbf{U}}_1(x,\theta,r,t) &= \underbrace{\sum_{n_1}\sum_{m_1} a_{1,(m_1n_1)} \times \hat{\mathbf{U}}^R_{1,(m_1n_1)}.e^{i\left(k_{1x,(m_1n_1)}\times x + k_{1\theta,(n_1)}\times\theta + \omega_{n_1}\times t\right)}}_{Outgoing\quad eigenmodes} \\ &+ \underbrace{\sum_{m_2} a_{2,(m_2n_2)} \times \hat{\mathbf{U}}^R_{2,(m_2n_2)}.e^{i\left(k_{2x,(m_2n_2)}\times x + k_{2\theta,(n_2)}\times\theta + \omega_{n_2}\times t\right)}}_{Incoming\quad eigenmodes}\end{aligned} \tag{4.6.87}$$

And the new coupled solution at the inter-row boundary in domain 2 by:

$$\begin{aligned}\tilde{\mathbf{U}}_2(x,\theta,r,t) &= \underbrace{\sum_{n_2}\sum_{m_2} a_{2,(m_2n_2)} \times \hat{\mathbf{U}}^R_{2,(m_2n_2)}.e^{i\left(k_{2x,(m_2n_2)}\times x + k_{2\theta,(n_2)}\times\theta + \omega_{n_2}\times t\right)}}_{Outgoing\quad eigenmodes} \\ &+ \underbrace{\sum_{m_1} a_{1,(m_1n_1)} \times \hat{\mathbf{U}}^R_{1,(m_1n_1)}.e^{i\left(k_{1x,(m_1n_1)}\times x + k_{1\theta,(n_1)}\times\theta + \omega_{n_1}\times t\right)}}_{Incoming\quad eigenmodes}\end{aligned} \tag{4.6.88}$$

Generalising these results to a case in which a harmonic linearised solution in domain i is coupled with several harmonic linearised solution in an adjacent blade-row, then (4.6.87) becomes:

$$\begin{aligned}\tilde{\mathbf{U}}_i(x,\theta,r,t) &= \underbrace{\sum_{n_i}\sum_{m_i} a_{i,(m_in_i)} \times \hat{\mathbf{U}}^R_{i,(m_in_i)}.e^{i\left(k_{ix,(m_in_i)}\times x + k_{i\theta,(n_i)}\times\theta + \omega_{n_i}\times t\right)}}_{Outgoing\quad eigenmodes} \\ &+ \underbrace{\sum_{j\in E_i}\sum_{m_j} a_{j,(m_jn_j)} \times \hat{\mathbf{U}}^R_{j,(m_jn_j)}.e^{i\left(k_{jx,(m_jn_j)}\times x + k_{j\theta,(n_j)}\times\theta + \omega_{n_j}\times t\right)}}_{Incoming\quad eigenmodes}\end{aligned} \tag{4.6.89}$$

where E_i represents the set of harmonic linearised solutions in the sub-domains j that are adjacent to sub-domain i.

Update of Boundary Data

The update of the flow data at the inter-row boundary is similar in nature to the update of the far-field boundaries data adopted for the 3-D non-reflecting boundary conditions of Section 4.6.3. The process is done as follows:

$$Step\,1: \quad \hat{\mathbf{U}}^n_{i,ext} := \hat{\mathbf{U}}^n_{i,ext} - \hat{\mathbf{U}}^n_{i,inc} \tag{4.6.90}$$

The first step is similar to that used in Section 4.6.3. Note that the incoming waves are now a function of the iteration number n. At the first iteration, the term $\hat{\mathbf{U}}^0_{i,inc}$

is equal to zero for flutter, or equal to the incoming wave extracted from the Fourier decomposition of the mean flow in the upstream blade-row for forced response.

$$Step\,2: \quad \hat{\mathbf{U}}^{n+1}_{i,ext} = \hat{\mathbf{U}}^{n}_{i,ext} + \sigma_{nrbc} F^{-1}\left(\left(\mathbf{U}^{L} F \hat{\mathbf{U}}^{n}_{i}\right)\mathbf{U}^{R} - F\hat{\mathbf{U}}^{n}_{i,ext}\right) \tag{4.6.91}$$

The second step is exactly the same as that used in Section 4.6.3. The external state in each domain is updated using a relaxation technique in order to successively drive the external state to be made of outgoing waves only.

$$Step\,3: \quad \hat{\mathbf{U}}^{n+1}_{i,inc} = \textstyle\sum_{j\in E_i} F_i^{-1} M_j^i \left(\mathbf{U}^{L}_{j} F_j \hat{\mathbf{U}}^{n}_{j}\right)\mathbf{U}^{R}_{j} + \hat{\mathbf{U}}^{0}_{i,inc} \tag{4.6.92}$$

The third step requires further attention. E_i was previously defined. The operator F_j extracts the circumferential Fourier harmonic n_j from the harmonic linearised harmonic solution $\hat{\mathbf{U}}^{n}_{j}$ in domain j, which is equivalent to applying the following operation:

$$\hat{\mathbf{U}}_{j,(n_j)} = \frac{1}{P_j}\int_{P_j} \hat{\mathbf{U}}_j . e^{i(k_j + n_j B_j)\theta} d\theta \tag{4.6.93}$$

$\mathbf{U}^{L}_{j}$ and $\mathbf{U}^{L}_{j}$ are the left and right eigenvectors respectively associated to the circumferential mode n_j, in the domain j. These eigenvectors are used to delete unwanted reflected waves. F_i^{-1} is the inverse Fourier operator in the domain i, which performs the following operation:

$$\hat{\mathbf{U}}_i = \hat{\mathbf{U}}_{j,(n_j)} . e^{i(k_i + n_i B_i)\theta} \tag{4.6.94}$$

Since the number of radial levels may differ between computational domains, an operator M_j^i is applied to interpolate the numerical solution for each radial level in domain j, to each radial level in domain i.

$$Step\,4: \quad \hat{\mathbf{U}}^{n+1}_{i,inc} := \sigma_{mr}\hat{\mathbf{U}}^{n+1}_{i,inc} + (1-\sigma_{mr})\hat{\mathbf{U}}^{n}_{i,inc} \tag{4.6.95}$$

In the fourth step, the vector of incoming waves is updated using a relaxation factor σ_{mr}.

$$Step\,5: \quad \hat{\mathbf{U}}^{n+1}_{i,ext} := \hat{\mathbf{U}}^{n+1}_{i,ext} + \hat{\mathbf{U}}^{n+1}_{i,inc} \tag{4.6.96}$$

Finally, in the fifth step, the update vector of incoming waves is added to the external state in the domain i.

4.7 Iterative Solution of the Harmonic Multi Blade-row Equations

The harmonic linearised Euler or Navier-Stokes equations that are used for an isolated blade-row analysis, can be viewed as a complex linear system of the form:

$$L\hat{\mathbf{U}} = \hat{\mathbf{f}} \tag{4.7.97}$$

where the matrix L is given by:

$$L = i\omega I + A \tag{4.7.98}$$

The matrix A is defined as:

$$A = \frac{\partial \mathbf{R}}{\partial \mathbf{U}} \tag{4.7.99}$$

where the vector $\mathbf{R}$ is the nodal residual of nonlinear steady-state equations.

The right hand side term in (4.7.97) can also be decomposed in two parts:

$$\hat{\mathbf{f}} = \hat{\mathbf{f}}_b + \hat{\mathbf{f}}_g \tag{4.7.100}$$

where $\hat{\mathbf{f}}_b$ represents the residual sensitivity to incoming harmonic perturbations:

$$\hat{\mathbf{f}}_b = -\frac{\partial \mathbf{R}}{\partial \mathbf{U}_b}\hat{\mathbf{U}}_b \tag{4.7.101}$$

and $\hat{\mathbf{f}}_g$ represents the residual sensitivity to harmonic deformations of the grid. It is given by:

$$\hat{\mathbf{f}}_g = -\left(\frac{\partial \mathbf{R}}{\partial \mathbf{X}}\hat{\mathbf{X}} + \frac{\partial \mathbf{R}}{\partial \dot{\mathbf{X}}}\hat{\dot{X}}\right) \tag{4.7.102}$$

For an isolated blade-row analysis, both vectors $\hat{\mathbf{f}}_b$ and $\hat{\mathbf{f}}_g$ are independent from the unsteady perturbation solution $\hat{\mathbf{U}}$. As a result, these two vectors must be determined prior to the harmonic linearised computation and they do not vary during the iterative solution procedure.

For a multi blade-row analysis, the right hand side term $\hat{\mathbf{f}}_b$ now depends on the perturbation solutions in the neighbouring blade-rows. In this case, the harmonic linearised equations can be viewed as a complex linear system of the form:

$$L\hat{\mathbf{U}} = \hat{\mathbf{f}}_b\left(\hat{\mathbf{U}}\right) + \hat{\mathbf{f}}_g \tag{4.7.103}$$

Although (4.7.103) does not have the form of a linear equation, since both the left-

and right- hand sides terms now depend on the perturbation solution $\hat{\mathbf{U}}$, it can still be seen as a linear equation since the term $\hat{\mathbf{f}}_b$ will vary indirectly only as a result of solution variations in neighbouring blade-rows, but not directly due to solution variations in the current blade-row. The compactness of (4.7.103) hides several sub-matrix operations, which can be expressed as follows:

$$\begin{bmatrix} L_1 & & \\ & \ddots & \\ & & L_N \end{bmatrix} \begin{pmatrix} \hat{\mathbf{U}}_1 \\ \dots \\ \hat{\mathbf{U}}_N \end{pmatrix} = \begin{pmatrix} \hat{\mathbf{f}}_{b,1}\left(\hat{\mathbf{U}}_j|_{j\in E_1}\right) \\ \dots \\ \hat{\mathbf{f}}_{b,N}\left(\hat{\mathbf{U}}_j|_{j\in E_N}\right) \end{pmatrix} + \begin{pmatrix} \hat{\mathbf{f}}_{g,1} \\ \dots \\ \hat{\mathbf{f}}_{g,N} \end{pmatrix} \tag{4.7.104}$$

It is crucial to emphasise that (4.7.103) becomes a linear equation, exactly like (4.7.97), once the harmonic perturbation solutions in the adjacent blade-rows are converged, or when the variation of these solutions is not yet apparent at the inter-row boundaries. The elements forming the lines and columns of the matrix L that are not indicated in (4.7.104) are all made of zeros. Thanks to the edge-based data structure, the generalised matrix L is never constructed. Instead the perturbation solutions are computed at the nodes, exactly like in the discretised form of the harmonic linearised isolated blade-row equations. As will be shown in the following sections, the harmonic linearised analysis inherits solution elements from the non-linear steady-state analysis of in Chapter 3, namely the local Jacobi preconditioner, Runge-Kutta smoothing, and multigrid acceleration method. Additionally, an optimisation algorithm, know as GMRES, is used to accelerate the convergence rate of the perturbation solution. Although (4.7.97) and (4.7.104) are different, it will also be that the procedure used to obtain the solution of the harmonic linearised isolated blade-row equations, can also be used to obtain the solution of the harmonic multi blade-row equations, with only minor adaptations.

4.8 Smoothing iteration

The 5-stage Runge-Kutta algorithm of Chapter 3 is used to time-march in pseudo-time the solution of the harmonic linearised Euler or Navier- Stokes equations. Let $\hat{\mathbf{U}}_I^n$ be the harmonic linearised perturbation solution at the n-th iteration and at the I-th grid node, then the Runge-Kutta iterative solution is then given by:

$$\begin{aligned} \hat{\mathbf{U}}_I^0 &= \hat{\mathbf{U}}_I^n \\ \hat{\mathbf{U}}_I^k &= \hat{\mathbf{U}}_I^n - \alpha_k \Delta\tau_I \mathbf{R}_I^{k-1}, \quad k = 1,2,3,4,5 \\ \hat{\mathbf{U}}_I^{n+1} &= \hat{\mathbf{U}}_I^5 \end{aligned} \tag{4.8.105}$$

where

$$\begin{aligned} \mathbf{R}_I^{k-1} &= \mathbf{C}_I\left(\hat{\mathbf{U}}^{k-1}\right) - \mathbf{B}_I^{k-1} \\ \mathbf{B}_I^{k-1} &= \beta_k \mathbf{D}_I\left(\hat{\mathbf{U}}^{k-1}\right) + (1-\beta_k)\,\mathbf{B}_I^{k-2} \end{aligned} \tag{4.8.106}$$

The constant coefficients α_k and β_k are given in Chapter 3. The vector $\mathbf{C}_I$ in (4.8.106) is constructed from the convective part of the flow residual, i.e by using (4.5.48) without numerical dissipation correction. On the other hand, the vector $\mathbf{D}_I$ is composed of all the other terms used for the evaluation of the perturbation residual, i.e. source terms, viscous fluxes, non-homogeneous terms, and numerical smoothing. The term $\Delta\tau_I$ is the local time-step used to time-march the flow solution in pseudo-time. When local time-stepping is not used alone, a local Jacobi preconditioner [23] is also added to improve the convergence properties of the harmonic time-linearised Euler or Navier-Stokes equations. Neither the Runge-Kutta smoother nor the preconditioner need modification for the multi blade-row analysis, which means that they remain the same as for the harmonic linearised isolated blade-row analysis. This results from the fact that the multi blade-row analysis is carried on by computing several "individual" harmonic solutions, and each of them is treated as if it was a harmonic isolated blade-row solution.

The preconditioner is a function of the base steady-state flow solution $\bar{\mathbf{U}}$ only. Thus, it is computed once for all prior to the harmonic linearised iterative produce. With preconditioning, the iterative solution of the harmonic linearised multi blade-row equations can be expressed in algebraic form as:

$$\hat{\mathbf{U}}^{n+1} = \hat{\mathbf{U}}^{n} + R\left(\bar{\mathbf{U}}\right)\left(L\hat{\mathbf{U}}^{n} - \hat{\mathbf{f}}\left(\hat{\mathbf{U}}^{n}\right)\right) \tag{4.8.107}$$

where R includes the Runge-Kutta matrix and the Jacobi preconditioner, and thus it does not depend on the harmonic perturbation solution.

4.9 Multigrid

As described for the nonlinear steady-state analysis in Chapter 3, a multigrid method is used to accelerate the convergence properties of the numerical scheme represented by (4.8.107). The linearised version of the Full Approximation Scheme used in Chapter 3, will here be referred to as the Linear Correction Method. The overall strategy is based on the use of a succession of coarser grid levels which are necessary to correct the harmonic perturbation solution on the finest grid.

For clarity, the multigrid strategy is first presented for an harmonic linearised isolated blade-row analysis using two grid levels, one coarse and one fine. However,

the same methodology can easily be applied to an increased number of grid levels. Subscript f is used to refer to quantities related to the fine grid level, while c refers to the coarse grid. The harmonic perturbation solution is obtained on the fine grid by:

$$L_f \hat{\mathbf{U}}_f = \hat{\mathbf{f}}_f \tag{4.9.108}$$

and the harmonic solution on the coarse grid by:

$$L_c \hat{\mathbf{U}}_c = \hat{\mathbf{f}}_c \tag{4.9.109}$$

The left hand side terms L_f and L_c in (4.9.108) and (4.9.109) represent the flow sensitivity to harmonic perturbations. Although these two terms have the same physical nature, they are constructed independently. The sensitivity matrix on the fine grid is computed from the steady-state flow solution on that grid, while the sensitivity matrix on the coarse grid is obtained from the fine grid steady-state solution interpolated onto the coarse grid. The right hand side vector $\hat{\mathbf{f}}_f$ in (4.9.108) is the physical source of unsteadiness on the fine grid, and can be decomposed in two terms as seen in (4.7.100). (4.9.108) is solved in the traditional way by using (4.8.107). By contrast, the right hand side vector $\hat{\mathbf{f}}_c$ in (4.9.109) does not represent a physical source of unsteadiness. Instead, this term is constructed from the transfer of the residual obtained on the previous iteration on the fine grid, onto the coarse grid:

$$\hat{\mathbf{f}}_c = I_f^c \left(L_f \hat{\mathbf{U}}_f - \hat{\mathbf{f}}_f \right) \tag{4.9.110}$$

The role of the right hand side term in (4.9.109) is to drive the solution on the coarse grid so as to provide a correction to the solution of the fine grid. The correction provided by the coarse grid aims to damp out the high frequency modes from the perturbation solution on the fine grid, or equivalently, to smooth the long wavelength error modes computed on the fine grid.

The blade-row coupling boundary condition is only applied during the iterations on the finest grid level for the multi blade-row analysis. Consequently, the harmonic solutions for each set of frequency and IBPA become independent during the iterations on the coarse grids. The harmonic perturbation solution on the fine grid is then given by:

$$L_f \hat{\mathbf{U}}_f = \hat{\mathbf{f}}_f \left(\hat{\mathbf{U}}_f \right) \tag{4.9.111}$$

while the harmonic perturbation solution on the coarse grid are still given by:

$$L_c \hat{\mathbf{U}}_c = \hat{\mathbf{f}}_c \tag{4.9.112}$$

with

$$\hat{\mathbf{f}}_c = I_f^c \left(L_f \hat{\mathbf{U}}_f - \hat{\mathbf{f}}_f \left(\hat{\mathbf{U}}_f \right) \right) \tag{4.9.113}$$

In the present thesis, the V linear multigrid cycle is used, which is described in Chapter 3.

To summarise what was said previously, harmonic linearised isolated blade-row solutions are obtained through a fixed-point iterative method, which can be represented by:

$$\hat{\mathbf{U}}^{n+1} = \left(\mathbf{I} - M^{-1} L \right) \hat{\mathbf{U}}^n + M^{-1} \hat{\mathbf{f}} \tag{4.9.114}$$

and for the multi blade-row analysis:

$$\hat{\mathbf{U}}^{n+1} = \left(\mathbf{I} - M^{-1} L \right) \hat{\mathbf{U}}^n + M^{-1} \hat{\mathbf{f}} \left(\hat{\mathbf{U}}^n \right) \tag{4.9.115}$$

In these expressions, the matrix M^{-1} is the preconditioning operator which includes the Runge-Kutta smoothing, the Jacobi preconditioner, and the multigrid method. In the present code, the multigrid method is implemented at the highest level of the numerical scheme. Hence (4.9.114) can also be written as:

$$\hat{\mathbf{U}}^{n+1} = mg \left(L, \hat{\mathbf{U}}^n, \hat{\mathbf{f}}, n_{cl} \right) \tag{4.9.116}$$

Similarly, for the harmonic multi blade-row analysis (4.9.115) can be re-expressed as:

$$\hat{\mathbf{U}}^{n+1} = mg \left(L, \hat{\mathbf{U}}^n, \hat{\mathbf{f}} \left(\hat{\mathbf{U}}^n \right), n_{cl} \right) \tag{4.9.117}$$

where n_{cl} represents the number of multigrid cycles, and mg refers to the core routine, which includes the preconditioned fixed point iteration represented in (4.9.115) and the application of all the boundary conditions.

4.10 GMRES

The stability analysis of (4.9.114) shows that the solution of this equation can only converge if all eigenvalues of the matrix $(\mathbf{I} - M^{-1}L)$ lie within the unit circle centred at the origin of the complex plane. Equivalently, all eigenvalues of matrix $M^{-1}L$ must lie within the unit circle centred at $(1, 0)$. In most aeroelastic problems of practical interest, this condition is satisfied and the code converges satisfactorily. However, when this condition is not fulfilled, an exponential growth of the flow residual is observed, which is usually caused by a few complex conjugate eigenvalues lying outside the unit circle, known as *outliers*. Campobasso [10] determined that outliers usually appear when the steady-state solution has failed to converge, and

instead exhibits small-amplitude limit-cycle behaviour caused by numerical instabilities such as flow separation, or vortex shedding at a blunt trailing edge. To avoid this problem, Campobasso developed a generalised minimal residual (GMRES) algorithm, which is theoretically guaranteed to converge, even in the presence of outliers. This method is used to help the numerical solution of the harmonic time-linearised multi blade-row equations to converge on complex test cases representative of real turbomachinery applications. The base-line of this methodology is now explained.

The GMRES algorithm uses the Krylov subspace of dimension m generated by a combination of the preconditioned operator $M^{-1}L$ and the vector $M^{-1}\hat{\mathbf{f}}$. The base vectors that form the Krylov vectorial space are given by:

$$\mathcal{K}_m = < M^{-1}\hat{\mathbf{f}}, (M^{-1}L)M^{-1}\hat{\mathbf{f}}, \ldots, (M^{-1}L)^{m-1}M^{-1}\hat{\mathbf{f}} > \tag{4.10.118}$$

The GMRES algorithm uses a succession of reduced Arnoldi factorisations of $M^{-1}L$ given by:

$$M^{-1}L\hat{Q}_m = \hat{Q}_{m+1}\hat{H}_m, \quad m = 1, \ldots, n_{Kr} - 1 \tag{4.10.119}$$

where n_{Kr} is the total number of Krylov vectors included in the analysis, m is the number of Krylov vectors obtained at the end the previous GMRES iteration, $\hat{H}_m \in C^{m+1\times m}$ is a Hessenberg matrix, and the columns of the matrix $\hat{Q}_m \in C^{k\times m}$ are formed by the vectors $\hat{\mathbf{q}}_j \in C^{k\times 1}, \forall j = 1, \ldots, m$, which form an orthogonal basis for the Krylov subspace $\mathcal{K}_m$. It can be seen in (4.10.119) that $\hat{\mathbf{q}}_{m+1}$ is a function of all other $\hat{\mathbf{q}}_j, j = 1, \ldots, m$ as follows:

$$\hat{\mathbf{q}}_{m+1} = \frac{1}{h_{m+1,m}} \left(M^{-1}L\hat{\mathbf{q}}_m - \left(\sum_{j=1}^{m} h_{j,m}\hat{\mathbf{q}}_j \right) \right), \quad m = 1, \ldots, n_{Kr} - 1 \tag{4.10.120}$$

Equivalently:

$$\hat{\mathbf{q}}_{m+1} = \frac{1}{h_{m+1,m}} \left(\hat{\mathbf{q}}_m - mg\left(L, \hat{\mathbf{q}}_m, 0, n_{cl}\right) - \left(\sum_{j=1}^{m} h_{j,m}\hat{\mathbf{q}}_j \right) \right), \quad m = 1, \ldots, n_{Kr} - 1 \tag{4.10.121}$$

At the m-th GMRES iteration, the iterative solution $\hat{\mathbf{U}}^m$ of (4.7.97) is computed from the linear combination of the m vectors $\hat{\mathbf{q}}_j$, and the starting GMRES solution $\hat{\mathbf{U}}^0$ is shown below:

$$\hat{\mathbf{U}}^m = \hat{\mathbf{U}}^0 + \hat{Q}_m\mathbf{t}_m \tag{4.10.122}$$

where the components of the vector $\mathbf{t}_m \in C^k$ are determined to minimise the 2-norm of the flow residual:

$$\mathbf{R}^m = M^{-1}\left(\hat{\mathbf{f}} - L\hat{\mathbf{U}}^m\right) \tag{4.10.123}$$

The first Krylov vector $\hat{\mathbf{q}}_1$ is the residual of the preconditioned system. It is given by:

$$\hat{\mathbf{q}}_1 = \mathbf{R}^1 = mg\left(L, \hat{\mathbf{U}}^0, \hat{\mathbf{f}}, n_{cl}\right) - \hat{\mathbf{U}}^0 \tag{4.10.124}$$

The number n_{Kr} of Krylov vectors required for full convergence is much smaller than the size of the matrix L in (4.7.97), though this number is usually too large for available computing resources. In fact, all $\mathbf{q}_m$ Krylov vectors, $m = 1, \ldots, n_{Kr}$, need to be stored at the same time at the $n_{Kr} - th$ GMRES iteration. This problem can be overcome by using the restart option, which involves restarting the full GMRES procedure from the solution $\mathbf{U}^0 = \hat{\mathbf{U}}^{n_{Kr}}$ obtained after a number n_{Kr} of GMRES iterations. Typically, the use of 10 to 30 Krylov vectors makes the method computationally affordable, and less than 30 restarts are usually necessary to obtain full convergence. A potential issue associated with the restart option is that it can lead to the numerical stagnation of the residual. With significant resources, Campobasso [9] showed that this problem can be overcome by choosing n_{Kr} and n_{cl} above certain values, which are case dependent.

Note that only the determination of the first Krylov vector $\hat{\mathbf{q}}_1$ in (4.10.124) uses explicitly the values of the forcing vector $\hat{\mathbf{f}}$. All other Krylov vectors $\hat{\mathbf{q}}_m, m = 2, \ldots, n_{Kr}$ are determined using the recursive procedure given by (4.10.121) which uses all the previous Krylov vectors $\hat{\mathbf{q}}_i, i < m$, and a multigrid operation $mg\left(L, \hat{\mathbf{q}}_m, 0, n_{cl}\right)$ deprived of its forcing vector $\hat{\mathbf{f}}$. This results from the fact that the GMRES method was designed on the assumption that the perturbation vector $\hat{\mathbf{f}}$ is constant during the iterative procedure. This is consistent with the definition of the vectors constituting the Krylov subspace in (4.10.118), which use the same forcing vector $\hat{\mathbf{f}}$.

However, as seen in (4.7.103), the harmonic blade-row coupling method requires an update of the perturbation vector $\hat{\mathbf{f}}_1(\hat{\mathbf{U}})$ at each iteration of the numerical scheme. This update is not consistent with the above GMRES algorithm and would cause the code to diverge. It is possible to overcome this problem by updating the forcing vector $\hat{\mathbf{f}}_1(\hat{\mathbf{U}})$ during the determination of the first Krylov vector only. No coupling between harmonic time-linearised solutions is achieved during the determination of all other Krylov vectors. This way, the forcing function $\hat{\mathbf{f}}$ does not vary during the GMRES iterations, which satisfies the convergence criteria of the GMRES algorithm.

One of the drawbacks with this approach is that the convergence of the iterative solution is no longer guaranteed. Typically, saw-teeth patterns can be observed in the convergence history of the residual, like shown in Fig. 4.5. However, these are usually eliminated after the GMRES is restarted a sufficient number of times.

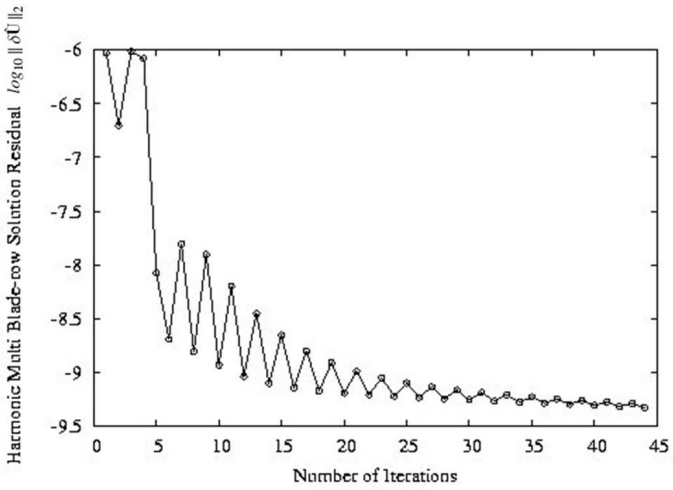

Figure 4.5: Example of saw-teeth pattern in the convergence of the residual for the harmonic linearised multi blade-row method using GMRES with a number of restarts

.

4.11 Memory Requirements

Running the harmonic linearised multi blade-row solver can require substantially more CPUs in comparison with conventional harmonic linearised isolated blade-row analyses. There are at least two obvious reasons for this: (i) the multi blade-row analysis includes several computational sub-domains, instead of just one; (ii) the application of 3-D non-reflecting boundary conditions at the inter-row boundaries requires the storage of many radial eigenmodes.

Consider an harmonic linearised multi blade-row analysis and further consider one local sub-domain and one of the far-field boundaries associated with this domain (i.e. inlet, or outlet). At this boundary, let N_c be the number of circumferential lines (i.e. lines at constant radius) on which the eigenmodes are computed. Let also N_r and N_n be the number of radial modes and circumferential modes respectively. The dimension of each eigenvector is thus equal to $5N_cN_rN_n$, each component being a complex number. Hence, the amount of memory also scales with $5N_cN_rN_n$. The present code uses real arithmetic to solve complex equations, and data are stored in double precision. Under these conditions the amount of hard disk memory per file containing the eigenvectors on one boundary is equal to:

$$M_b^{eig} = 8 \times 5N_cN_rN_n \ (bytes)$$

Since, the eigenmodes need to be stored for the “inlet” and “outlet” boundaries of

each computational sub-domain, the total amount of CPU memory required is equal to:

$$M_{tot}^{eig} = \sum_{i=1}^{N_{sub}} 2 \times 8 \times 5 N_c^i N_r^i N_n^i \ (bytes) \tag{4.11.125}$$

in which N_{sub} is the total number of sub-domains included in the multi blade-row analysis. Note that the number of circumferential lines are considered equal at the inlet and outlet boundaries of each local sub-domain.

For a harmonic linearised blade-row analysis, the total CPU requirement is estimated to be about 1500 bytes per grid node, including the eigenvector files. This number was evaluated by considering the 3-D Navier-Stokes equations solved on one grid level (without GMRES). Running GMRES will increase this number by NPDES $\times$ number of Krylov vectors per grid node. Under the same conditions, the total CPU requirement for a multi blade-row analysis scales with the number of sub-domains as follows:

$$M_{tot}^{files} = k \times \sum_{i=1}^{N_{sub}} 1500 \times N^i \ (bytes) \tag{4.11.126}$$

in which N^i is the number of nodes in the i-th sub-domain (see Fig. 4.3) and k is an amplification factor representing the additional storage due to new arrays used by the solver for the application of the inter-row boundary condition. For the test cases studied in this thesis, the factor k varied between 1.01 and 1.03 depending on the total mesh size.

Chapter 5

Inter-row Boundary Condition Validation

5.1 Introduction

As seen in Chapter 4, the development of the harmonic linearised multi blade-row code required the implementation of an inter-row boundary condition. This boundary condition has two functionalities: (i) it must delete numerical reflections at the inter-row boundary; (ii) it must allow outgoing spinning modes to propagate across the blade-rows. In this chapter, the inter-row boundary condition is tested over a series of simple test cases, in which spinning modes are propagated in linear ducts split into several sub-domains. The numerical results are then compared with available analytical solutions to make sure that the spinning modes are correctly passed from one domain to the next. Previous studies [13] using second-order numerical schemes like the one used in this thesis have shown that enough accuracy can be obtained by using 20-30 grid points per wave length on structured grids. In order to make sure that the resolution for each case is adequate, it was chosen to use structured meshes with about 40 points per wave length. The test cases used in this chapter aim to cover a wide range of wave configurations for which analytical solutions are known, ranging from: non-swirling to swirling uniform flows; "cut-on" to "cut-off" modes; and 2-D to 3-D waves. Note that all 2-D cases presented in this chapter are solved in a 3-D manner by giving a small radial variation to the geometry. The theory used for the set up of these test cases is presented in Appendices A and B. Finally, the specific case when waves propagate with negative frequencies in the absolute frame is also treated.

5.2 Non-swirling Uniform Flows

Appendix A demonstrates that any solution from the linearised Euler equations can always be decomposed into the elementary waves, namely: acoustic upstream, acoustic downstream, vortical, and entropic waves. In this section we use this result with the aim to evaluate the accuracy of the linear inter-row boundary condition. The flow is forced to propagate in linear ducts split into several sub-domains, some of which are rotating. We then ensure that each elementary wave of the flow is correctly passed from one domain to the next. For simplicity, this section deals only with non-swirling uniform steady-state flows for which analytical solutions are known. The case of swirling uniform flows will be treated later.

5.2.1 Acoustic Upstream Waves

The propagation of acoustic waves is governed by the balance between the compressibility and the inertia of the fluid. From the 1-D wave theory, it can be seen that acoustic waves can propagate either in the direction of the fluid, or in the opposite direction. In the former case, one refers to acoustic downstream waves, while in the latter case one refers to acoustic upstream waves. See [62] for a full discussion on the propagation of acoustic waves.

The propagation of an acoustic upstream wave is studied in this section and an acoustic downstream waves in studied in the following section. In the first test case, the underlying steady-state flow is uniform, subsonic ($M = 0.5$) passing through a channel made of three domains having the same dimensions. None of the domains are rotating ($\Omega_i = 0, i = 1, 2, 3$) and there is no obstacle to the flow since there is no physical blade included in the computation. The flow is inviscid and is going in the axial direction, the radial and circumferential flow angles being set to zero.

A purely 1-D upstream acoustic wave, having an analytical solution of the form $\tilde{\mathbf{U}} = \hat{\mathbf{U}} e^{i(\omega t + k_x x)}$, is imposed at the exit of the third domain and is expected to propagate in the upstream direction, i.e. from the right to the left. The circumferential wave number is set to zero since $k_\theta = 0$. No scattering effect of the circumferential wave number can occur since there is no geometric variation. From the inter-row boundary condition standpoint, only the wave having the circumferential wave number $k_\theta = 0$ - here referred as the fundamental spinning mode - is allowed to propagate across the blade-rows. As seen in Appendix A, we know that pressure and density perturbations should propagate in phase for acoustic waves. The computed contours of pressure and density are presented in Fig. 5.1 showing a perfect phase agreement.

The computed solution presented in Fig. 5.2 propagates across all three domains without attenuation and is in very good agreement with the analytical solution.

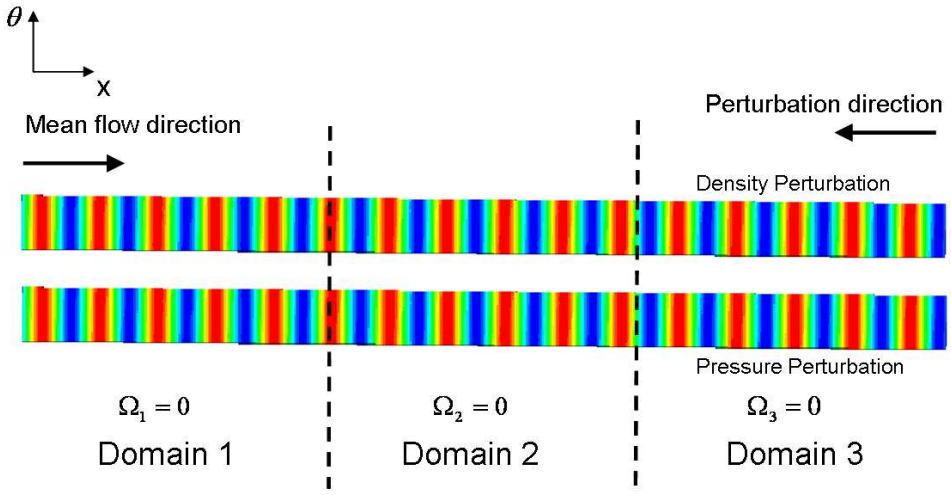

Figure 5.1: Real part of unsteady density and unsteady pressure for the 1-D acoustic upstream wave test case consisting of three flow domains with interface

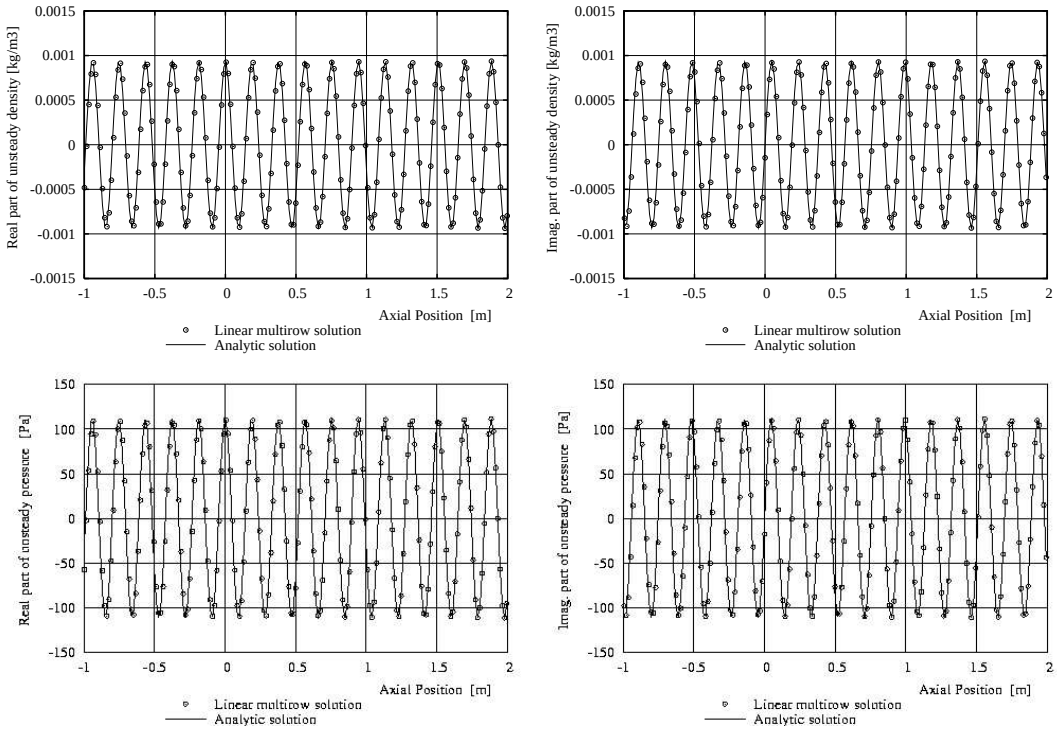

Figure 5.2: 1-D acoustic upstream wave (interface at x=0 and x=1 represented in Fig. 5.1). Comparison between analytical and computed solutions using linear multirow method

5.2.2 Acoustic Downstream Waves

In this test case, the computational domain is split into two domains. The mean flow enters in the first domain uniform, axially, and subsonic ($M = 0.5$). The circumferential length of the second domain is twice the size of the first domain, and the second domain is rotating ($\Omega_1 = 0, \Omega_2 \neq 0$).

A 2-D acoustic downstream wave, having an analytical solution of the form $\tilde{\mathbf{U}} = \hat{\mathbf{U}} e^{i(\omega_1 t + k_{x1} x + k_{\theta 1}\theta)}$, is imposed at the inlet of the first domain and is expected to propagate in the downstream direction, i.e. from the left to the right. Only the fundamental spinning mode - here corresponding to $k_\theta = k_{\theta 1}$ - is allowed to propagate across the two domains. When passing from one domain to the next, the axial and circumferential wave numbers remain identical. However, since the second domain is rotating the temporal-frequency of the wave must be modified in the relative frame. Calling ω_1 and ω_2 the wave's frequency in the first and second domains respectively and using the theory developed in Chapter 4, we immediately see that the frequencies in both domains are related by the relationship: $\omega_2 = \omega_1 + k_{\theta 1}\Omega_2$.

As mentioned earlier, pressure and density perturbations travel in phase for acoustic

waves. The computed pressure and density contours are presented in Fig. 5.3 showing again an excellent phase agreement. The computed solution in Fig. 5.4 propagates across the two domains without attenuation and is also in very good agreement with the analytical solution.

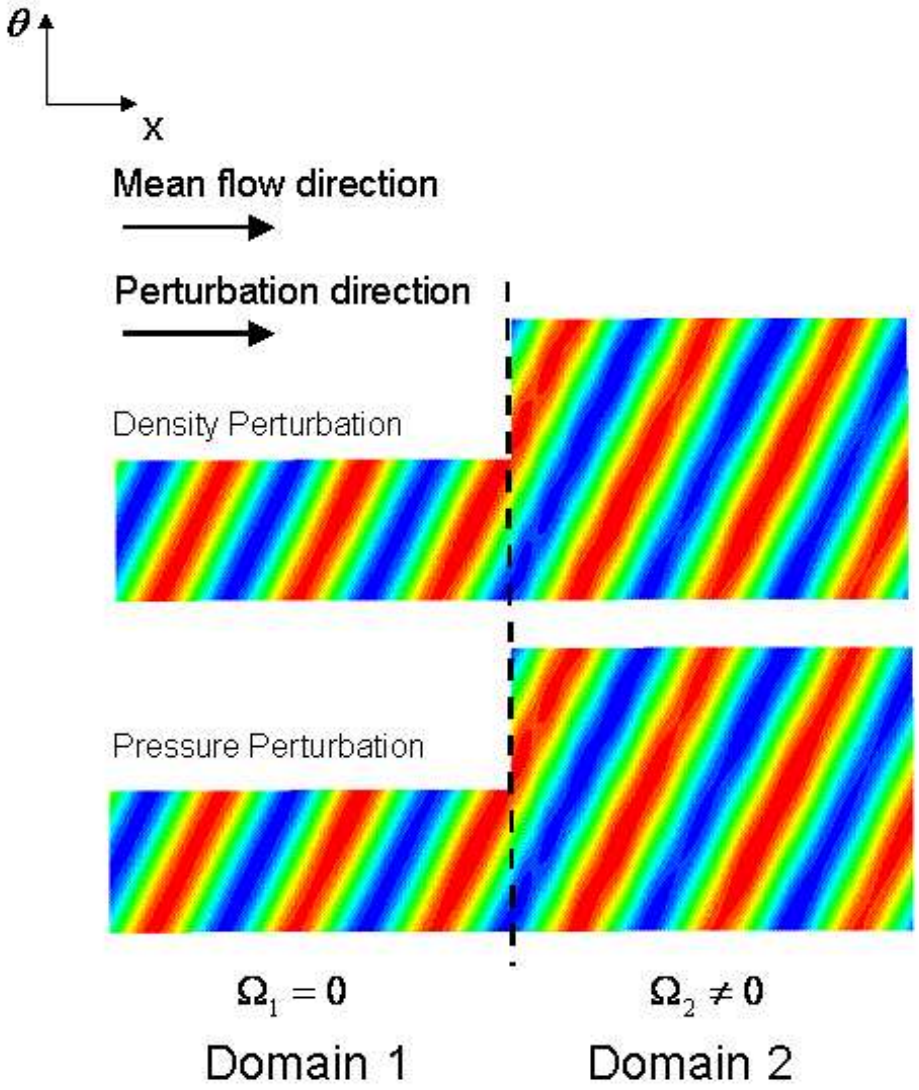

Figure 5.3: Real part of unsteady density and unsteady pressure for the 2-D acoustic downstream wave test case consisting of two flow domains with interface and 1 spinning mode

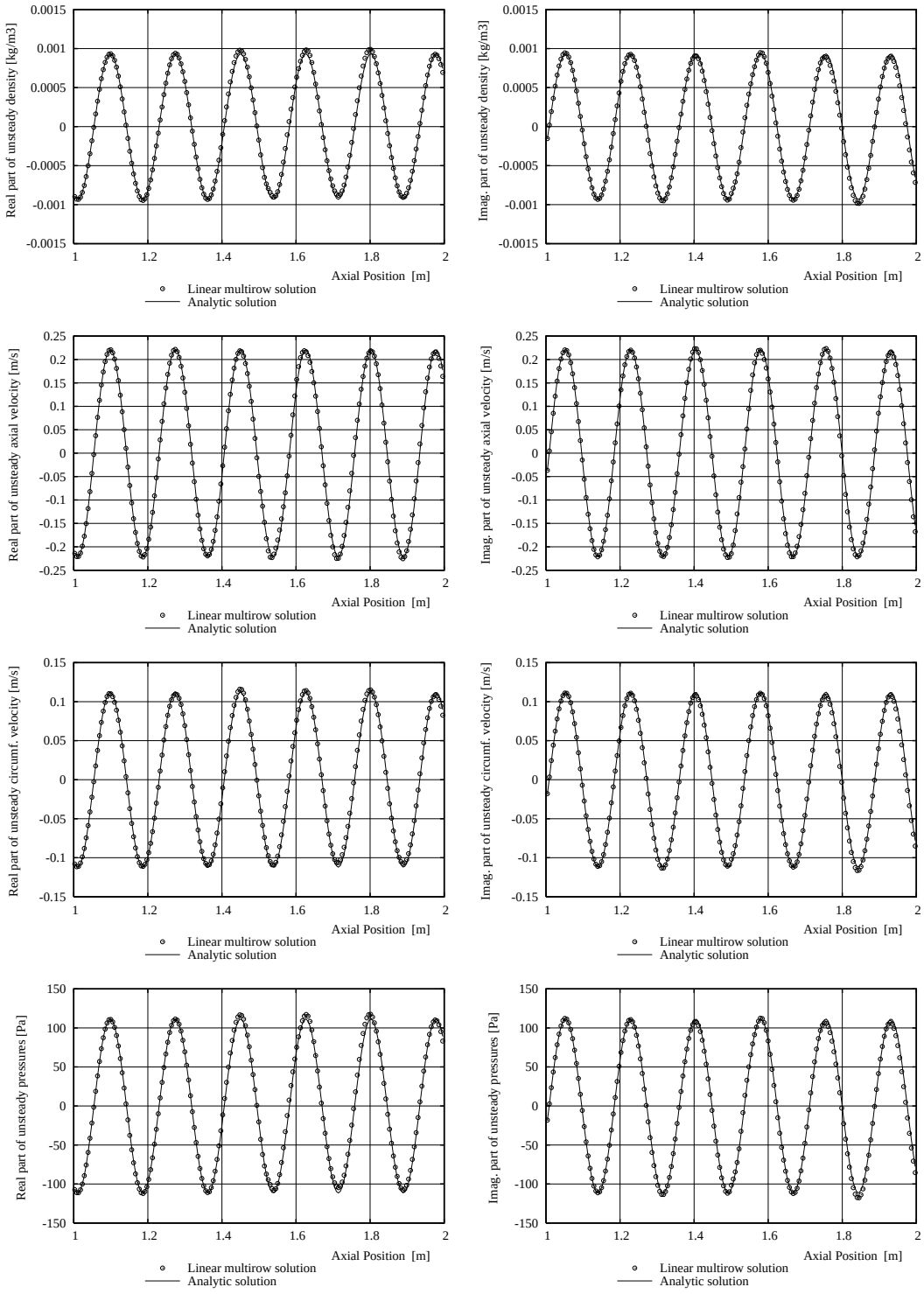

Figure 5.4: 2-D acoustic downstream wave solution (interface at x=1.5 represented in Fig. 5.3). Comparison between analytical and computed solutions using linear multirow method

In a further study using the same geometry and mean flow conditions, two superimposed 2-D acoustic downstream waves with an analytical solution of the form $\tilde{\mathbf{U}} = \hat{\mathbf{U}}_1 e^{i(\omega t + k_{x1} x + k_{\theta 1}\theta)} + \hat{\mathbf{U}}_2 e^{i(\omega t + k_{x2} x + k_{\theta 2}\theta)}$ are applied at the inlet of the first domain. The waves are expected to propagate in the downstream direction. The circumferential wave numbers of the waves are related to each other by the simple relation $k_{\theta 2} = k_{\theta 1} - B_1$, where $B_1 = 2\pi/P_1$, and P_1 is the circumferential pitch of the first domain. Since the circumferential wave numbers of these two waves are different, they will propagate in the next domain with different frequencies, given by $\omega_1 = \omega + k_{\theta 1}\Omega_2$ and $\omega_2 = \omega + k_{\theta 2}\Omega_2$.

The real part of the unsteady pressure is shown in Fig. 5.5. The solution in the first domain represents the superposition of the two waves, while the solution in the second is split in two, one for each circumferential wave number. Both waves propagate into the next domain without distortion or attenuation. The computed solution is in excellent agreement with the analytical solution, though the latter is not shown here.

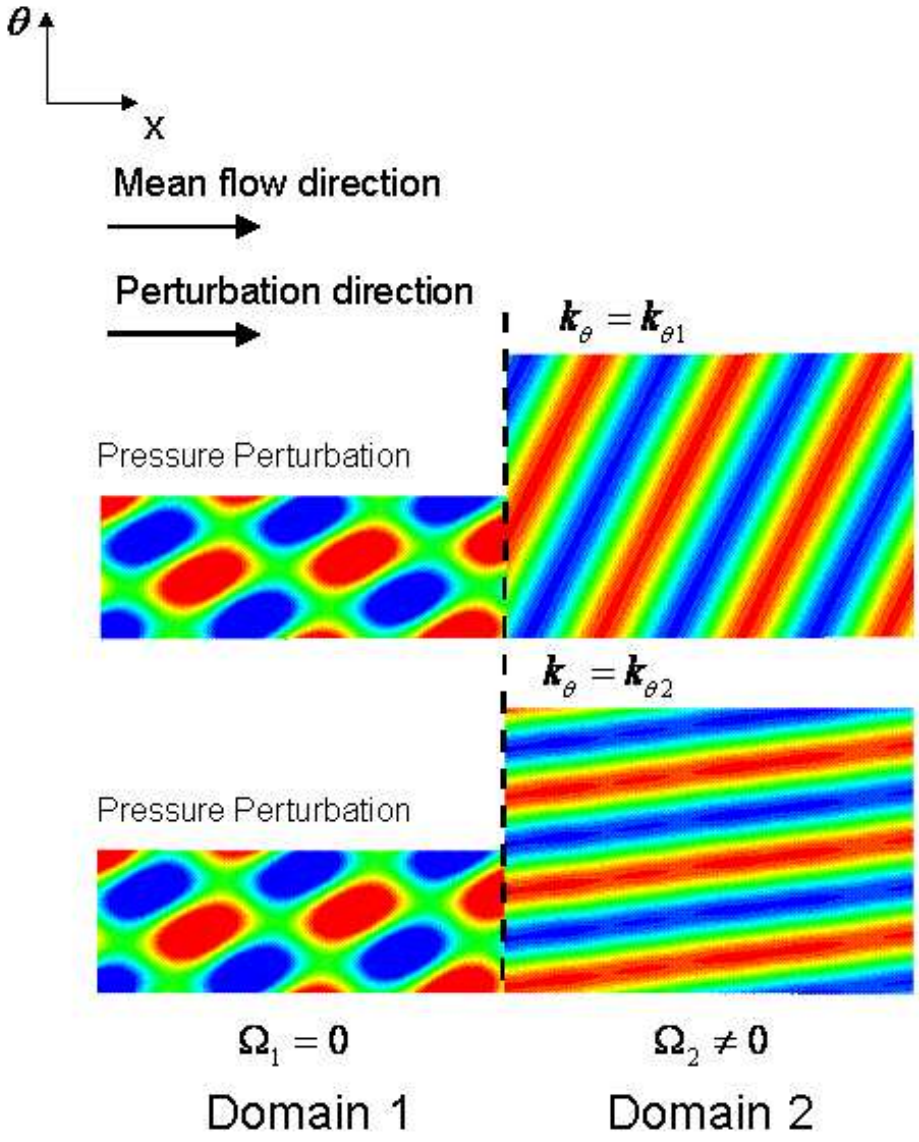

Figure 5.5: Real part of unsteady pressure for the two 2-D downstream acoustic wave test case

In a further test case, a 3-D acoustic downstream wave is forced to propagate across two domains. The two domains have the same pitch (180^o), the same length, the same inner radius (rmin = 0.5m), and the same outer radius (rmax = 1m). The first domain remains stationary while the second domain is rotating ($\Omega_1 = 0, \Omega_2 \neq 0$)

The flow enters the first domain axially, uniformly, and subsonic ($M = 0.5$). The first radial acoustic mode is imposed at the inlet of the domain and is expected to propagate from left to right. As seen in Fig. 5.6, the first radial mode computed near axial mid-length of the first domain agrees well with the analytical solution.

The computed unsteady pressure and density are shown in Fig. 5.7. In Fig. 5.8,

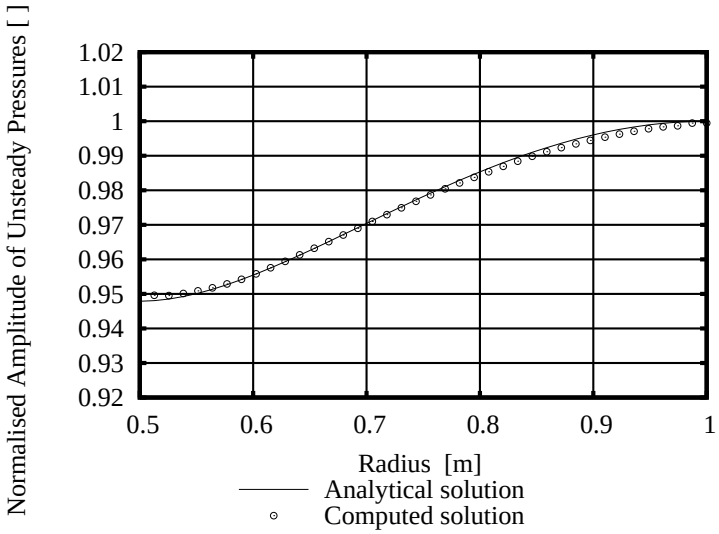

Figure 5.6: Predicted and analytically-obtained radial mode shape for the first radial acoustic mode near axial mid-length of first domain

the variation of each primitive variable was compared at the inner radius across the two domains and excellent agreement with the analytical solution was obtained.

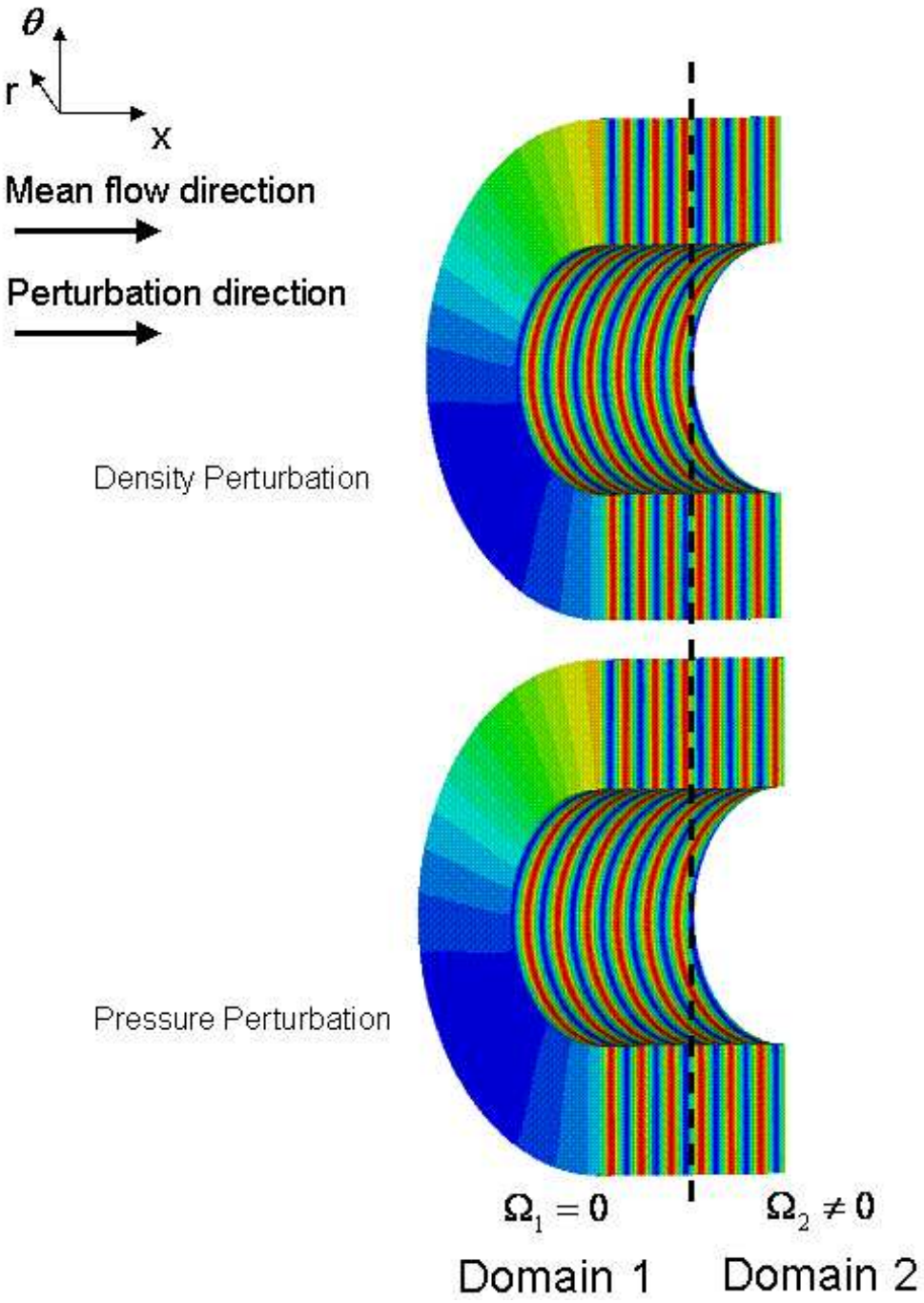

Figure 5.7: Real part of unsteady density and unsteady pressure for the 3-D acoustic downstream wave test case

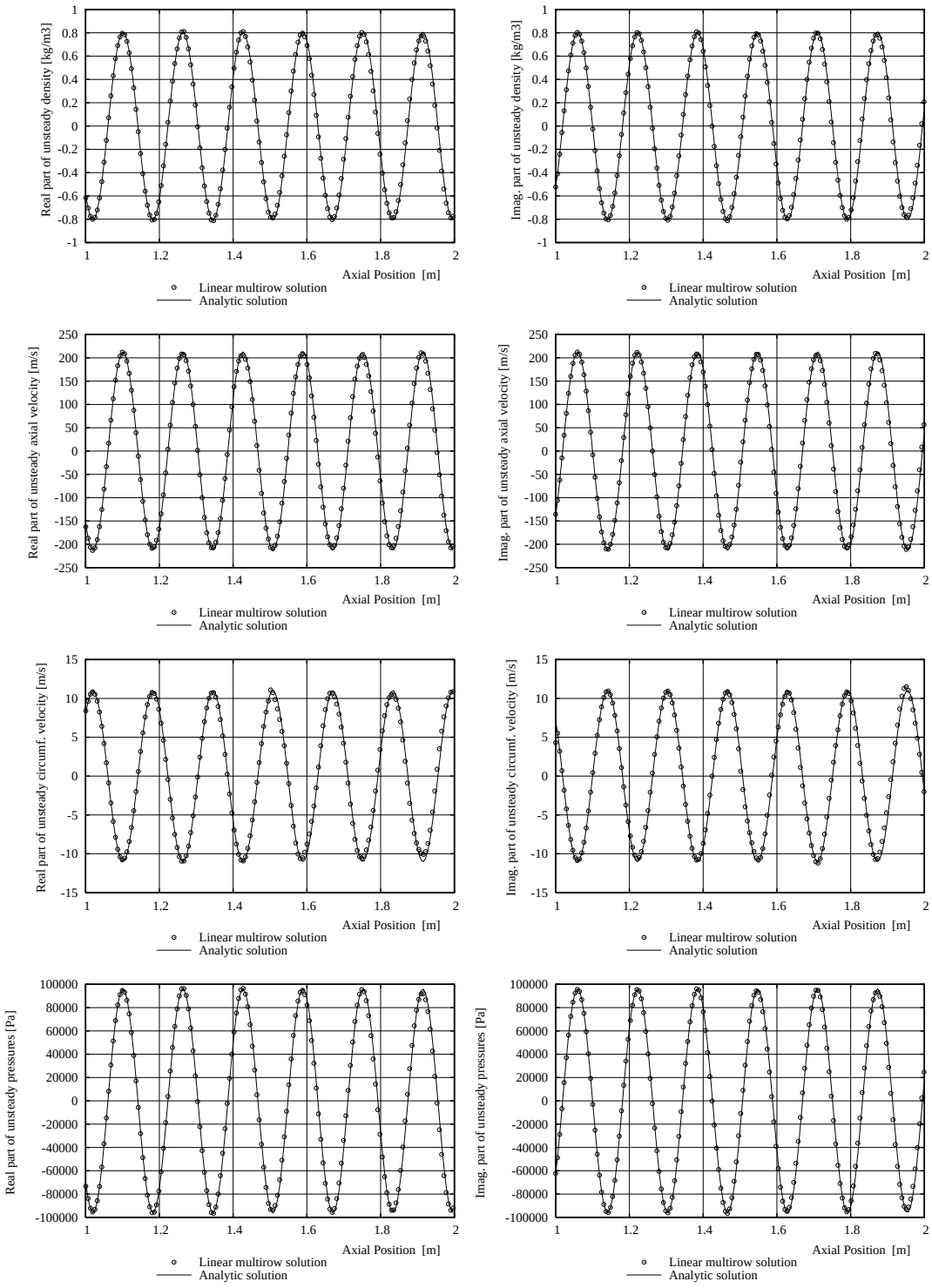

Figure 5.8: 3-D acoustic downstream wave solution at r=rmin (interface at x=1.5 represented in Fig. 5.7); Comparison between analytical and computed solutions using linear multirow method

5.2.3 Vortical Wave

Vortical waves are velocity perturbations that are created by variations of vorticity. In practical applications, it may be difficult to identify them as they can easily mix up and scatter into the acoustic waves due to the presence of obstacles in the mainstream.

This test case aims to study the propagation of a vortical wave across two domains in idealised flow conditions for which analytical solutions are known. For simplicity, this test case and the next (which propagates an entropic wave) use the same geometry and mean flow conditions. Hence, these will be described only once. A purely axial mean flow which is subsonic, uniform, with Mach number $M = 0.5$ enters a channel made of two flow domains having the same pitch, the same length, and only the second domain is rotating ($\Omega_1 = 0, \Omega_2 \neq 0$).

A 2-D vortical wave having an analytical solution of the form $\tilde{\mathbf{U}} = \hat{\mathbf{U}} e^{i(\omega t + k_x x + k_\theta \theta)}$ is imposed at the inlet of the first domain and is expected to propagate in the downstream direction as it will be convected by the flow. This wave carries variations of axial and circumferential velocities only. All other primitive variables do not fluctuate. Figure 5.9 shows the computed real part of axial and circumferential velocities. The flow variables, presented in Fig. 5.10, are in excellent agreement with the corresponding analytical solution.

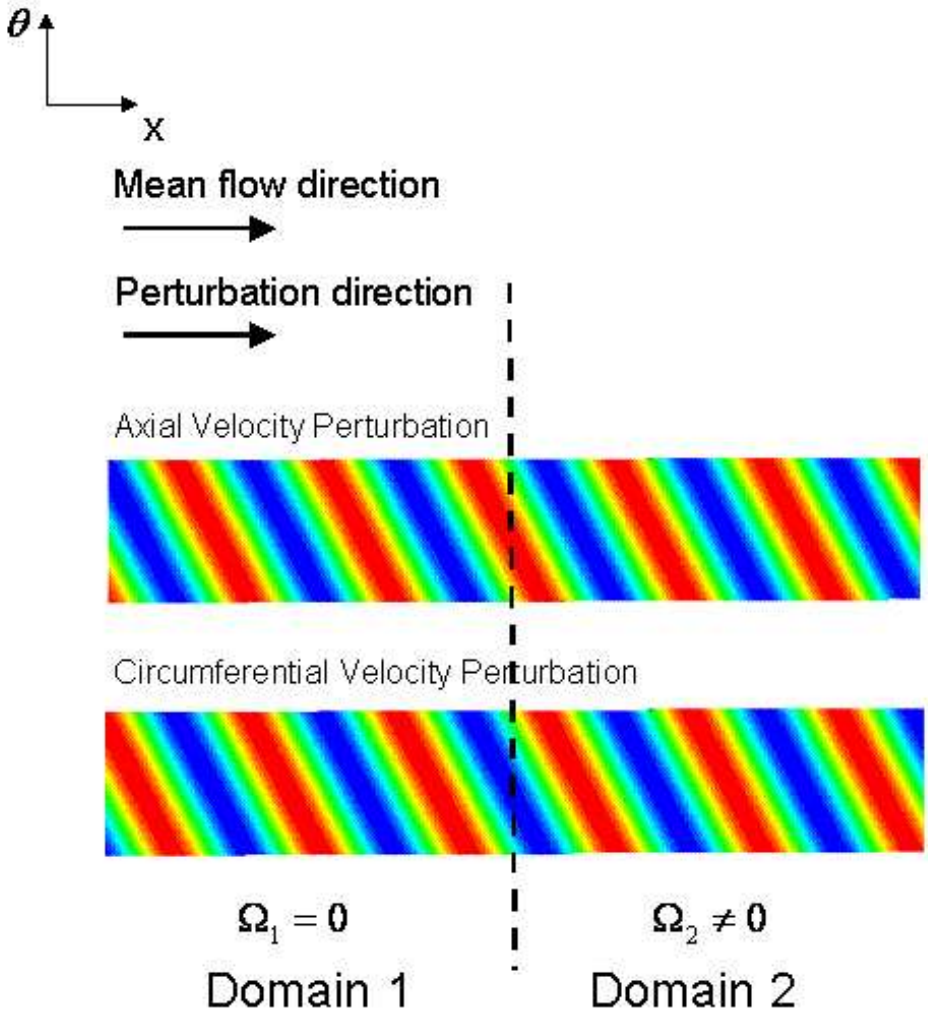

Figure 5.9: Real part of unsteady axial velocity and real part of circumferential velocity for the 2-D vortical wave test case

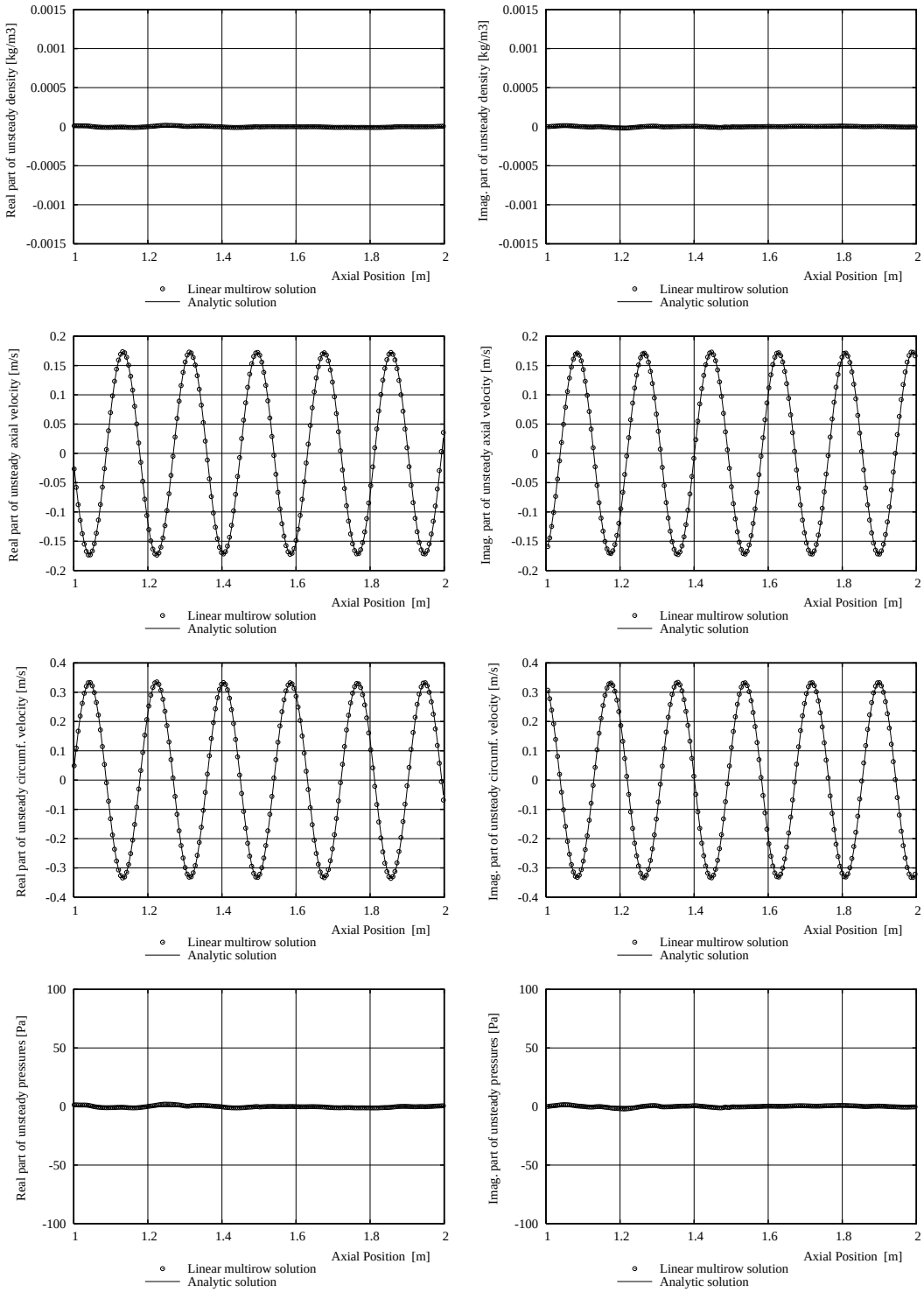

Figure 5.10: 2-D vortical wave solution (interface at x=1.5 represented in Fig. 5.9). Comparison between analytical and computed solutions using linear multirow method

5.2.4 Entropic Wave

Entropic waves are generated by variations of entropy and indicate a degree of dissipation in the flow. Such dissipations are usually influenced by flow viscosity or heat transfer. Using CFD, it is generally difficult to assess entropy accurately as numerical dissipation is also an inherent part of the numerical solution and mixes up with the real flow dissipation. Numerical dissipation is generally influenced by the numerical scheme used to discretise the governing equations as well as by the grid resolution used for the analysis. Entropic waves are purely convected by the mean flow and their amplitude is proportional to $\delta p - c^2 \delta \rho$.

This test case aims to study the propagation of an entropic wave across several domains in idealised flow conditions for which analytical solutions are known. This test case uses the same geometry and mean flow conditions as the previous one but the length of each domain is longer in the axial direction.

A 2-D entropic wave having an analytical solution of the form $\tilde{\mathbf{U}} = \hat{\mathbf{U}} e^{i(\omega t + k_x x + k_\theta \theta)}$ is imposed at the inlet of the first domain and is expected to propagate in the downstream direction. This wave is represented by fluctuations of density only. The computed density contours are presented in Fig. 5.11 and the computed solution in Fig. 5.12 is in excellent agreement with the analytical solution.

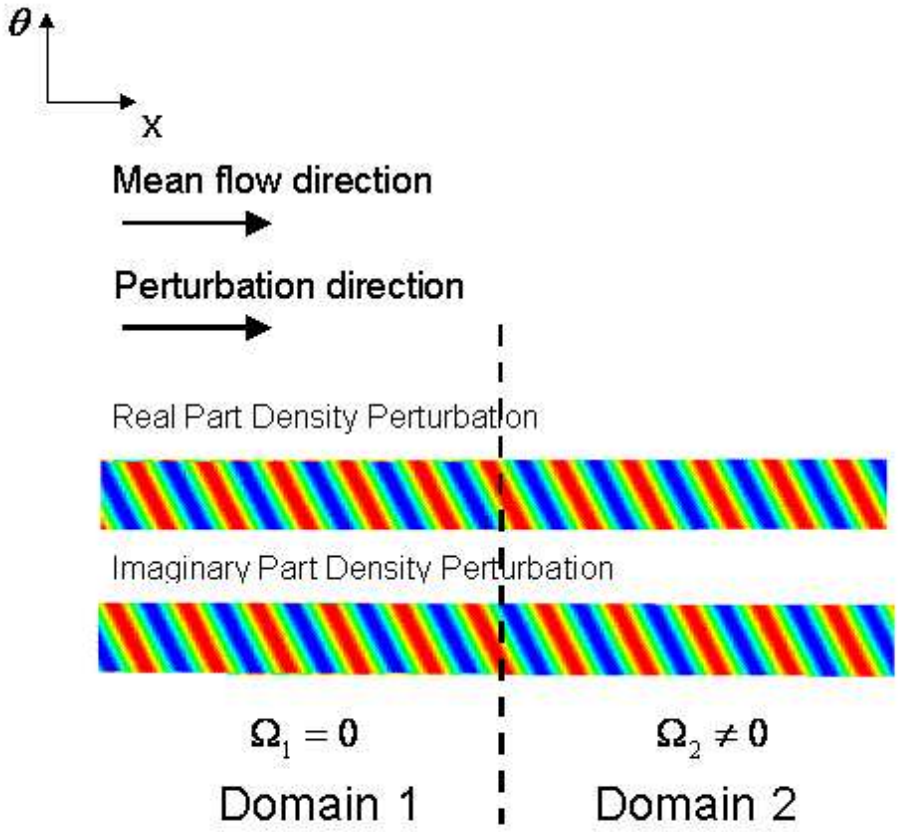

Figure 5.11: Real part and imaginary part of unsteady density for the 2-D entropic wave

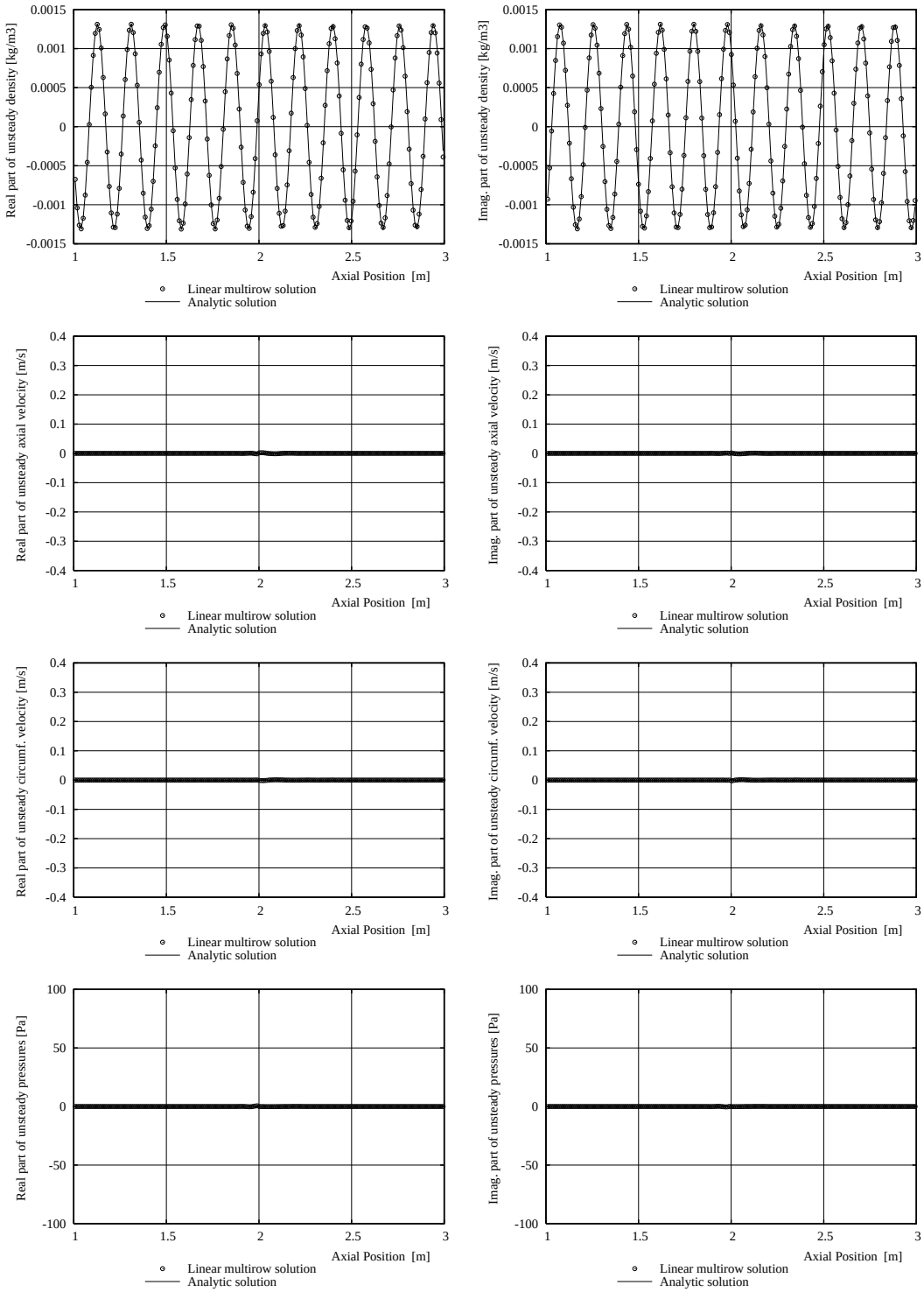

Figure 5.12: 2-D entropic wave solution (interface at x=2 represented in Fig. 5.11). Comparison between analytical and computed solutions using linear multirow method

5.3 Swirling Uniform Flows

The validity of the inter-row boundary condition will now be assessed for the case of uniform swirling flows for which analytical solutions are known. In the following test cases, the full flow domain is divided into several smaller domains having the same circumferential pitch, some of which are rotating. For each domain, the stagger angle and rotational speed were determined so that the flow remains perfectly aligned with the blades. As a result, the relative circumferential flow angle and Mach number are all equal to $\pm 45^o$ and $M = 0.7$ respectively. More details about the geometry, flow conditions, and boundary conditions, are given in Chapter 6, in which the same geometry and flow conditions are used for a multi blade-row flutter analysis. The wave propagation study is considered in several steps. First, the propagation of an acoustic cut-on mode is investigated for "empty" and "bladed" domains. For simplicity, the blades are represented by flat plates that are perfectly aligned with the mean flow and hence they induce no turning. Second, a test case using an acoustic downstream cut-off mode is presented. Finally, the special case of a wave propagating with a negative frequency in the absolute frame is discussed.

5.3.1 Cut-on Modes

This test case uses three "blade-less" flow domains and the second domain is rotating. As specified above, the mean flow in each domain is uniform, subsonic, with Mach number $M = 0.7$.

A cut-on 2-D acoustic downstream wave is imposed at the inlet of the first domain and is expected to propagate from left to right. The computed real part of unsteady pressure is presented in Fig. 5.13. One can clearly see that the wavelength is longer than the full domain. The amplitude of this wave, and the corresponding numerically reflected wave at the inter-row and far field boundaries, were evaluated across the three domains and the results are presented in Fig. 5.14. As expected, the downstream mode propagates across the three domains without attenuation. The amplitude of the same, but numerically-reflected wave, which goes in the upstream direction, is about 45 dB smaller compared to the original downstream wave and thus does not contaminate the quality of the overall solution. Note that the amplitudes of upstream and downstream waves are continuous across all three domains. This result confirms the excellent quality of the overall solution.

In a second analysis, flat plate blades are inserted into each domain. A detailed description of the geometry and boundary conditions are given in Chapter 6.

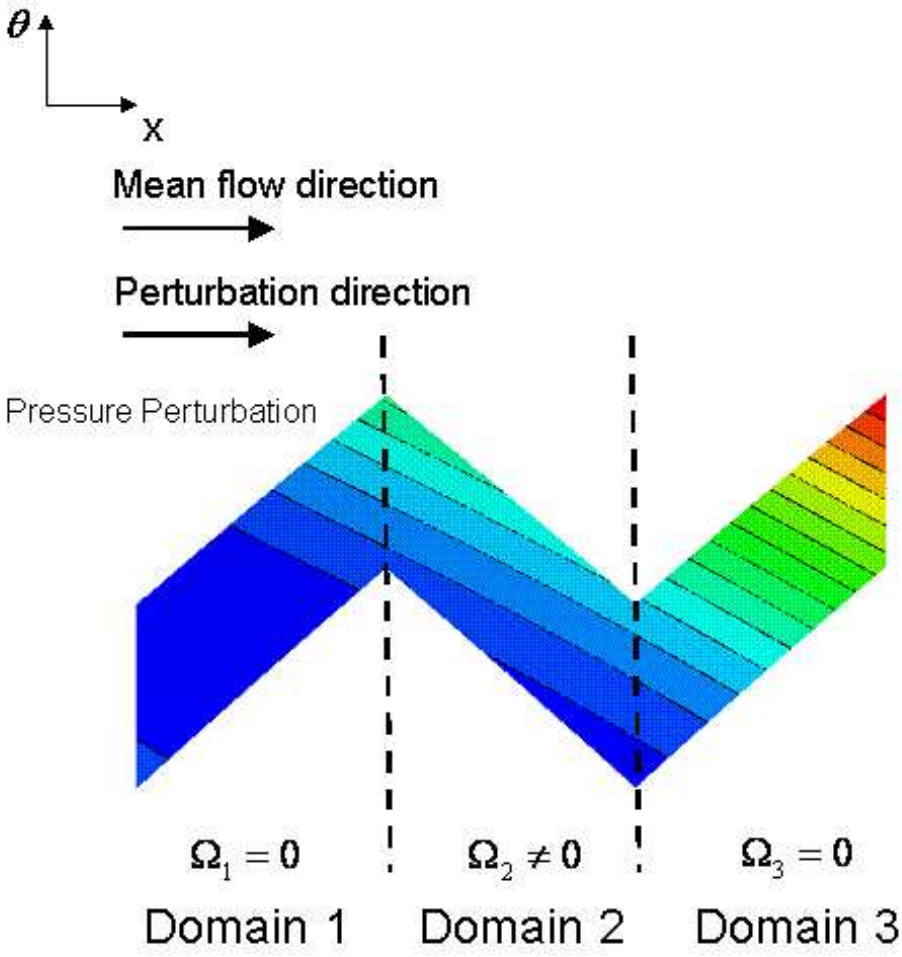

Figure 5.13: Real part of unsteady pressure for the 2-D acoustic downstream wave with non-zero swirl angle

The 2-D acoustic downstream cut-on mode which was used in the previous study was again imposed at the inlet of the first domain and is expected to propagate from left to right. This time, the wave's fundamental mode - i.e. the mode imposed at the inlet of the first domain - is expected to scatter into several modes due to the presence of the blades. However, the amplitude of the wave is expected to remain unchanged at the axial locations between the blade-rows where there are no blades.

The computed real part of unsteady pressure is presented in Fig. 5.15. The contours are no longer continuous between the blade-rows. The reason is that the blades have scattered the fundamental acoustic mode into several modes but only the fundamental acoustic mode can propagate across the blade-rows. The amplitudes of the fundamental acoustic downstream and upstream modes were measured in the axial locations between the blade-rows and are presented in Fig. 5.16. As expected, the amplitudes of these two modes are constant at the inter-row regions.

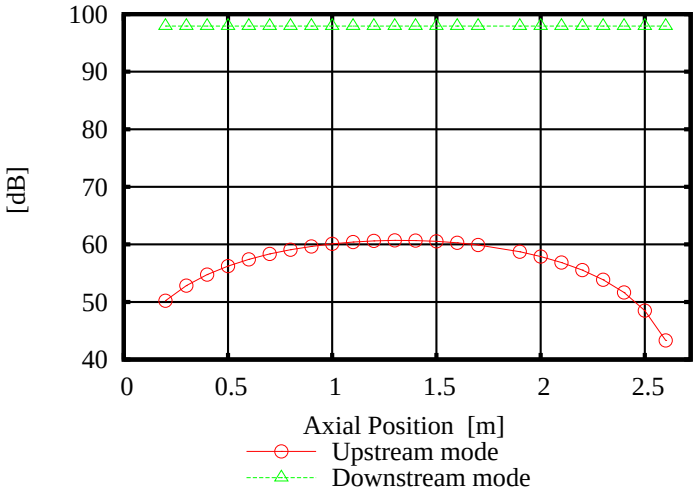

Figure 5.14: Computed amplitude of 2-D acoustic downstream mode above a mean flow with non-zero swirl angle, with corresponding reflected acoustic upstream mode. Three flow domains with interfaces at x = 0.9 and x = 1.8 represented in Fig. 5.13

In this case, the acoustic upstream mode is not due to numerical reflections, but to the scattering effects from the blades. As a result, the amplitude of the upstream mode is of the same order of magnitude as the corresponding downstream mode. The low amplitude level of the upstream mode recorded near the outlet boundary of the last domain clearly indicates that the level of numerical reflections is very small compared to the true amplitude. Even though no reference solution for this case is available, the present numerical solution is intuitively correct, which goes some way towards a validation.

5.3.2 Cut-off Modes

This test case uses the last two domains of the above geometry without the blades. The first domain is rotating while the second one is stationary ($\Omega_1 \neq 0, \Omega_2 = 0$).

A cut-off 2-D acoustic downstream wave is imposed at the inlet of the first domain and is expected to propagate from left to right. For these flow conditions, the imaginary part of the axial wave number for this wave is equal to 1.606875, which means that we expect to see the wave's amplitude to decay at a rate of 13.957 dB/m.

The real and imaginary parts of unsteady pressure are presented in Fig. 5.17. The pressure contours are completely different compared to those of the cut-on modes. Here, the iso-pressure contours propagate as "ellipses" away from the source of

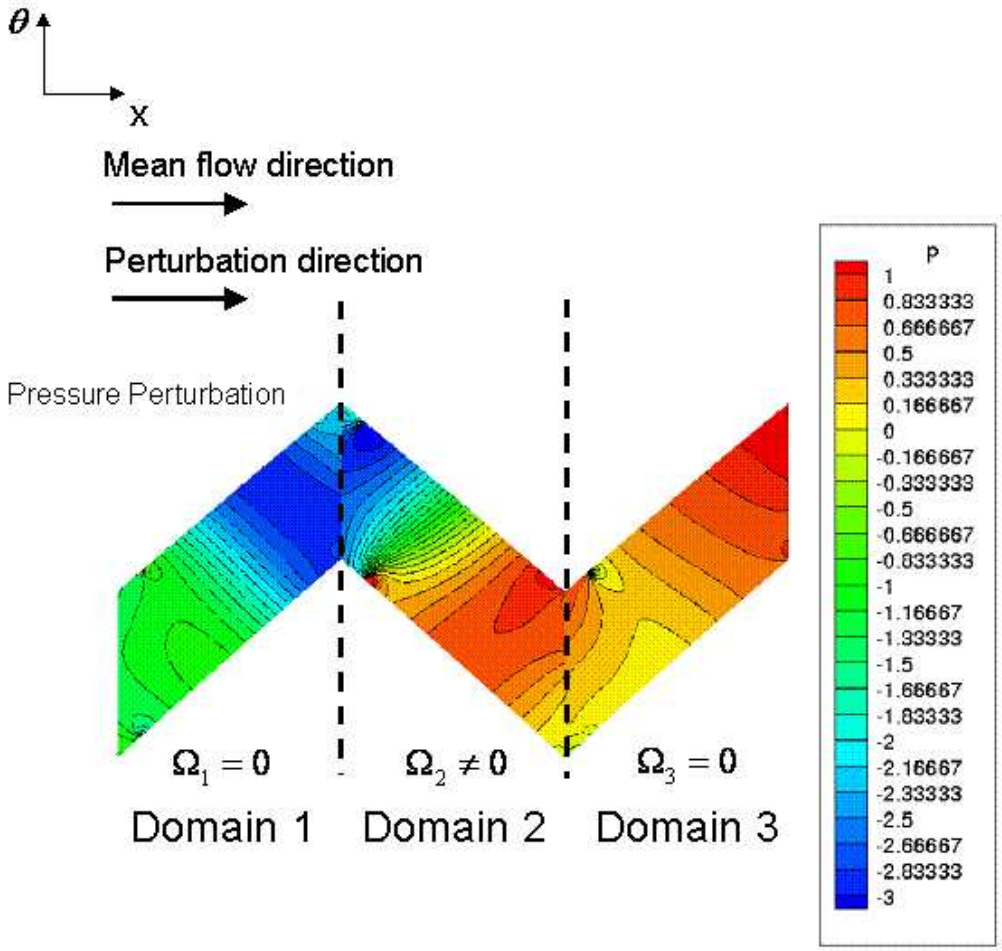

Figure 5.15: Real part of unsteady pressure normalised by reference mean pressure (101300 Pa) - 2-D acoustic downstream wave with non-zero swirl angle

excitation, which is full domain inlet plane. Note that the iso-pressure contours would be represented by perfect circles if the source of excitation was a single point instead.

The amplitudes of the imposed acoustic downstream wave and of the corresponding numerically reflected wave going upstream are plotted in Fig. 5.18. The amplitude of the downstream wave propagates across the two domains without any noticeable distortion and with a perfect linear decay on this scale. The computed decay rate of the downstream mode is 13.957 dB/m, which is exactly the theoretical value. One can also see that the reflected wave's amplitude is about 50 dB lower than that of the imposed wave, which demonstrates the excellent quality of this solution.

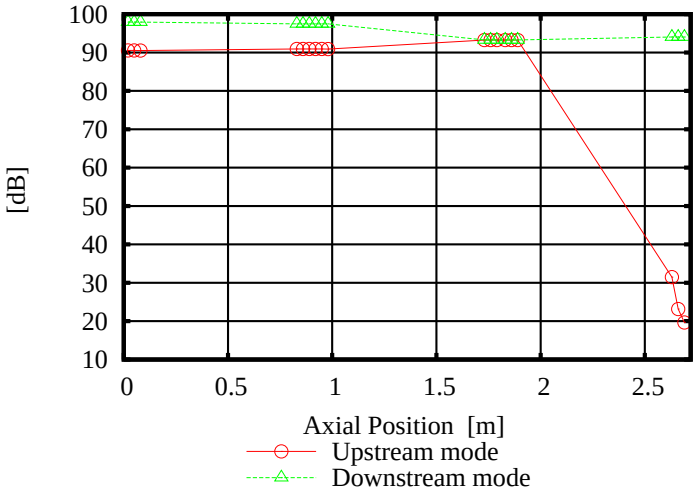

Figure 5.16: Computed amplitude of 2-D acoustic downstream wave with non-zero swirl angle with corresponding reflected acoustic upstream mode. Three flow domains with blades and interfaces at x = 0.9 and x = 1.8 represented in Fig. 5.15

5.4 The Special Case of Waves with Negative Frequencies

Consider the flow attached to a blade-row rotating at speed Ω_1. If this flow is subject to an excitation at frequency ω_1 and IBPA σ_1 (or nodal diameter $k_1 = B_1\sigma_1/2\pi$) in the relative frame, any wave associated with the circumferential mode n_1 will propagate from this flow into the next stationary blade-row at frequency $\omega_2 = \omega_1 - (k_1 + n_1 B_1)\Omega_1$. The frequency ω_2 in the absolute frame can thus be negative for $\omega_1 < (k_1 + n_1 B_1)\Omega_1$. Hence a fundamental question becomes: "Can this situation cause a problem for the numerical scheme developed in this thesis?". The answer is "no", and the reasons are explained below.

To validate a numerical scheme with wave propagation with negative frequencies in some blade-rows, two fundamental aspects need to be considered: (i) the inter-row boundary condition; (ii) the numerical solution scheme for each domain.

In the present code, the inter-row boundary condition is not affected by negative frequencies since the choice of the upstream and downstream travelling waves is made upon the sign of the imaginary part of the axial wave number (see Chapter 4 for more details). The direction of propagation for each wave is dictated by the sign of this value irrespective of the sign of the frequency. A decaying mode in one direction must travel in that direction, otherwise it would be growing exponentially

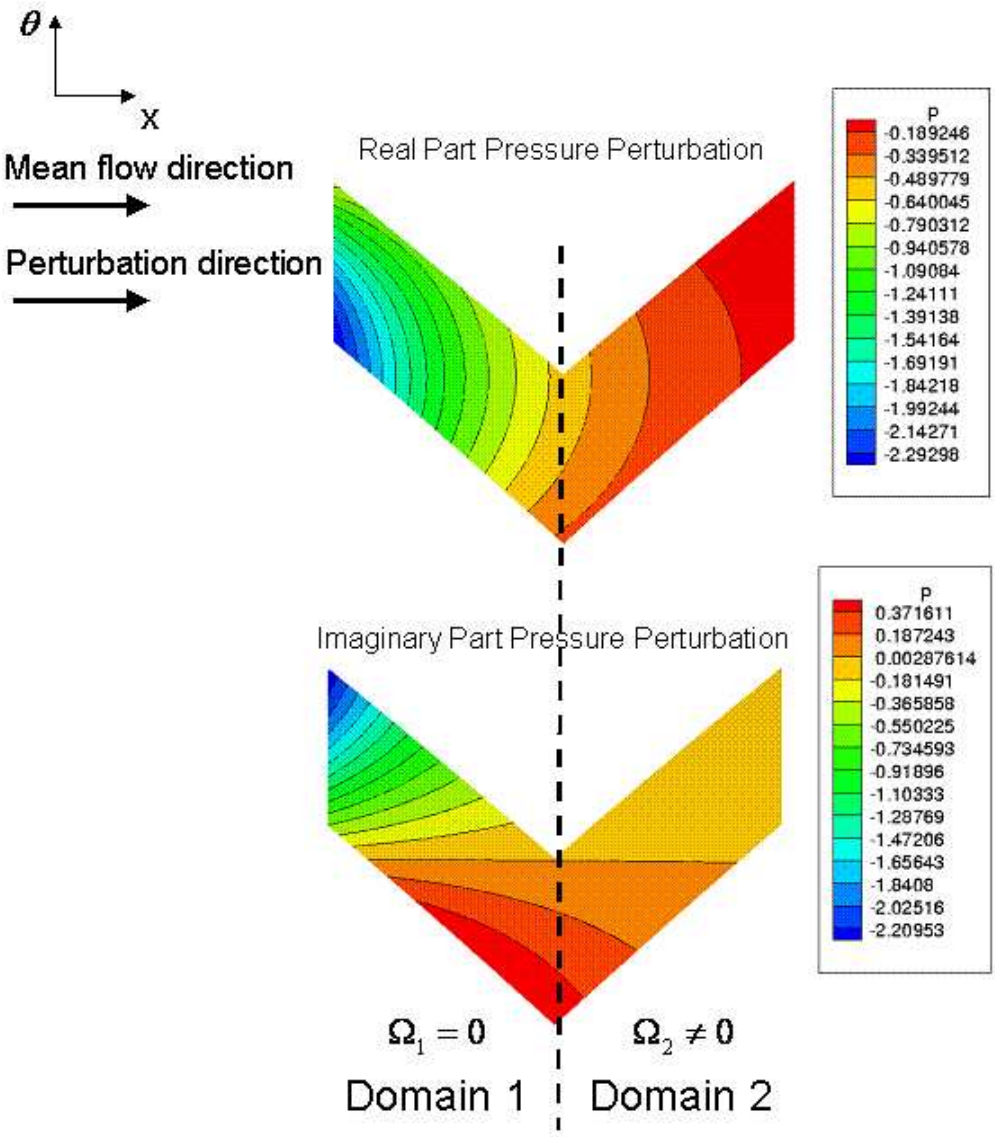

Figure 5.17: Real part and imaginary part of unsteady pressure normalised by reference mean pressure (101300 Pa) - 2-D acoustic downstream cut-off wave with non-zero swirl angle

without any physical reason which could justify such behaviour.

In order to verify that the numerical scheme can handle negative frequencies, the following mathematical result pointed out by Giles [34] is used: *the harmonic linearised solution of the governing equations to a problem in which the original excitation varies with frequency ω and IBPA σ, is the complex conjugate of the solution to the "mirror" problem for which the original excitation varies at frequency $-\omega$ and IBPA $-\sigma$.* Therefore, one way to avoid negative frequencies is to compute the solutions with positive frequencies by reversing the sign of the corresponding IBPA. However, the inter-row boundary condition must be slightly modified in the

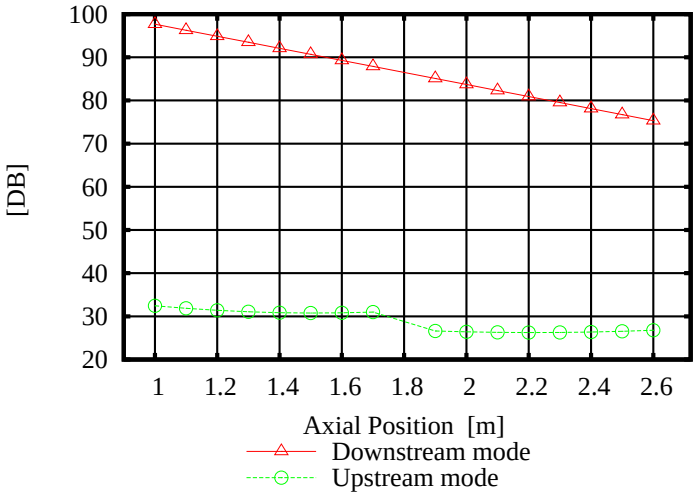

Figure 5.18: Computed amplitude of a cut-off 2-D acoustic downstream mode with non-zero swirl angle with corresponding reflected acoustic upstream mode. Two flow domains with interface at x = 1.8 represented in Fig. 5.17

harmonic linearised multi blade-row solver if positive frequencies are to be used in places of negative frequencies. To explain this further, consider the test case above where a cut-off acoustic downstream wave was propagated across two blade-rows. This case is particularly interesting because the frequency of the cut-off mode considered in this study was in fact negative in the frame of the second domain. The fact that this cut-off mode propagated across the two domains without attenuation already indicates that the numerical model can handle negative frequencies. However, the same test case is now re-visited for completeness to obtain the propagated wave solution in the second domain with a positive frequency and reverse-sign of IBPA. By doing so, we must ensure that the correct circumferential wave number is allowed to propagate across the blade-rows. The communication between Domains 1 and 2 can be expressed as follows:

$$(\omega_1, \sigma_1, n_1) \leftrightarrow (\omega_2, \sigma_2, n_2)$$

If ω_2 and σ_2 are to be replaced by $-\omega_2$ and $-\sigma_2$, then n_2 must also be replaced $-n_2$.

- Proof: Consider that $\hat{\mathbf{U}}_1$ is the harmonic linearised solution at frequency ω_1 and IBPA σ_1 in the first domain, and that $\hat{\mathbf{U}}_2$ is the harmonic linearised solution at frequency $\omega_2 < 0$ and IBPA σ_2. At the inter-row boundary the solution $\hat{\mathbf{U}}_1$ can be decomposed into a Fourier series as

follows:

$$\hat{\mathbf{U}}_1 = \sum_{n_1} \hat{\mathbf{U}}_{1,n_1} . e^{\frac{i(\sigma_1 + 2\pi n_1)}{P_1}\theta}$$

where

$$\hat{\mathbf{U}}_{1,n_1} = \frac{1}{P_1} \int_{P_1} \hat{\mathbf{U}}_1 . e^{\frac{-i(\sigma_1 + 2\pi n_1)}{P_1}\theta} d\theta$$

In the same manner, the solution $\hat{\mathbf{U}}_2$ can be decomposed into a Fourier series as follows:

$$\hat{\mathbf{U}}_2 = \sum_{n_2} \hat{\mathbf{U}}_{2,n_2} . e^{\frac{i(\sigma_2 + 2\pi n_2)}{P_2}\theta}$$

where

$$\hat{\mathbf{U}}_{2,n_2} = \frac{1}{P_2} \int_{P_2} \hat{\mathbf{U}}_2 . e^{\frac{-i(\sigma_2 + 2\pi n_2)}{P_2}\theta} d\theta$$

At the inter-row boundary, the following equality is verified:

$$\hat{\mathbf{U}}_{1,n_1} . e^{\frac{i(\sigma_1 + 2\pi n_1)}{P_1}\theta} = \hat{\mathbf{U}}_{2,n_2} . e^{\frac{i(\sigma_2 + 2\pi n_2)}{P_2}\theta} \tag{5.4.1}$$

If σ_2 is replaced by $-\sigma_2$, then if we choose to also replace n_2 by $-n_2$, it becomes clear that the new right hand terms of (5.4.1) are equal to the complex conjugate of the left hand side terms:

$$\hat{\mathbf{U}}_{1,n_1} . e^{\frac{-i(\sigma_1 + 2\pi n_1)}{P_1}\theta} = \hat{\mathbf{U}}_2 . e^{\frac{i(-\sigma_2 - 2\pi n_2)}{P_2}\theta}$$

Using this result, the communication between Domains 1 and 2 becomes:

$$(\omega_1, \sigma_1, n_1)^* \leftrightarrow (-\omega_2, -\sigma_2, -n_2)$$

The harmonic linearised multi blade-row calculation was re-made using the parameters $(-\omega_2, -\sigma_2, -n_2)$ in the second domain. The computed contours of real and imaginary parts of unsteady pressures are presented in Fig. 5.19. By comparing Figs. 5.17 and 5.19, it can be seen that the two solutions are exactly the complex conjugate of one another. This result is a proof that the present numerical model propagates correctly waves in multi blade-row domains, even when negative frequencies are involved in some of the domains.

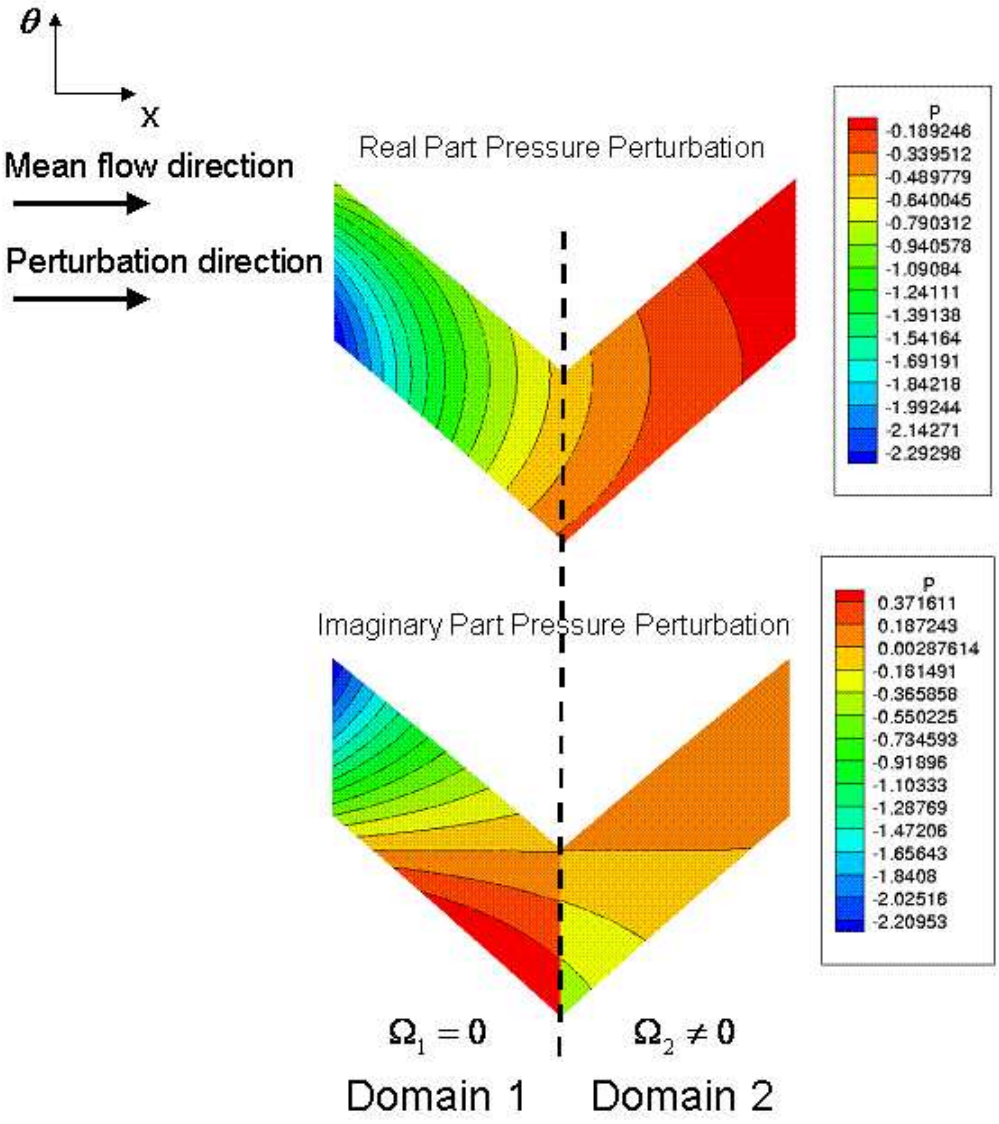

Figure 5.19: Real part and imaginary part of unsteady pressure normalised by the reference mean pressure (101300 Pa) - 2-D acoustic downstream cut-off wave with non-zero swirl angle

5.5 Conclusions for Chapter 5

Several types of waves were forced to propagate in uniform subsonic non-swirling and swirling mean flows across several domains some of which were rotating. Since the axial and circumferential wave numbers are not changed in relative frames, analytical solutions can be used to assess the accuracy of the inter-row boundary condition associated with the harmonic linearised multi blade-row method. The main findings of this chapter are listed below:

- For a given circumferential wave number 2-D and 3-D acoustic, vortical, and entropic waves are correctly transmitted between sub-domains using this inter-row boundary condition.
- When several circumferential wave numbers are present, these are correctly separated and passed onto the next domain with appropriate frequencies.
- Cut-on and cut-off acoustic waves are successfully transmitted between sub-domains without distortion or attenuation.
- All the test cases studied by the author, some not reported here, showed excellent agreements with available analytical solutions.
- The special case of waves with negative frequencies in absolute frame is discussed. It is demonstrated that this special case is not causing any particular problems in the present solver.
- Stator wakes are essentially made of waves, hence the test cases studied in this chapter also serve as validation cases for wake-interaction analysis since no analytical solutions are available to assess the validity of the present method for real turbomachineries configuration.
- Finally, the author believes that the present solver can be used as a valuable tool to study the propagation of sound in turbomachinery multi blade-rows. No tool of comparable accuracy exists at the time of writing this thesis. It should also be emphasized that linearised methods solve the perturbation directly, hence they are much less dissipative than other nonlinear methods.

Chapter 6

Flutter Analysis of Cascades of Flat Plates

6.1 Introduction

This chapter presents the flutter analysis of a multi blade-row test case. The particular geometry and flow conditions selected for this study are such that exact semi-analytical solutions exist for the corresponding isolated blade-row problem. Acoustic resonances are also present for a couple of inter-blade phase angles. This test case was originally introduced by Ekici and Hall [39], where the authors presented the first time-linearised multi blade-row solution for a bending flutter case. This solution will therefore serve as a reference to evaluate the accuracy of the harmonic linearised multi blade-row solver developed in this thesis. First, the present work analyses the influence of several spinning modes in determining the blade lift coefficient. Second, the analysis looks at the importance of the axial gap on multi blade-row interaction. Finally, the effect of multi blade-row interaction on acoustic resonance is discussed.

6.2 Harmonic Isolated Flutter Analysis

6.2.1 Flow Conditions

In this section, the flow past a two-dimensional annular cascade of blades is analysed, where the flow solution is determined within a thin layer at a particular radius position R. Within this thin layer, the flow is considered to be two-dimensional. The

cascade is rotating at speed Ω. The flow entering the cascade is uniform, subsonic, with relative Mach number M = 0.7. Viscous effects are completely neglected in this study, and thus the Euler equations are used to approximate the flow behaviour. The blades are represented by flat plates that have no thickness. The blade chord has a unit length ($c = 1$), and the pitch-to-chord ratio is $\frac{P \times R}{c} = 0.75$, where P is the circumferential pitch (in rad). The blade profile and stagger-angle have been chosen such that the flow enters the cascade with no incidence to the blade, and thus the flow does not turn. Consequently, the mean blade lift is equal to zero.

Under these conditions, the unsteady part of the flow plays a major role in the overall aerodynamics of the cascade and, in particular, in the blade lift coefficient. In this work, a flutter problem in which blades vibrate either in bending or torsional motion is studied. Particular emphasis is placed on the role played by the inter-blade phase angle on the blade lift coefficient.

Blade-row	Rotor
Number of blades	72
Blade chord	1
Stagger angle	-45^o
Mach Number	0.7
$\mid \Omega R \mid$	1.41421
Frequency	$\omega_0 = 1$ rad/s
Inter-blade phase angle	$-180^o \leq \sigma \leq 180^o$

Table 6.1: Geometric parameters and flow conditions for isolated blade-row analysis

An overview of the flow conditions and geometric parameters is given in Table 6.1. A point of interest is the determination of the acoustic resonances. Appendix A describes the theory that is used to model the occurrence of acoustic resonance for the case of two-dimensional, inviscid, and uniform mean flows. Applying this theory to the flow conditions presented in Table 6.1, provides two wave numbers k for which acoustic resonance can occur. These are given by:

$$k_{1,2} = -\frac{k_{\theta 0}}{R} \times (M_{\theta 0} \pm \sqrt{1 - M_{x0}^2}), \tag{6.2.1}$$

where $k_{\theta 0}$ is the circumferential wave number of the fundamental acoustic mode. M_{x0} and $M_{\theta 0}$ are respectively the mean flow Mach number in the axial and circumferential directions. If c_0 represents the speed of sound of the mean flow, and noticing that:

$$\begin{aligned} k &= \tfrac{\omega_0}{c_0}, \\ k_{\theta 0} &= \tfrac{\sigma}{P} \end{aligned} \tag{6.2.2}$$

The two inter-blade phase angles σ satisfying (6.2.1) are:

$$\sigma_{1,2} = \frac{\omega_0 \times P \times R}{c_0 \times (1 - M_0^2)}(M_{\theta 0} \pm \sqrt{1 - M_{x0}^2}) \tag{6.2.3}$$

The numerical values are: $\sigma_1 = -80.38^o$ and $\sigma_2 = 22.07^o$. Still referring to Appendix A, it can be concluded that when $\sigma_1 < \sigma < \sigma_2$, the fundamental acoustic mode is cut-on, i.e. it propagates without change in amplitude, whereas when $\sigma < \sigma_1$ or $\sigma > \sigma_2$, the fundamental acoustic mode is cut-off and decays exponentially as it propagates axially.

Figure 6.1 plots the axial wave numbers k_x of the fundamental acoustic modes that have been computed for the above flow conditions, and for a series of nodal diameters which are multiples of 6, i.e. -30,-24,-18,.., 24, 30. Note that nodal diameter (ND) and inter-blade phase angle are related by the relationship: $\sigma = \frac{2\pi \times ND}{B}$, where B is the number of blades in the cascade. A complex axial wave number represents a cut-off acoustic mode, while a real axial wave number represents an acoutic mode which is cut-on. From Fig. 6.1, note that the cut-off acoustic upstream and downstream modes for the positive nodal diameters decay more rapidly than for the corresponding negative nodal diameters. Finally, Fig. 6.2 presents the computed axial wave numbers of both the fundamental entropic and vortical modes, obtained for the same mean flow conditions. Note that the axial wave numbers for the entropic and vortical modes are identical and always real, which means that these modes do not decay when propagating on a uniform mean flow.

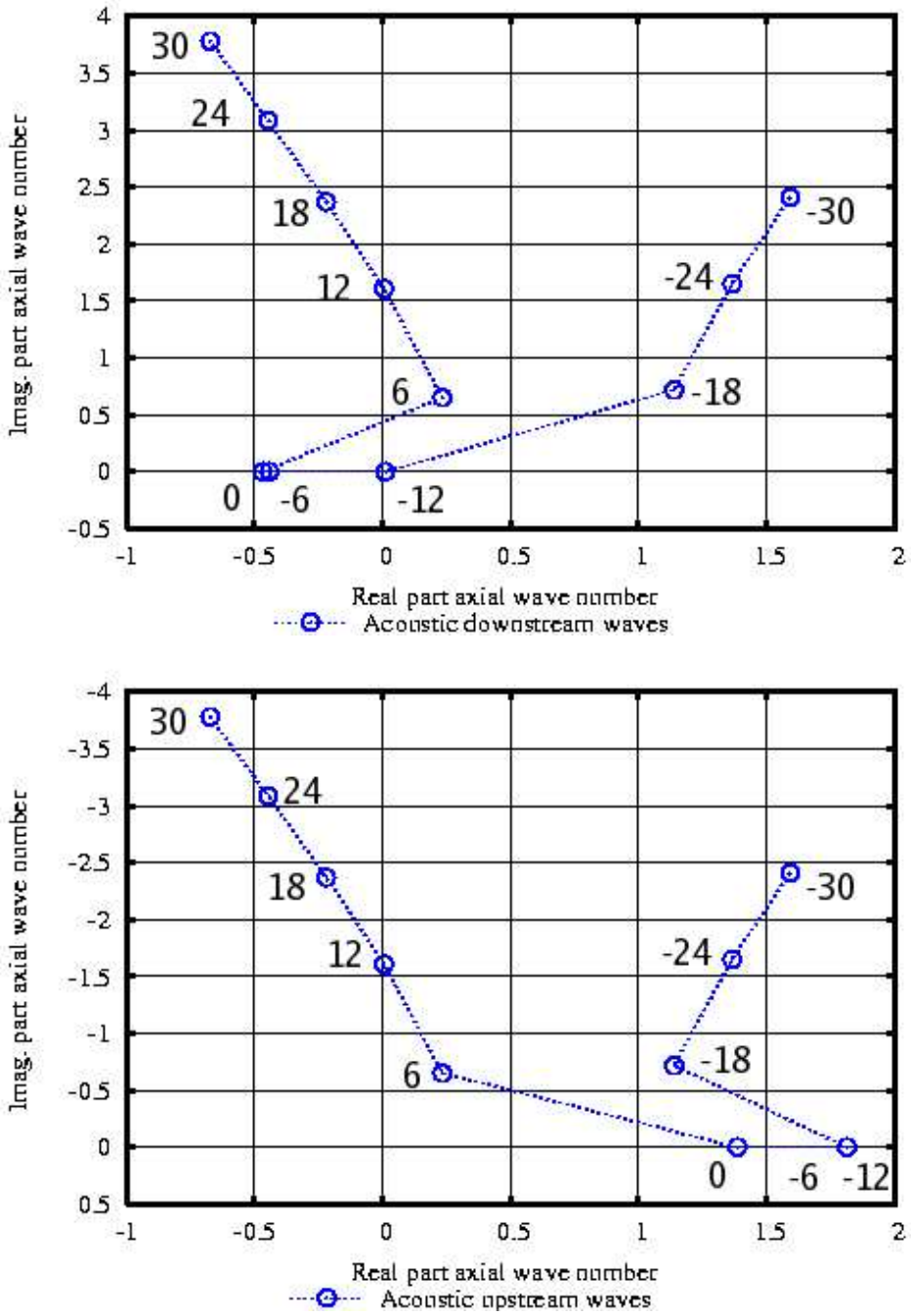

Figure 6.1: Axial wave numbers for the fundamental acoustic downstream (upper) and upstream (lower) mode

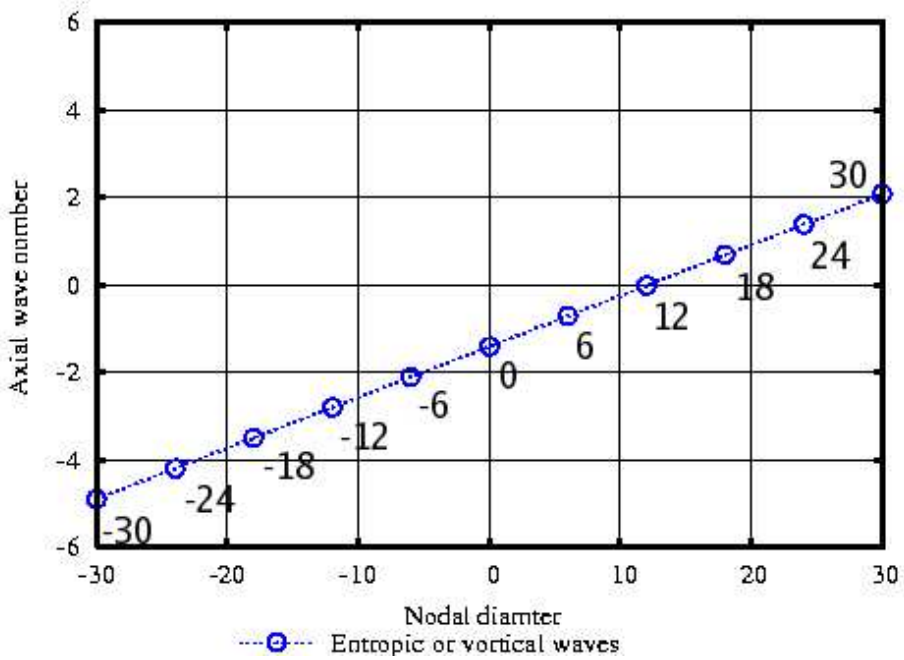

Figure 6.2: Axial wave numbers for the fundamental vortical and entropic modes

6.2.2 Computational Mesh

The computational mesh represents a single blade-passage and was designed to deal with two important aspects of the present case:

- The blade has no thickness. Thus to avoid any singularity problems at the leading or trailing edges, the blade surface has been divided in two parts located at the periodic boundaries. The suction side of the blade is at the lower periodic boundary, while the pressure side of the next blade is at the upper periodic boundary.
- In order to assess the efficiency of the 3-D non-reflecting boundary conditions presented in Chapter 4, the two-dimensional problem is solved in a quasi 3-D manner, i.e. by applying a small radial variation to the geometry, and the far-field boundaries are positioned at 10 % chord away from the blade leading and trailing edges.

The domain geometry and computational mesh were generated using GAMBIT[1]. This mesh generation tool has been used for two main reasons. First, the application

[1]http://www.fluent.com/software/gambit/index.htm

combines a single interface for geometry creation and meshing, and second, it is a rapid and easy to-use tool for generating quasi 3-D unstructured meshes, including any mesh refinement procedures.

The mesh generated for this study is unstructured. This choice was made in order to efficiently and accurately capture the high pressure gradients caused by the sharp blade geometry that appear at the leading and trailing edges of the blades. At the same time, a far coarser mesh level was maintained near the far-field boundaries since these boundaries do not need as much mesh resolution. However, it should be mentioned that the mesh used in this study was generally fine. On average, 30 points or above were attributed per wave length. Here, the main focus was not computational efficiency, but rather accuracy in order to capture precisely all wavelengths encountered throughout the unsteady analysis. A two-dimensional view of the mesh is given in Fig. 6.4. The computational mesh comprises a total number of 38,430 points with five equi-distant radial layers. On the two-dimensional view shown in Fig. 6.4, 40 mesh points have been attributed to the inlet and outlet boundaries, and 89 points for each blade surface. Since the geometry was given a third dimension, it was also necessary to define two additional boundaries, the hub and the casing, which gives a total of eight boundaries. The boundaries and boundary conditions are shown in Table 6.4, and the corresponding number of boundary faces in Table 6.3.

No. of nodes	38430
No. of elements (prisms)	60152
No. of triangles	30076
No. of quadrilaterals	1328

Table 6.2: Statistics for flat plate mesh

Surface label	No. of Faces
hub	15038
casing	15038
inlet	160
outlet	160
upper periodic	152
lower periodic	152
upper blade	352
lower blade	352

Table 6.3: Number of faces per boundary for the flat plate mesh

Surface label	Boundary condition type
hub	Inviscid Wall
casing	Inviscid Wall
inlet	Subsonic Inflow
outlet	Subsonic Outflow
upper periodic	Periodic boundary
lower periodic	Periodic boundary
upper blade	Inviscid Wall
lower blade	Inviscid Wall

Table 6.4: Boundary conditions for the flat plate mesh

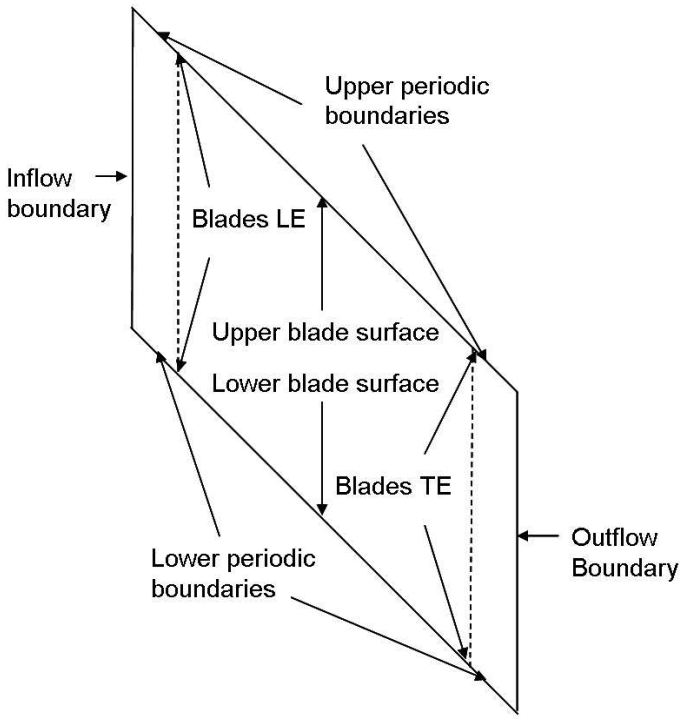

Figure 6.3: 2-D view of the boundaries used for the flat plate case

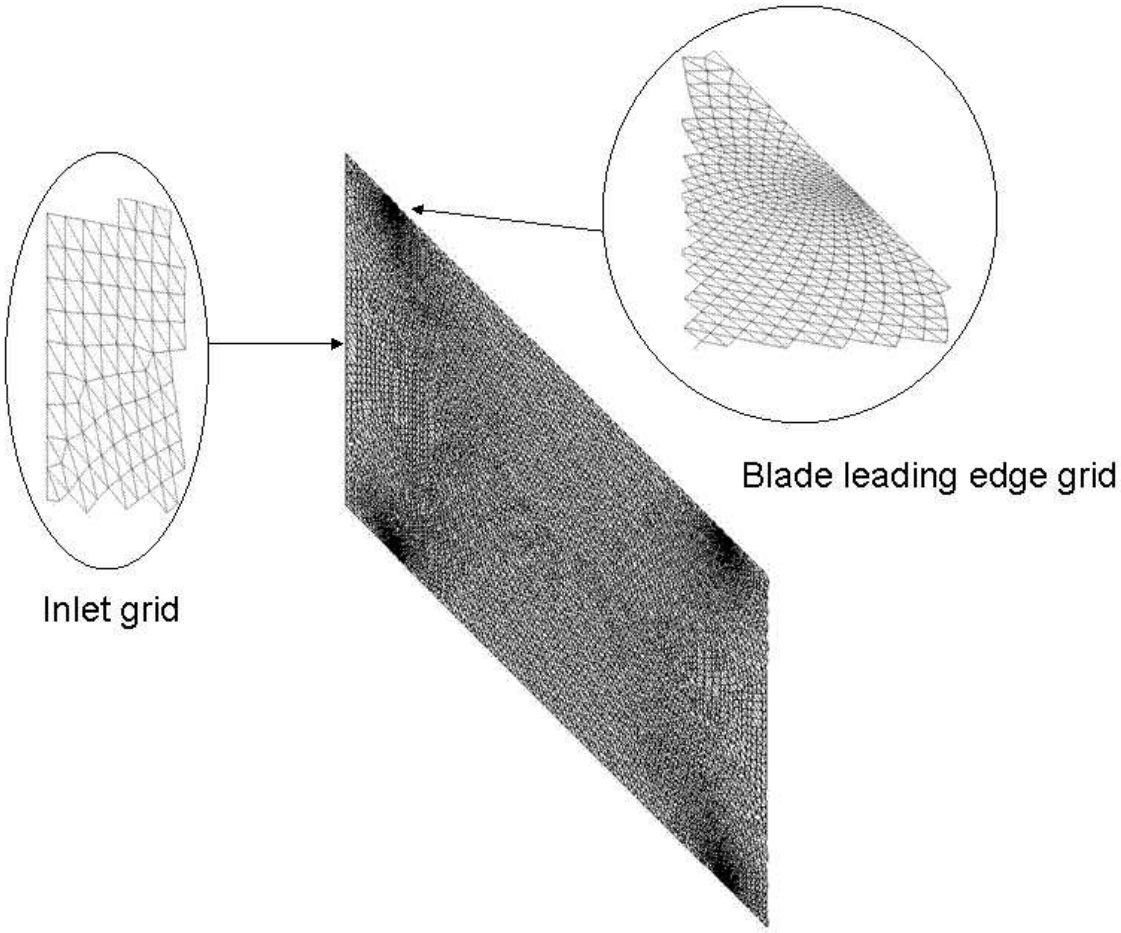

Figure 6.4: 2-D rotor mesh view

6.2.3 LINSUB Solution

The particular geometry and flow conditions defined for this test case have been chosen so that exact semi-analytical solutions for the isolated blade-row problem can be used to verify the correctness of the present frequency-domain time-linearised code.

In this work, reference semi-analytical solutions were produced by the LINSUB code of Whitehead [124]. The LINSUB code analyses unsteady two-dimensional subsonic, uniform, and isentropic flows past an infinite cascade of flat plates. The LINSUB code requires only a few input parameters:

- Two geometrical parameters: the cascade stagger-angle and the pitch-to-chord ratio

- One parameter for the description of the steady-flow conditions: the Mach number of the steady-state flow

- Two parameters of unsteadiness: the reduced frequency and the inter-blade phase angle

In addition to these inputs, LINSUB implicitly assumes unit chord length blades and a uniform mean flow of relative velocity aligned with the blade. Having inserted all these parameters, LINSUB provides unsteady flow solutions for blades vibrating in bending or torsion modes.

LINSUB analyses the flow past an infinite linear cascade of flat plates. Since the cascade is linear, it cannot rotate. However, in this work, a rotating annular cascade is analysed. Equivalence between the two problems is obtained by matching the relative Mach number and the relative velocity entering the linear and the annular cascades. The LINSUB outputs, which are useful for the present validation, are the real and imaginary parts of the harmonic pressure around the blade, calculated as a function of the axial chord. Finally, note that LINSUB can only compute solutions for isolated blade-rows, and thus it cannot be applied to multi blade-row configurations.

6.2.4 Torsional Flutter

In this first flutter case, the flat plate is assumed to vibrate in torsional motion, such that the blade normal displacement varies linearly from zero at the leading edge,

to a maximum at the trailing edge. The normal displacement imposed to the blade during vibration is defined by:

$$q_{ni} = \frac{(x - x_{le})}{cos\,(sa)}, \tag{6.2.4}$$

where x_{le} is the axial location of the blade leading edge, and sa is the stagger angle of the cascade.

It was shown in Table. 6.1 that the total number of blades in the current bladerow is 72, hence the possible nodal diameter values are within the range $-36 \leq ND \leq 36$. Because of circumferential periodicity, any nodal diameter value outside this range has an equivalent into that range. For example, the unsteady solution of the problem for $ND = 42$ is equivalent to the solution of the same problem for $ND = 42 - 72 = -30$. In this study, the unsteady problem will be solved for nodal diameters that are multiples of 6, in the range -30 to 30.

Prior to starting the unsteady calculations, the acoustic upstream radial eigenmodes that will be used for the application of the 3-D non-reflecting boundary conditions must be determined. The complete set of radial eigenmodes which are determined based on the mean flow solution, is composed of acoustic upstream, acoustic downstream, vortical, or entropic modes. During the selection of acoustic eigenmodes, the practical problem is the identification and avoidance of vortical modes. Indeed, it may happen that vorticity modes get inserted into acoustic modes during the eigenmode sorting process. The reason is that vortical modes are clustered around the same value for two-dimensional flows, their tiny imaginary parts making them seem like upstream travelling modes. In order to avoid vortical modes, a combination of two techniques is used.

First, the eigenvalues corresponding to vortical and entropic modes are identified using the theory from Appendix A and these are taken out of the sorting process. For example, consider the whole eigenvalue solutions corresponding to the problem of $ND = -30$ plotted in Fig. 6.5. We can see that most vortical and entropic modes are clustered around the same value, $\Re\,(k_v) = -\frac{k + k_{\theta 0} M_\theta / R}{M_x} \approx -4.9$. Hence, the eigenmodes corresponding to these eigenvalues are eliminated.

Second, one can distinguish between vortical and acoustic modes based on the knowledge of theoretical acoustic eigenmodes profiles. The first radial acoustic upstream and acoustic downstream eigenmodes are flat ($k_r = 0$ in Appendix B), as the steady flow insignificantly varies in the radial direction, whereas vortical eigenmodes typically vary in the radial direction with steep gradients. An example of first radial vortical eigenmode is presented in Fig. 6.6, and of first radial acoustic eigenmode

in Fig. 6.7.

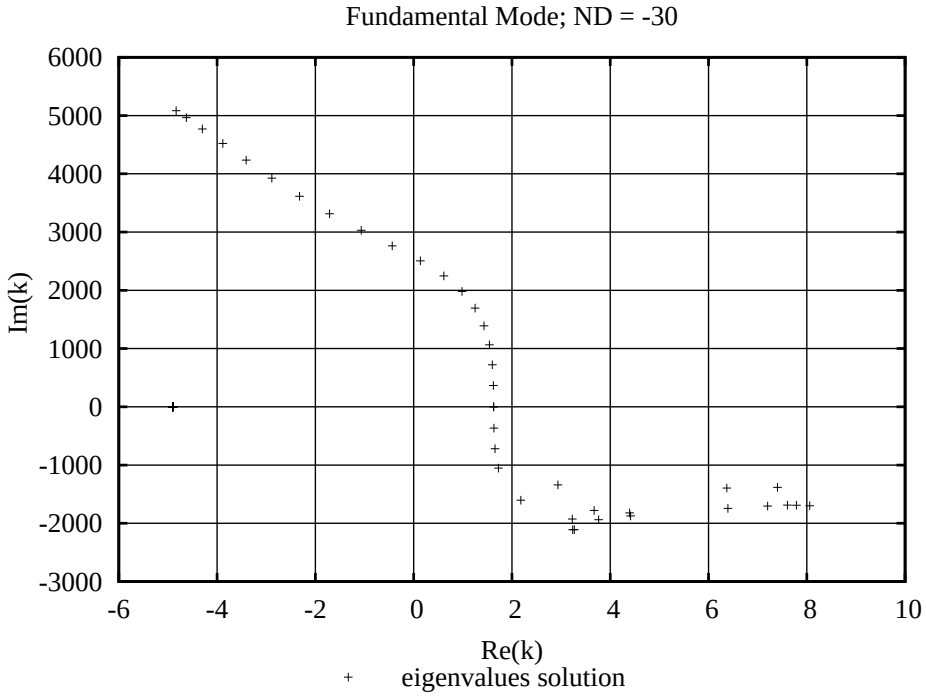

Figure 6.5: General eigenvalues solution (ND = -30)

As previously discussed, the flow conditions and blade geometry have been selected such that the steady-state lift is equal to zero. As a consequence, the unsteady lift is also the total lift. Therefore, one can determine a lift coefficient C_L based on the unsteady perturbation as follows:

$$C_L = \frac{L}{\rho U_0 \dot{q} c} \tag{6.2.5}$$

where U_0 is the relative mean flow velocity, L represents the total lift, ρ is the mean density, and $\dot{q}$ is the peak amplitude of the plunging velocity. The lift coefficients are computed using the present time-linearised code and the results are compared with those obtained by the LINSUB code in Fig. 6.8.

The agreement is excellent for all computed nodal diameters. These results prove the accuracy of the 3-D non-reflecting boundary conditions, since the far-field boundaries were positioned very close to the blade leading and trailing edges. The predicted pressure jumps around the blade are also in excellent agreement between the present code and LINSUB, though they are not shown here to be concise. A more detailed analysis will be presented for the bending flutter case.

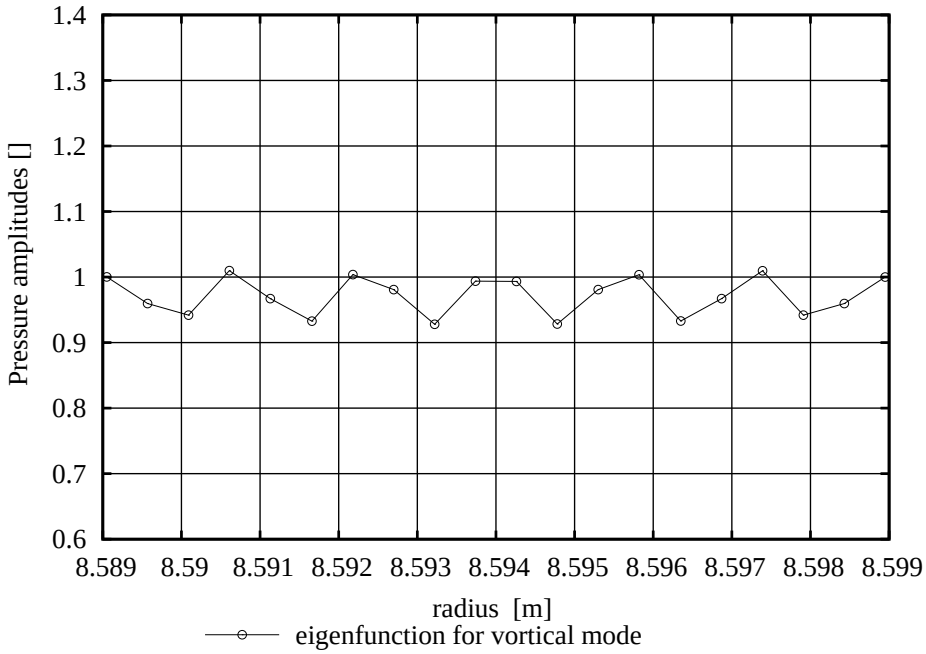

Figure 6.6: Normalised eigenvector for vortical mode eigenmode (ND = -30)

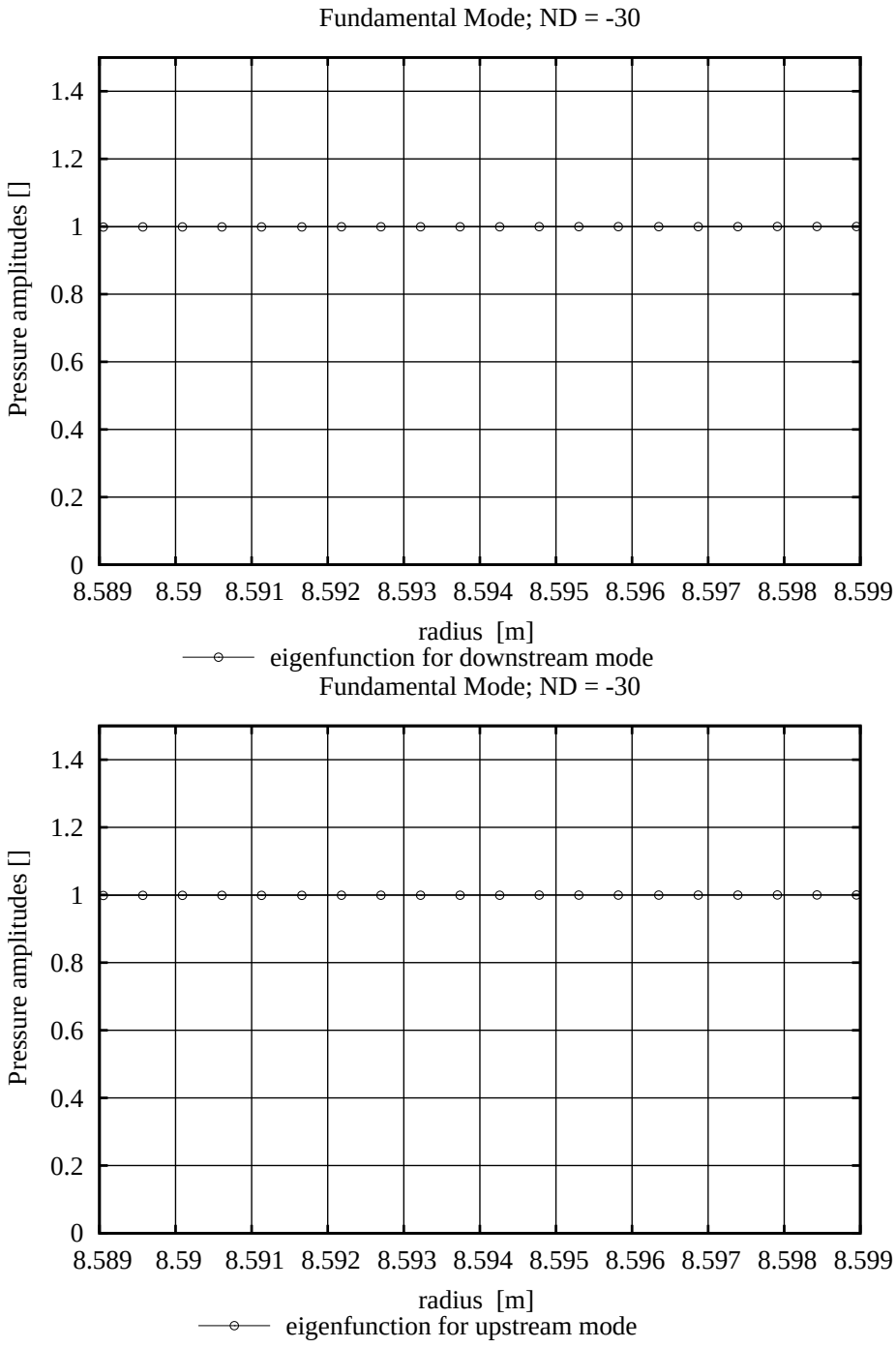

Figure 6.7: Normalised eigenvector for first acoustic downstream mode (upper) and first acoustic upstream mode (lower) (ND = -30)

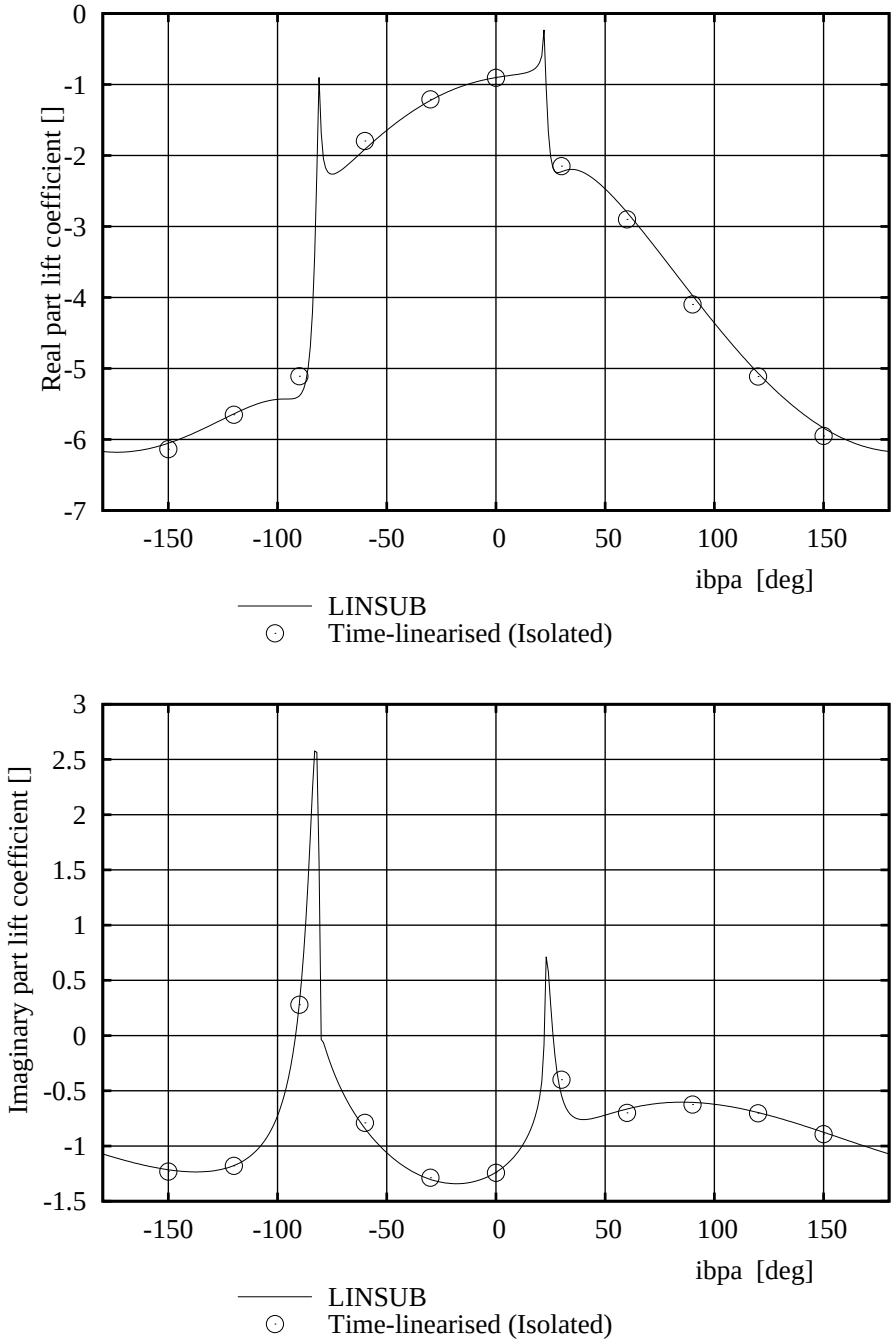

Figure 6.8: Real part (upper) and imaginary part (lower) of lift coefficient for the torsional flutter case

6.2.5 Bending Flutter

The flat plate is now vibrating in a "bending" mode as a rigid body with its displacement normal to the blade surface. The modeshape's amplitude is equal to unity in order to comply with the non-dimensional nature of the LINSUB code. Additionally, the imaginary part of the lift coefficient represents somewhat the measure of a normalised aerodynamic worksum on the rotor blades (see Eq. 8.4.5) since the vibration amplitude is equal to unity for this bending case. Since the steady flow field and the geometric parameters are the same, the radial eigenmodes for the 3-D non-reflecting boundary conditions are identical to the ones obtained for the previous torsional flutter case.

The lift coefficients and pressure jumps around the blade are computed for a range of nodal diameters, ND= -30,-24,..,30, and the results are compared with those from LINSUB. From Figs. 6.10 to 6.15, it can be seen that there is excellent agreement between the present code and LINSUB solutions. It should be noted that, at the leading edge, the semi-analytical unsteady pressure amplitude features a $\frac{1}{\sqrt{x-x_{le}}}$ singularity, which is accurately captured by the present code. Very small discrepancies are seen near the blade trailing edge, but these are unlikely to affect the accuracy of the lift coefficient plots of Fig. 6.9. In this figure, it can be seen that the LINSUB classical theory provides a couple of unsteady lift peaks. These peaks correspond to a marginal condition occurring when the waves are on the verge of propagation. This is also referred to as an acoustic resonance condition, which are discussed in Section 1.3.4 and Appendix A. At acoustic resonance, a singular term appears in the infinite series expression for the pressure field, and there is no finite solution. Two unsteady flow solutions were computed with the present code near the two acoustic resonance conditions occurring for ND = -18 and ND = 6. Both flow conditions were quite unstable, and the present code's convergence has been much slower using the 3-D non-reflecting boundary conditions. Only fine tuning of the 3-D non-reflecting boundary condition relaxation parameter allowed the solutions to be obtained.

The present harmonic linearised code can also provide a measure of the fluid acoustic response caused by the blade vibration. The response level of the first family of radial modes ($k_r = 0$), and of the fundamental circumferential modes ($k_{\theta 0} = \frac{\sigma}{P}$), is computed for each unsteady flow condition and some of the results are plotted in Figs. 6.16 to 6.19 . In these plots, the amplitude of the acoustic modes is calculated between the inflow boundary and the blade leading edge (i.e. $0 \leq x \leq 0.1$) and between the blade trailing edge and the outflow boundary (i.e. $0.8 \leq x \leq 0.9$). Note that the upstream-going mode, seen near the outflow boundary, is only a numerically reflected mode without any physical meaning. The same applies for the

downstream-going mode at the inflow boundary. Therefore, it is not surprising to see that these modes are completely distorted, as the 3-D non-reflecting boundary conditions are trying to delete them. The first important result to notice is that 3-D non-reflecting boundary conditions have been very effective in reducing the level of the reflected mode by about 50 DB. From these plots, it is easy to see which modes are cut-on, and which ones are cut-off. The modes propagating without attenuation in amplitude are the cut-on modes, and correspond to $ND > -12$ and $ND < 0$. The modes decaying exponentially, but only linearly in the present log_{10} scale, are the cut-off modes, and correspond to $ND < -12$ and $ND > 0$. Another important observation is that, as the unsteady flow nodal diameter is further away from the resonance mode, the fundamental mode decays more rapidly. One would expect this to happen as discussed in Section 6.2.1. Therefore, the present results are in agreement with the theory and thus confirm the accuracy of the present formulation.

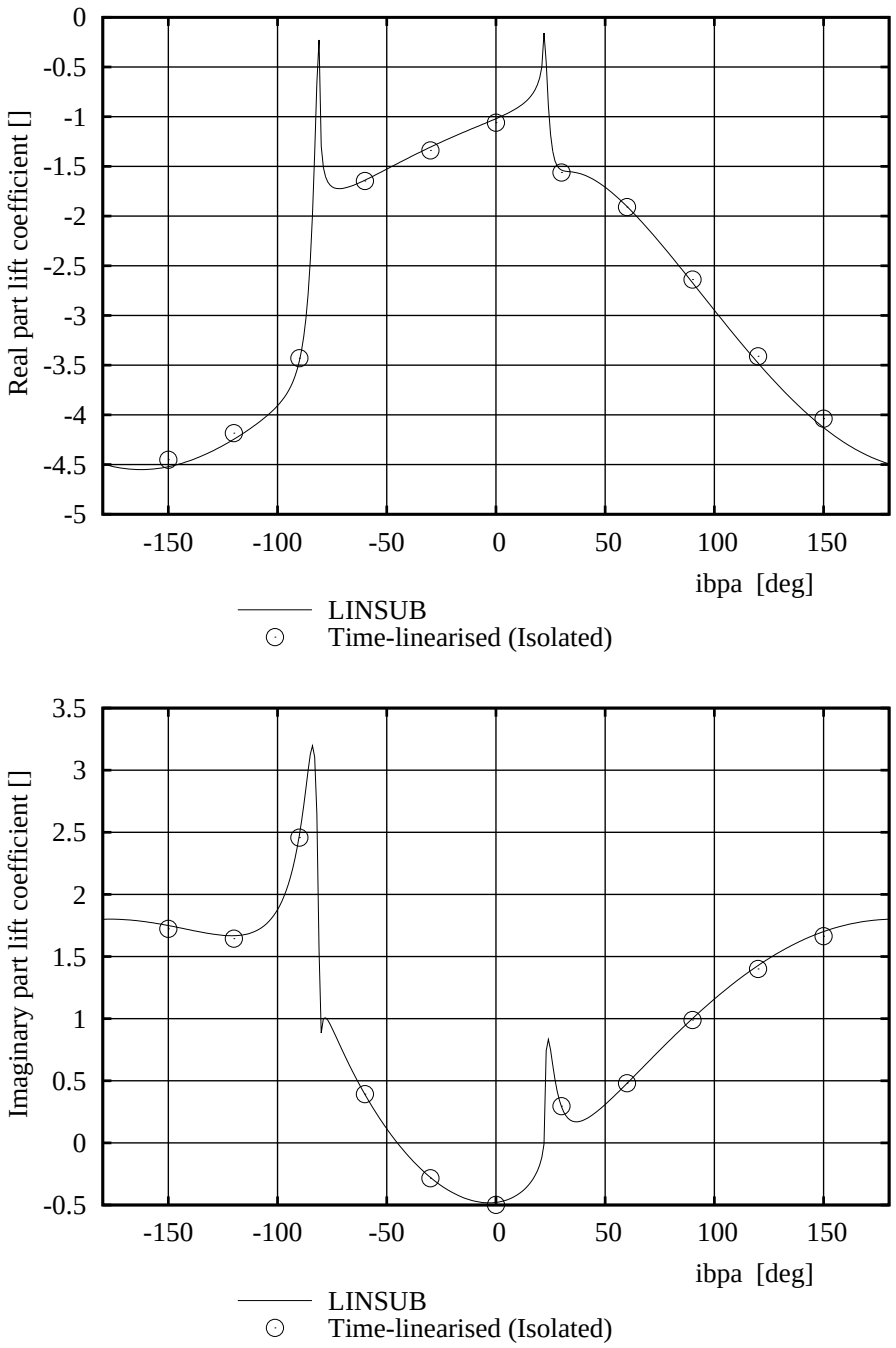

Figure 6.9: Real part (upper) and imaginary part (lower) of lift coefficient for the bending flutter case.

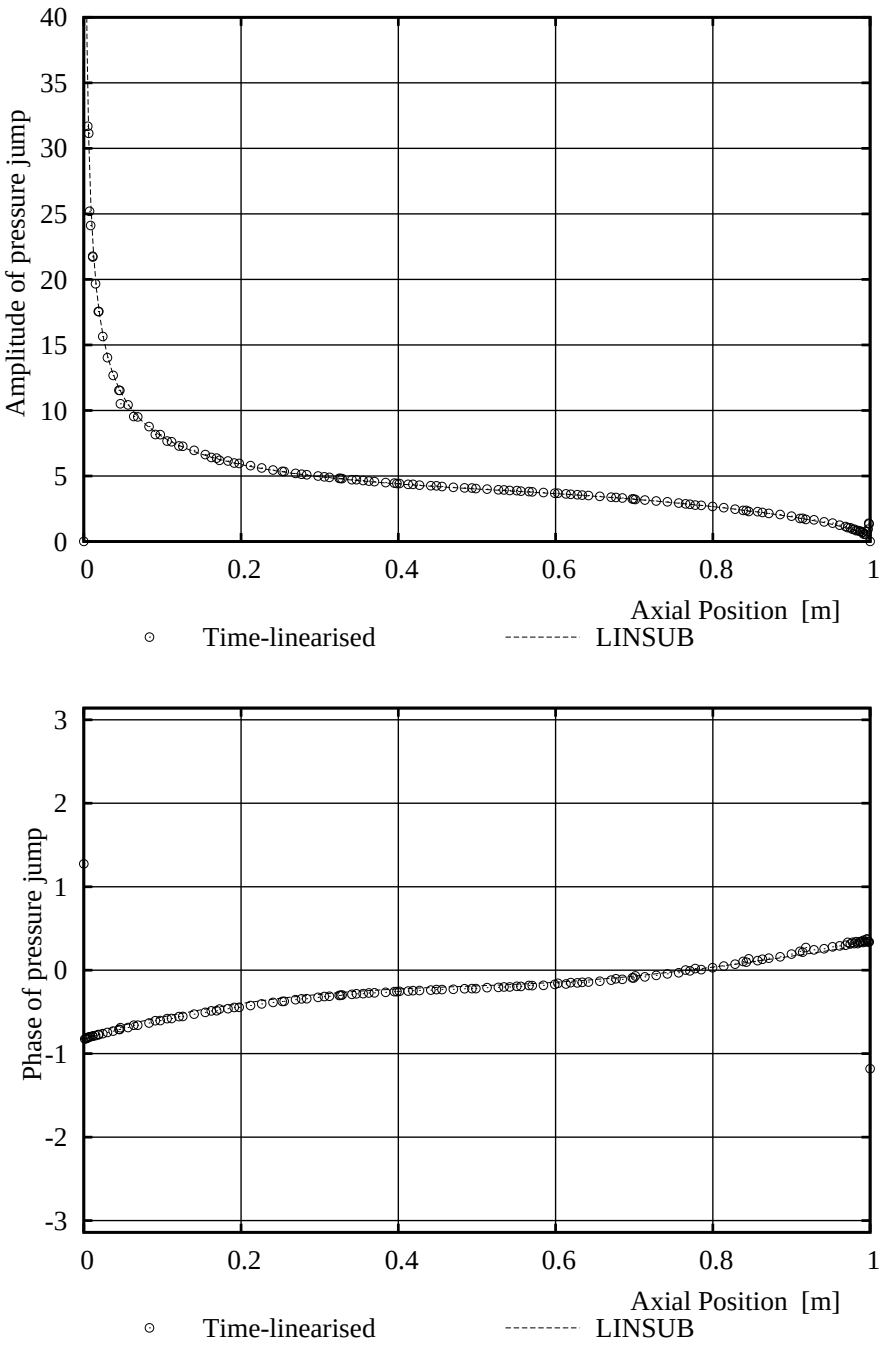

Figure 6.10: Amplitude (upper) and phase (lower) of pressure jumps around the blade for ND = -30. Harmonic linearised single blade-row versus LINSUB

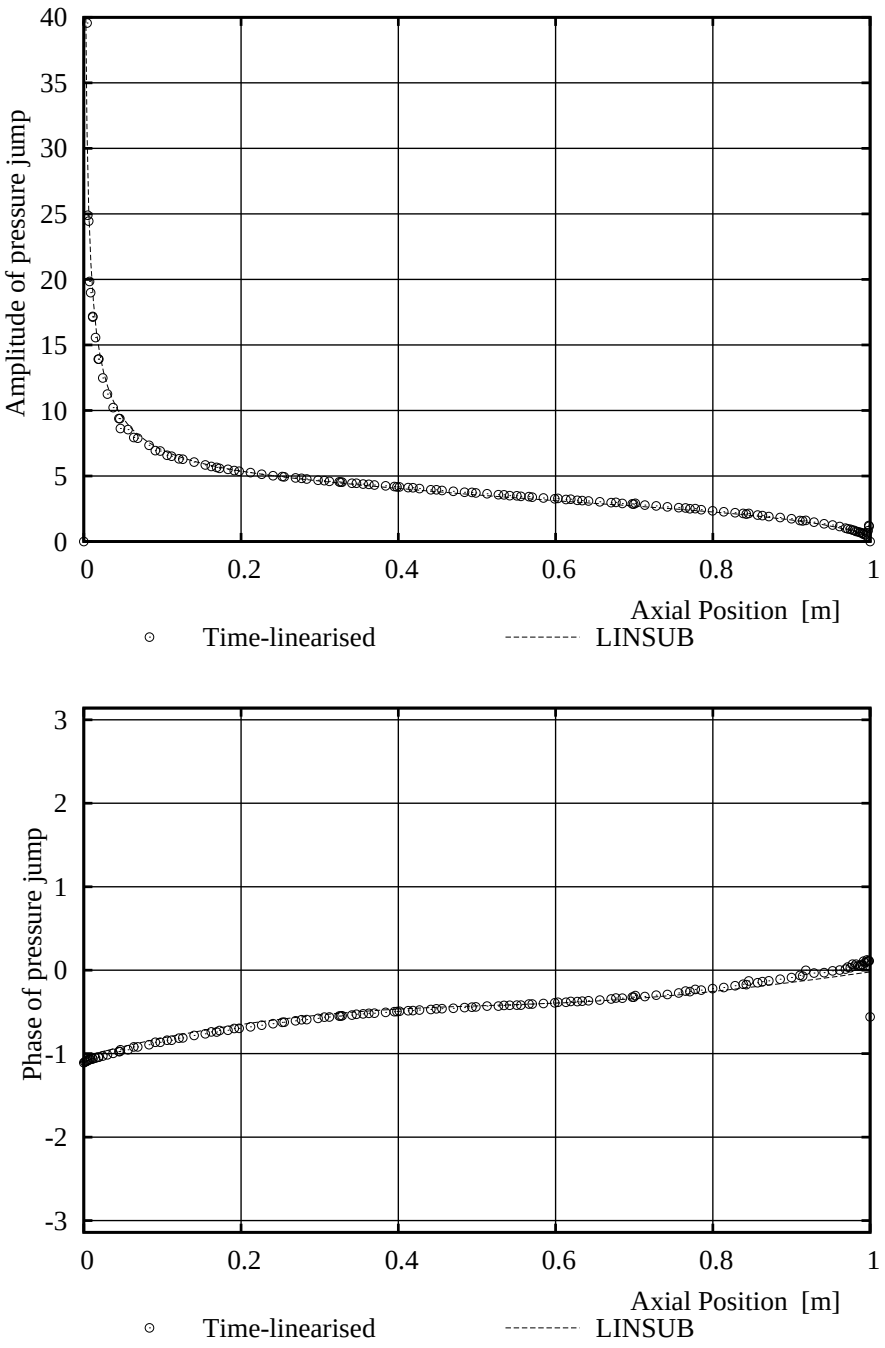

Figure 6.11: Amplitude (upper) and phase (lower) of pressure jumps around the blade for ND = -18. Harmonic linearised single blade-row versus LINSUB

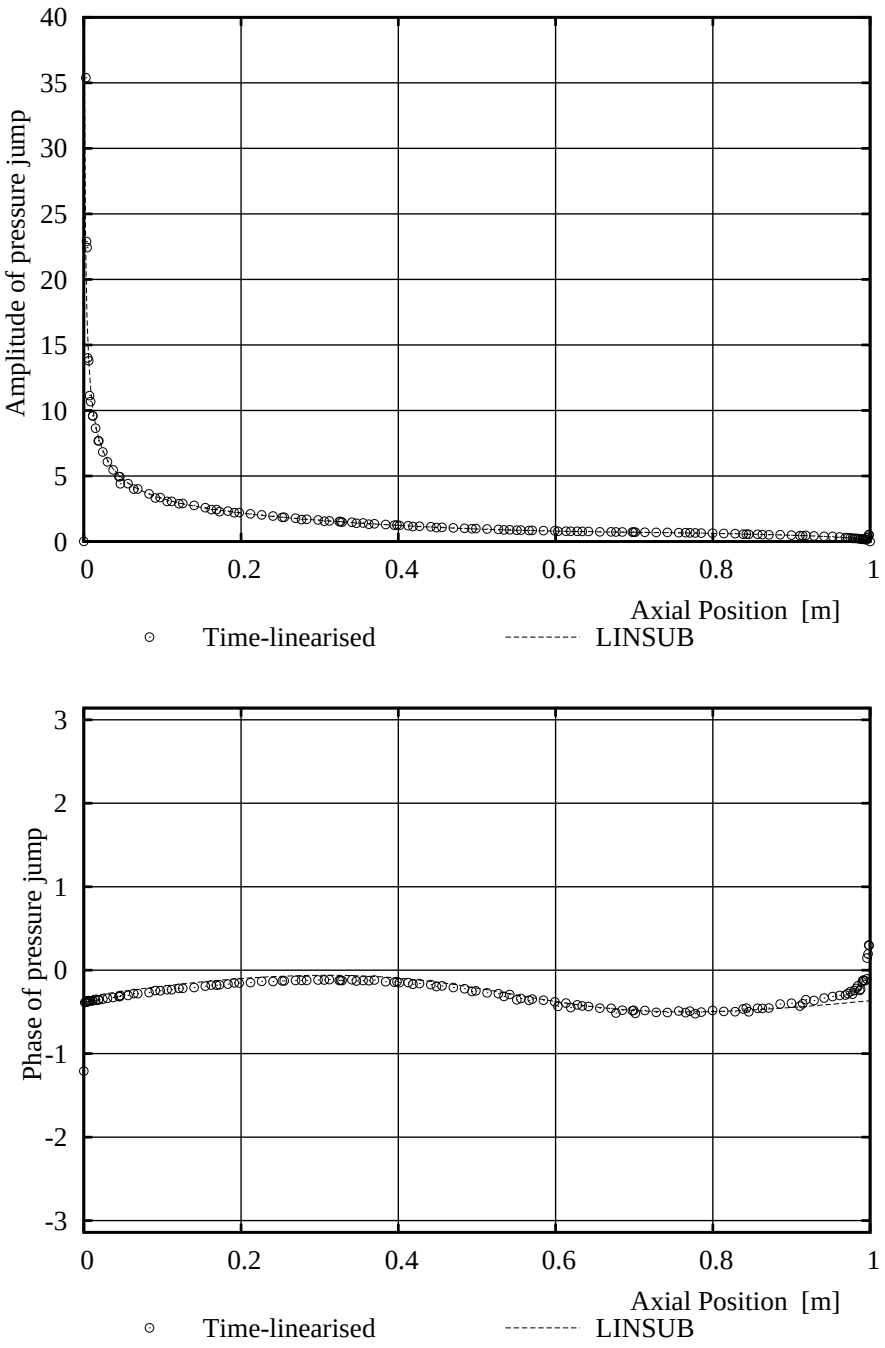

Figure 6.12: Amplitude (upper) and phase (lower) of pressure jumps around the blade for ND = -12. Harmonic linearised single blade-row versus LINSUB

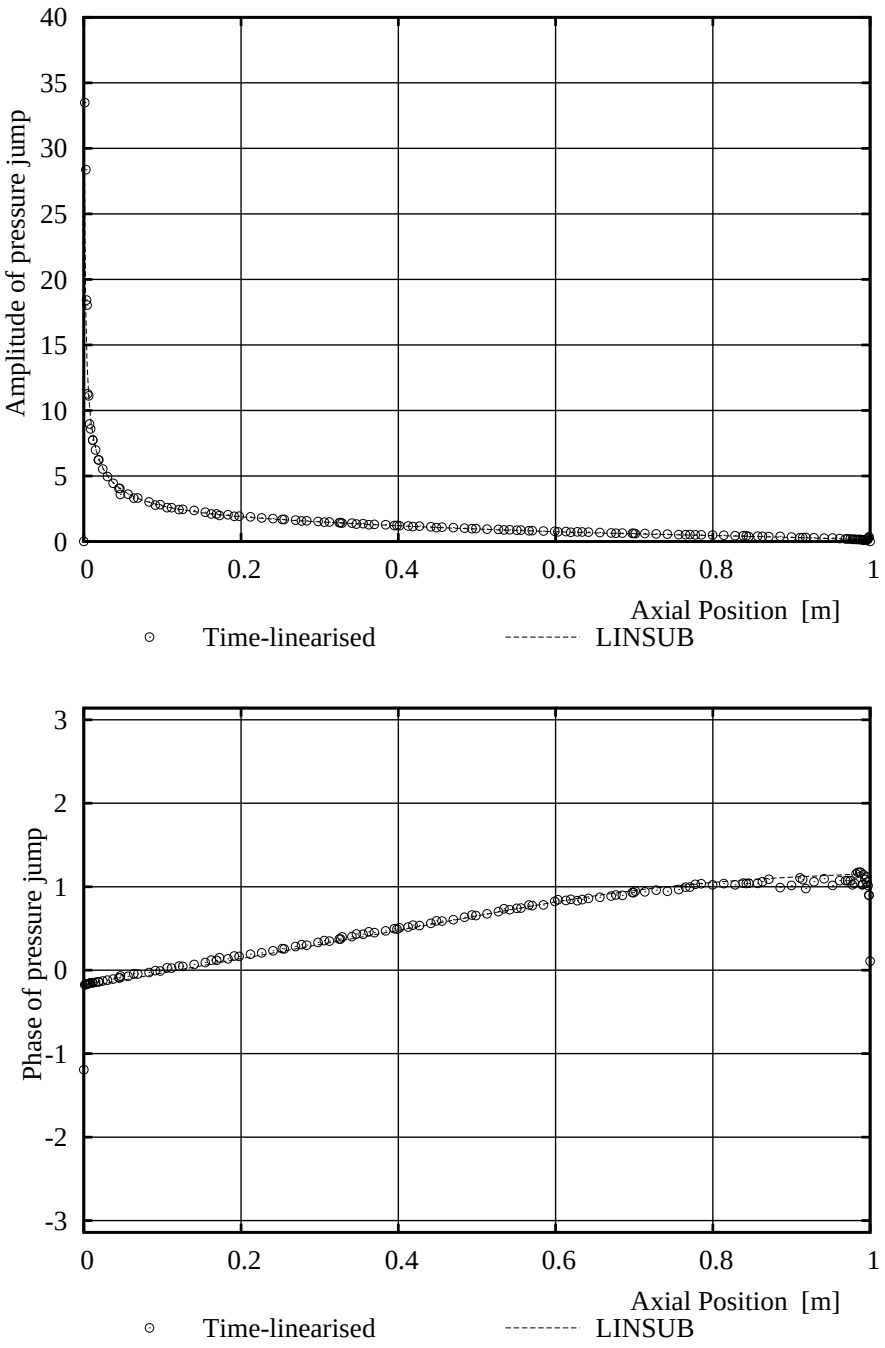

Figure 6.13: Amplitude (upper) and phase (lower) of pressure jumps around the blade for ND = -6. Harmonic linearised single blade-row versus LINSUB

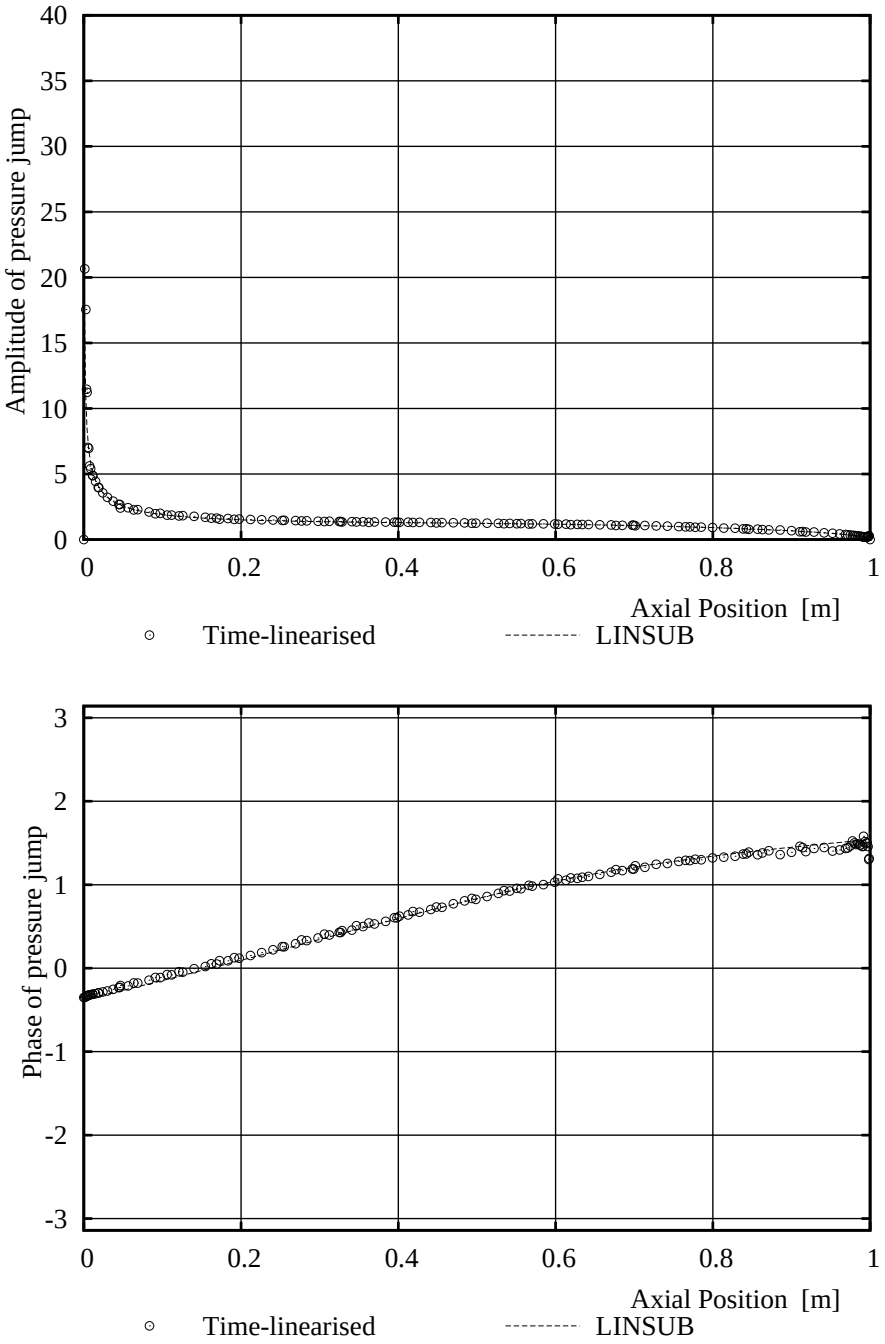

Figure 6.14: Amplitude (upper) and phase (lower) of pressure jumps around the blade for ND = 0. Harmonic linearised single blade-row versus LINSUB

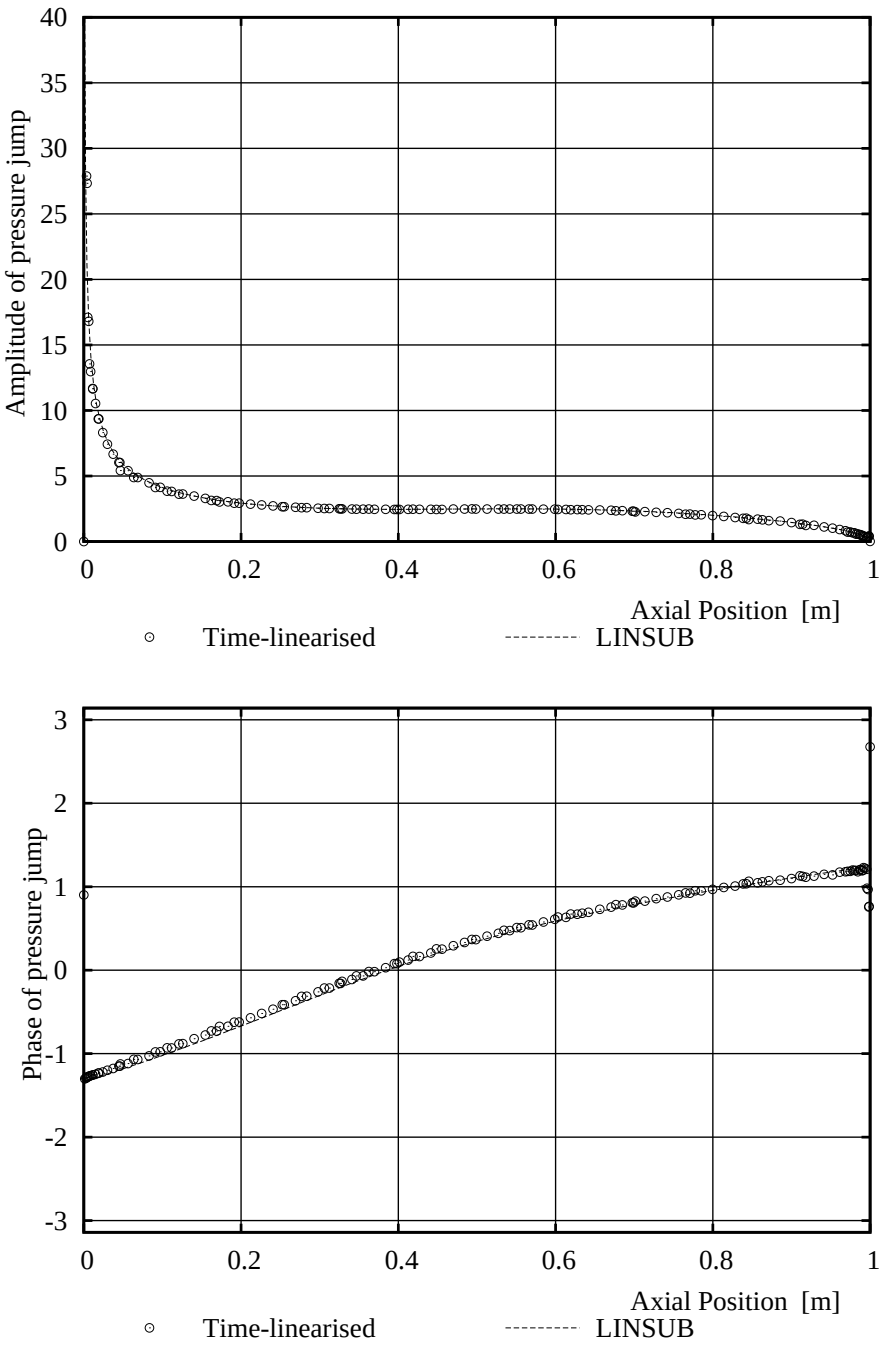

Figure 6.15: Amplitude (upper) and phase (lower) of pressure jumps around the blade for ND = 12. Harmonic linearised single blade-row versus LINSUB

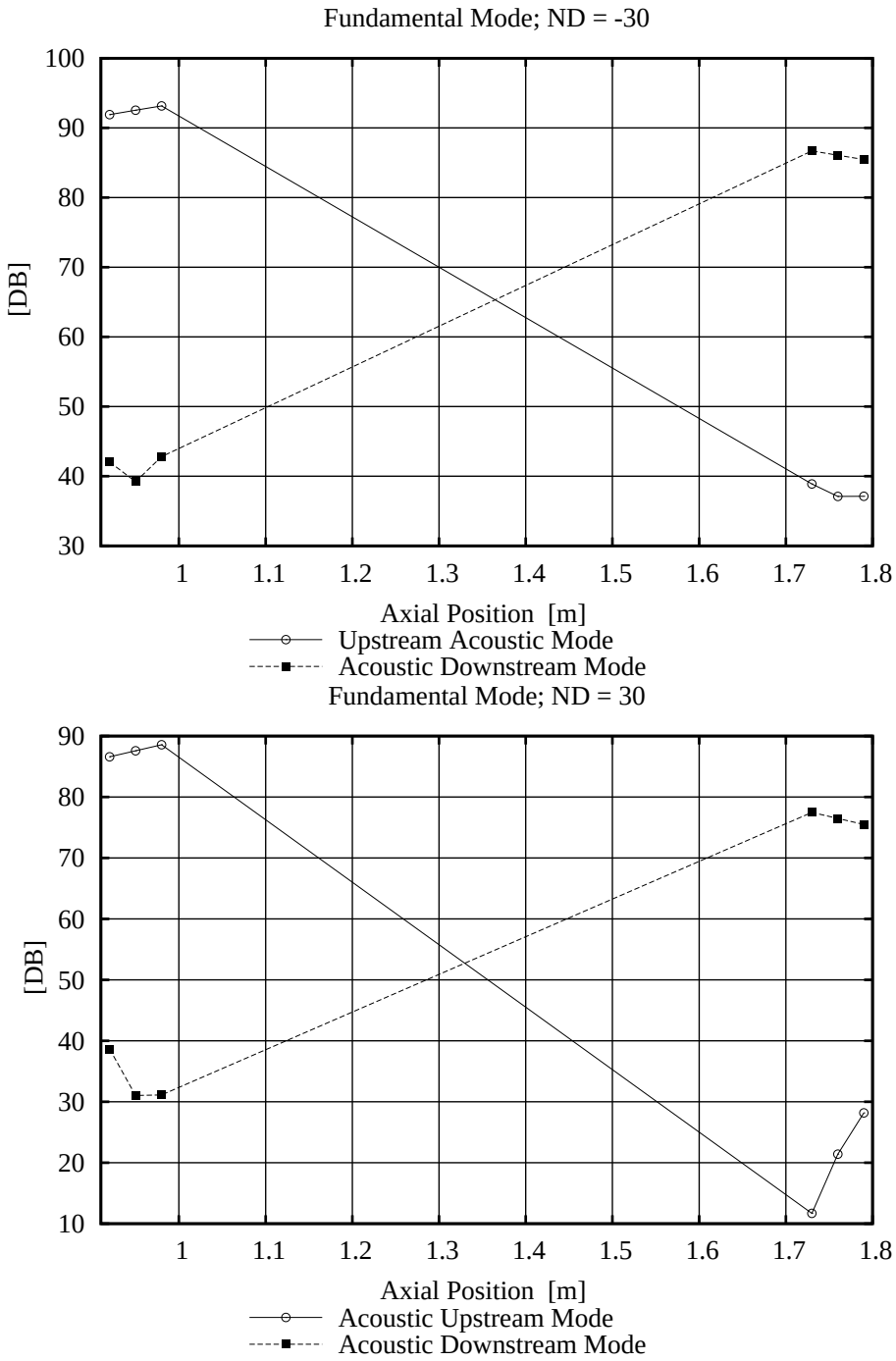

Figure 6.16: Propagation of fundamental acoustic modes for ND = -30 (upper) and ND = 30 (lower)

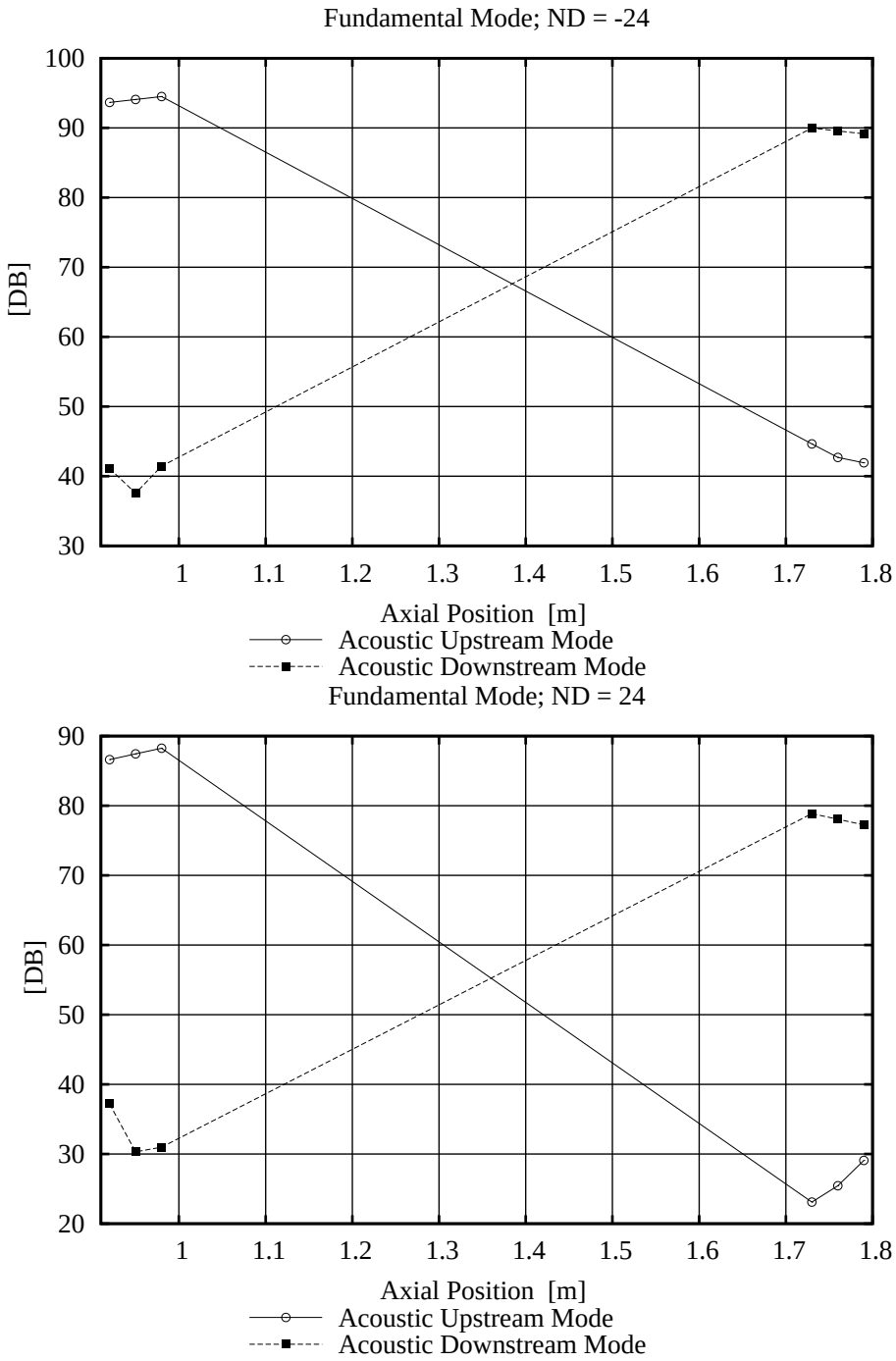

Figure 6.17: Propagation of fundamental acoustic modes for ND = -24 (upper) and ND = 24 (lower)

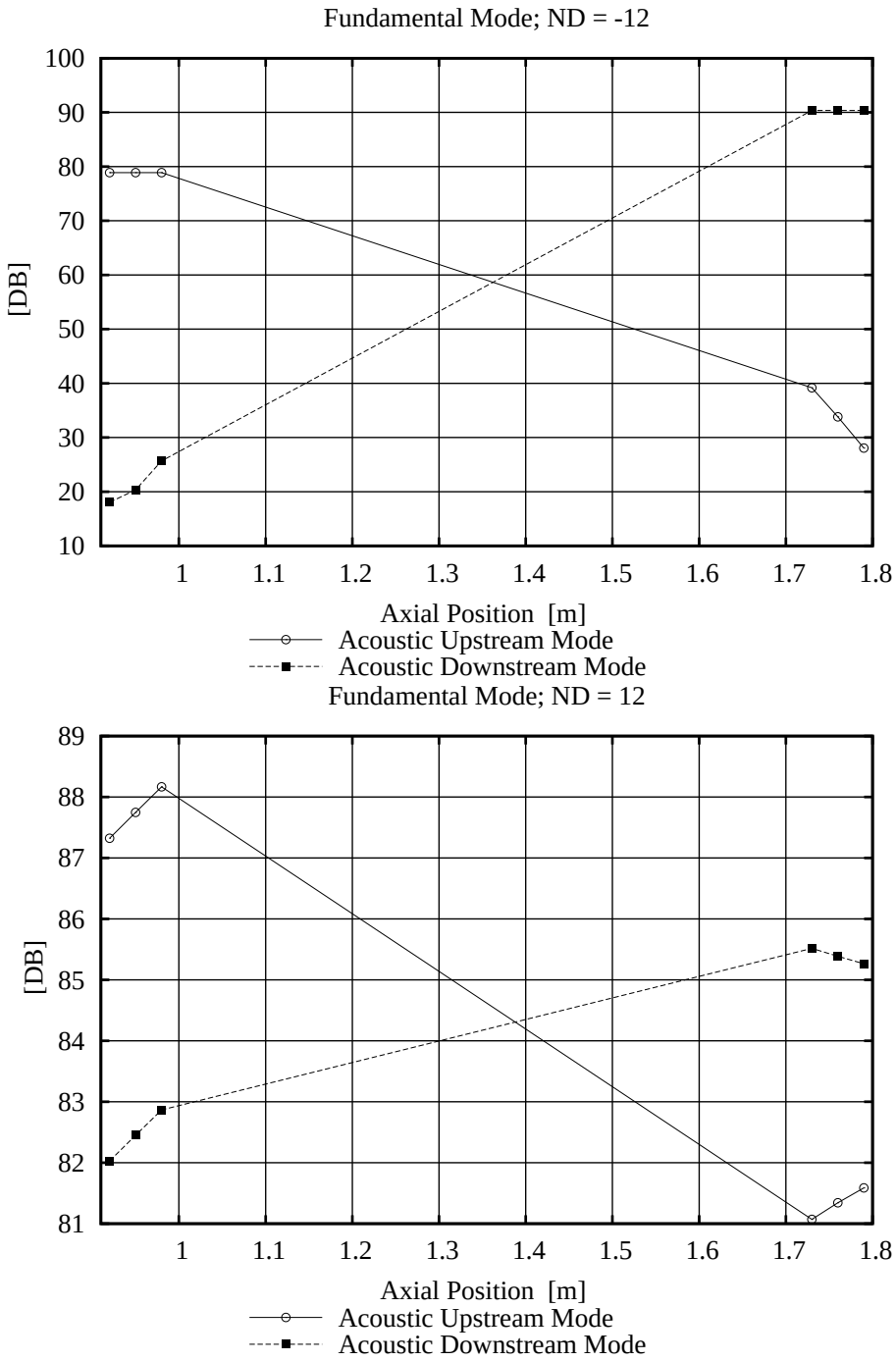

Figure 6.18: Propagation of fundamental acoustic modes for ND = -12 (upper) and ND = 12 (lower)

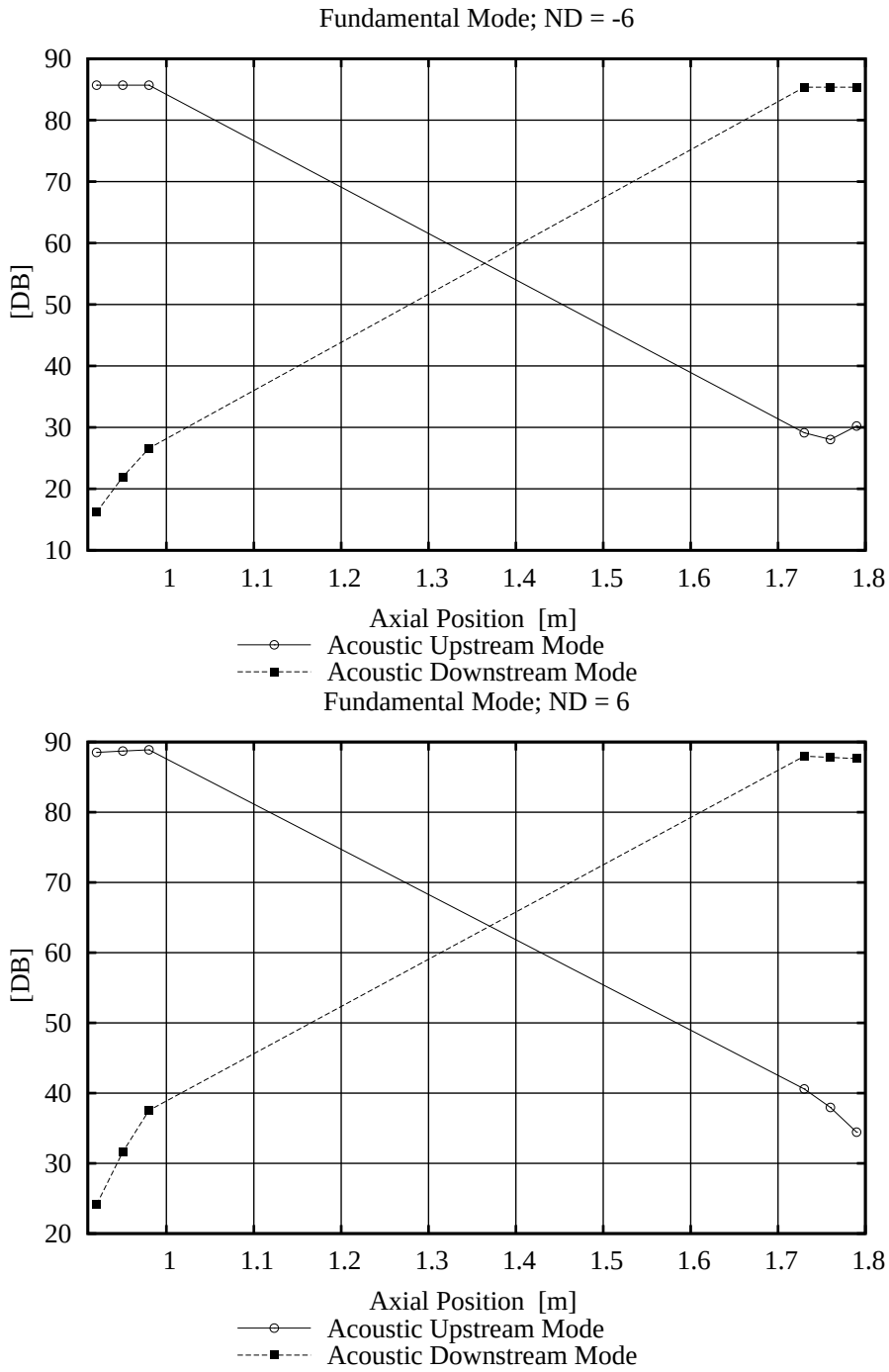

Figure 6.19: Propagation of fundamental modes for ND = -6 (upper) and ND = 6 (lower)

6.3 Harmonic Three-blade-row Flutter Analysis

The same basic bending flutter problem as in the previous section is now given another dimension by adding two neighbouring blade-rows, one upstream and one downstream of the vibrating blade-row. As a result, this study is more representative of a real turbomachinery configuration than an isolated blade-row.

6.3.1 Flow Conditions

The case geometry now consists of three blade-rows arranged as stator/rotor/stator. The blades in each blade-row are represented by flat plate airfoils with no thickness and the number of blades in each blade-row is identical. The mean flow passing through the blade-rows is two-dimensional, inviscid, isentropic, and subsonic. The rotational speed and flow angles have been determined so that the flow is perfectly aligned with the blades in each blade-row; there is no turning of the flow; and the relative Mach number is identical in each blade-row. The flow conditions and geometric parameters are shown in Table. 6.5. Given this configuration, the mean flow conditions in the rotor are equivalent to those studied in the isolated blade-row analysis.

Blade-row	Stator	Rotor	Stator
Number of blades	72	72	72
Blade chord	1	1	1
Stagger angle	45^o	-45^o	45^o
Mach Number	0.7	0.7	0.7
$\mid \Omega R \mid rad.m.s^{-1}$	0	1.41421	0
Frequency (rad/s)		$\omega_o = 1$	
Inter-blade phase angle	0	$-180^o \leq \sigma \leq 180^o$	0

Table 6.5: Main parameters for the stator/rotor/stator flutter case

6.3.2 Computational Mesh

The computational mesh for the rotor blade-row is the same as that used in Section 6.2.2. Each blade-row is represented by a single blade-passage and the blade is split into two surfaces located at the periodic boundaries. The meshes generated for both stator blade-rows are identical, and have been obtained by simply re-staggering the rotor mesh to 45^o. Note that it is possible to use the same mesh quality for each blade-row, since the axial and circumferential wave numbers remain identical when

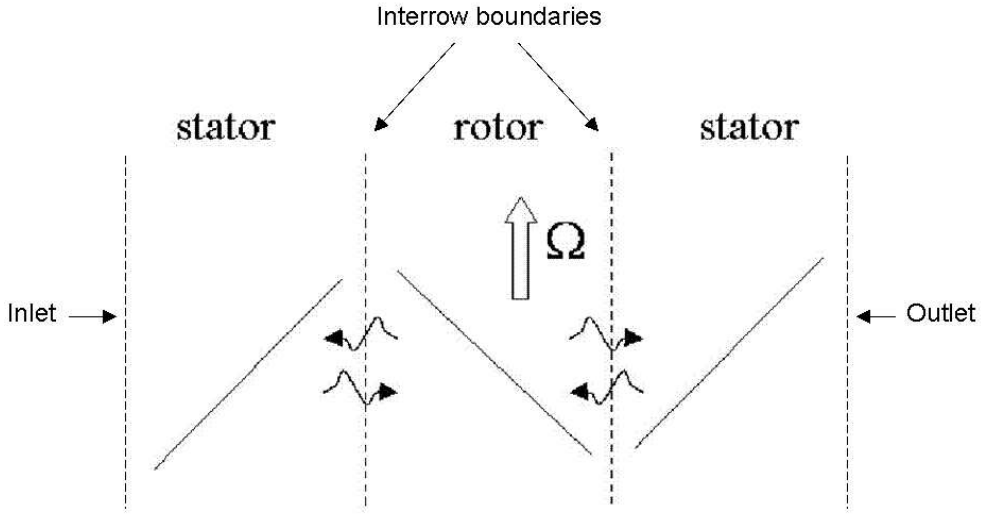

Figure 6.20: 2-D view of the three blade-rows of flat plates

these are travelling across the blade-rows. However, a mesh refinement study was carried out, and another mesh, finer than this one by about 50% in each direction, was also produced for validation purposes. The following flutter analysis was made using both meshes, both analyses producing the same results. A view of the refined mesh used for the three blade-row analysis is shown in Fig. 6.21.

6.3.3 Multi Blade-row Bending Flutter Analysis

As for the previous isolated blade-row analysis, here the rotor blades are also vibrating with modeshapes of unit amplitude normal to the blade, at reduced frequency $\omega_0 = 1$. The time-linearised multi blade-row unsteady solutions are computed for a series of nodal diameters that are multiples of 6 (i.e ND_r = -30,..,-6,0,6,..,30), and the lift coefficients are computed for each of these nodal diameters.

The multi blade-row analysis is decomposed into several parts. First, only the fundamental spinning mode is allowed to propagate across the three blade-rows. Given the frequency $\omega_r = \omega_0$, and the nodal diameter ND_r of the blades vibration in the rotor, the frequency ω_s and nodal diameter ND_s of the waves in the neighbouring stator are determined as follows:

$$ND_s = ND_r \tag{6.3.6}$$

and,

$$\omega_s = \omega_r - ND_r \times \Omega \tag{6.3.7}$$

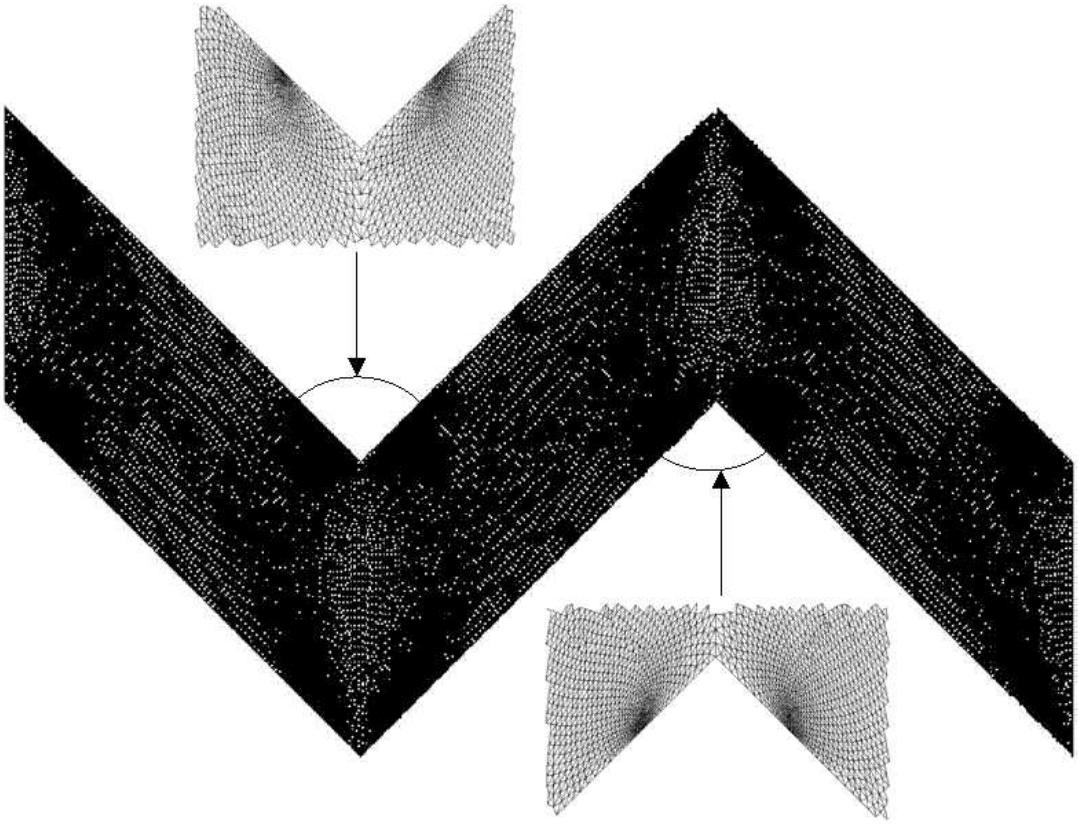

Figure 6.21: Three blade-row flat plate mesh

The calculated frequencies and nodal diameters are presented in Table 6.6.

Stator 1			Rotor			Stator 2		
ω_s *(rad/s)*	ND_s	n_s	ω_r *(rad/s)*	ND_r	n_r	ω_s *(rad/s)*	ND_r	n_s
5.9365	-30	0	1.0000	-30	0	5.9365	-30	0
4.9492	-24	0	1.0000	-24	0	4.9492	-24	0
3.9619	-18	0	1.0000	-18	0	3.9619	-18	0
2.9746	-12	0	1.0000	-12	0	2.9746	-12	0
1.9873	-6	0	1.0000	-6	0	1.9873	-6	0
1.0000	0	0	1.0000	0	0	1.0000	0	0
0.0127	6	0	1.0000	6	0	0.0127	6	0
-0.9746	12	0	1.0000	12	0	-0.9746	12	0
-1.9619	18	0	1.0000	18	0	-1.9619	18	0
-2.9492	24	0	1.0000	24	0	-2.9492	24	0
-3.9365	30	0	1.0000	30	0	-3.9365	30	0

Table 6.6: Fundamental mode generation for the three blade-row problem

From this table, it is clear that a time-linearised solution, including three blade-rows

and one spinning mode, can be obtained by computing only one time-linearised solution per blade-row. In Fig. 6.22, the computed unsteady lift solutions are compared to the only reference solution, showed by Ekici and Hall in [39], who used the same approach to solve this problem. Note the excellent agreement for each computed nodal diameter. There are several interesting remarks to make about these results. First, there is excellent agreement between the solutions obtained with the present code and Ekici and Hall's solutions, which validates the current code. Second, for this case, neighbouring stator blade-rows have significant impact on the aerodynamics of the rotor blade-row, even when including one spinning mode only. As can be seen from Fig. 6.23, the lift coefficient varies by as much as 70% from the single blade-row results. Third, the acoustic resonance peaks predicted in the isolated blade-row case are absent from the multi blade-row solution. This seems to indicate that neighbouring blade-row interactions may help towards the avoidance of acoustic resonances in multi stage engines. The physical reason behind the disappearance of the resonance peaks is not clear to the author. A possible explanation is this. It has long been known that cut-off acoustic waves carry no energy since the acoustic pressure and particle velocity are 90 degrees out of phase. Acoustic resonance occurs exactly at the transition between cut-on and cut-off acoustic modes in an isolated blade-row. In the former situation, acoustic modes can transport energy, but not in the latter. However, it has been demonstrated [82] that the coupling between two cut-off acoustic waves travelling in opposite directions allows energy to be transfered. The presence of neighbouring blade-rows allows cut-off acoustic waves to be reflected back in the vibrating blade-row, and thus an energy transfer occurs, which can dissipate some of the energy of vibration. Lastly, neighbouring blade-row interactions may still be significant when the fundamental spinning mode is cut-off. In the present study, the influence of neighbouring blade-rows is generally higher when the fundamental acoustic mode is cut-off.

Next, nine spinning modes are included into the multi blade-row analysis (Table 6.7). Since we are now dealing with multi blade-row calculations including several spinning modes, it is essential to distinguish between the value of the current nodal diameter ND_i of the i^{th} blade-row, and that of the circumferential wave numbers k_θ, also referred as the total nodal diameter TND, which can now takes different values. Note that this table is a special case of that presented in Section 4.2.5. The fact that the number of blades is the same in each blade-row has several implications on the spinning modes determination: the current nodal diameter in each blade-row can be the same for each considered mode; the total nodal diameters of different modes are identical; the circumferential modes n_s in the stators are symmetric. This is why only one stator column is presented in Table 6.7, which applies to both stators.

Also note that different combinations of (n_r, n_s) can result in the same total nodal diameter.

Figure 6.24 shows the computed solutions when one, three, and nine spinning modes are included in the multi blade-row analysis. The analysis with one mode is conducted with the first mode shown in line 1 of Table 6.7, the analysis with three modes with the first three modes listed in the first three lines, and so on. It is clear that most of the multi blade-row coupling is captured using only one mode, namely the fundamental spinning mode. Small, yet noticeable differences are observed when three modes are used. The nine-mode solution differs very slightly from the three-mode solution, which indicates that the solution with nine modes is probably almost mode converged.

		rotor			stator		
Mode	TND	ω_r	CND_r	n_r	ω_s	CND_s	n_s
1	k_0	ω_0	k_0	0	$\omega_0 - k_0\Omega$	k_0	0
2	$k_0 + B_s$	ω_0	k_0	1	$\omega_0 - (k_0 + B_r)\,\Omega$	k_0	1
3	$k_0 - B_s$	ω_0	k_0	-1	$\omega_0 - (k_0 - B_r)\,\Omega$	k_0	-1
4	$k_0 + B_s$	$\omega_0 + B_s\Omega$	k_0	1	$\omega_0 - k_0\Omega$	k_0	1
5	$k_0 + 2 \times B_s$	$\omega_0 + B_s\Omega$	k_0	2	$\omega_0 - (k_0 + B_r)\,\Omega$	k_0	2
6	k_0	$\omega_0 + B_s\Omega$	k_0	0	$\omega_0 - (k_0 - B_r)\,\Omega$	k_0	0
7	$k_0 - B_s$	$\omega_0 - B_s\Omega$	k_0	-1	$\omega_0 - k_0\Omega$	k_0	-1
8	k_0	$\omega_0 - B_s\Omega$	k_0	0	$\omega_0 - (k_0 + B_r)\,\Omega$	k_0	0
9	$k_0 - 2 \times B_s$	$\omega_0 - B_s\Omega$	k_0	-2	$\omega_0 - (k_0 - B_r)\,\Omega$	k_0	-2

Table 6.7: Nine modes generation for the three blade-row problem, for k_0 = -30,-24,..,30

In the next set of results shown in Fig. 6.25, only the fundamental spinning mode is allowed to propagate across the blade-rows, but the axial gap between the blade-rows is now increasing. From this figure, two main observations can be made. First, as the axial gap increases, and when the fundamental acoustic mode is cut-off, the multi blade-row effects decrease. This can be observed for an inter-blade phase angle $\sigma < -80.38^o$, or $\sigma > 22.07^o$. From physical considerations, cut-off modes decay exponentially as they propagate, and thus we expect these modes to have less contribution on the aerodynamics of the further away blade-rows as they need to travel longer distances. However, when the fundamental acoustic mode is cut-on, i.e for $-80.38^o < \sigma < 22.07^o$, the multi blade-row effects seem to work differently. It seems that multi blade-row effects are greater for the largest axial gaps. However, it is not possible to identify an obvious relationship between the axial gap and the lift coefficients, as the variation differs from one nodal diameter to the next. One possible explanation proposed by the author is as follows. The unsteady lift L, also

total lift in our case, is an integrated value of pressures around the blade:

$$L = \oint_S \hat{p}\,(\mathbf{x})\, dS, \tag{6.3.8}$$

where $\hat{p}$ is the complex unsteady pressure function, with amplitude and phase depending on the local position $\mathbf{x}$. Therefore, $\hat{p}\,(\mathbf{x})$ can be decomposed as:

$$\hat{p}\,(\mathbf{x}) = |\hat{p}\,(\mathbf{x})\,|.e^{i\phi(\mathbf{x})}. \tag{6.3.9}$$

The local amplitudes and phases of the unsteady pressure distribution around the blade will then exclusively depend on both the amplitude and phase of the acoustic, vortical and entropic waves impinging on the blades, as well as on the blade vibration. For the case of cut-on acoustic modes which are travelling on a uniform mean flow with no obstacle, it is known that the waves's amplitudes remain constant. However, the phases of the waves are direct functions of the distance that they travel. Therefore, a variation in the axial gap leads to a variation in the incoming wave's phase, and therefore to a variation in lift coefficients.

An alternative way to explain the lift coefficient solutions of Fig. 6.25 is to inspect closely the results presented in Figs. 6.26 to 6.35. These plots represent the amplitudes of the acoustic modes measured in the axial gaps between the blade-rows. There is no measure of the acoustic modes at the axial locations corresponding to the blades, but what we know is that the presence of the blades scatters these modes. For each axial gap configuration, the blade's axial position is given in Table 6.8.

Axial Gap	stator	rotor	rotor
$0.2 \times c$	$1.0 < x < 1.707$	$1.907 < x < 2.614$	$2.814 < x < 3.521$
$0.4 \times c$	$0.8 < x < 1.507$	$1.907 < x < 2.614$	$3.014 < x < 3.721$
$0.8 \times c$	$0.4 < x < 1.107$	$1.907 < x < 2.614$	$3.414 < x < 4.121$

Table 6.8: Axial positions of the blades for each axial gap configuration

For cut-off acoustic modes (i.e. $ND < -12$, or $ND > 0$), it is seen that the acoustic mode's amplitude decays exponentially (linearly in the plot because of the logarithmic scale) as they travel is the axial direction. The decay rate depends on the imaginary part of the axial wave number (Fig. 6.1). From Figs. 6.28 to 6.30, it is clear that for larger axial gaps, the amplitude of the acoustic modes are much smaller once they arrive at the neighbouring blade-row. Therefore these acoustic modes will have weaker effects on the aerodynamics of the blade-row on which they impinge. Note that the cut-off acoustic downstream modes exit the second stator row with greater amplitude than when they first entered it, but this effect is not

seen in the first stator row with the cut-off acoustic upstream modes. The difference is attributed to the degeneration of vortical modes into acoustic downstream modes in the second stator row caused by the presence of the blades in the main stream. It can also be observed that the upstream and downstream acoustic modes propagating away from the rotor LE and TE respectively are not significantly affected by the axial distances between the blade-rows. This indicates that the incoming mode, impinging on the LE or TE of the rotor, has very little impact on the aerodynamics of the other end of the blade. Consequently, when the fundamental acoustic mode is cut-off, it is more than likely that only the nearest upstream and downstream blade-rows play a major role in the overall aerodynamics of the middle blade-row.

Looking at the cut-on acoustic modes results, shown in Figs. 6.26, 6.27 and 6.31 to 6.35, different conclusions can be drawn. First, one can see that the amplitude of the fundamental acoustic mode, reflected back to the rotor blade, can be up to 10 dBs higher when the axial gap is 80 % of the blade's chord than for smaller axial gaps. This fact probably explains the marked differences observed in the lift coefficients for various axial gaps. It can also be seen that increasing the axial gap does not automatically lead to an increase in the acoustic mode's amplitude reflected back onto the rotor. This feature again leads the author to believe that the phases of the acoustic waves probably play an important role in the multi blade-row coupling. Finally, it is important to notice that the upstream and downstream acoustic modes, that have been generated by the rotor blade's vibration, cross the neighbouring stator blade-rows with little attenuation in magnitude. The author therefore concludes that, when the fundamental acoustic mode is cut-on, it is more than likely that the adjacent neighbouring blade-rows play a significant role in the overall aerodynamics of the middle blade-row.

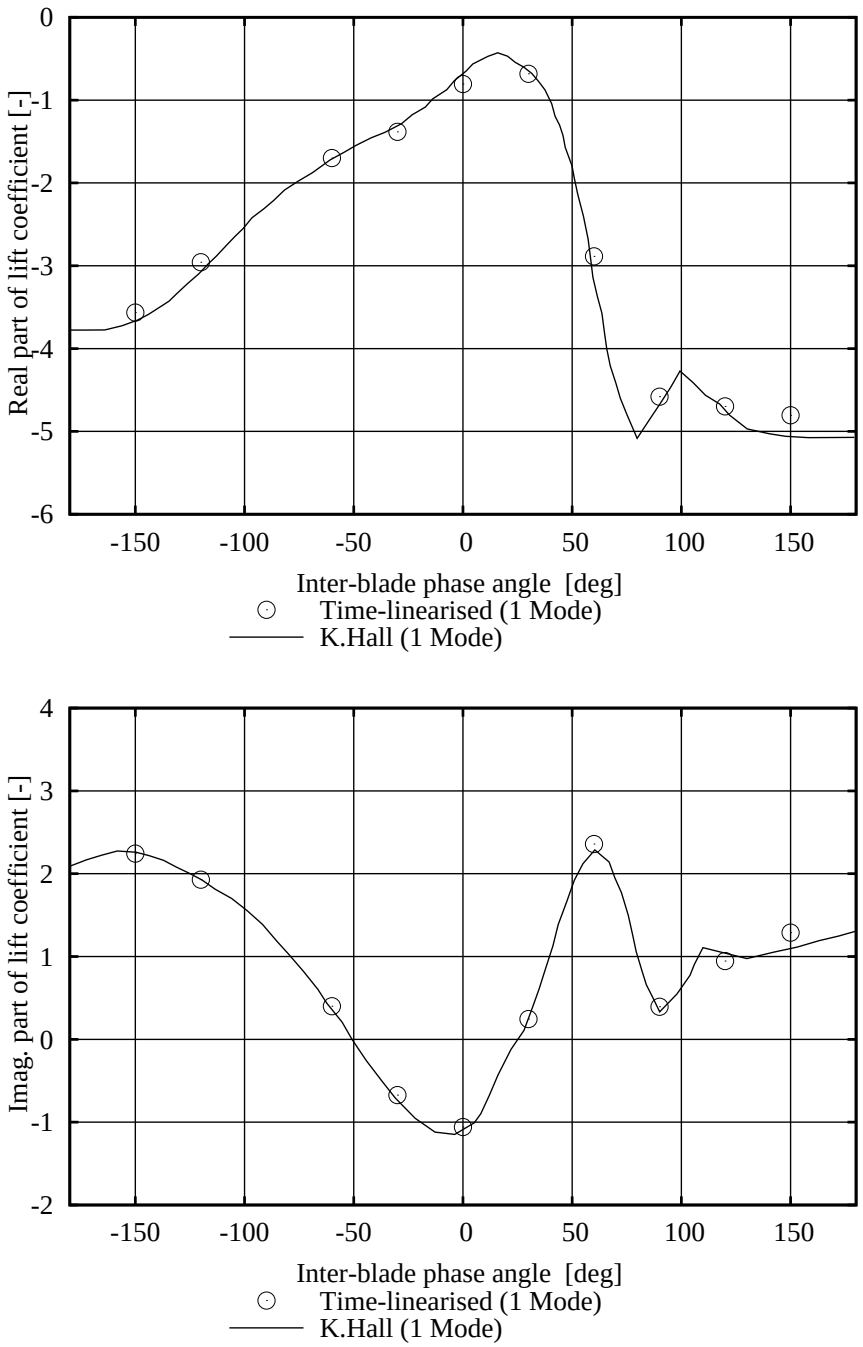

Figure 6.22: Real part (upper) and imaginary part (lower) of the lift coefficient. Harmonic linearised multi blade-row code versus reference solution for 1 mode.

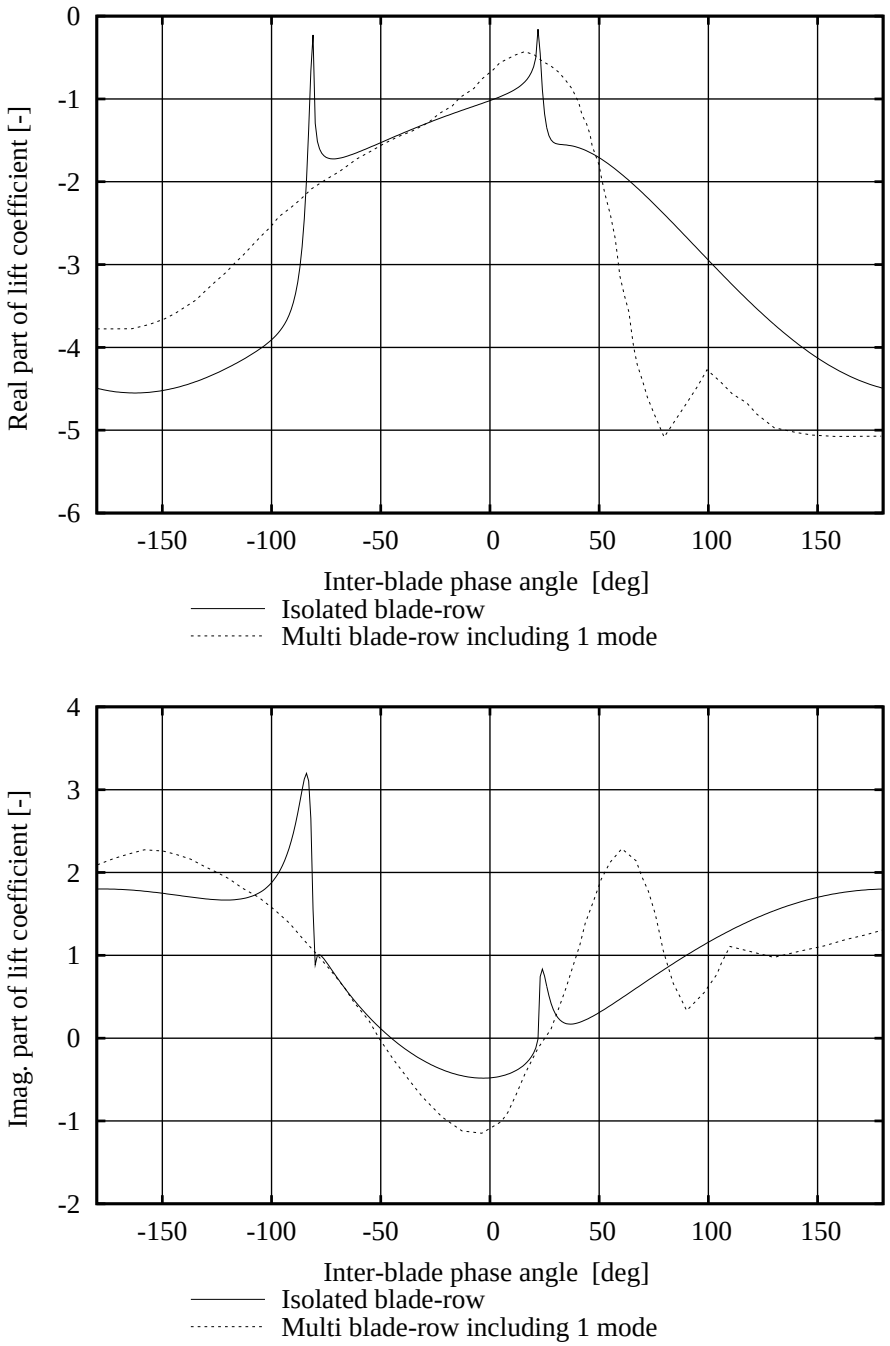

Figure 6.23: Real part (upper) and imaginary part (lower) of the lift coefficient. Harmonic linearised isolated blade-row solution versus three blade-row solution including 1 mode.

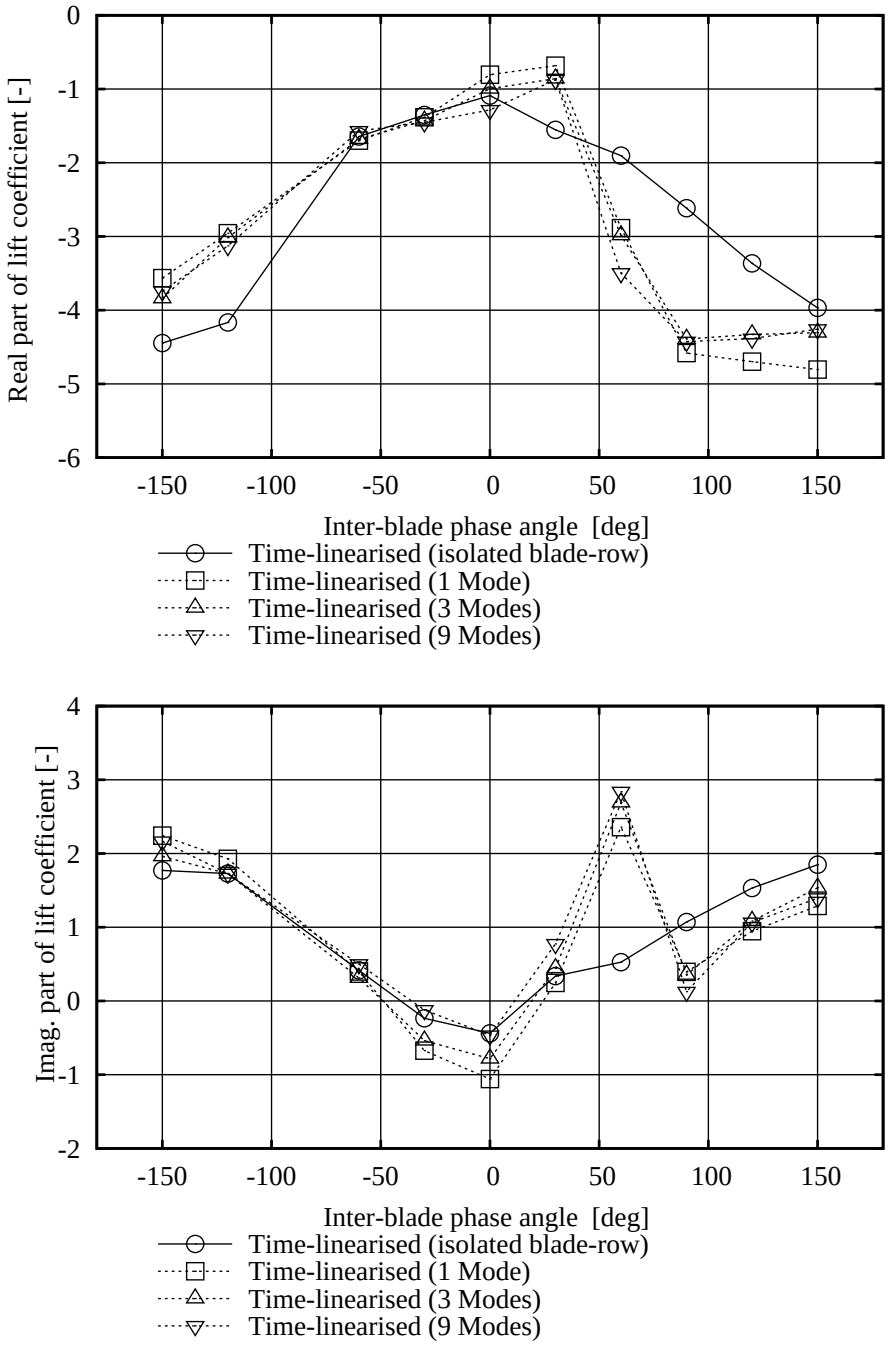

Figure 6.24: Real part (upper) and imaginary part (lower) of the lift coefficient using 1,3 and 9 modes

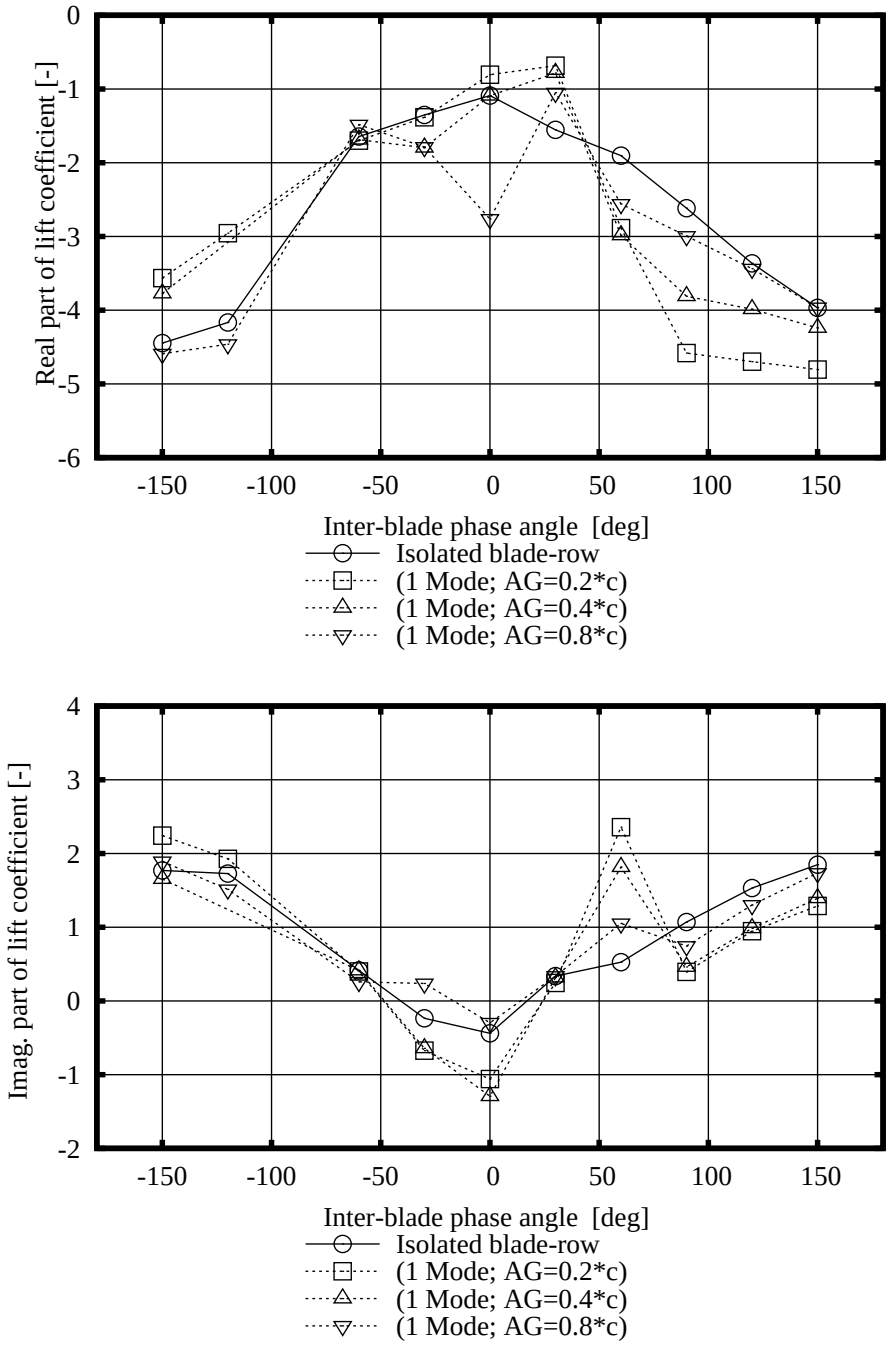

Figure 6.25: Real part (upper) and imaginary part (lower) of the lift coefficient using one mode and several axial gaps between the blade-rows

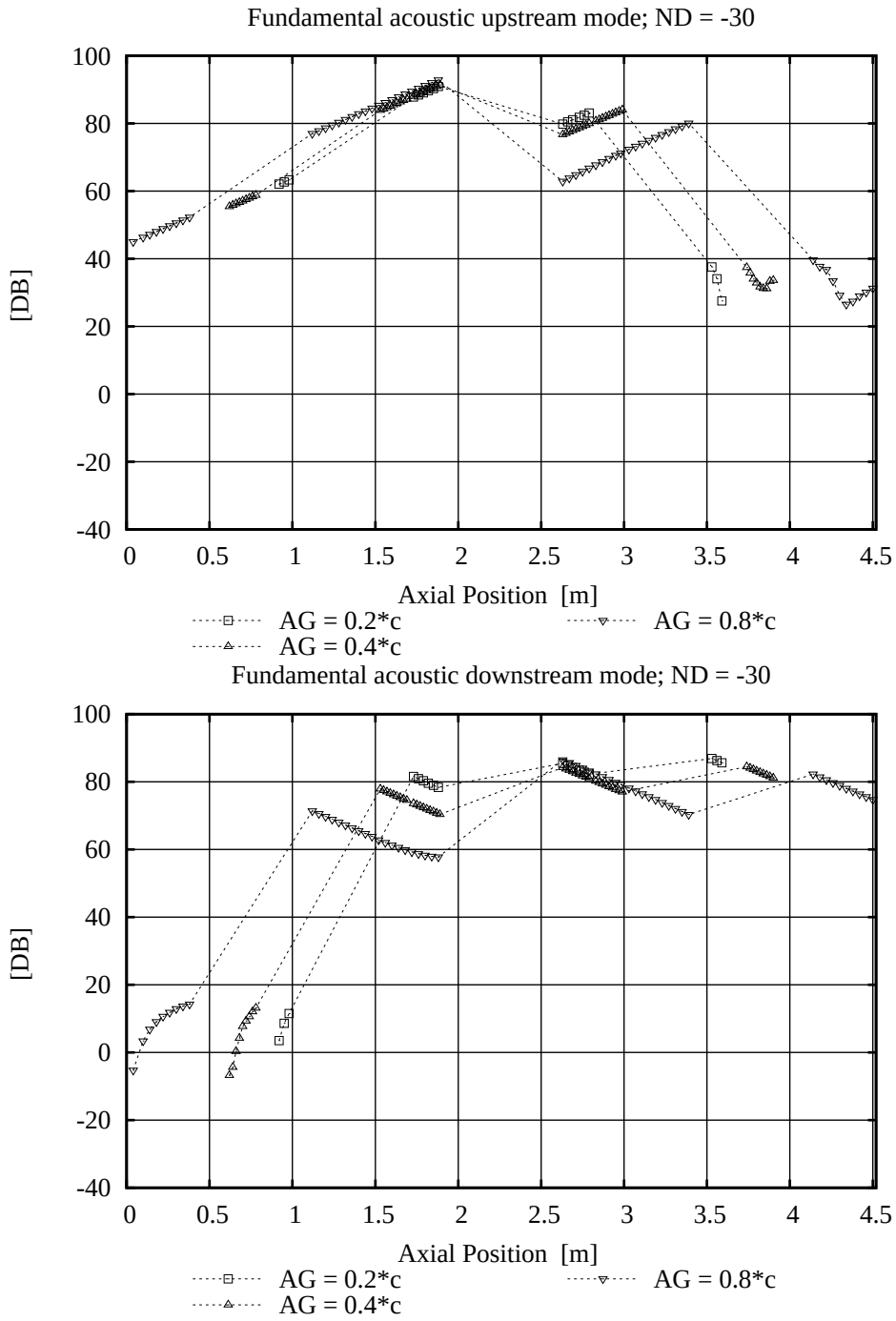

Figure 6.26: Amplitude of acoustic modes across the three blade-rows for ND = -30

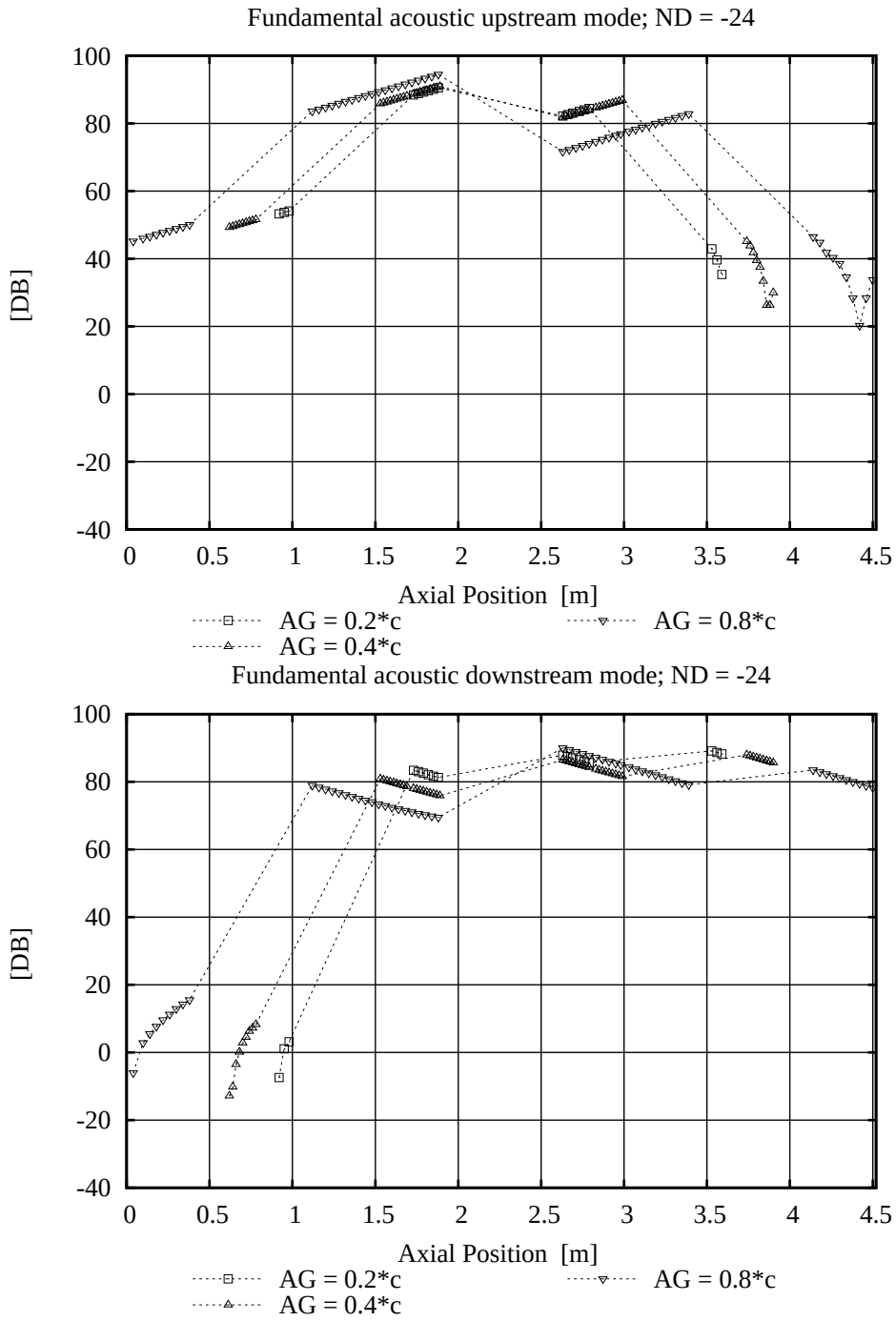

Figure 6.27: Amplitude of acoustic modes across the three blade-rows for ND = -24

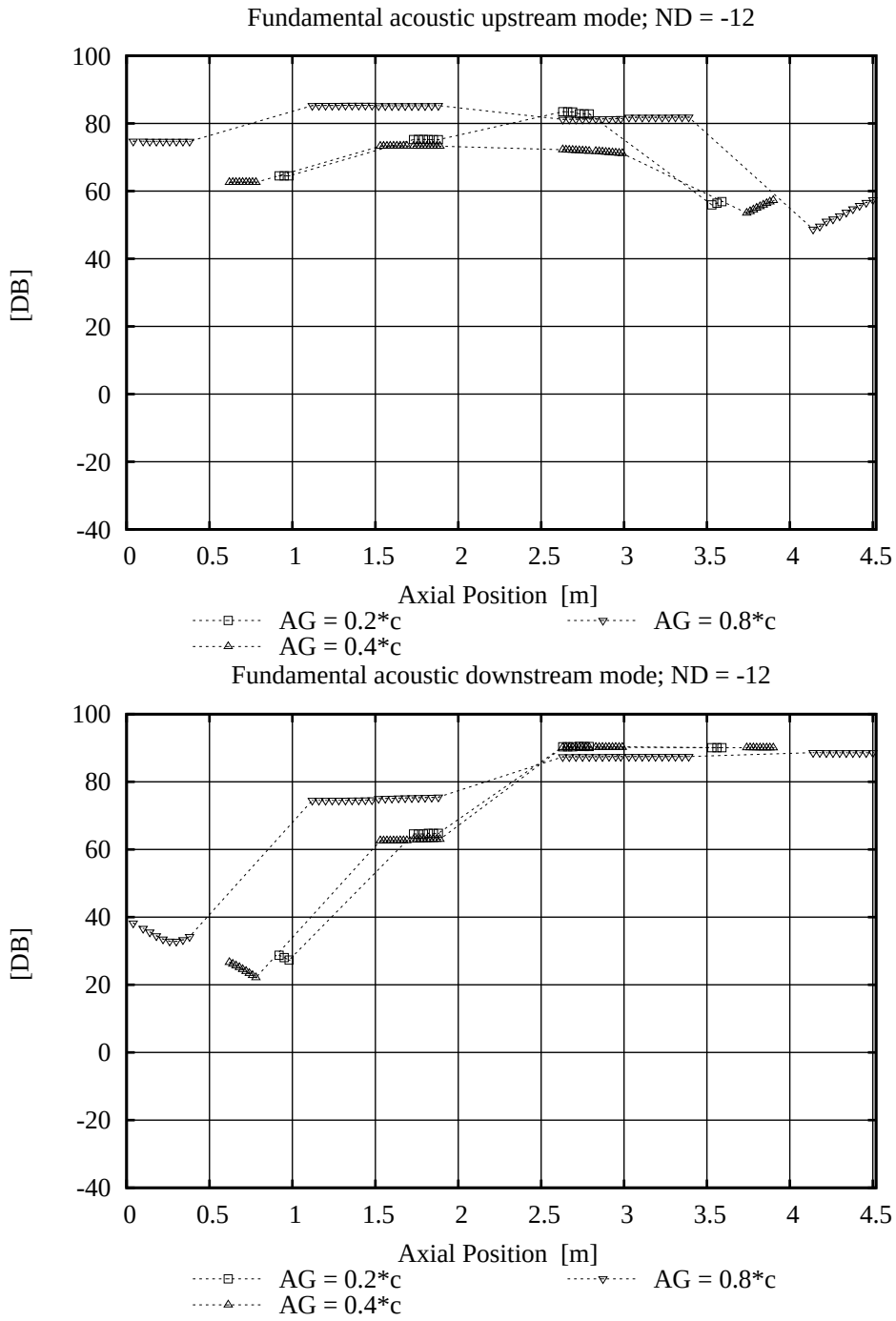

Figure 6.28: Amplitude of acoustic modes across the three blade-rows for ND = -12

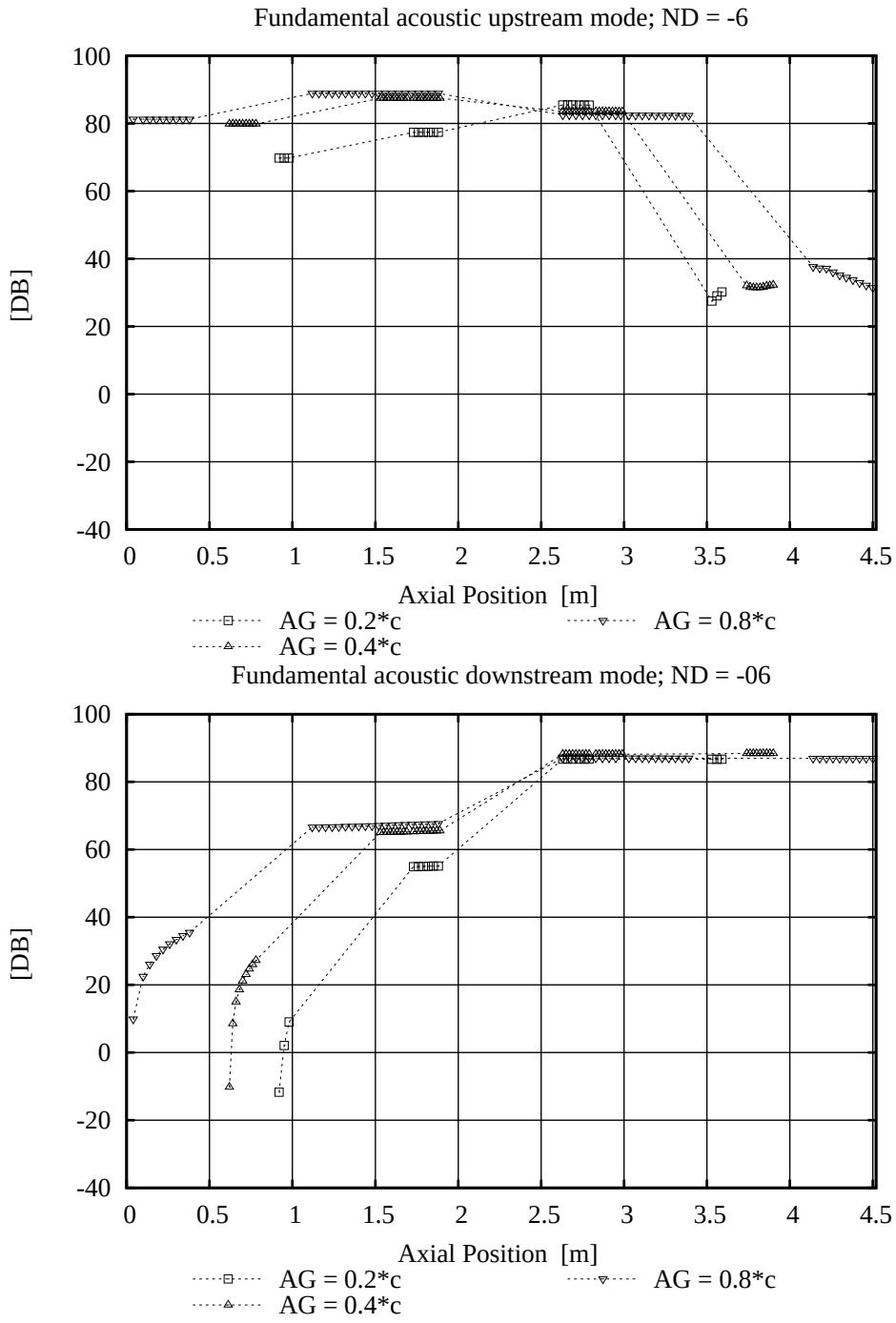

Figure 6.29: Amplitude of acoustic modes across the three blade-rows for ND = -6

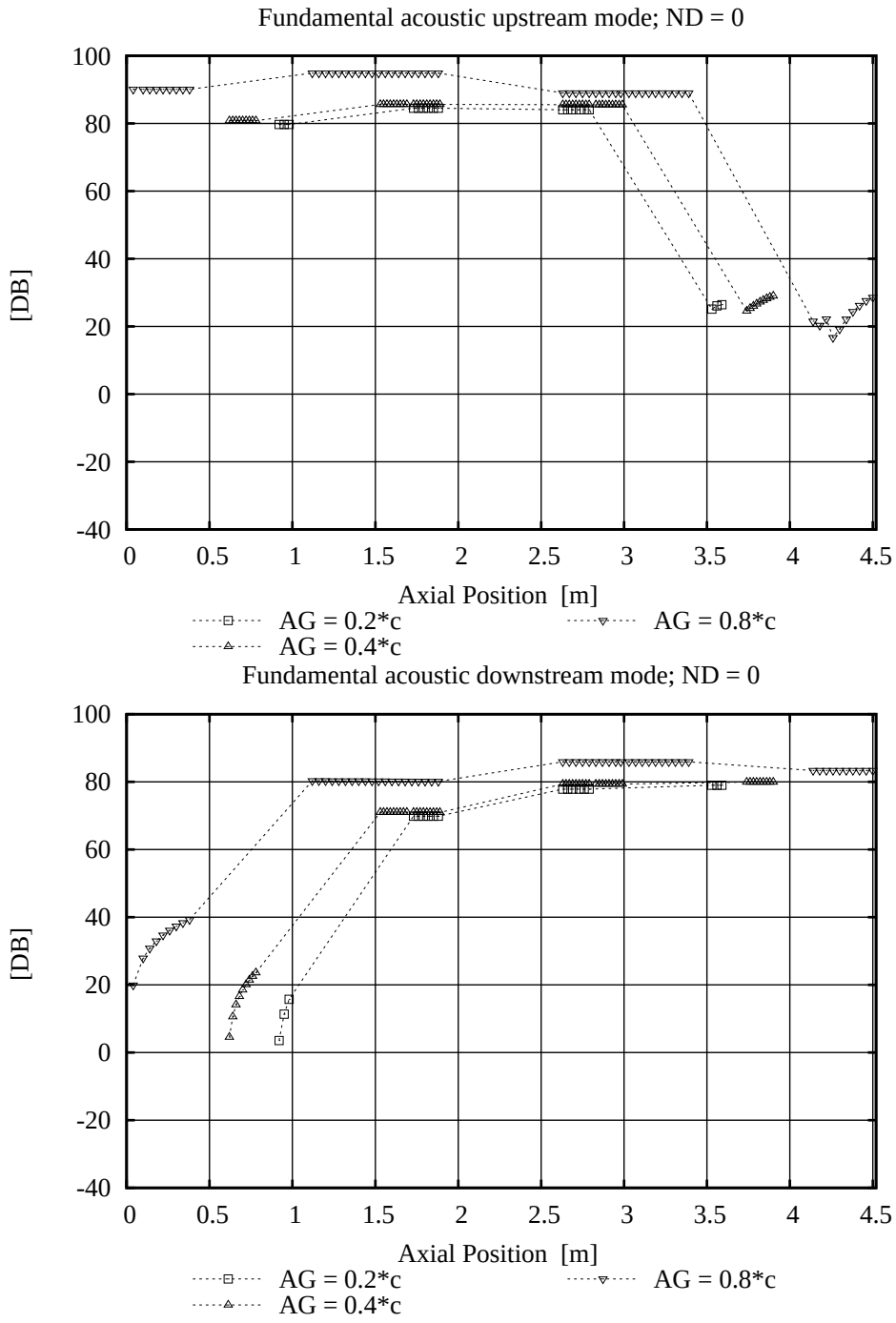

Figure 6.30: Amplitude of acoustic modes across the three blade-rows for ND = 0

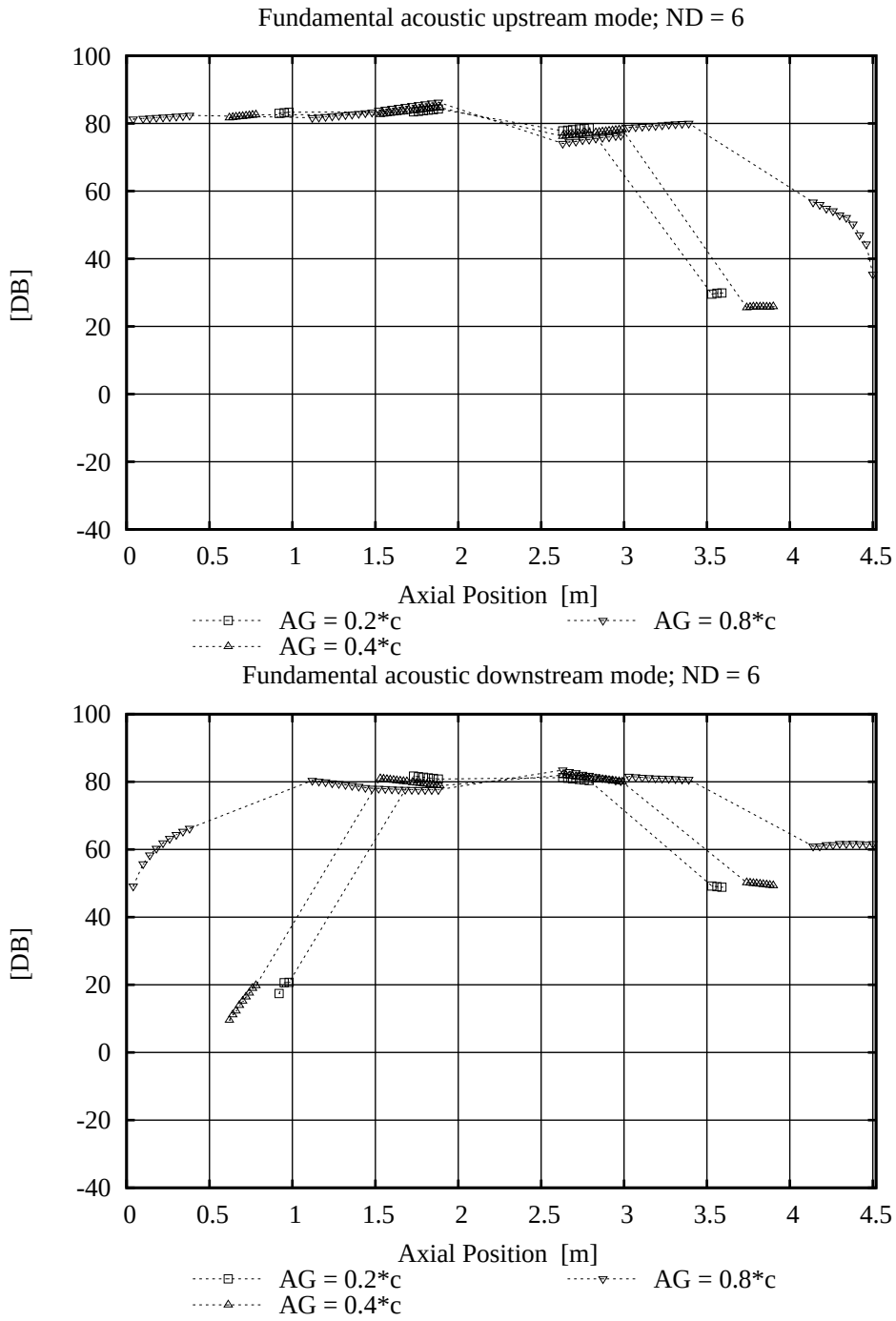

Figure 6.31: Amplitude of acoustic modes across the three blade-rows for ND = 6

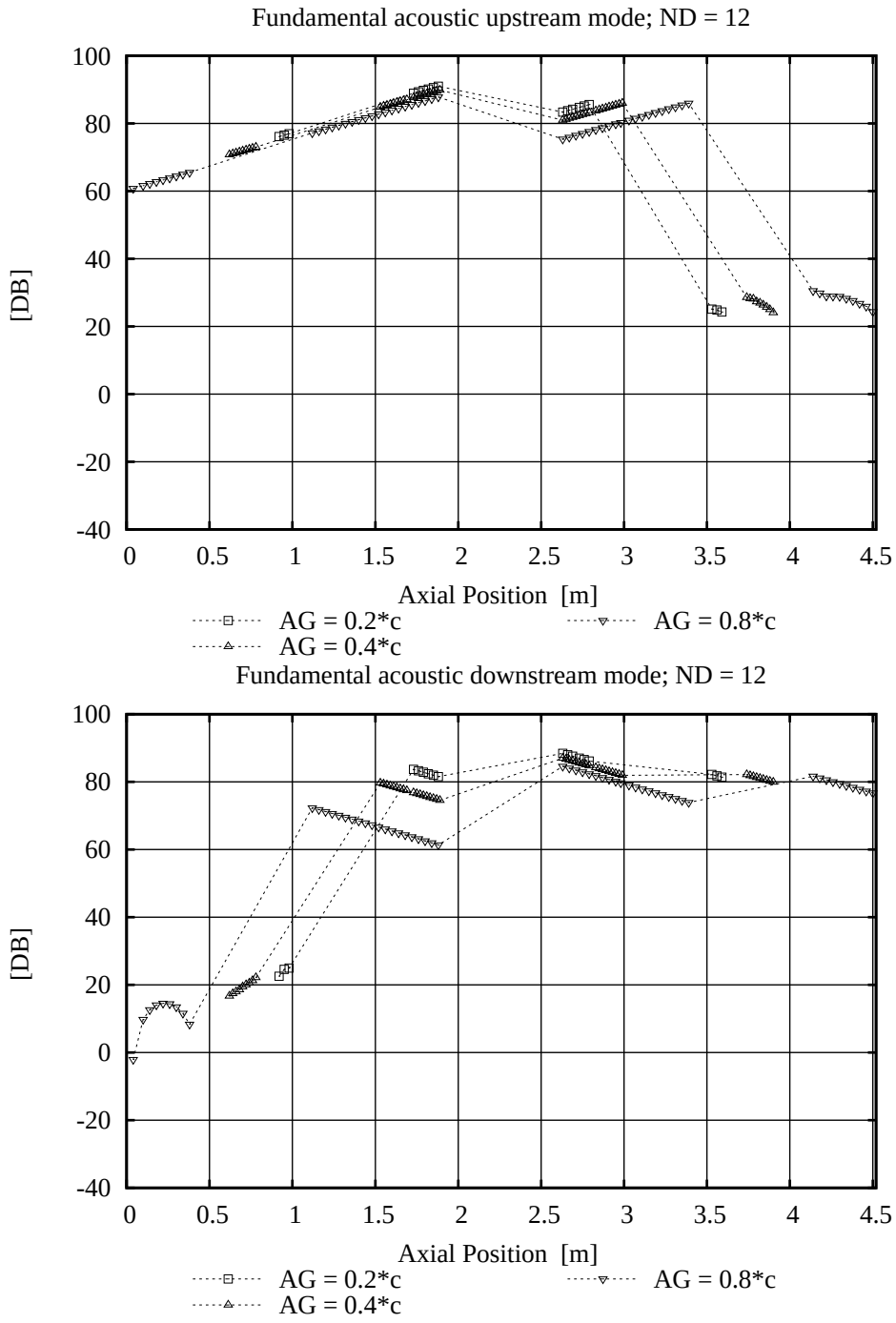

Figure 6.32: Amplitude of acoustic modes across the three blade-rows for ND = 12

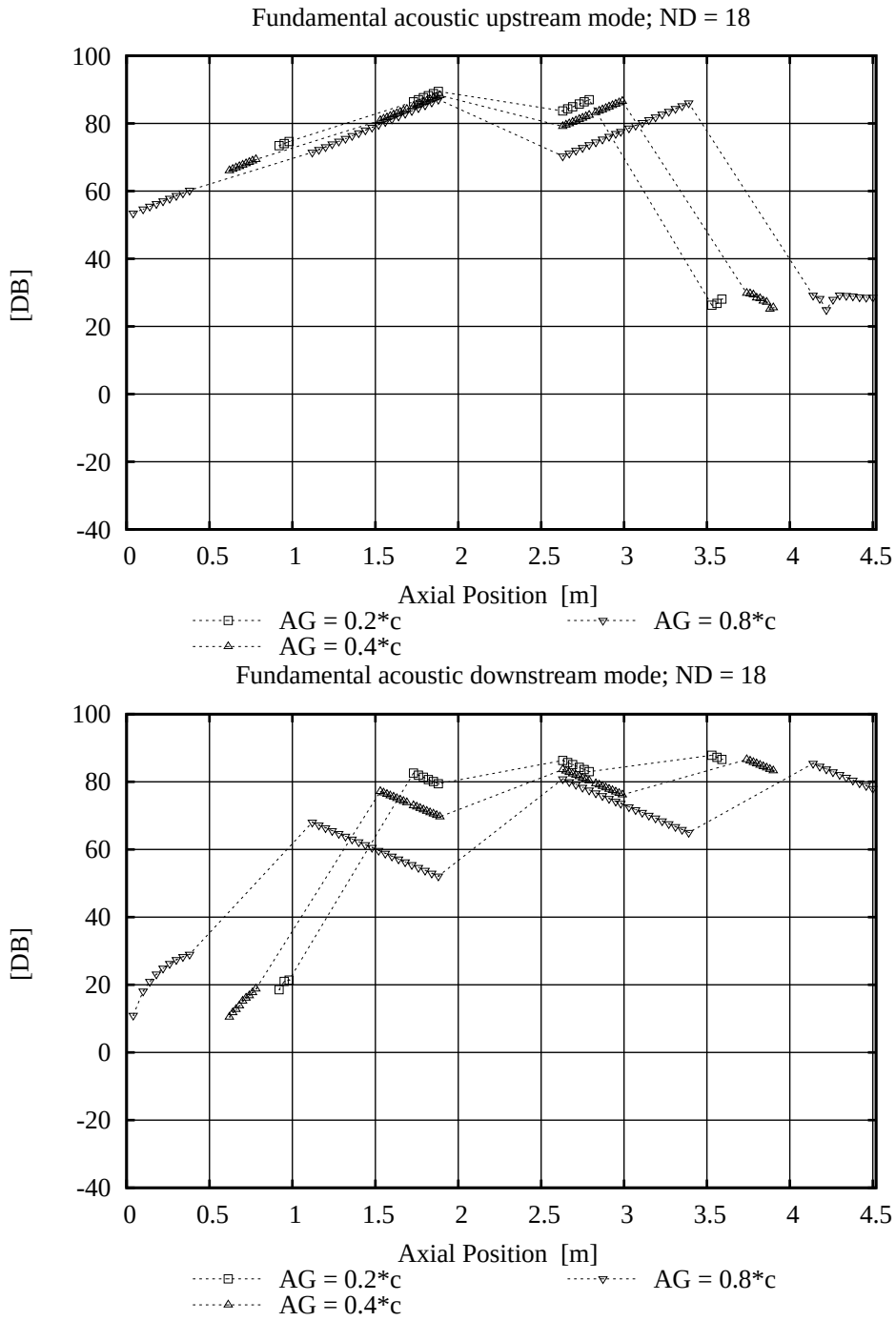

Figure 6.33: Amplitude of acoustic modes across the three blade-rows for ND = 18

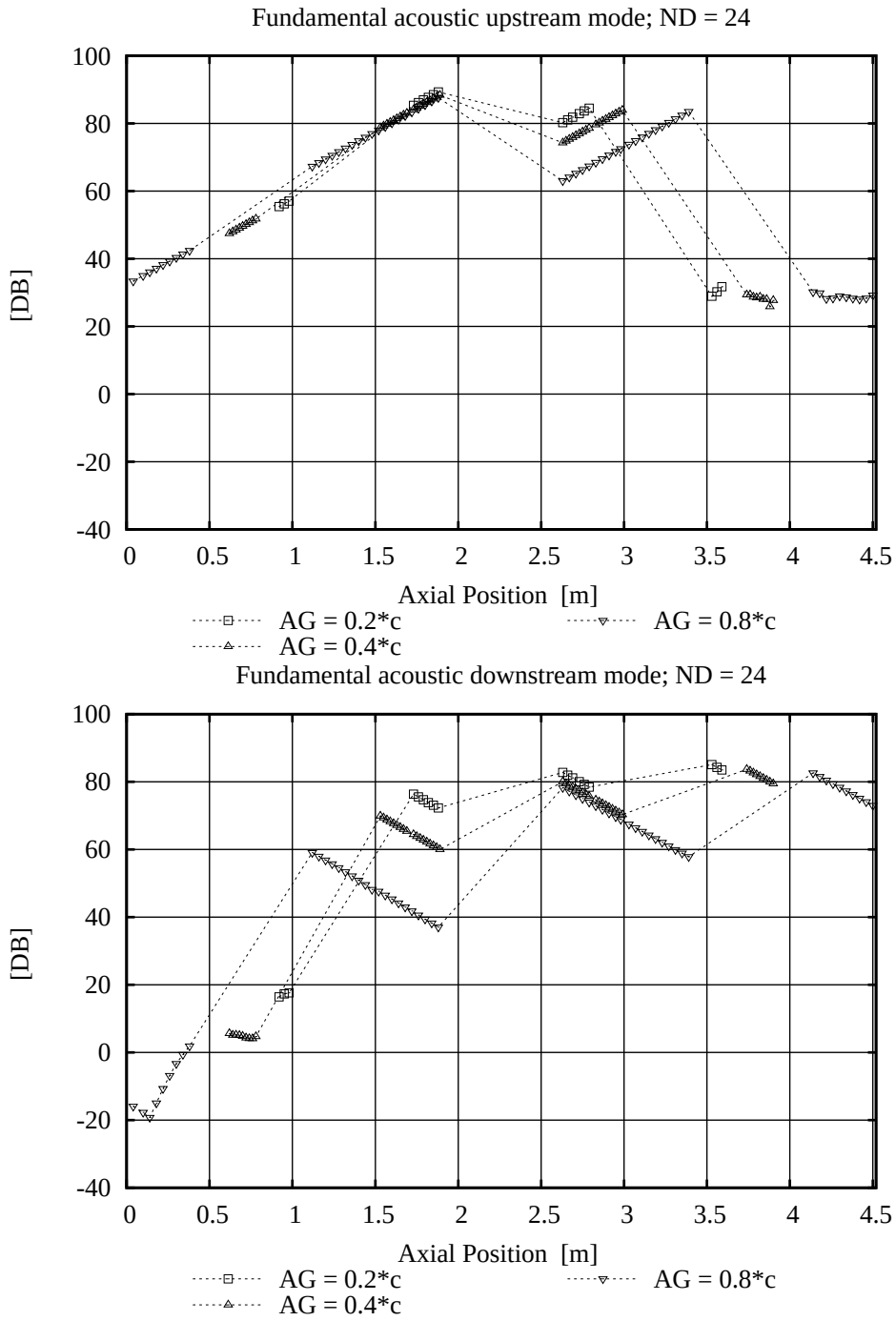

Figure 6.34: Amplitude of acoustic modes across the three blade-rows for ND = 24

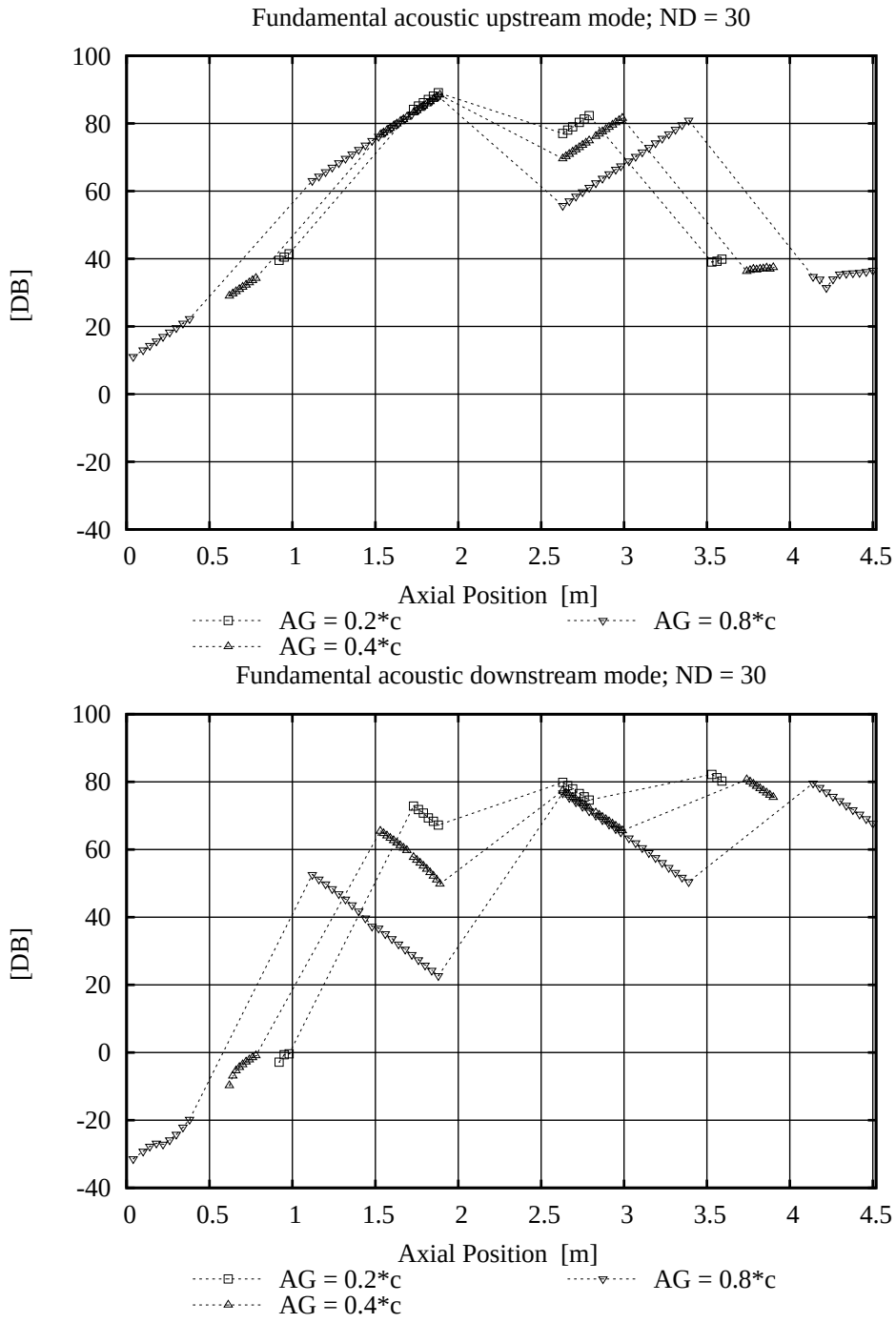

Figure 6.35: Amplitude of acoustic modes across the three blade-rows for ND = 30

6.4 Conclusions for Chapter 6

The flutter analysis of a rotating cascade of flat plates (rotor) is presented in this chapter. Multi blade-row effects on the rotor blade lift coefficient are evaluated by inserting the cascade between two other static cascades in order to represent stator/rotor/stator interactions. The influence of the axial gap between the blade-rows on multi blade-row interactions is also analysed. The simple test case geometry and the uniform mean flow conditions made it possible to verify the correctness of the present code solutions against available exact semi-analytical solutions for the isolated blade-row analysis, and against reference solutions for the multi blade-row analysis, for one axial gap configuration. Although this is a simplified representation of turbomachinery blade-rows, several important conclusions can be drawn from this work:

- The present time-linearised multi blade-row model has been successfully validated for flutter analysis via comparisons with available reference multi blade-row solutions.
- Neighbouring blade-rows have significant impacts on the aerodynamics of a given blade-row. In the present study, the rotor blade lift coefficient varied by as much as 70% with and without the presence of neighbouring blade-rows, for several nodal diameter numbers.
- The solutions obtained in the present study seem to indicate that interaction between neighbouring blade-rows has a positive impact on the avoidance of acoustic resonances in multi-stage engines.
- The effects of the interactions between neighbouring blade-rows can be significant even when the fundamental spinning mode is cut-off, depending on the axial gap between the blade-rows. In this case, the phase of the acoustic waves is the main design parameter.
- Most of the multi blade-row coupling is captured by including only the fundamental spinning mode in the analysis.
- When the fundamental acoustic mode is cut-off, only the directly adjacent neighbouring blade-rows play a major role in the overall aerodynamics of a particular blade-row. If the fundamental acoustic mode is cut-on, further blade-rows can have a significant impact on the overall aerodynamics of a blade-row.

Chapter 7

Stator-Rotor Interaction Analysis in a Turbine Stage

7.1 Introduction

The Oxford Rotor Facility designed a turbine stage (stator/rotor) to provide steady-state and unsteady flow measurements of stator-rotor interaction in a 3-D transient flow. The geometry and flow conditions were representative of real engine conditions and thus this turbine constitutes a good test case for the validation of a numerical method for unsteady stator-rotor interaction analysis.

Moss [74] used UNSFLO, the 2-D unsteady viscous code written by Giles [30], for the computation of the stage unsteady flow. The simulation results were compared with static pressure data measurements on the rotor blade surface. The agreement was satisfactory near the blade mid-height, but the overall simulation results were over-predicted. No attempt was made to compute the flow near the end-walls because the 2-D code was unlikely to provide satisfactory results where the flow includes significant radial velocity components.

Later, Vahdati [114] studied this turbine using ACE [88], which is a 3-D nonlinear time-accurate unsteady viscous flow solver. In this study, the blade-rows were represented by a number of blades such that the blades covered the same circumferential pitch in each blade-row. This way the computational requirements were reduced instead of using whole-annulus. Vahdati's steady-state and unsteady results showed a satisfactory agreement with the available data near the rotor blade midspan, though most results were over-predicted, but the agreement was really poor near the hub and the tip-gap. Vahdati attributed these differences to the fact that the rotor tip

gap was not represented in the simulation, and because the mesh was relatively coarse near the end-walls to fit with the available computational resources.

Sbardella [98] used a 3-D harmonic linearised viscous code to study the effect of the stator wake on the rotor. The stator wake was decomposed into Fourier harmonics so that the effects of each harmonic could be studied independently. Sbardella showed that the wake had a significant potential component, especially for the first harmonic. He showed that the second harmonic predictions were significantly better than the first harmonic ones, though it was later discovered that the first harmonic experimental data that his used for validation were incorrect near the rotor midspan. He validated his linearised results against the ACE nonlinear time-accurate unsteady solution, where he repeated Vahdati 's simulation, but including a rotor tip-gap and using a fine mesh near the end-walls. The overall agreement between the two codes was satisfactory but the nonlinear results were in better agreement with the data. Like Vahdati's results, the steady-state and unsteady solutions were in general satisfactory near the rotor midspan, though over-predicted, but the agreement was poor near the end-walls.

Calza [6] carefully studied this turbine using ACE and three different flow models: (i) sliding plane; (ii) single-passage multi blade-row; (iii) whole-annulus. He compared each model 's solution together and with the available experimental data on the rotor blade. The results from all three methods were, for the most part, over-predicted compared to experimental data. Calza 's results also showed, surprisingly perhaps, that the whole-annulus predictions, which included more physics, agreed less with experimental data than the other methods. Due to this, Calza could not isolate the effect of unsteady multi blade-row coupling in the solutions.

In the present analysis, the unsteady flow in this turbine is studied using the harmonic linearised multi blade-row code developed in this thesis. This analysis aims to test the new method for stator-rotor interaction analysis and to isolate the effect of the unsteady interaction between the blade-rows on the rotor blade static pressures. For that, the results from three different numerical methods, namely: harmonic linearised isolated blade-row, harmonic linearised multi blade-row and fully nonlinear time-accurate, which have various degrees of approximation of the flow governing equations, will be compared together and with experimental data.

7.2 Details of the Oxford Rotor Facility

This turbine stage was designed by the Oxford Rotor Facility to provide steady-state and unsteady flow data for 3-D transient flows. The experimental tests and the data acquisition procedure are fully explained in [74].

The design flow conditions were typical for the high pressure turbine stage of modern aircraft. The main nominal running parameters are presented in Table 7.1.

Parameter	Unit	Stator	Rotor
Number of blades		36	60
Tip diameter	mm		554
Tip clearance	mm		0.5
Axial chord	mm		24.35
Exit isentropic Mach number		0.96	0.959
Exit Reynolds number Re_{Ca_x}		1.554×10^6	
Design speed	rad/s		883.209
Inlet total pressure	Pa	804505	
Inlet total temperature	K	374.4	
Inlet circumferential flow angle	rad	0.0	

Table 7.1: Turbine stage geometry and performance data at nominal conditions.

A total of 78 flush-mounted miniature kulite pressure transducers were positioned around the rotor blades in order to provide unsteady flow data. The kulite surface coverage is shown in Fig. 7.1.

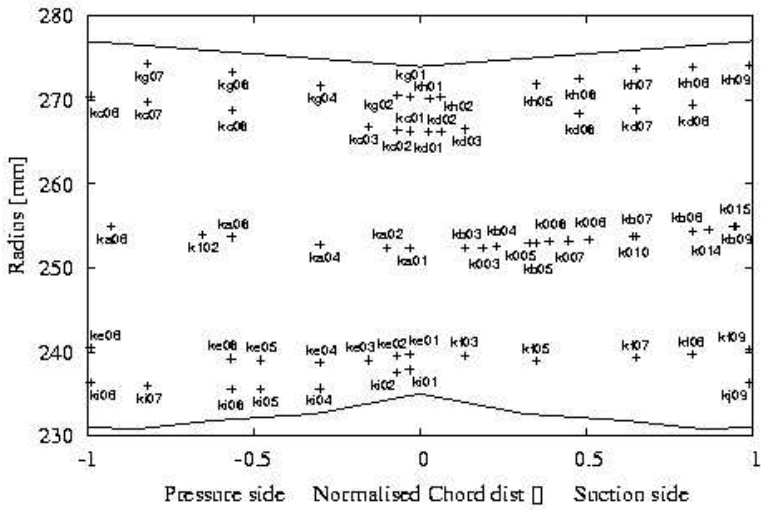

Figure 7.1: Kulites position and nomenclature

From this picture, it can be seen that the kulites have been arranged at span-wise positions of 5, 10, 50, 90 and 95 % of annulus height. These positions are usually referred as to respectively root, mid-root, midspan, mid-tip and tip sections. Additionally 13 transducers were also mounted as pitots, with a bell-mouth projecting slightly in front of the rotor blades leading edge. From these data, it is possible to recover the time-mean and first Fourier harmonic of unsteady pressures around the rotor blades. These data will be used to assess the accuracy of the results obtained by several numerical methods.

7.3 Computational Mesh

The steady-state analysis required a computational mesh spanning only one blade-passage per blade-row. The mesh was generated using LEVMAP [96, 99, 100], which is a semi-structured mesh generator. A view of the mesh can be seen in Figs. 7.2 and 7.3.

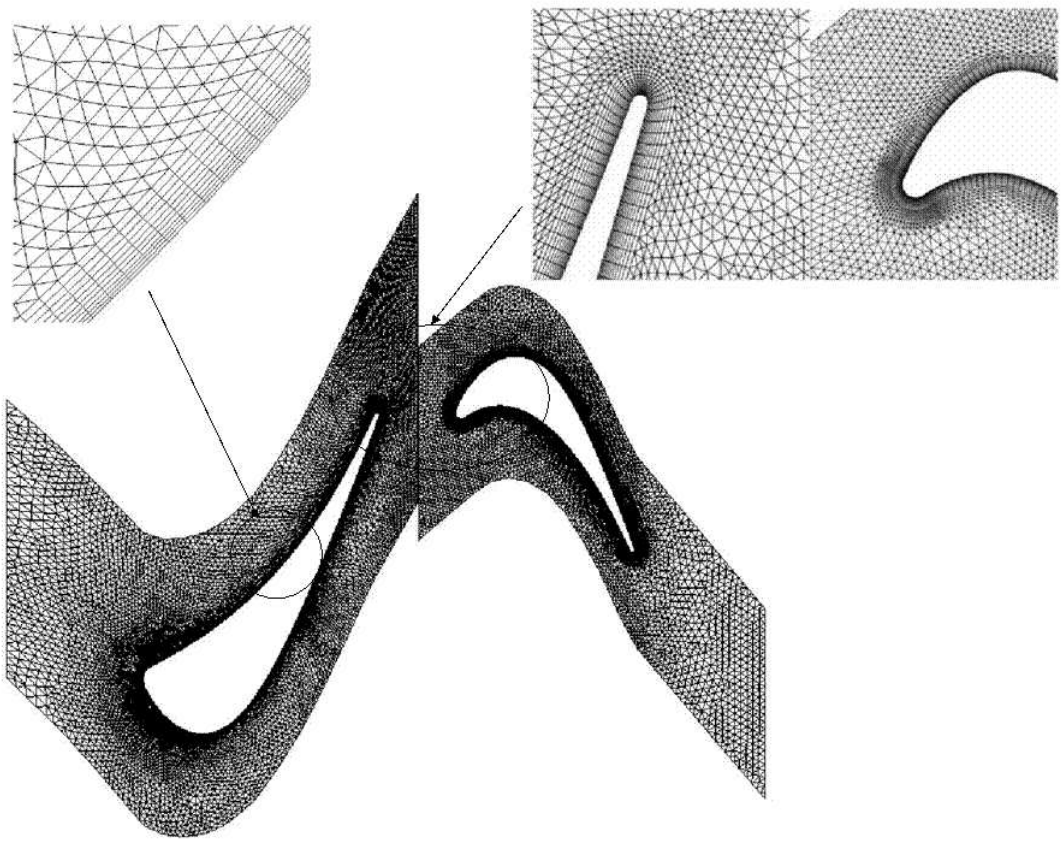

Figure 7.2: 2-D view of the turbine stage computational mesh near the midspan

A body-fitted O-grid was inserted around the aerofoil to resolve the boundary layer. This core mesh was then extended in an unstructured fashion up to the far-field

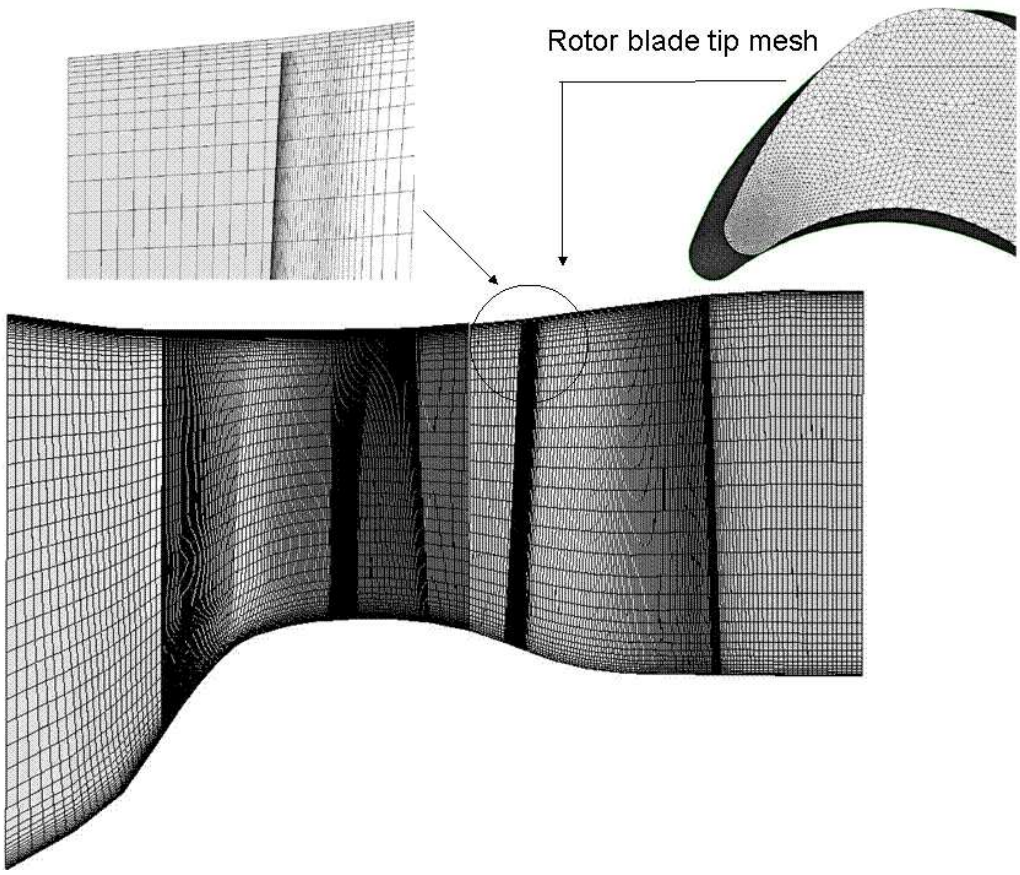

Figure 7.3: 3-D view of the turbine stage computational mesh

boundaries by ensuring the periodicity of the mesh at the periodic boundaries. Once the 2-D mesh grid was generated near the blade midspan, it was projected in the radial direction in a structured fashion. The number of mesh points in the stator and rotor passages were approximately equal to 260,000 and 330,000 respectively.

The computational mesh included only one blade-passage in the rotor domain and nothing in the stator domain for the harmonic linearised isolated blade-row analysis. The harmonic linearised multi blade-row analysis shown in this chapter included a maximum of nine spinning modes, and therefore, three blade-passage meshes were included per blade-row for this analysis. As explained in Chapter 4, the number of blade-passage meshes per blade-row allows the computation of several linearised solutions per blade-row. Therefore a copy of the same physical blade-passage mesh can be used to compute each solution in the blade-row.

A fully nonlinear time-accurate unsteady analysis is also presented in this chapter. For this analysis, the computational mesh included just enough blade-passages per blade-row to cover the same circumferential length, instead of the whole-annulus. The repeat ratio of vanes:blades is 36:60; therefore the number of blades per blade-

row could be reduced to 3:5 as can be seen in Fig. 7.4.

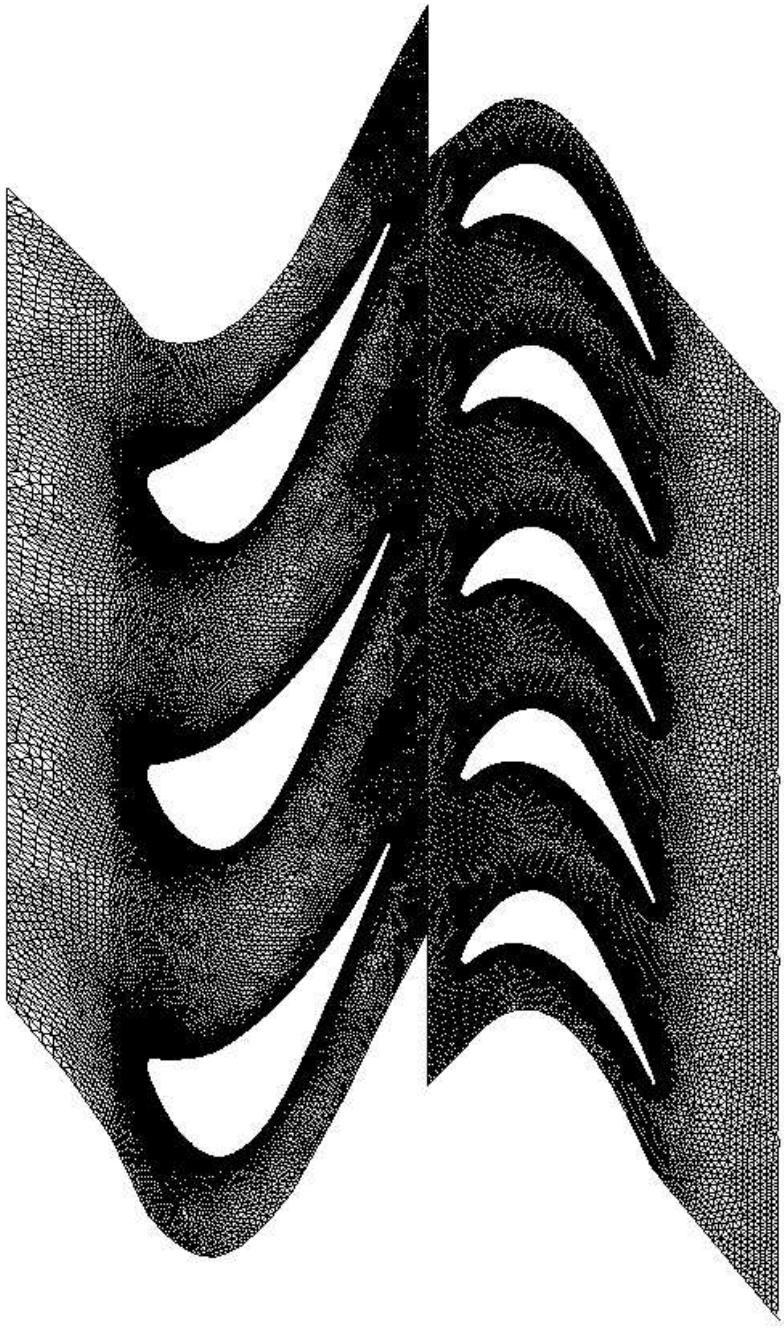

Figure 7.4: 2-D view of mesh which includes eights blade-passages for the nonlinear analysis

7.4 Steady-state Flow Analysis

With the premise that the harmonic linearised multi blade-row computation will be based on both the stator and the rotor steady-state solutions, it is important that the steady-state flow be representative of the real flow in the region between the blade-rows. One of the drawbacks with the mixing plane boundary condition that was available to the author, was that the pressure field is circumferentially averaged at the stator exit boundary. Such averaging causes the potential component of the stator wake to disappear from the real wake. This is an important issue because the stator wake is then imposed as the flow forcing at the rotor inlet boundary for the subsequent rotor harmonic linearised unsteady flow analysis. An alternative approach commonly used in the industry to avoid this problem is to artificially move the stator exit boundary further away from the vanes, and to decompose the stator wake into Fourier harmonics, sufficiently away from the exit boundary, so that it is not corrupted by the way the exit boundary is applied. Such strategy is not applicable in the present case. In fact, the harmonic linearised multi blade-row analysis requires that the flow be continuous at the inter-row boundary, where the spinning modes are numerically transfered from one blade-row to the next. Therefore, the wake's decomposition into harmonics must be achieved exactly at the stator exit boundary. Because of this restriction, the author decided to compute the stator and rotor steady-state solutions using through flow boundary conditions and by imposing a stator exit boundary condition such that the pressure field is allowed to vary circumferentially. Therefore, the through flow boundary conditions were assumed to be sufficiently representative of the real flow conditions in the following sections, but comparisons with the mixing plane solution will also be shown for completeness.

7.4.1 Stator Steady-state Flow

No measured data were available to validate the stator steady-state solution. However, Moss [74] who studied the same test case, gave some indications on what the flow looks like. This information, plus comparisons with the available boundary conditions, will be used to verify the correctness of the present stator solution.

Figures 7.5 and 7.6 compare the stator inflow through flow boundary conditions with the computed steady-state solution, showing a good agreement. Very small discrepancies are noticeable near the inner radius but these only occur because the flow solution has been measured slightly away from the stator inlet boundary and the end-walls boundary conditions are already affecting the flow.

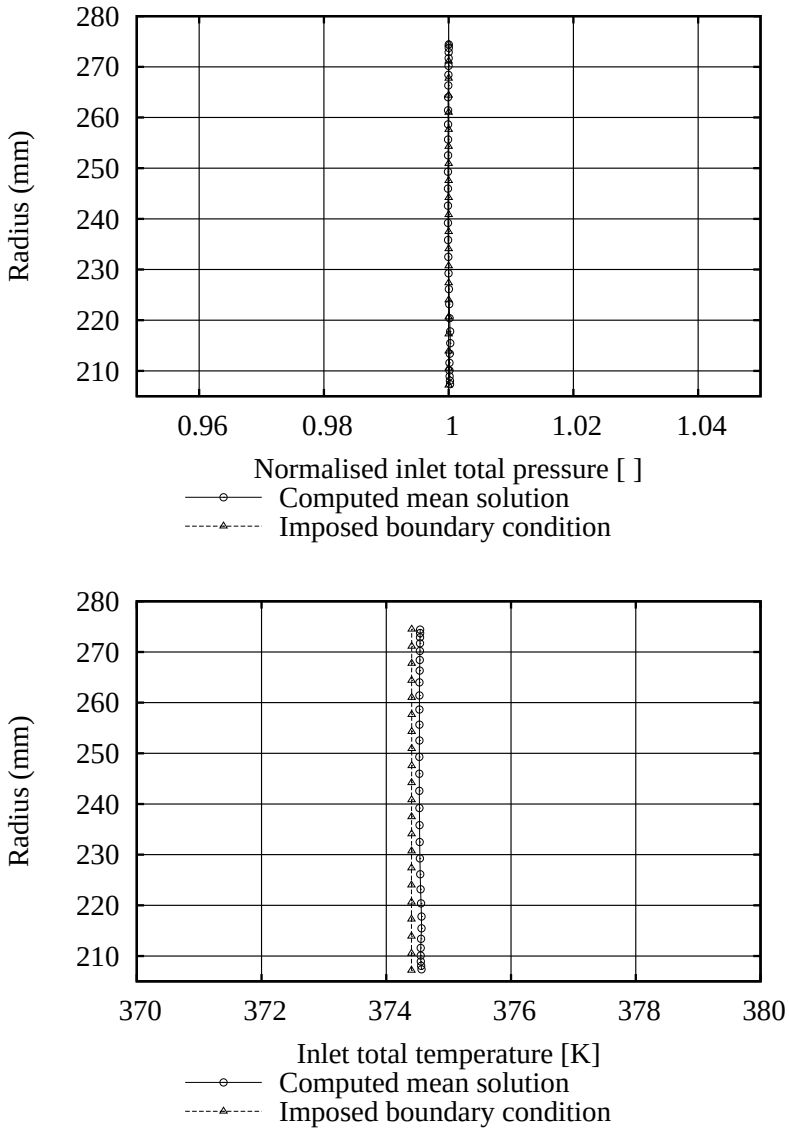

Figure 7.5: Computed stator inflow total pressures (upper) and total temperatures (lower) compared with through flow boundary conditions

A constant total pressure and total temperature profile is imposed at the stator inlet so as to match the experimental conditions. As the flow approaches the stator vanes, it is accelerated by the reduction of the cross section of the annulus, the inner radius increases rapidly, while the outer radius decreases slightly as shown in Fig. 7.7. This trend is reflected by the radial flow angle profile, which goes from small negative values at the outer radius to large positive values at the inner radius.

Figure 7.8 compares the circumferentially averaged static pressure profile computed at the stator outlet boundary with the imposed boundary conditions. In this figure, the static pressures are normalised by the inlet total pressure. Again, a very good match is found between both results.

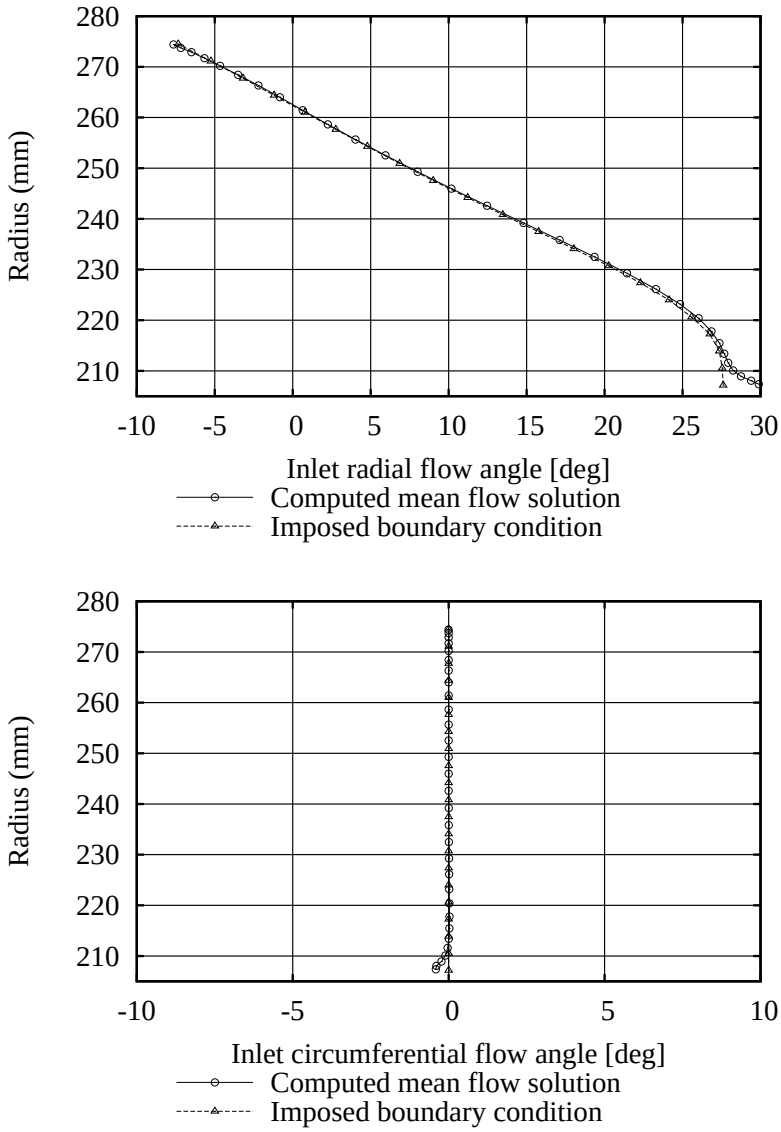

Figure 7.6: Computed stator inflow radial flow angle (upper) and circumferential flow angle (lower) compared with through flow boundary conditions

At convergence, the computed mass flow rate going through the stator was predicted as approximately 29.3 kg/s. First, the computed steady-state solution is examined near the midspan of the vanes. At this location, Fig. 7.9 plots the computed entropy and total pressure contours. The entropy contours are useful in that they show the vane wake and more generally areas of dissipation as the flow passes through the vanes. It can be seen that the vane wake is not very thick and its main path is a straight line from the vane's suction side line to the vane's trailing edge. The total pressure contours also indicate that the total pressure losses are localised on the vane wake near the midspan.

Figure 7.10 shows the relative Mach number contours near the vane's midspan. It

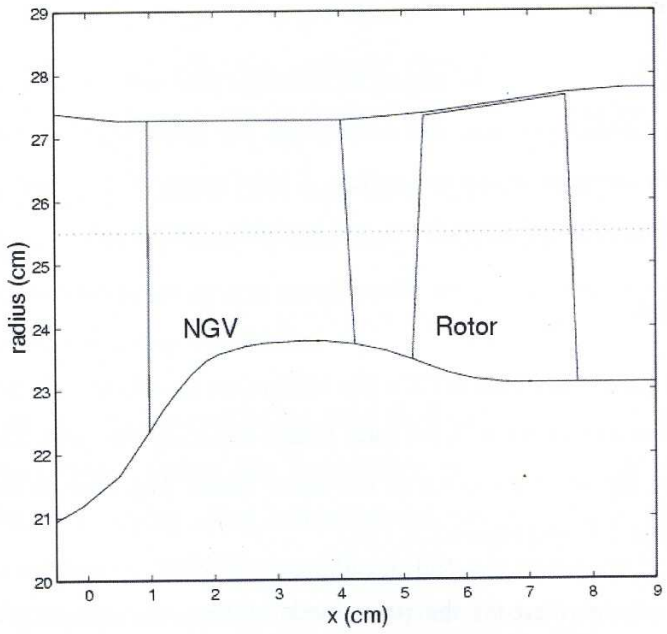

Figure 7.7: Meridional view of the RT27 turbine stage.

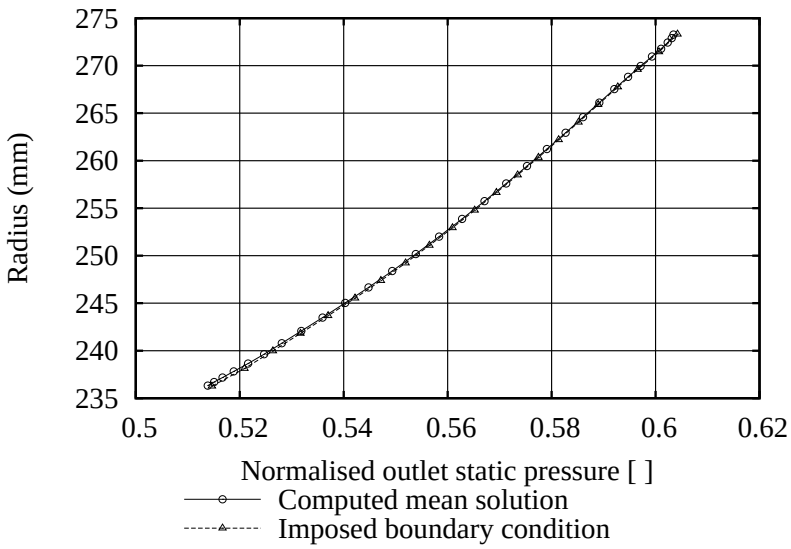

Figure 7.8: Computed stator outlet static pressures compared with boundary conditions from through flow analysis

can be seen that the steady-state flow is transonic. The nominal vane exit Mach number is 0.96, which means that there might be a shock wave near the vane exit. Crossed hot wires were mounted at the mid-height section of the rotor during the tests. These hot wires provide relative Mach number and inlet angle data to complement the kulite total pressure readings. In the measured data, Moss [74] observed

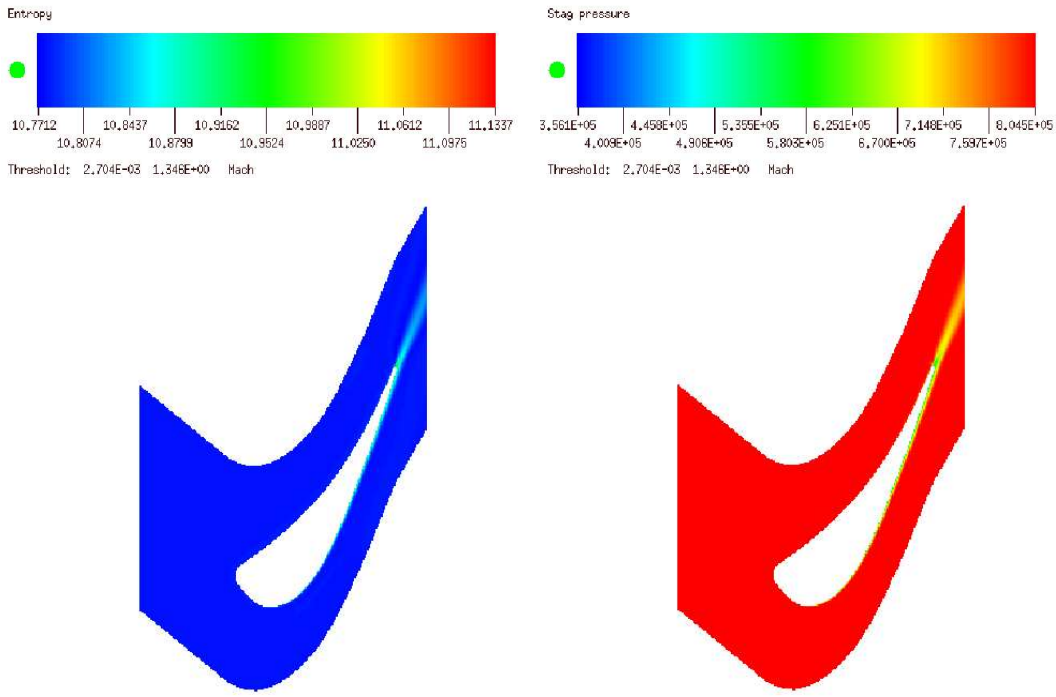

Figure 7.9: 2-D mean entropy contours (left) and total pressure contours (right) near the vane's midspan

sharp peaks of total pressure corresponding to peaks in static pressures, which suggests that there could be a weak shock wave at that location. However, no such shock is visible from the 2-D contours shown in Fig. 7.10. To confirm this observation, a constant x line was drawn across this 2-D section near the outlet boundary. The steady-state quantities were taken along this line and plotted in Fig. 7.11. The line plot exhibits a profile of high relative Mach number gradients at the vane outlet, but it does not show any shock wave in this region of the flow. Also from Fig. 7.10, one can see that a segment of lower Mach number expands from the vanes trailing edge in the direction quasi normal to the wake. This segment has two effects: (i) it yields to a local Mach number peak between this low Mach number segment and the vane wake; (ii) it creates a zone of higher static pressure as shown in the right hand side plot of Fig. 7.11.

Figures 7.12 presents the total pressure contours at the stator exit plane. For a better interpretation, consider Figs. 7.7 and 7.13. It can be seen that the mean flow is mostly running inwards, i.e. towards the region of lower radius in order to follow the shape of the annulus. Figure 7.12 shows that the total pressure in the wake decreases as the flow goes from tip to root. Near the inner annulus radius, there is a region of higher total pressure loss which probably occurs because the wake merges with the inner end-wall secondary flow. Experimental data suggest

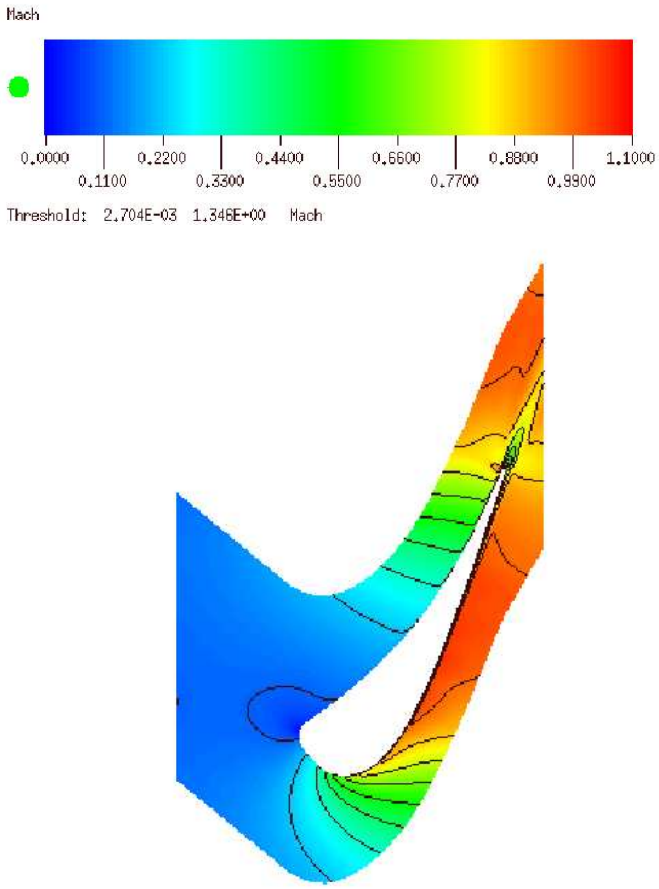

Figure 7.10: 2-D mean relative Mach number contours near the vane's midspan

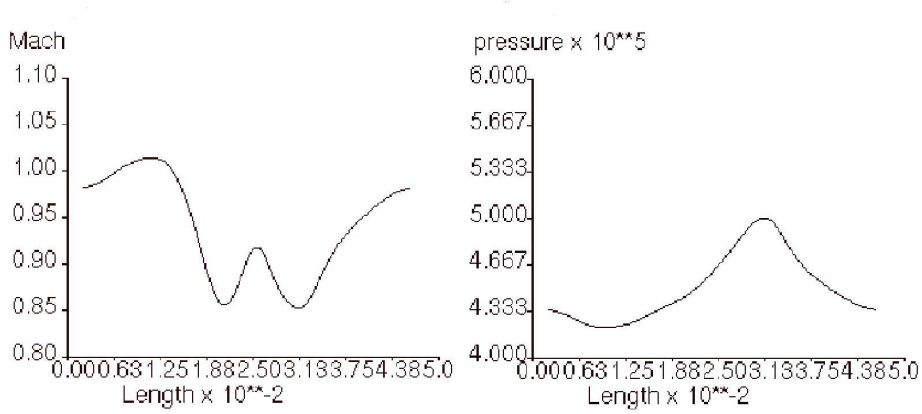

Figure 7.11: Constant x line plot near the vane outlet boundary at the vane midspan

that a large pressure deficit occurs at about 40% of a wake cycle earlier than the mid-height wake. Such a feature is not seen in the present vane mean flow solution, though the pressure loss is slightly shifted from the rest of the wake in this region of the flow. This result is not surprising as Moss [74] attributed this shift in total

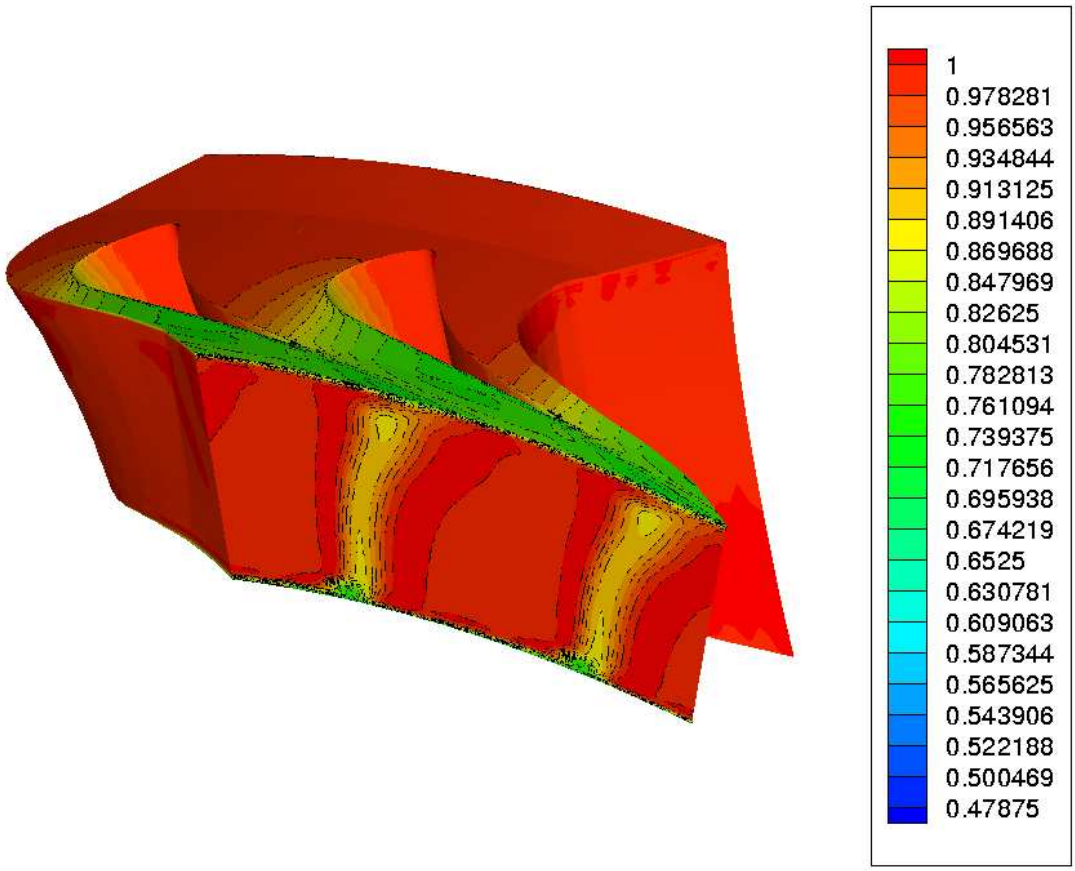

Figure 7.12: Stator outlet total pressure normalised by inlet total pressure

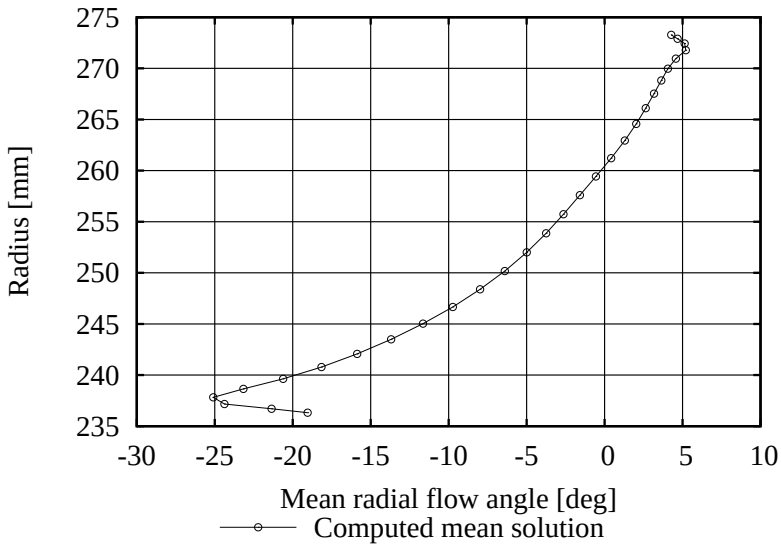

Figure 7.13: Circumferentially-averaged radial flow angle at vane outlet plane

pressure loss at the root to unsteady stator-rotor interaction effects.

Another point of interest in Fig. 7.12 is that the wake appears to run almost radially at the vane exit plane. This is an expected feature of the flow since the trailing edge of the stator blades is stacked radially as seen in Fig. 7.14. Moss [74] presented an ensemble-averaged 2-D plot of the relative total pressure field measured during the experiment at the vane exit. These data confirm that the vane wake ran almost radially during the experiment, which supports the present solution.

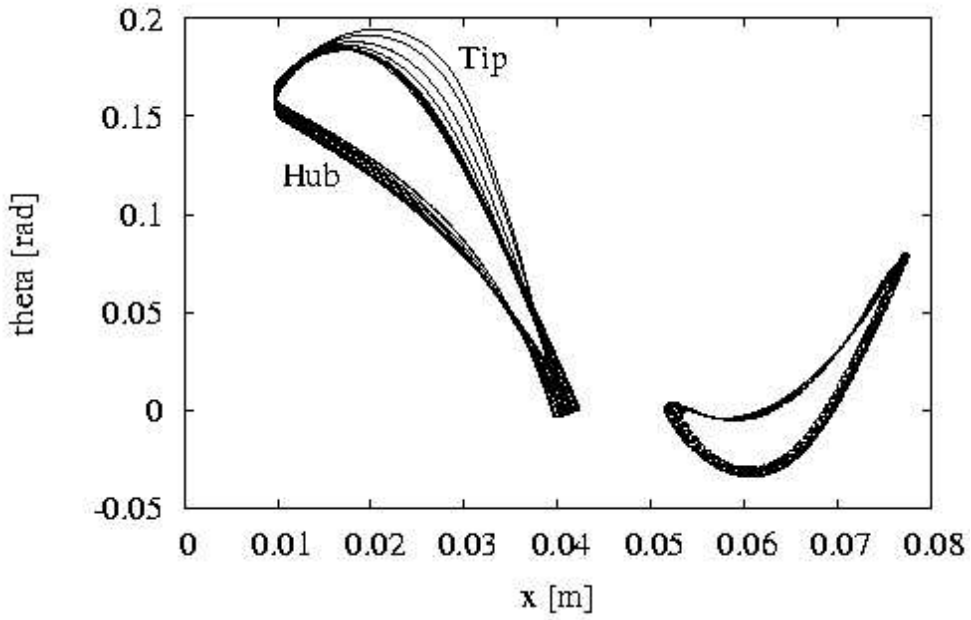

Figure 7.14: Radial sections of stator and rotor blades at several radial levels showing radial alignment of vane's trailing edge and rotor leading edge

Finally, Fig. 7.15 shows the radial profile of the computed circumferential angle and Mach number of the mean flow at the vanes exit plane. It can be seen that the circumferential flow angle is greater in magnitude at the outer radius. This feature is understood by looking at Fig. 7.14 where it can be seen that the stator blade exit flow angle increases towards the outer radius.

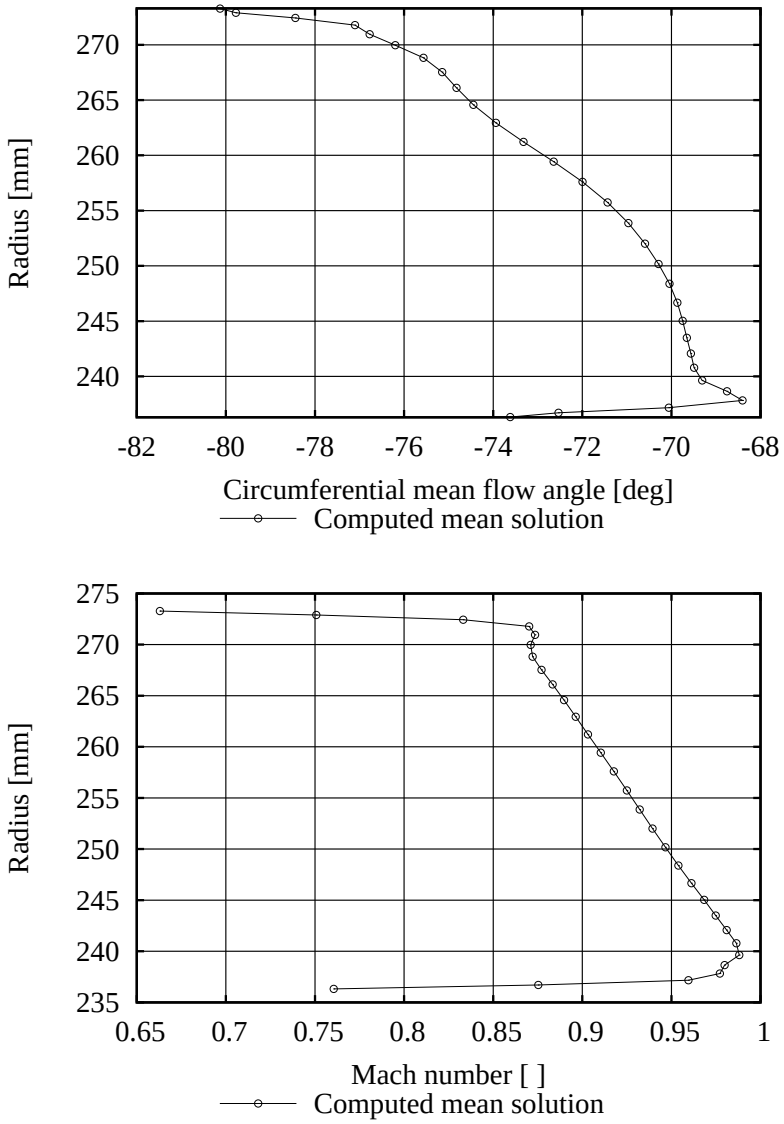

Figure 7.15: Radial variation of the circumferential mean flow angle (upper) and mean flow Mach number (lower) at the vane exit plane

7.4.2 Rotor Steady-state Flow

First, the computed rotor solution at the inflow/outflow boundaries is compared with the imposed boundary conditions. It is then verified that the boundary conditions are both consistent between the stator and the rotor rows. Finally, measured static pressures around the rotor blade are used to validate further the computed solution in the rotor passage.

As for the stator solution, the rotor steady-state solution was computed using through flow far-field boundary conditions. The numerical solution obtained at the far-field boundaries is compared with the imposed boundary conditions. The results are presented in Figs. 7.16 and 7.17, which show that the boundary conditions are again well matched. At convergence, the computed mass flow rate passing through the rotor was approximately 29.29 kg/s, which is very close to the mass flow rate computed in the stator. Hence, the stator and rotor steady-state solutions are both consistent in terms of mass flow rate.

With the aim to validate completely the boundary conditions which have been used for this computation, three different steady-state solutions are now considered: (i) the present vane outlet solution; (ii) the present rotor inlet solution; (iii) the inter-row solution obtained from a mixing plane calculation. The absolute values of total pressures, total temperatures, and flow angles are compared in Figs. 7.18 and 7.19. These figures show that the three solutions match reasonably well everywhere except near the end-walls. The agreement is worst at the hub. The through flow analysis seems to have overestimated the rotor total pressure losses near the hub, while the mixing plane solution and the vane exit solution match quite well at this location. The circumferential flow angle prescribed by the through flow analysis is also lower near the hub than that obtained by the two other solutions. The radial flow angle exhibits the greatest discrepancy between the solutions, up to five degrees near the midspan. None of the three solutions agree for this parameter, thereby making difficult the assessment of which solution represents better the correct boundary conditions at the inter-row boundary.

Figure 7.20 shows the relative Mach number contours computed near the blade midspan. The scale of this figure reveals that the flow is transonic in the rotor passage.

Figure 7.21 presents the computed static pressure contours around the rotor blade. From this plot, it appears that the flow is mostly 2-D near the midspan of the pressure side, though the particle traces highlight significant radial migrations. From the midspan, the particles are driven by the pressure gradients and go in the direction

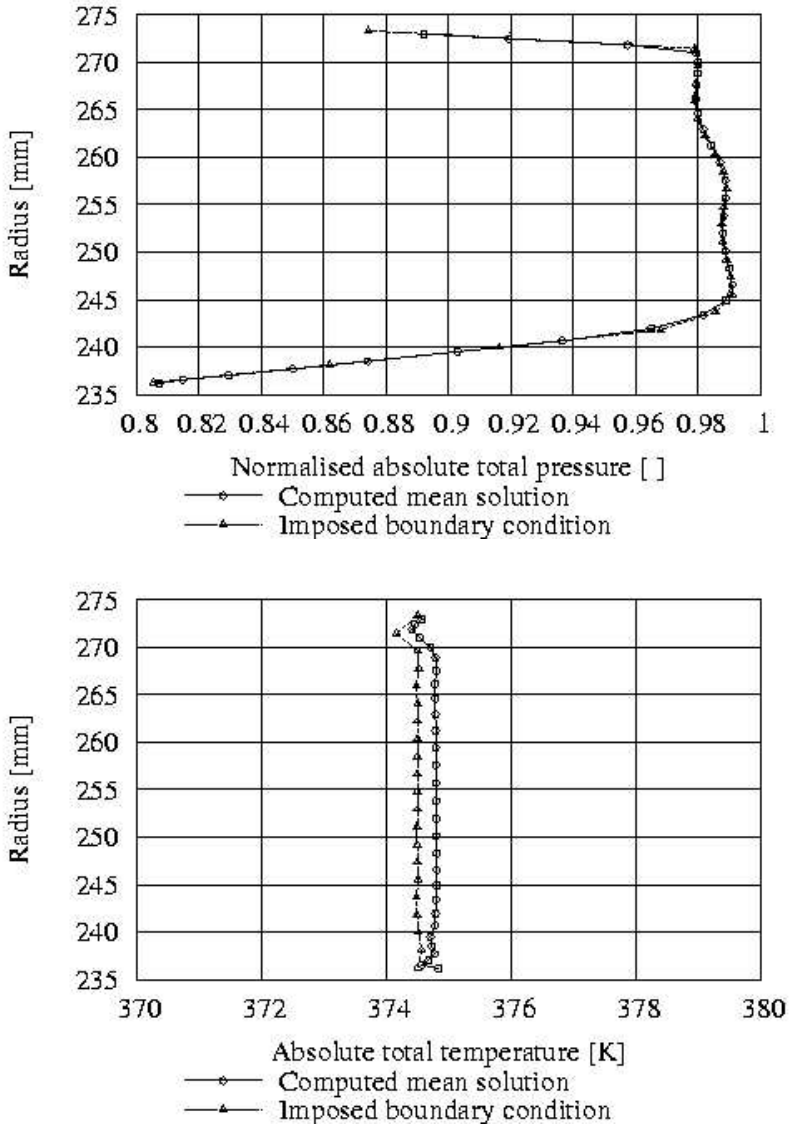

Figure 7.16: Comparisons rotor inlet absolute total pressure solution (upper) and absolute total temperature solution (lower) with the imposed boundary conditions

of the tip leakage. On the other side of the blade, the flow is somewhat more complicated. Near the midspan, the flow is quasi 2-D with the particles going mainly in the axial direction. Near the hub, there is a clear separation line from which the particles migrate towards the midspan, which is caused by the hub passage vortex. Near the tip, a separation line can also be seen, which results from the interaction between the passage and tip leakage vortices.

Next, the radial profiles of total pressures are compared with available experimental data near the rotor leading edge. The results of these comparisons are shown in Fig. 7.22. Importantly, it can be seen that the total pressures are over-predicted at

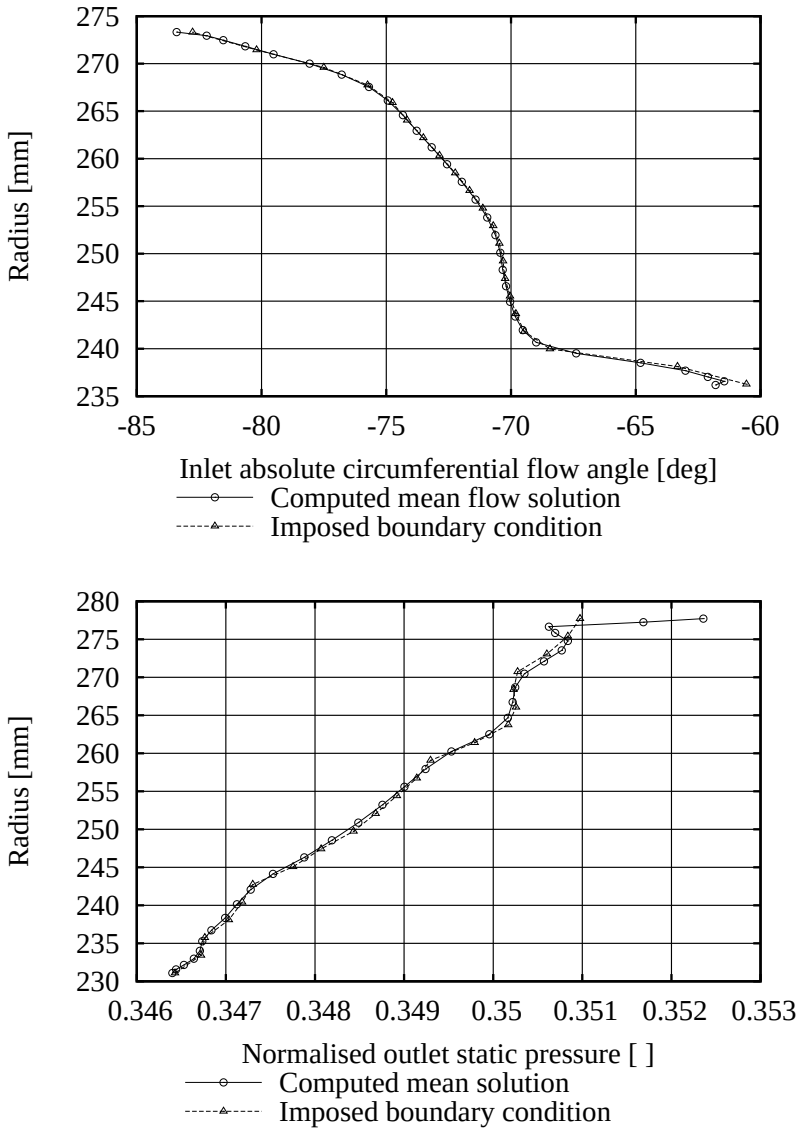

Figure 7.17: Comparisons rotor inlet absolute flow angle solution (upper) and static pressure solution (lower) with the imposed boundary conditions

most radial levels, though the overall trend seems to be correct. The level of total pressure is correctly predicted only near the tip. Since these data were measured near the rotor LE, and thus near the rotor inlet boundary as well, these results seem to indicate that either: (i) the boundary conditions used for the computations are not totally correct, and thus induce a level of total pressure which is too high; (ii) something is not correctly represented in the simulation. For example, it may be wondered whether there is a bleed missing, or if the results' discrepancies could be caused by blade profile variability due to manufacturing tolerances.

Figure 7.23 compares the static pressures computed at several kulite positions around the rotor blade with experimental data. These results are in good overall agreement

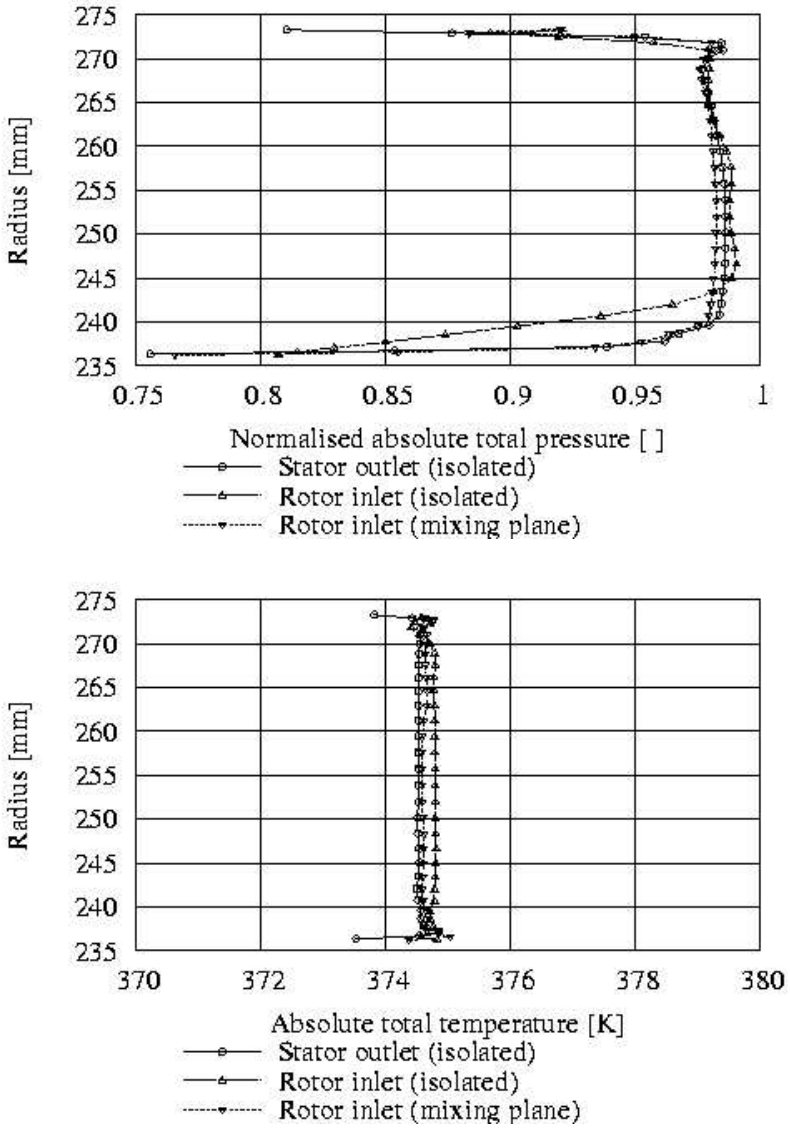

Figure 7.18: Absolute total pressure (upper) and total temperature (lower) compared at the stator 's exit plane and rotor inlet plane - Mixing plane boundary condition

with available measured data except near the hub. Such a result was expected since the total pressure distribution shown in Fig. 7.22 already highlighted significant discrepancies in this region.

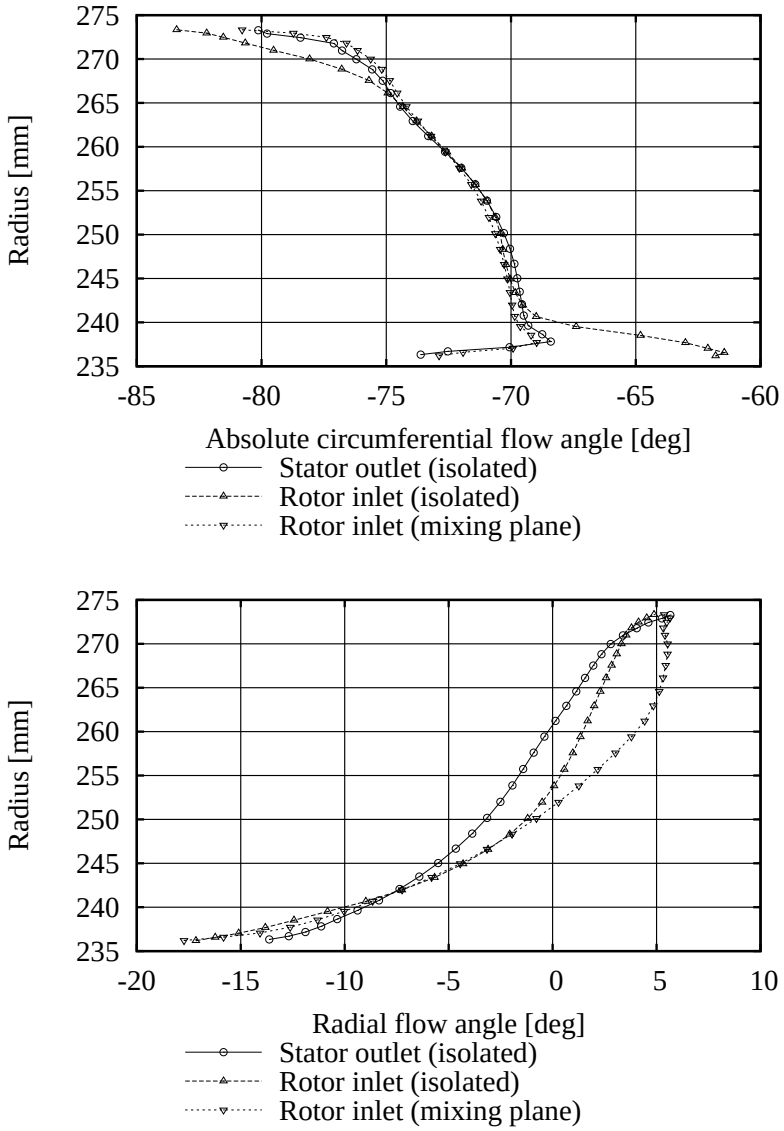

Figure 7.19: Absolute circumferential flow angle (upper) and radial flow angle (lower) compared between stator exit plane and rotor inlet plane - Mixing plane boundary condition

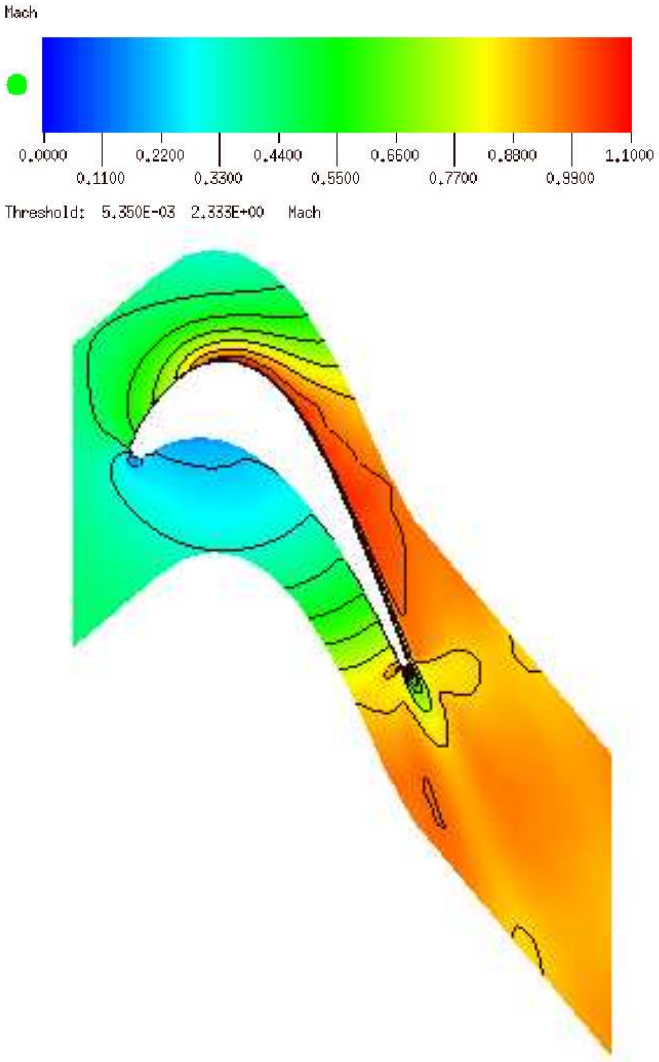

Figure 7.20: 2-D relative mean Mach number contours at rotor's midspan

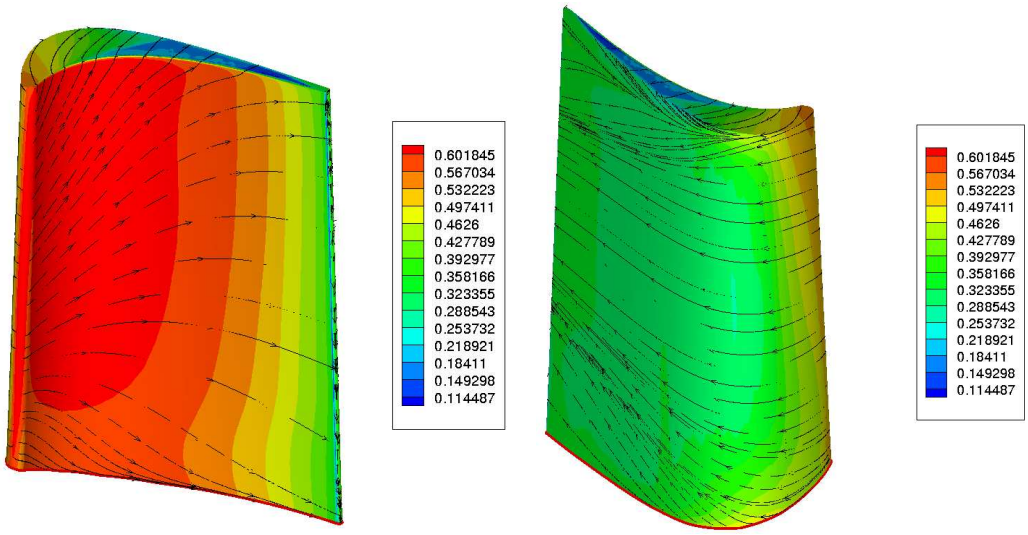

Figure 7.21: Static pressures normalised by stage inlet total pressure; pressure side (left) and suction side (right) with particle traces

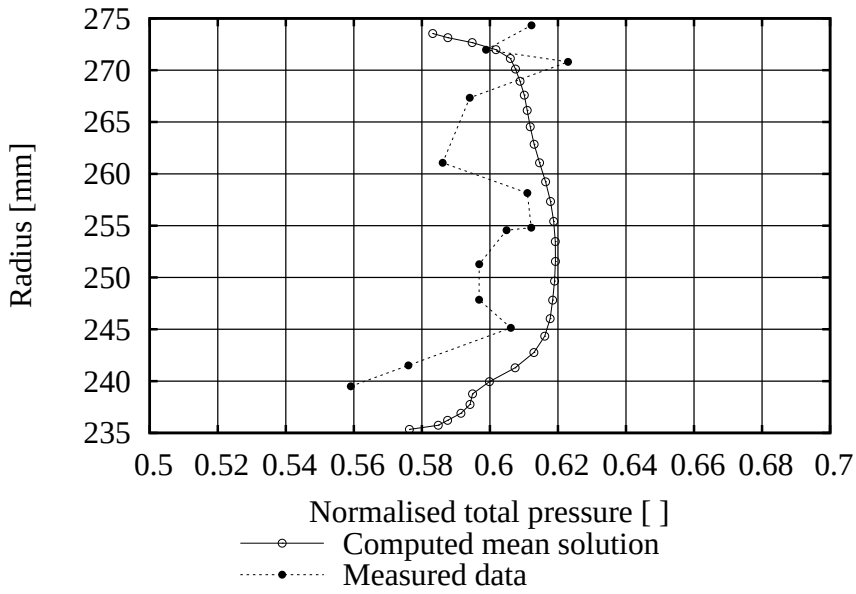

Figure 7.22: Radial variation of relative total pressures near the rotor leading edge

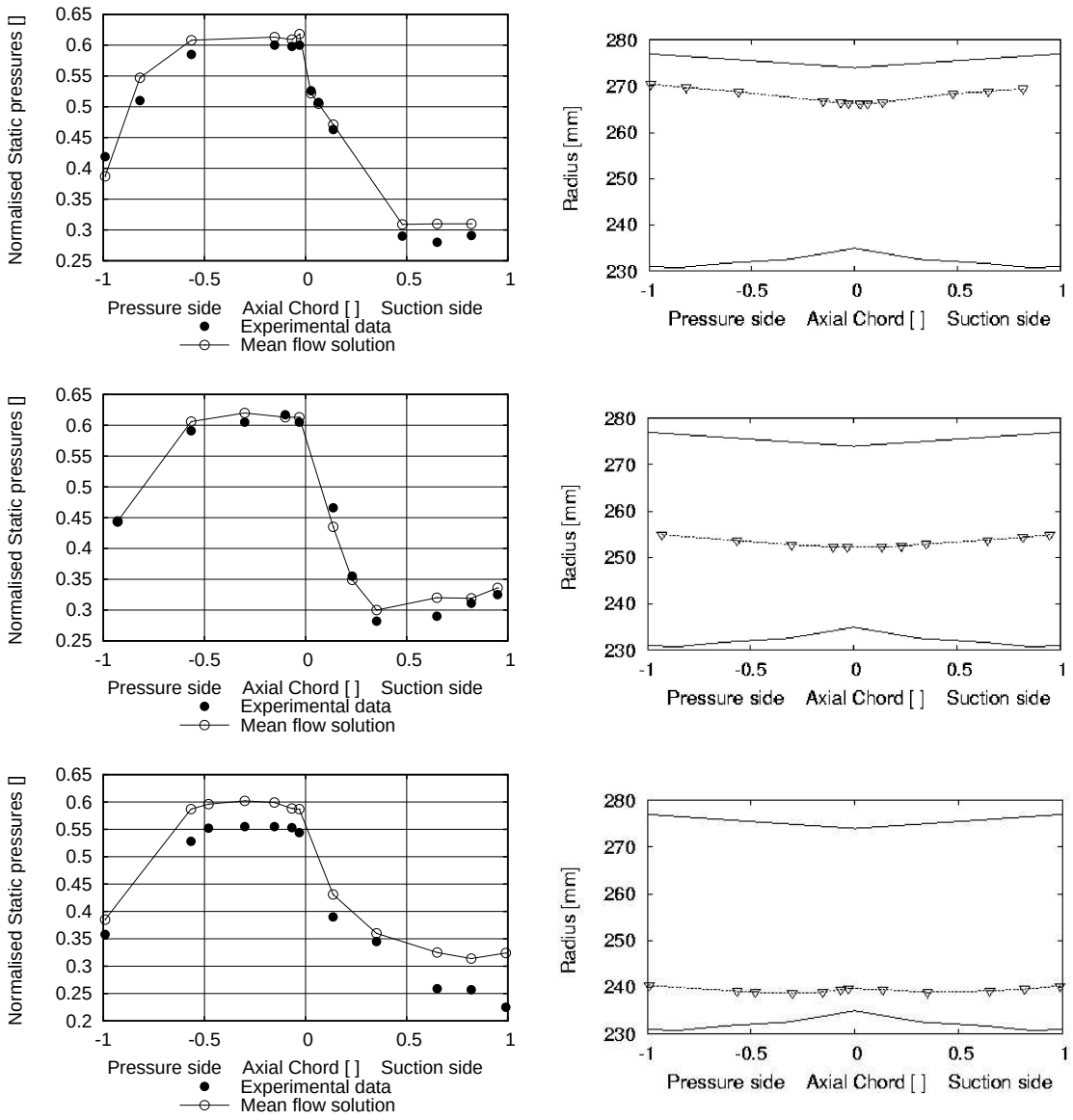

Figure 7.23: Steady-state pressures at the tip (top), midspan (middle), and hub (bottom); measured vs. computed

7.4.3 Concluding Remarks for Steady-state Flow

It is shown in this section that the steady-state solution in this turbine stage agrees well with experimental data, though some local discrepancies are also apparent. An overview of the main results is listed below.

Regarding the stator solution:

- The computed stator wake has the correct shape and directionality when compared against measurements. The measurements also show a loss of total pressure near the hub, which occurs about one quarter of a cycle earlier than the wake losses. This feature has not been captured by the numerical simulation. Finally, measurements highlighted the possibility of a small shock wave occurring near the midspan, slightly upstream of the rotor LE, but no evidence of such shock could be found in the numerical solution.

Regarding the rotor solution:

- The mean static pressures, that are computed around the rotor blades, agree well with experimental data, especially near the blade midspan and near the tip. Significant discrepancies with experimental data are observed near the hub, where the static pressures are over-predicted. It was found that the total pressure loss in this region has not been correctly captured by the present simulation. Two main reasons could explain such results: (i) incorrect boundary conditions at the rotor inlet plane; (ii) something may not be represented in the simulation of this turbine, maybe a bleed or blade profile variability?

7.5 Unsteady Flow Analysis

Based on the previous steady-state solutions, a detailed analysis of the unsteady stator-rotor interaction for this turbine stage will now be presented. For this analysis, three different numerical methods have been used: (i) harmonic linearised isolated blade-row; (ii) harmonic linearised multi blade-row; (iii) the fully nonlinear time-accurate unsteady. As discussed in Chapter 2, each of these methods approximates differently the Navier-Stokes equation. It will be shown that the harmonic linearised multi blade-row results are an improvement compared to the harmonic isolated blade-row results.

7.5.1 Harmonic Linearised Isolated Blade-row Analysis

For the harmonic linearised analysis, it is assumed that the unsteady disturbances are small compared to the underlying steady-state flow. Based on this assumption, an harmonic linearised analysis including solely the rotor blade-row, can be conducted as follows. First the stator outlet steady-state solution is decomposed into a Fourier series. Then, each Fourier harmonic of interest can be independently imposed as an unsteady perturbation impinging on the rotor. The unsteady perturbation is imposed at the rotor inlet boundary condition, and a rotor harmonic linearised unsteady solution can be determined using an harmonic linearised isolated blade-row method. The results for each of these steps, when applied to this turbine stage, are presented below.

Stator Wake Extraction

The flow field attached to the stator is steady but has spatial non-uniformities in both the circumferential and radial directions. For each radial level, the steady-state primitive variables are decomposed into an axisymmetric steady-state part plus a steady-state non-uniform part in a quasi-3-D manner. Using the subscript 1 to refer to the steady-state flow solution in the stator frame, this decomposition can be written as follows

$$\mathbf{U}_1\left(x_1, r_1, \theta_1\right) = \bar{\mathbf{U}}_1\left(x_1, r_1\right) + \tilde{\mathbf{U}}_1\left(x_1, r_1, \theta_1\right) \tag{7.5.1}$$

Because of circumferential periodicity, the steady-state non-uniform part of the flow can be decomposed into Fourier series as follows:

$$\tilde{\mathbf{U}}_1(x_1, r_1, \theta_1) = \sum_{n_1} \hat{\mathbf{U}}_{n_1}(x_1, r_1) . e^{i n_1 B_1 \theta_1} \tag{7.5.2}$$

In the present analysis, the rotor rotational speed is negative ($\Omega < 0$) due to the θ sign convention adopted in the blade definition. In order to maintain the frequency of unsteadiness positive in the rotor frame, the values for n_1 have to be negative. Hence from now on in this chapter, the first Fourier harmonic solution will always refer to the choice of $n_1 = -1$. For this value of n_1, the frequency and inter-blade phase angle of the stator passing wake in the rotor are given by:

$$\omega_2 = -B_1 \Omega \tag{7.5.3}$$

and,

$$\sigma_2 = -\frac{2\pi B_1}{B_2} \tag{7.5.4}$$

The solutions for the circumferentially-averaged first Fourier harmonic amplitudes and phases of the primitive variables at the stator outlet are presented in Fig. 7.24. The velocities and density amplitudes are plotted in their real units while the pressures are normalised by the stage inlet total pressure. As would be expected, the greatest amplitudes are seen at near the hub, where secondary flow effects are dominant. By comparing Figs. 7.24 and 7.8, it can also be seen that the amplitudes of the first harmonic of unsteady pressures are only about ten times smaller than their steady-state counterparts. Therefore, we are within the limit of validity of the linear assumption here. In fact, it could be challenged whether the rotor unsteady flow is really linearisable in this case. The answer to this question will be given later in this chapter by comparing various unsteady solutions.

Figure 7.24 also shows the three dimensionality of the stator wake. This three dimensionality means that good overall unsteady flow predictions are unlikely to be obtained using a 2-D model. Also note from this figure that the radial profiles for density and pressure have some striking similarities, which is probably the sign that a strong acoustic component drives the pressure profiles at the stator outlet.

Numerical Solution

The stator wake perturbations, shown in Fig.7.24, generate an aerodynamic unsteady response in the rotor which is periodic in time and space at frequency ω_2 and IBPA σ_2 given by (7.5.3) and (7.5.4) respectively. The following results concern the

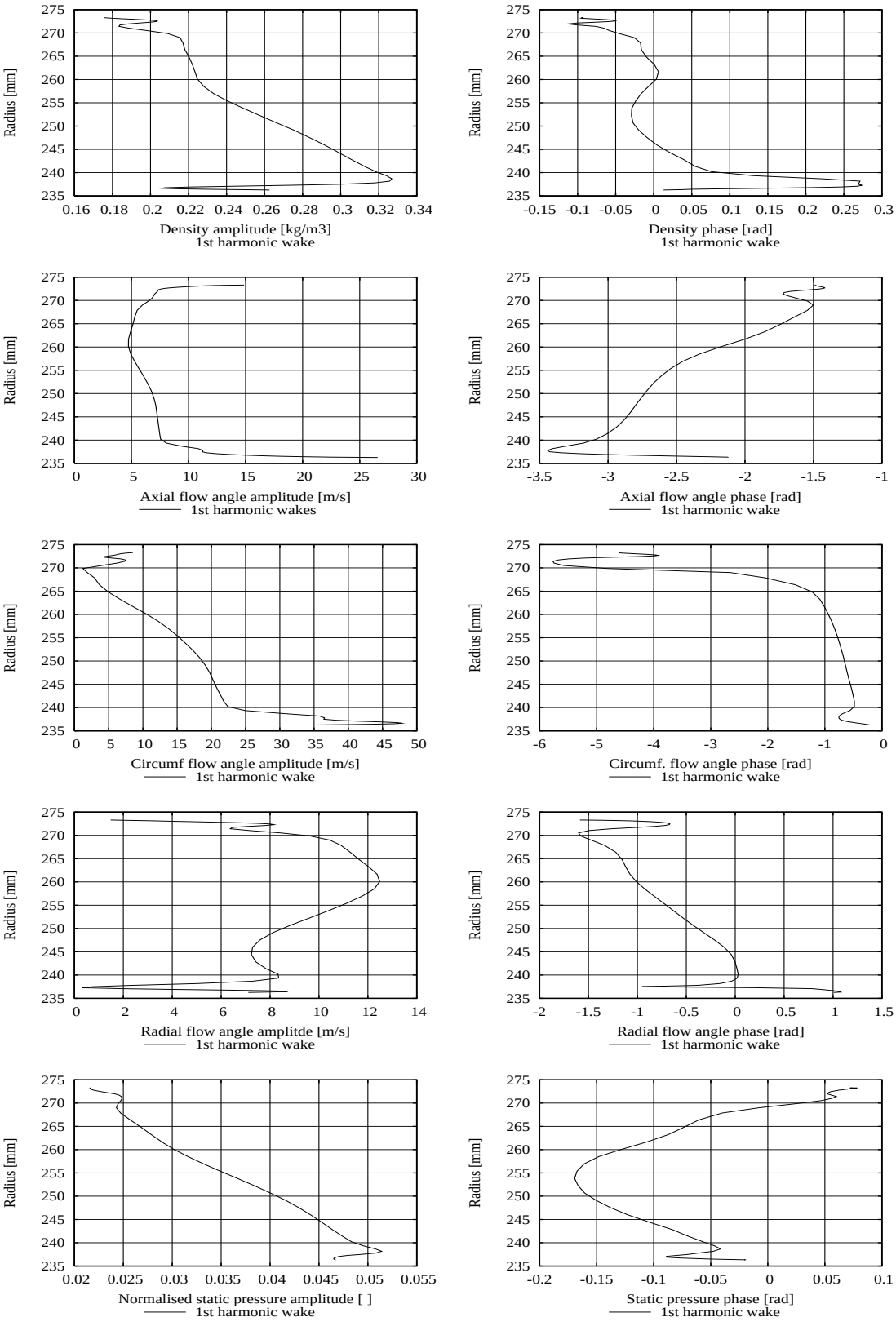

Figure 7.24: Stator wake circumferential Fourier harmonic = -1 of the primitive variables at several radial levels

1st harmonic unsteady flow response. Figure 7.25 shows the computed real part of unsteady pressures at the inter-row boundary as seen from the rotor blades. Five blade-passages are included to represent the direct periodicity. As explained earlier, the unsteady flow is directly periodic - i.e. with zero phase shift - between the lower periodic boundary of the first passage and the upper periodic boundary of the last passage, when all five blade passages are included. These results, in fact, represent a snapshot in time of the unsteady solution, which is varying in time at frequency ω_2 around the state presented in this figure. Figure 7.26 shows the contours of static pressures computed near the blades midspan. In this figure, the results are shown in terms of real and imaginary parts of unsteady pressures. One can see the complex features of the flow. The pressure disturbance impinges first on a large part of the rotor blade suction side due to its curvature. An animation of the results around the blade LE shows that the pressure perturbation "wraps around" during a large part of the time period, before it leaves the blade LE to go to the next blade crossing the stator wake. The animation also reveals that a pressure wave travelling downstream in the region of the blade pressure side is sucked towards the other side of the blade after it passes the TE. Once on the other side, the pressure wave travels in the upstream direction, and thus impinges on other downstream pressure waves in the suction side region. The author believes that this result is physically correct since the pressure gradients between the blade's pressure side and suction side would tend to drive the waves in the region of lower pressure. Also, some numerical reflections can be seen near the rotor outlet boundary. These are easily distinguishable by the wiggles that they produce. However, the reflected waves do not seem to corrupt the numerical solution near the blade as the rotor outlet boundary was placed sufficiently far away from the blade TE.

Figures 7.27 and 7.28 show the three dimensionality of the solution on the rotor blade. Even near the midspan, the solution can not be considered as 2-D. Looking at the end-walls, the flow is rather complicated near the tip clearance as a result of the flow migration towards it. At the hub, the effects of the horseshoe vortex can also be seen in the unsteady solution. The separation line shown in the steady flow solution clearly separates two regions of unsteady pressures.

Figures 7.29 and 7.30 compare the computed and measured amplitudes and phases of the first Fourier harmonic of unsteady pressures near the hub, midspan and tip of the rotor blade. The computed results are, in the main, satisfactory. The general trends match reasonably well at all three sections, the worst agreement being near the hub. Looking at the pressure side, the pressure amplitudes are mostly over-predicted, but the phases of unsteady pressures are accurately captured. Note that it is likely that the over-predictions of first order pressure amplitudes are caused by

the over-predictions of steady-state pressures. Looking at the suction side, it can be seen that the unsteady pressure phase agreements are not as good as on the pressure side. This can be explained by remembering that upstream and downstream pressure waves meet in this region, which may have led to difficulties in predicting accurately the perturbation phases.

The next section investigates whether the flow is really linearisable in this turbine. For that, the linear solution is compared with a fully nonlinear time-accurate unsteady solution.

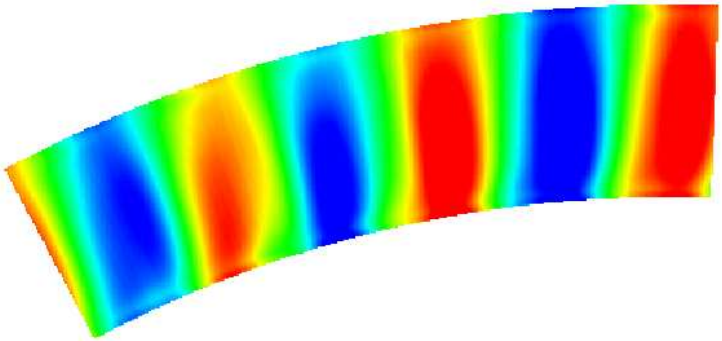

Figure 7.25: Real part of the 1st harmonic of unsteady pressures at the rotor inflow plane (constant x) for 5 blade passages - Harmonic linearised isolated blade-row solution

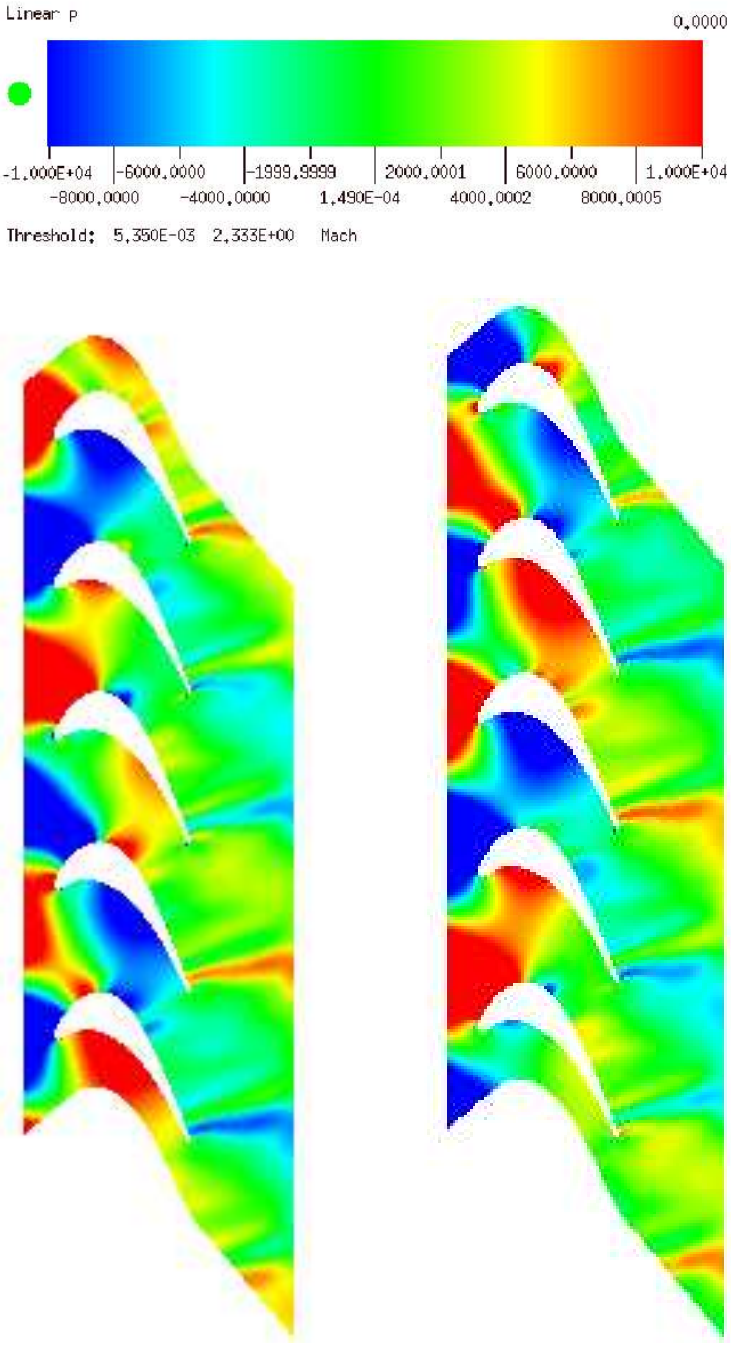

Figure 7.26: Real part (left) and imaginary part (right) of the 1st harmonic of unsteady pressures near the midspan for 5 blade passages - Harmonic linearised isolated blade-row solution

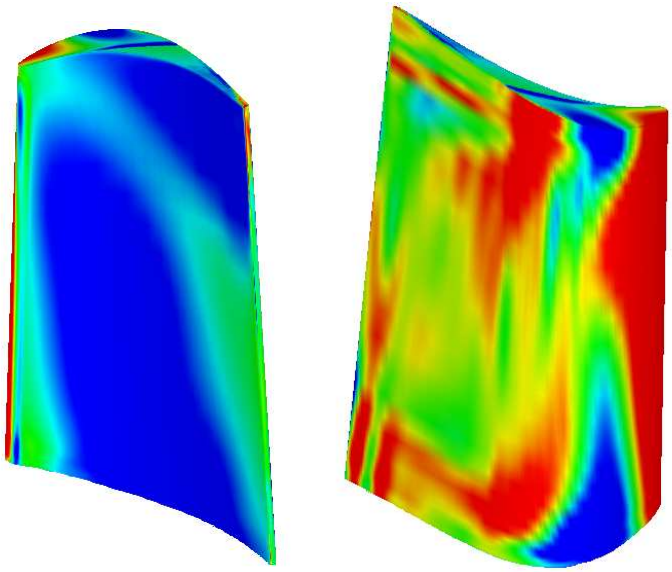

Figure 7.27: Real part of unsteady pressures on the blade pressure side (left) and suction side (right) - Harmonic linearised isolated blade-row solution

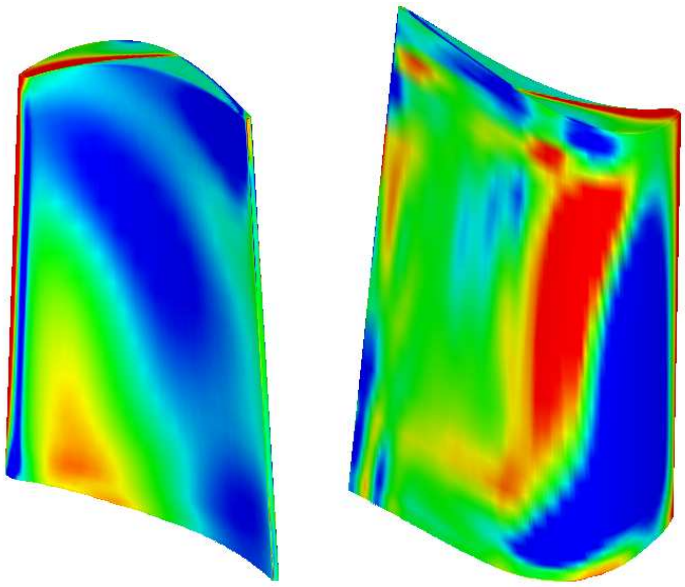

Figure 7.28: Imaginary part of unsteady pressures on the blade pressure side (left) and suction side (right) - Harmonic linearised isolated blade-row solution

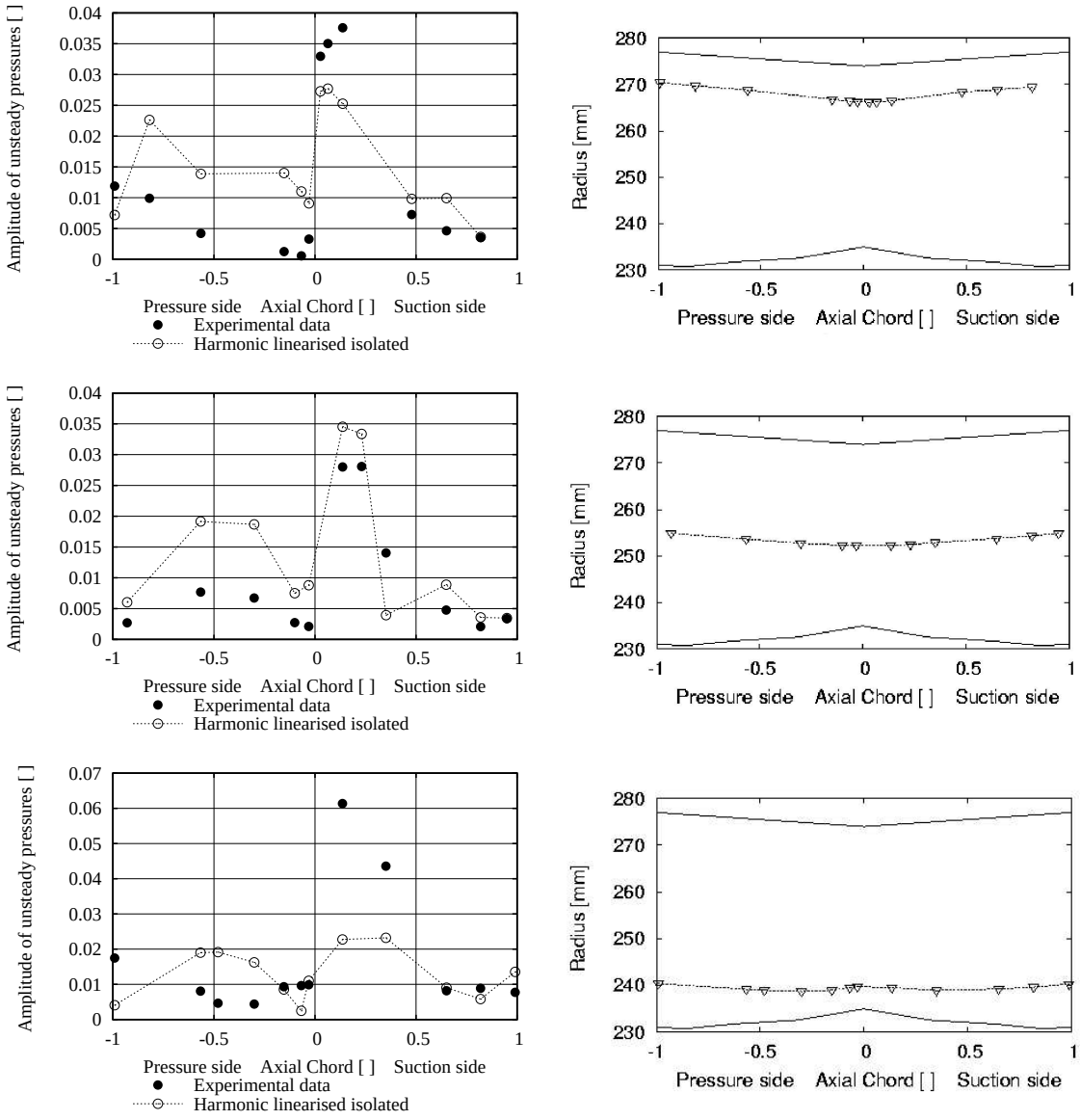

Figure 7.29: First harmonic unsteady pressure amplitudes at the tip (top), midspan (middle), and hub (bottom); measured vs. harmonic linearised isolated blade-row solution

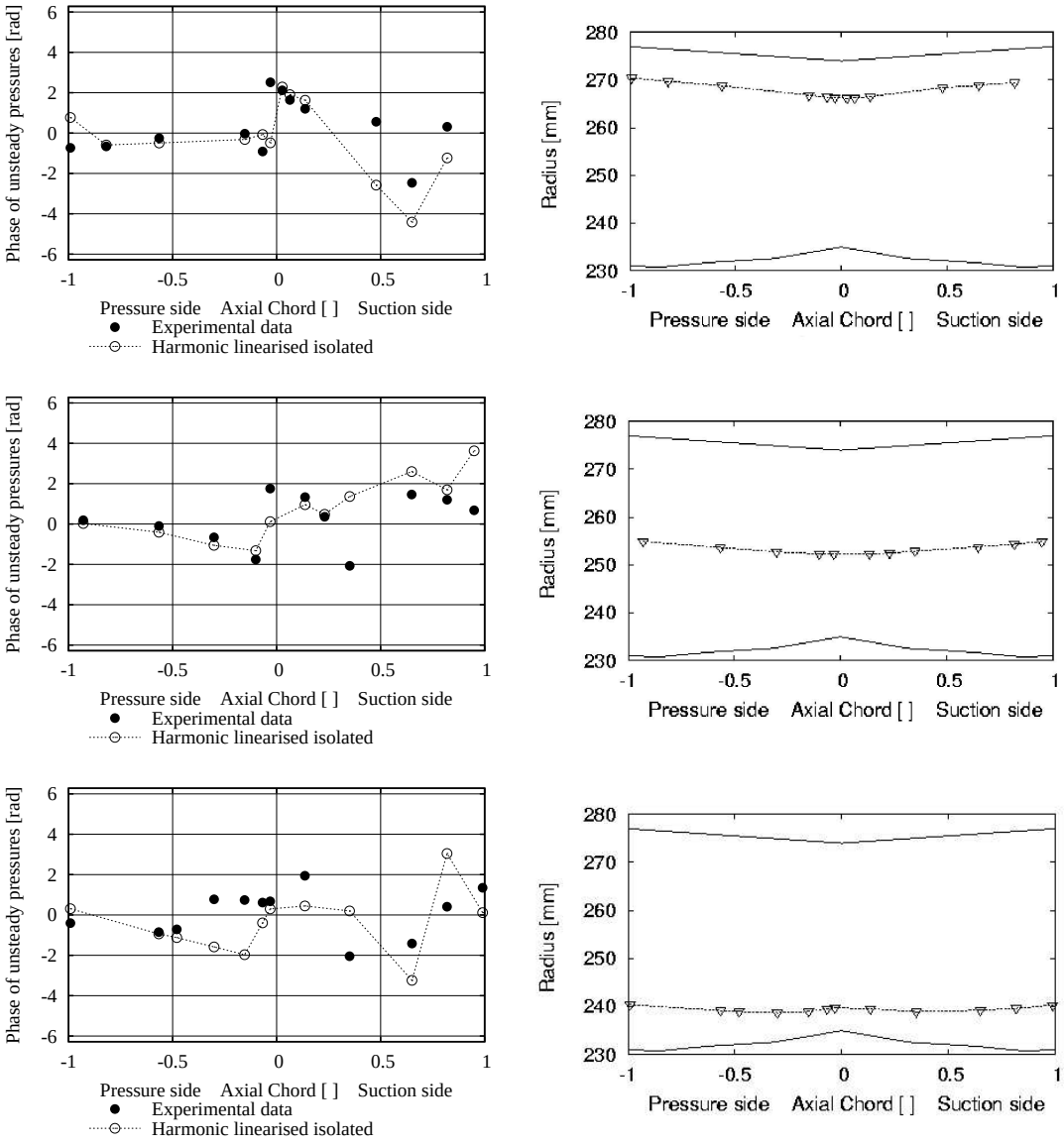

Figure 7.30: First harmonic unsteady pressure phases at the tip (top), midspan (middle), and hub (bottom); measured vs. harmonic linearised isolated blade-row solution

7.5.2 Fully Nonlinear Time-accurate Analysis

The fully nonlinear unsteady flow analysis allows one to quantify how much of the discrepancies between the experimental data and harmonic linearised results can be attributed to physical nonlinear effects, and how much can be attributed to modelling issues such as the boundary conditions, turbulence model, or grid quality.

The computational mesh used for the present nonlinear analysis includes three stator and five rotor blades. This mesh was designed to cover the same circumferential length in both blade-rows, which is a necessary requirement for the correct application of the periodic boundary conditions. The single-passage solutions for the stator and rotor were expanded to be used as initial conditions for the time-accurate unsteady viscous flow analysis. The nonlinear analysis uses the same turbulence model as that used in the steady-state and harmonic linearised analyses to ensure consistency between the solutions. The solution is time-marched using a dual time-stepping method, in which the flow is determined at several points until a periodic solution is reached. 200 points per cycle were computed, which is more than enough to obtain an accurate time resolution of the unsteady solution. The pressure convergence history of a point located near the LE and midspan of the rotor blade is shown in Fig. 7.31. It can be seen that a periodic solution was obtained after nearly 1500 interactions. It can also be seen that several harmonics are present in this solution.

A snapshot of the entropy contours computed near the annulus mid-height is shown in Fig.7.32. By looking at the flow into several blade-passages, this figure clearly shows how the stator wake is cut by the rotor blades, and is then convected through the passages.

It was not possible to save the whole time-history of the unsteady solution at every point of the computational domain due to computational storage limitations. Instead, only the time histories of all mesh points on one of the rotor blade surfaces were saved. These data allow one to Fourier transform in time the unsteady static pressure solution so as to compare the first harmonic unsteady pressures with experimental data. Figures 7.33 and 7.34 compare the computed and measured first Fourier harmonic of unsteady pressures. As expected, the overall fully nonlinear solution matches better the experimental data than the harmonic linearised isolated blade-row solution for the amplitudes of unsteady pressures. However, the agreement between the two methods is remarkably good for the phases of unsteady pressures.

Near the midspan, the nonlinear results are relatively good. The correct levels of

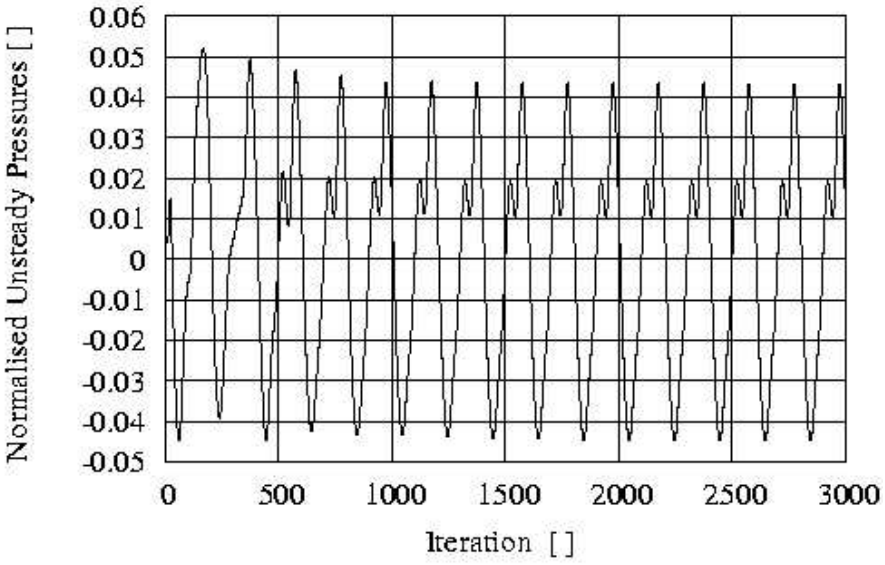

Figure 7.31: Time history of unsteady pressure perturbation, normalised by stage inlet total pressure, near the rotor blade LE and midspan and computed using nonlinear unsteady method

static pressure are reached on the suction side of the blade, while these are still over-predicted on the pressure side. It is worth again emphasising that all numerical simulations known to the author for this test case have over-predicted unsteady pressures on the blade pressure side [74, 114, 98, 6]. Hence, the present results are consistent with previous studies of this turbine stage.

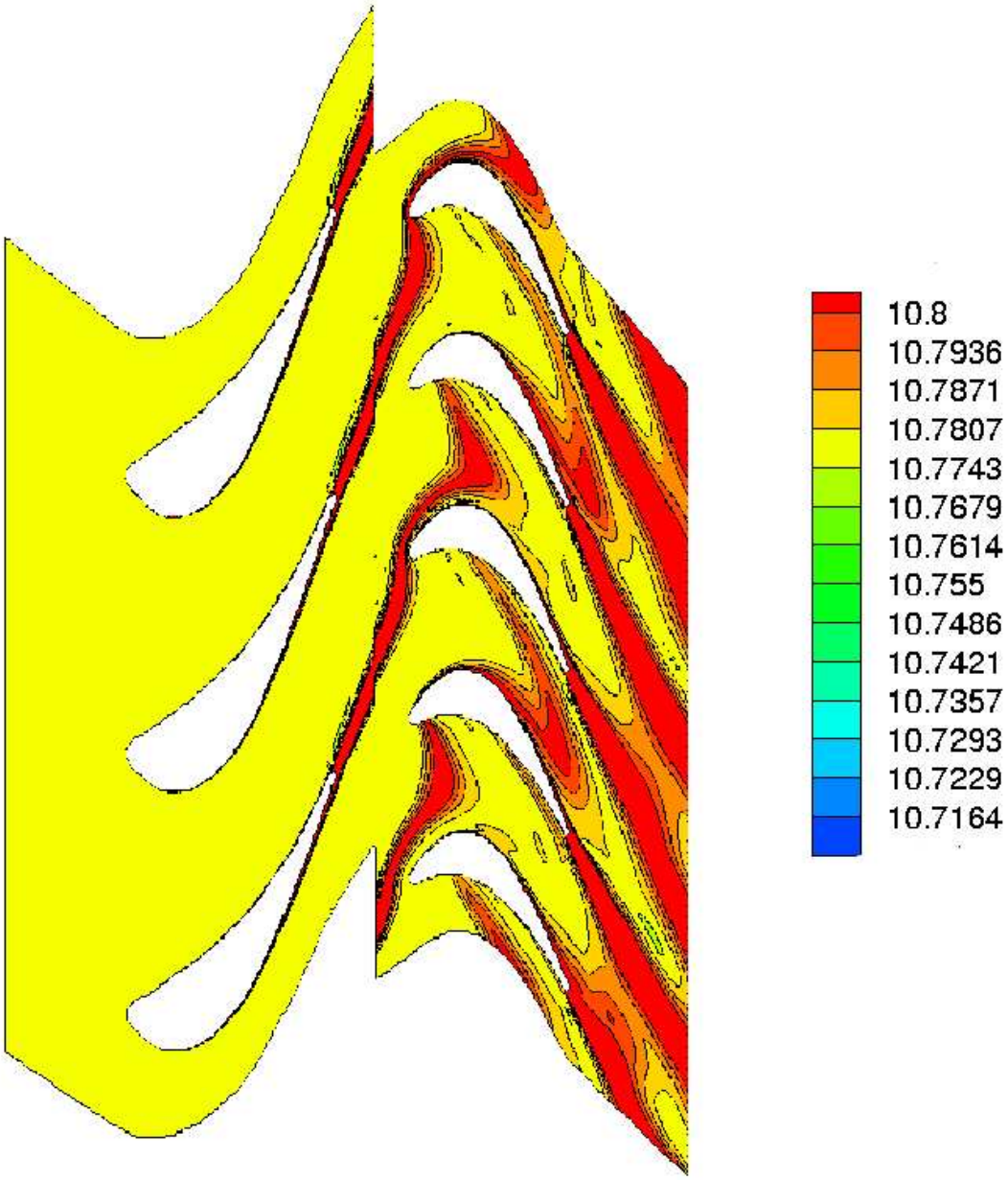

Figure 7.32: Snapshot of entropy contours near midspan computed using fully nonlinear unsteady method

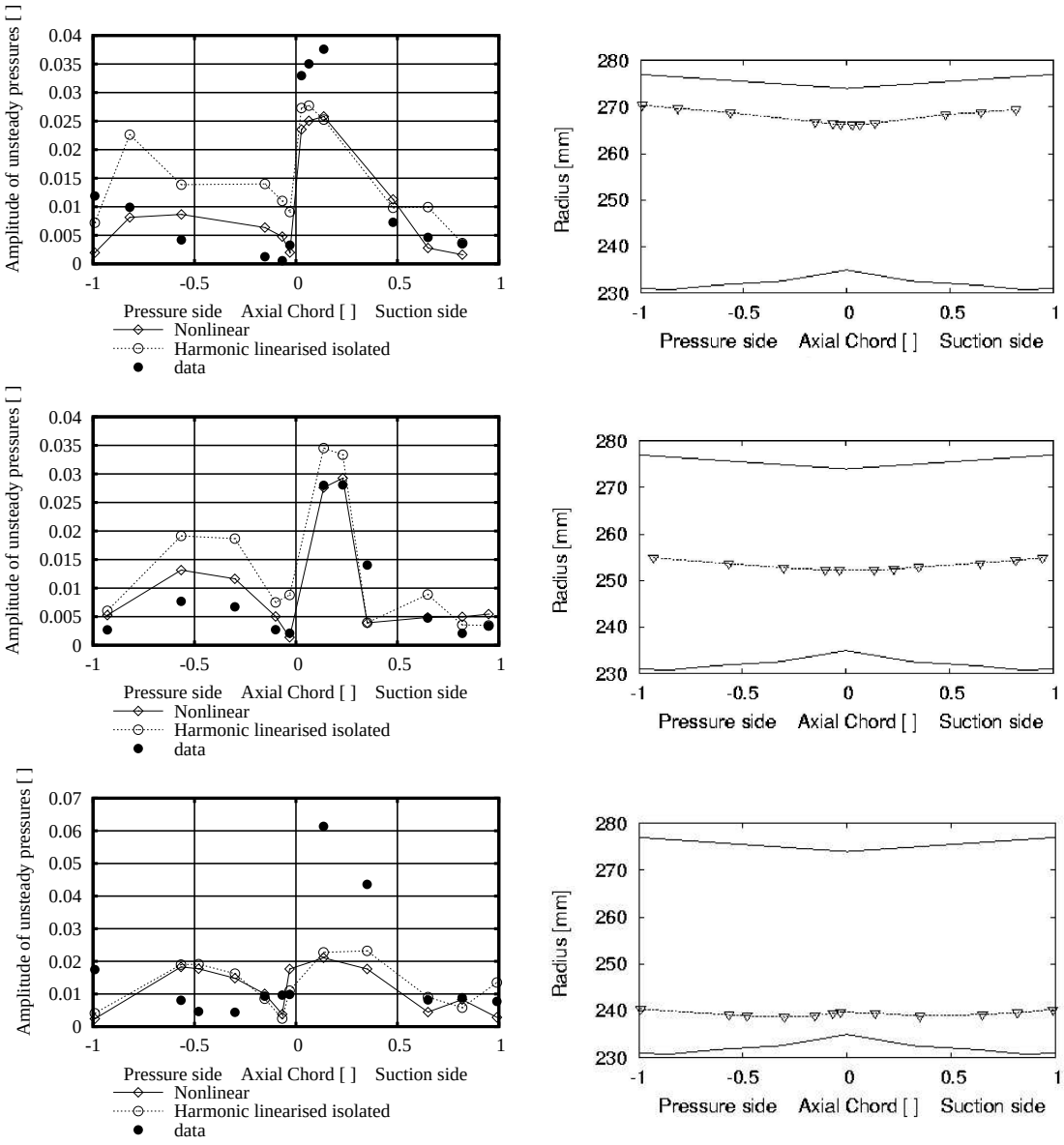

Figure 7.33: First harmonic unsteady pressure amplitudes at the tip (top), midspan (middle), and hub (bottom); measured vs. harmonic linearised isolated solution vs. fully nonlinear time-accurate solution

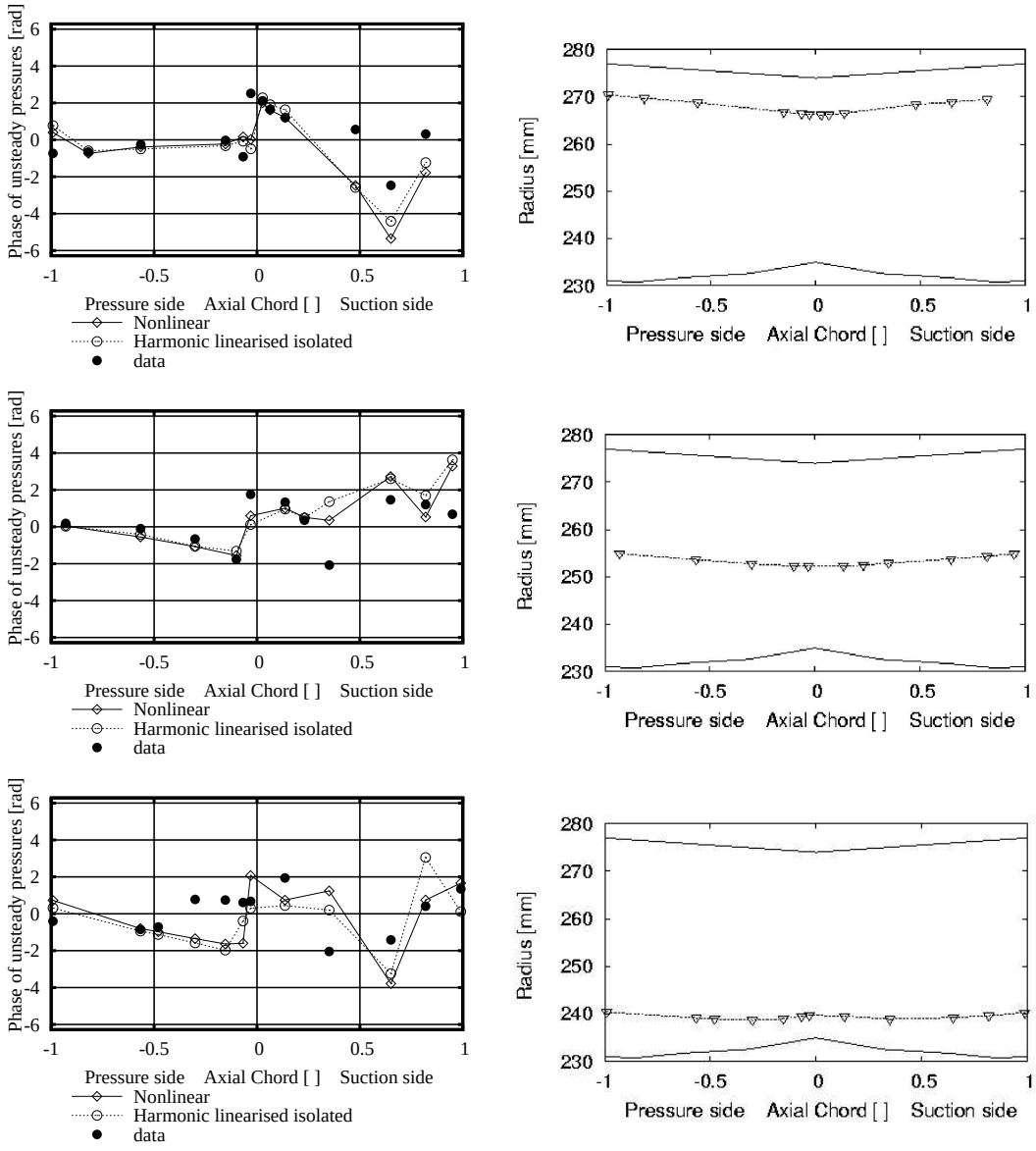

Figure 7.34: First harmonic unsteady pressure phases at the hub (tip), midspan (middle), and hub (bottom); measured vs. harmonic linearised isolated solution vs. fully nonlinear time-accurate solution

7.5.3 Harmonic Linearised Multi Blade-row Analysis

Section 7.5.2 shows that the nonlinear time-accurate solution agrees better with experimental data than its harmonic linearised isolated blade-row counterpart. Based on previous observations in this chapter, the discrepancies between the two results could be explained by nonlinear effects such as: (i) large amplitude perturbations carried by the stator wake; (ii) nonlinear interactions between perturbations with different frequencies; (iii) unsteady multi blade-row interactions. It is possible to investigate (iii) by computing a harmonic linearised multi blade-row solution, which is done in this section.

For the harmonic linearised multi blade-row analysis, 1 and 9 spinning modes were in turn included in the computation. It is worth pointing out that for wake-interaction problems, the fundamental spinning mode - i.e. that associated with the original disturbance in the rotor - comes back into the stator with zero frequency and zero inter-blade phase angle (in fact $\pm 360^o$ which is equivalent). Therefore, the fundamental spinning mode can be seen as a mean correction to the steady-state solution in the stator, due to the unsteadiness generated in the rotor. However, the linearisation is always based on the unchanged steady-state solution.

First, the stator and rotor unsteady solutions are determined by including the fundamental spinning mode only in the analysis. Considering this mode only, the rotor unsteady solution has a frequency ω_2 and an IBPA σ_2 given by (7.5.3) and (7.5.4). Figure 7.35 shows the computed real part of unsteady pressures at the inter-row boundary as seen from the rotor blades. These contours are compared with those obtained by the corresponding isolated blade-row analysis. It can be seen that both contours look similar, but the solution with one spinning mode is distributed differently with slightly lower pressure levels near the annulus hid-height and tip, and with higher pressure levels near the hub.

Figure 7.36 compares the static pressure perturbations near the rotor midspan computed using the harmonic linearised multi blade-row and the harmonic linearised isolated blade-row methods. From this 2-D plot, it can be seen that the overall unsteady flow solutions are similar, but local discrepancies are also apparent, mainly in the imaginary part of unsteady pressures. These changes occur because the flow perturbation directionality is slightly corrected when the blade-row coupling is included in the analysis. A 3-D plot of the pressure perturbation around the rotor blade (Figs. 7.37 and 7.38) also reveals that the blade-row coupling has the effect to decrease the radial flow variations, making the flow look more 2-D near the blade midspan.

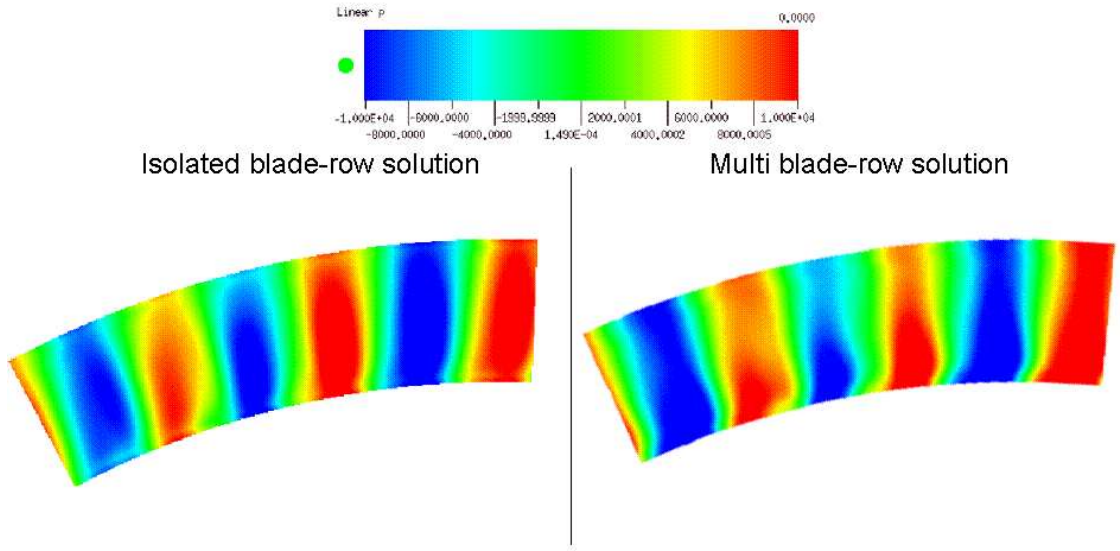

Figure 7.35: Real part of 1st harmonic of unsteady pressures at the rotor inflow plane (constant x) for 5 blade passages - Harmonic linearised isolated blade-row solution (left) and harmonic linearised multi blade-row method (right)

Figures 7.39 and 7.40 compare the pressure perturbations solutions around the rotor blade obtained by the harmonic linearised multi blade-row analysis, the harmonic linearised multi blade-row analysis, the nonlinear time-accurate analysis, and the experimental data. If the fully nonlinear time-accurate solution is used as a reference, then noticeable improvements are obtained near the blade tip and midspan using the linearised harmonic multi blade-row method compared to its isolated blade-row counterpart. Not much improvement could be obtained near the hub though, since these two methods already agree well in this region. It can thus be concluded that the blade-row coupling method slightly improves the rotor pressure perturbation predictions to drive finally the solution towards the nonlinear results.

Consider now the harmonic linearised multi blade-row analysis using nine spinning modes. As will be shown, this analysis highlights one of the limitations of the present harmonic linearised multi blade-row method. The propagation of all nine spinning modes in both blade-rows relies on the correct determination of the waves associated with the first three circumferential Fourier modes ($n_2 = -1, 0, 1$) in the whole rotor unsteady solution, and especially at the inter-row boundary. These three circumferential modes yield to circumferential wave numbers $k_\theta = -96, -36, 24$ respectively, with $k_\theta = -36$ representing the fundamental spinning mode. Tables. 7.2 and 7.3 present the computed axial wave numbers of the upstream and downstream acoustic modes for these three value of k_θ. It can be seen that all these acoustic modes are cut-off. The least cut-off of these modes is for $k_\theta = -36$, which corresponds to the

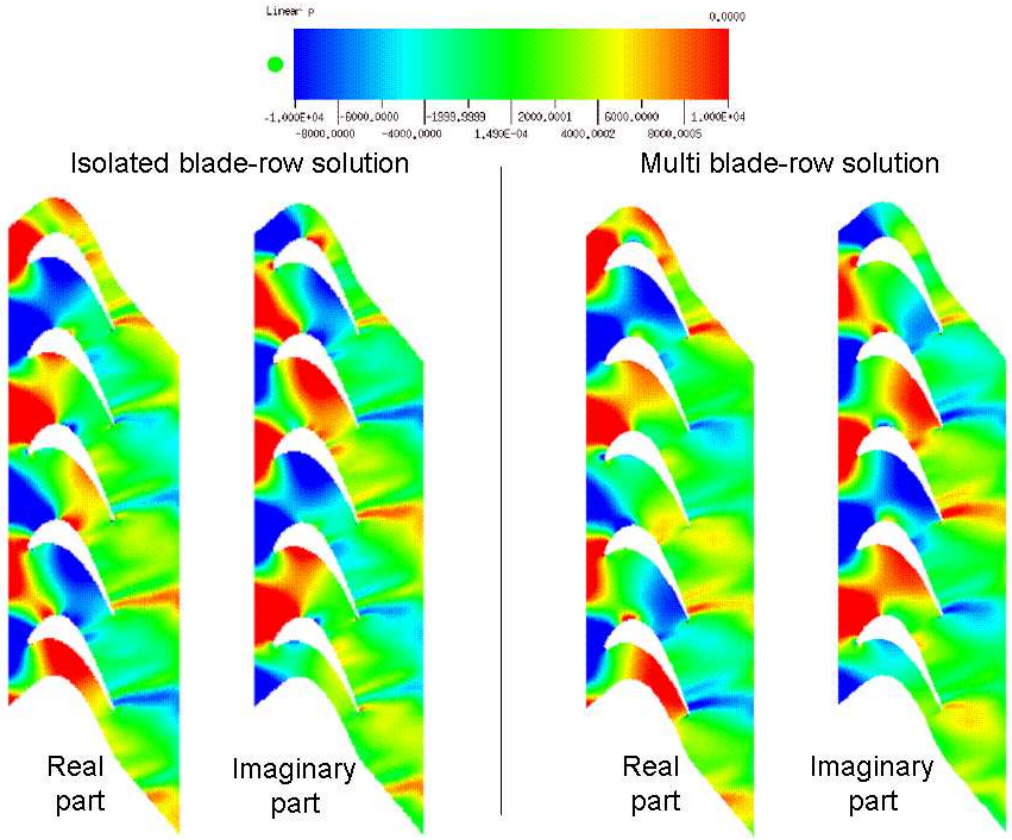

Figure 7.36: Real part and imaginary part of 1st harmonic of unsteady pressures near the midspan for 5 blade passages - Harmonic linearised isolated blade-row solution (left) and harmonic linearised multi blade-row solution (right)

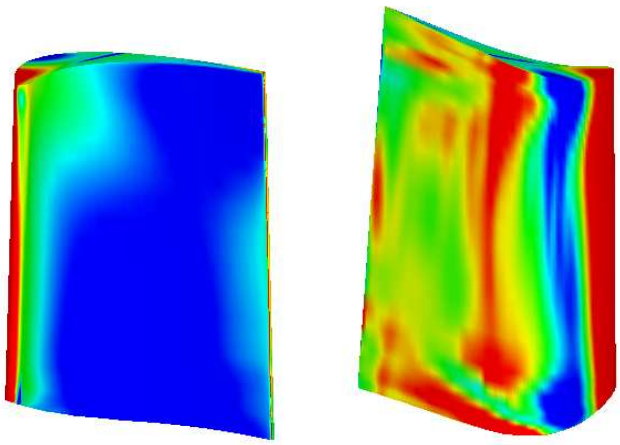

Figure 7.37: Real part of 1st harmonic of unsteady pressures on the rotor blade pressure side (left) and suction side (right) computed using the harmonic linearised multi blade-row method

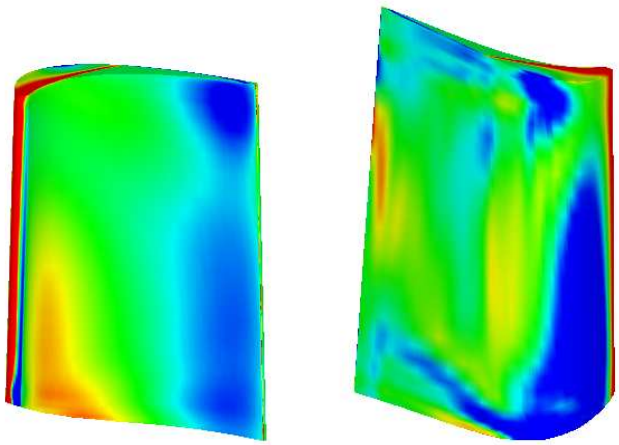

Figure 7.38: Imaginary part of unsteady pressures on the rotor blade pressure side (left) and suction side (right) computed using the harmonic linearised multi blade-row method

circumferential wave number of the fundamental spinning mode.

	$k_\theta = -96$		$k_\theta = -36$		$k_\theta = 24$	
x (m)	$\mathcal{R}(k_x)$	$\Im(k_x)$	$\mathcal{R}(k_x)$	$\Im(k_x)$	$\mathcal{R}(k_x)$	$\Im(k_x)$
0.04780	41.5140	328.290	41.1330	53.9684	18.7719	65.6958
0.04900	41.3079	328.020	40.2692	54.2336	18.5185	65.8183
0.05000	41.1411	327.981	39.6497	54.4244	18.3521	65.8935
0.05105	40.9559	328.292	39.1396	54.7086	18.2621	65.9001

Table 7.2: Computed axial wave numbers for the first three acoustic downstream modes

	$k_\theta = -96$		$k_\theta = -36$		$k_\theta = 24$	
x (m)	$\mathcal{R}(k_x)$	$\Im(k_x)$	$\mathcal{R}(k_x)$	$\Im(k_x)$	$\mathcal{R}(k_x)$	$\Im(k_x)$
0.04780	41.5215	-328.272	41.1270	-53.9649	18.7768	-65.6955
0.04900	41.3161	-328.002	40.2634	-54.2297	18.5236	-65.8180
0.05000	41.1498	-327.962	39.6440	-54.4202	18.3577	-65.8932
0.05105	40.9648	-328.273	39.1340	-54.7044	18.2683	-65.8999

Table 7.3: Computed axial wave numbers for the first three acoustic upstream modes

Not shown here, the amplitudes of the acoustic waves representing the fundamental spinning mode are much higher than for all other spinning modes, at least in the rotor domain. The problem in this calculation is that the amplitudes of the spinning modes, other than the fundamental one, are of the same order of magnitude as the level of numerical reflections at the inter-row boundary. This has the effect to "damp" or "hide" the spinning modes in the numerical results. This result clearly

highlights the dependency of the accuracy of the harmonic multi blade-row method on the accuracy of the inter-row boundary condition. In the present analysis, numerical reflections occur because the mean flow gradients are large, and waves interact with each other. Such a situation makes very difficult the distinction between entropic, vortical and acoustic modes. Hence, it cannot be concluded in this analysis whether more than one spinning mode can really have an impact on the multi blade-row coupling, as could possibly be the case in a real turbine stage. However, the fact that the numerical solution with one spinning mode got significantly closer to the nonlinear results, does not allow large effects to be represented by other spinning modes.

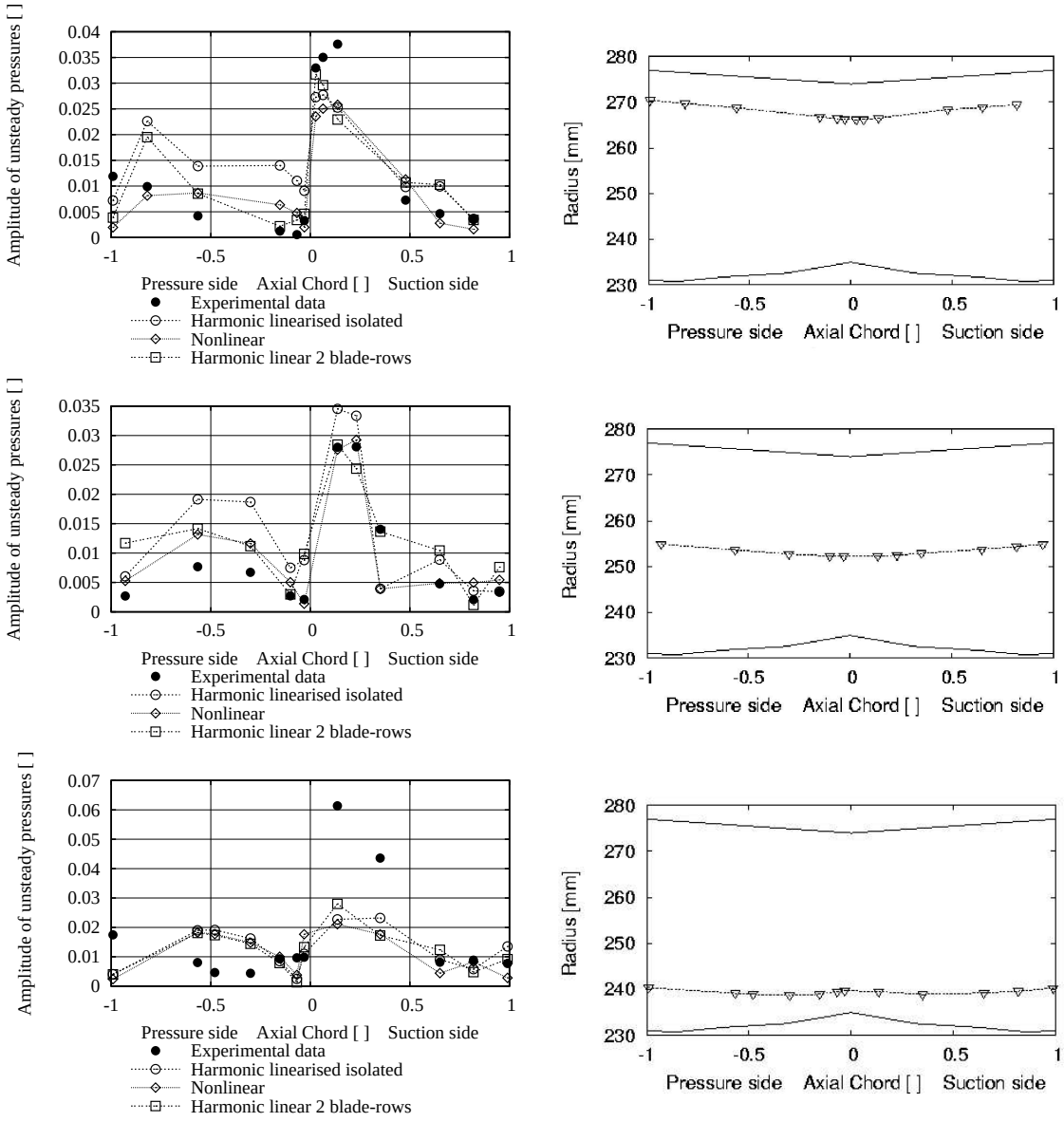

Figure 7.39: First harmonic unsteady pressure amplitudes at the tip (top), midspan (middle), and hub (bottom); measured vs. harmonic linearised isolated solution vs. harmonic linearised multi blade-row solution vs. fully nonlinear unsteady solution

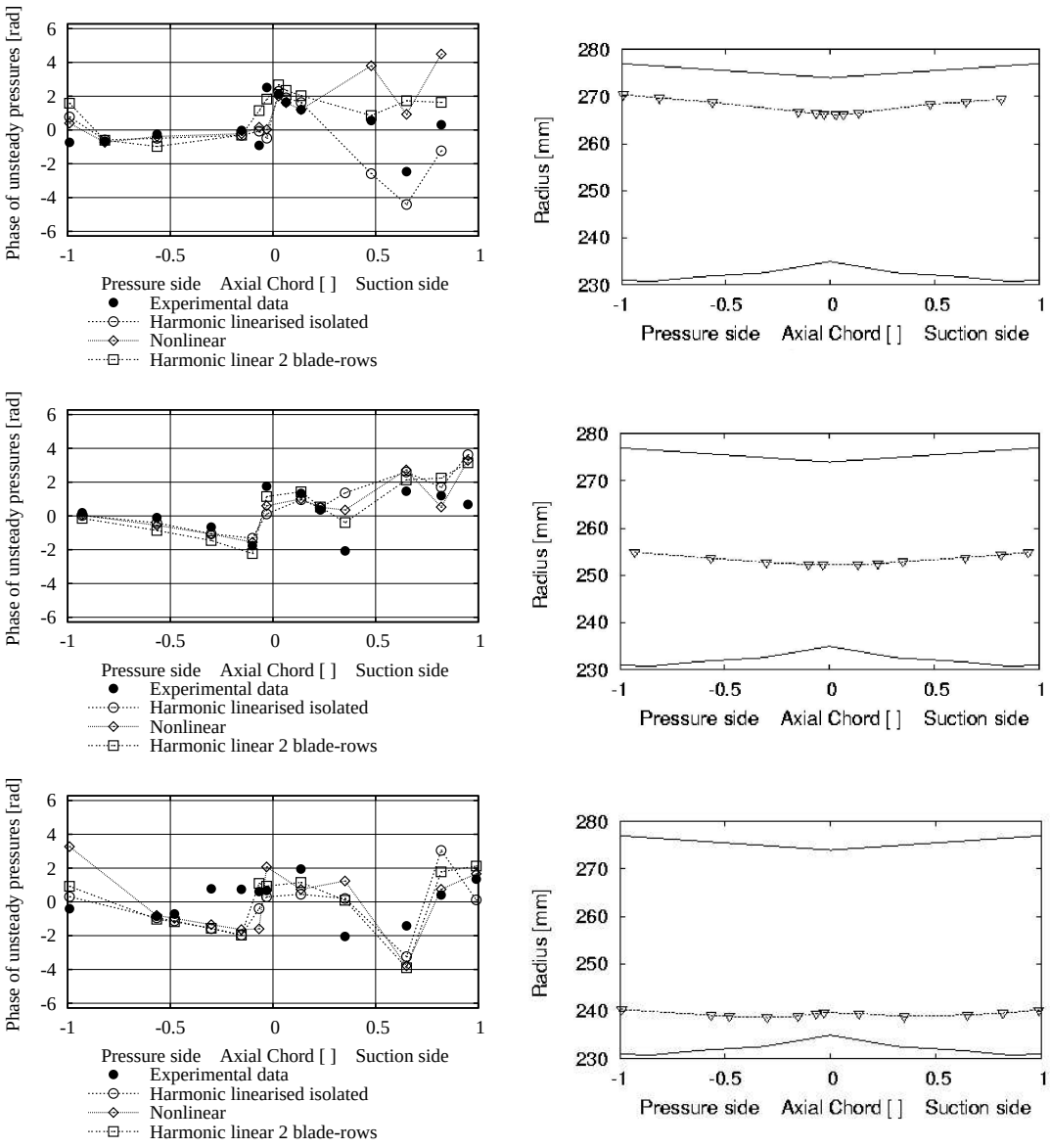

Figure 7.40: First harmonic unsteady pressure phases at the tip (top), midspan (middle), and hub (bottom); measured vs. harmonic linearised isolated solution vs. harmonic linearised multi blade-row solution vs. fully nonlinear unsteady solution

7.6 Conclusions for Chapter 7

The stator-rotor interaction analysis of a turbine stage is presented in this chapter. The test case is particularly useful because it provides experimental data to validate the steady-state and unsteady flow solutions. The results from three different numerical methods were compared: (i) harmonic linearised isolated blade-row; (ii) harmonic linearised multi blade-row; (ii) fully nonlinear time-accurate unsteady.

The main results are summarised below:

- The harmonic linearised multi blade-row solver is successfully tested for 3-D viscous stator-rotor interaction analysis.
- The large dependency of the multi blade-row solution on accurate inter-row boundary conditions is highlighted. It is shown that when large reflections of outgoing waves occur at the inter-row boundary, the effects of the corresponding spinning modes can be "damped" and thus not seen in the numerical solution.
- Another important issue is discussed, which is the computation of the steady-state solution. The only mathematically correct way to make a stator-rotor interaction analysis with the harmonic linearised multi blade-row method, is to decompose stator wake into harmonics at the same location as where the spinning modes are transmitted between the blade-rows, i.e. at the inter-row boundary. Therefore, it was chosen to compute the stator and rotor steady-state solutions using through flow boundary conditions instead of a mixing plane, because the mixing plane averages the static pressures circumferentially and thus eliminates the potential component of the stator wake.
- The steady-state solutions in both blade-rows contain, in the main, the correct flow features. The computed static pressures match reasonably well with experimental data near the rotor blade tip and midspan. Significant static pressure discrepancies are observed near the blade hub, but these results are consistent with other researchers work. These results lead the author to believe that something may be missing in the simulation of this turbine, maybe a bleed or other blade profile variability effects, to explain the discrepancies at the hub.
- Of the three methods being compared, the fully nonlinear time-accurate unsteady results agree best with experimental data, though most unsteady pressures are overestimated on the blades' pressure side. These nonlinear results are also consistent with other researchers work.
- Taking the fully nonlinear solution as reference, harmonic linearised multi blade-row results including only one spinning mode - the fundamental mode - are better compared to the linearised isolated blade-row results. The effects of other spinning modes (though probably small) are "damped" by numerical reflections at the inter-row boundary.

- Multi blade-row effects could be observed for this case. These effects represent about 25% of the unsteady lift amplitude near the blade midpan, and between 0-10% near the blade hub and midspan.

- The present harmonic linearised multi blade-row solver is efficient. The computational time roughly scales with the number of blade-rows and the number of spinning modes used in the analysis. The computational time required to compute this test case with one spinning mode was about 1.5 times that required to compute the time-linearised single row solution, and 4 times less than that needed to compute the fully nonlinear solution. The nonlinear solution required about 3 days using eight 3.0 Ghz Intel processors. Memory requirements were about 0.5 GB per CPU. It should be noted that the number of blades of the rotor and stator allow the nonlinear computation to be performed using a periodic sector of three stators and five rotors. In most cases, the blade numbering might require much larger numbers of passages for the nonlinear computation leading to much larger benefits in computer time when the linear multirow approach is used.

Chapter 8

Flutter Analysis of a Low-pressure Turbine

8.1 Introduction

During development-engine testing, the Stage 2 rotor of a low-pressure turbine was found to flutter near the working line for a range of rotational speeds. The design of the rotor was thus modified to eliminate the vibration problem. However, this original design constitutes a good test case for the validation of numerical models for flutter predictions.

Sayma et al. [90] analysed the flutter stability of the second-stage rotor in isolation. In their analysis, they used a whole-assembly time-accurate nonlinear unsteady flow model. The viscous effects in the unsteady flow were represented via a loss model based on a steady-state viscous flow calculation. The rotor was analysed for three rotational speeds, namely 88%, 94% and 99% of the maximum speed. Zero mechanical damping was assumed throughout the analysis. The investigation found that flutter occurred for all three speeds for the backward-travelling 5 to 15 nodal diameters, the 94% speed case yielding highest vibration levels. Flutter was predicted to be more severe than what was suggested by measured data both in terms of speed range and range of nodal diameters (Fig. 8.1). Although Sayma et al. had assumed zero mechanical damping in their analysis, it can be argued that the results could also been adversely affected because of using an inviscid unsteady flow plus loss model, and because of using an isolated blade-row.

The objective of the present analysis is to investigate the effects of multiple blade-rows for the 94% speed case only. This is done by not only looking at the overall

level of aerodynamic damping, but also by studying the contribution of various parts of the blade. In this analysis, the unsteady flow is computed using the harmonic linearised multi blade-row model, and 1, 3, 5 and 8 blade-rows are included in the unsteady analysis in a gradual fashion.

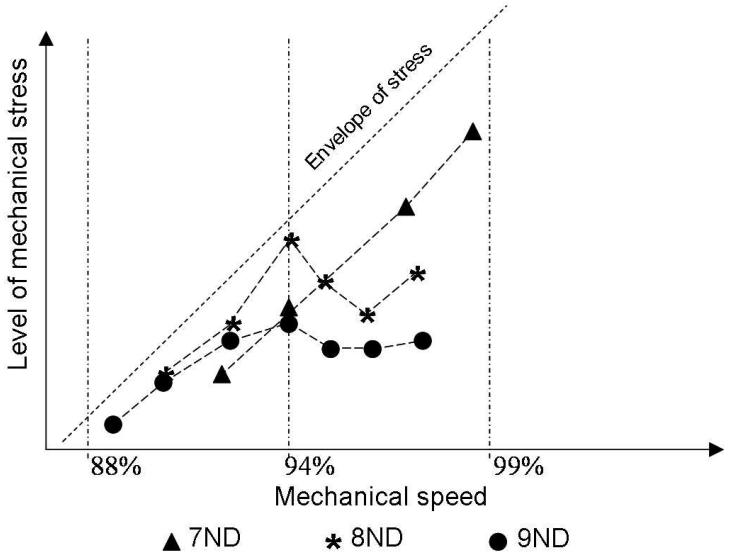

Figure 8.1: Sketch of high-stress for Rotor 2 based on experimental evidence

8.2 Structural Model and Modeshapes

The flutter mode of interest is the first flap, as indicated by experimental evidence. The rotor has 84 blades, and thus the highest nodal diameter is 42. The natural frequencies and modeshapes are computed using a standard FE analysis technique for a blade sector by assuming cyclic symmetry at the disk and the shroud. Table 8.1 presents the computed natural frequencies versus nodal diameter number for the first flap mode. Importantly, this table highlights that, unlike fan blades, the natural frequencies increase significantly with the nodal diameter. There is a factor of nearly five between the lowest and the highest assembly natural frequencies. This feature is known to be essentially due to the blade-to-blade coupling at the shroud, plus disk flexibility (see Fig. 8.4).

The computed structural modes are plotted in Fig. 8.2 for a series of nodal diameters ranging from 2 to 25. In this figure, the scale is normalised so that maximum displacement multiplied by the frequency (in Hz) is equal to 1 metre (like is shown in Fig. 8.3). Due to the cyclic symmetry, it can be seen that the deflection is mostly in the axial (flap) direction for the lowest nodal diameters. For the medium

ND	Frequency (Hz)
2	162.3
3	178.4
4	197.4
5	226.2
6	256.2
7	287.6
8	322.1
9	360.7
10	403.5
11	449.8
12	497.2
15	615.9
20	677.2
25	696.9
42	718.1

Table 8.1: Nodal diameter versus frequencies for the first flap mode

nodal diameters, the deflection is a mixture of flap and twist. For the high nodal diameters, the deflection becomes mostly a twist.

Figure 8.3 shows the bladed-disk axial displacements for ND = 7. It should be noted that, despite the fact that these blades are shrouded, the shrouds are flexible enough to move and the maximum blade displacement amplitude is achieved near the tip, as represented in Fig. 8.4.

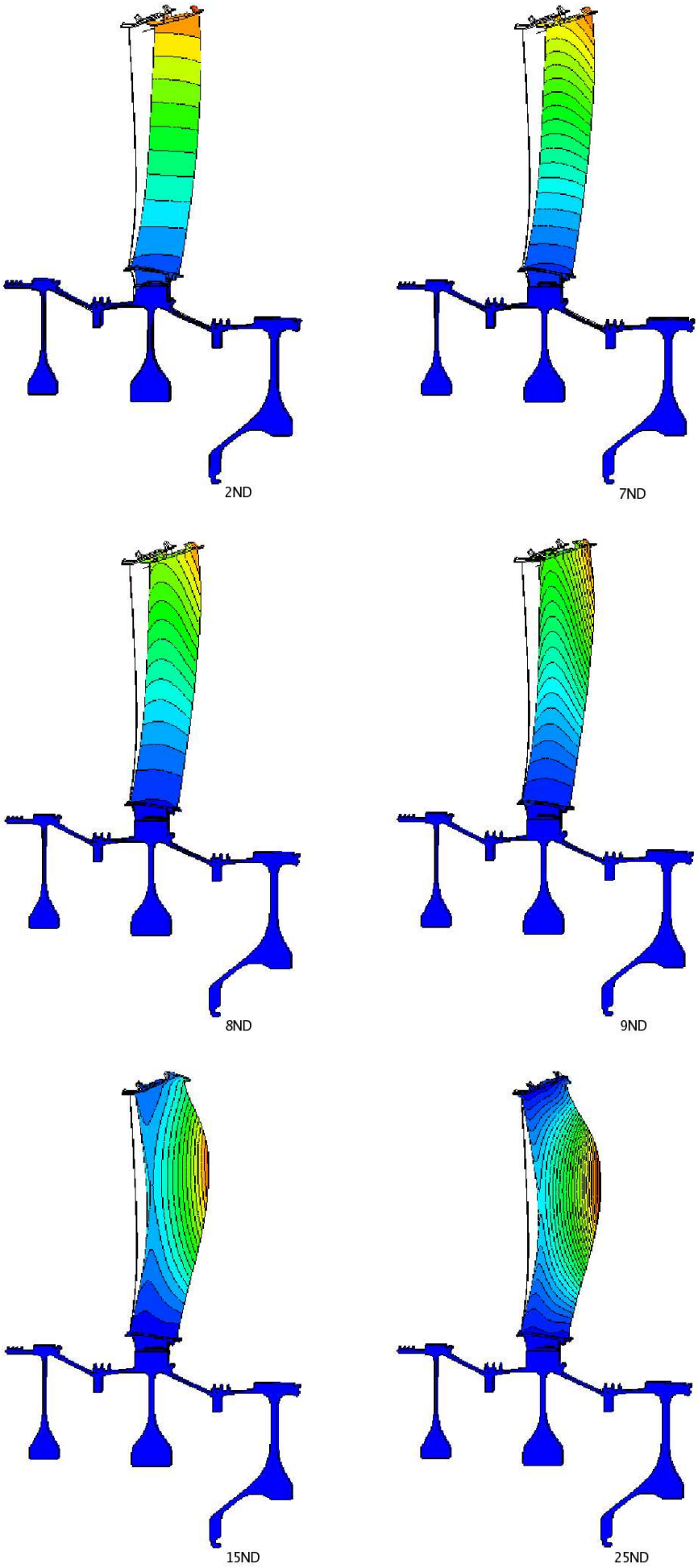

Figure 8.2: Contours of axial deflection for ND = 2, 5, 7, 9, 15, 25 (from top left to bottom right); scale shown in Fig. 8.3

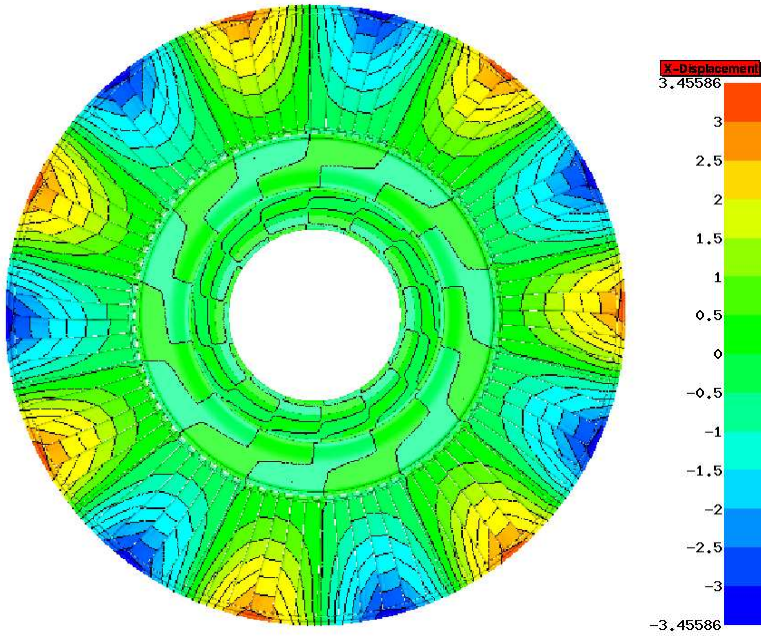

Figure 8.3: Whole-annulus maximum axial deflection for ND = 7

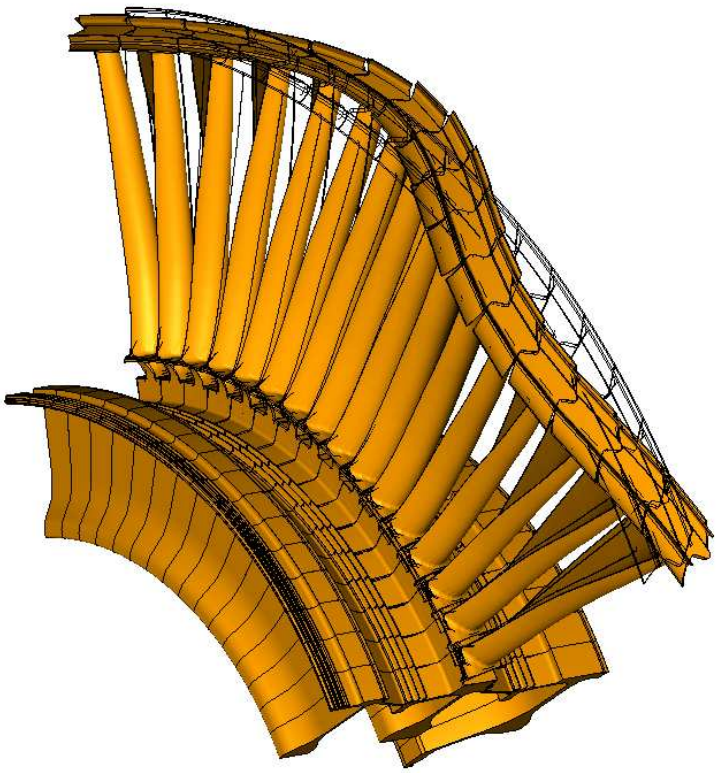

Figure 8.4: Modeshape for ND = 7, shown on a circumferential section of 16 blades

8.3 CFD Model

The modeshapes were interpolated from the structural mesh onto the CFD mesh shown in Figs. 8.5 and 8.6. The CFD mesh has about 666,600 points per blade-passage, and was determined after a mesh refinement study.

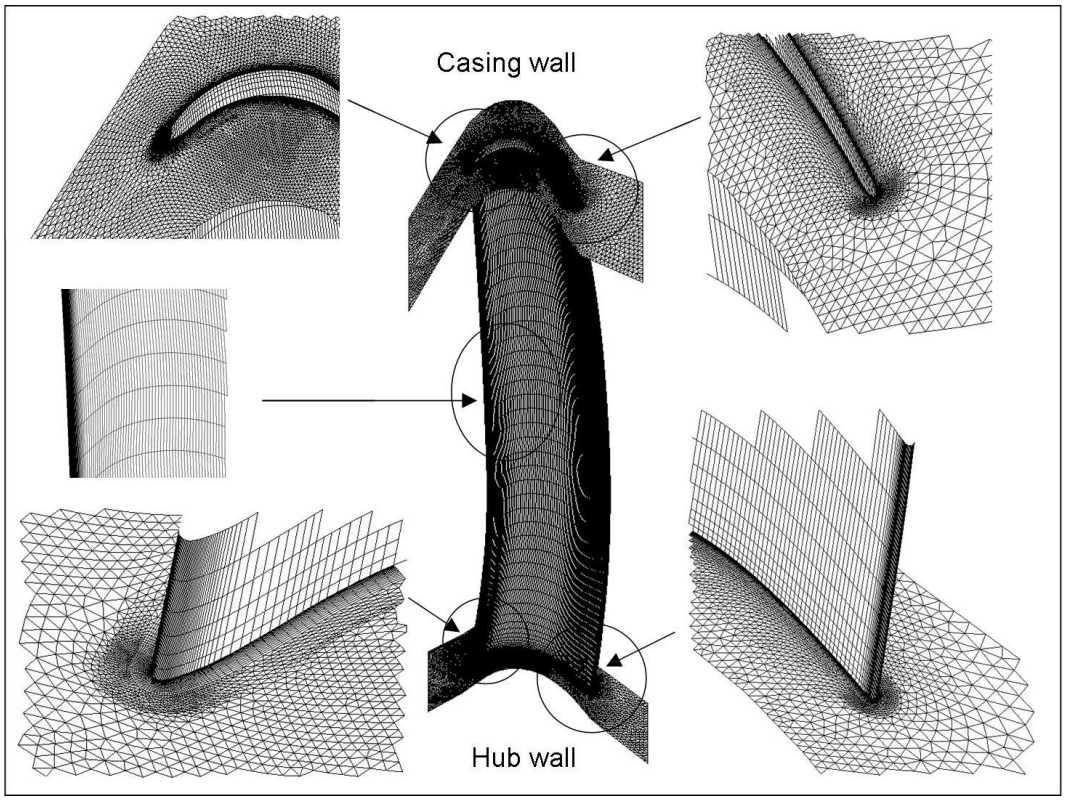

Figure 8.5: CFD mesh for LPT flutter analysis

8.4 Aerodynamic Damping Determination

The aerodynamic damping, ξ, characterises the aeroelastic properties of a blade-row for each mode of vibration. As will be explained below, if $\xi < 0$ then the blade-row is aerodynamically unstable, but the flutter vibration would be mechanically unstable only if, in the same configuration, the mechanical damping does not compensate for the aerodynamic excitation. The aerodynamic damping can be determined via harmonic methods, or via nonlinear methods.

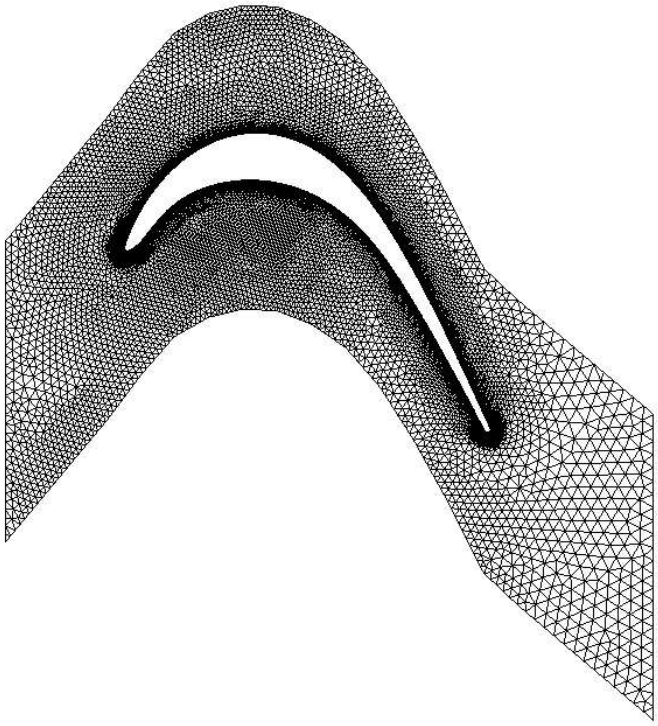

Figure 8.6: 2-D mesh section near the blade midspan

8.4.1 Harmonic Method

The basic equation of motion is given by:

$$[M]\,\ddot{\mathbf{X}} + [C]\,\dot{\mathbf{X}} + [K]\,\mathbf{X} = \mathbf{F}_X \tag{8.4.1}$$

where $\mathbf{M}$ is the mass matrix, $\mathbf{C}$ is the damping matrix, $\mathbf{K}$ is the stiffness matrix, $\mathbf{X}$ is the mechanical displacement, and $\mathbf{F}_X$ is the aerodynamic force. The structural modeshapes must be mass normalised before interpolation onto the blade surface of the CFD mesh. Assuming a harmonic motion, the vector displacement can be decomposed as follows:

$$\mathbf{X} = \mathbf{\Phi}.q.e^{i\omega t} \tag{8.4.2}$$

where $\mathbf{\Phi}$ represents the mass normalised modeshapes, q is a scaling factor, and ω is the vibration frequency.

Inserting (8.4.2) into (8.4.1) and pre-multiplying by $\mathbf{\Phi}^*$ gives:

$$-\omega^2\mathbf{\Phi}^*\,[M]\,\mathbf{\Phi} + i\omega\mathbf{\Phi}^*\,[C]\,\mathbf{\Phi} + \mathbf{\Phi}^*\,[K]\,\mathbf{\Phi} = \mathbf{\Phi}^*\mathbf{F}_X \tag{8.4.3}$$

By definition of the mass normalisation, the following simplifications can be made:

$$\mathbf{\Phi}^* [M] \mathbf{\Phi} = 1, \quad \mathbf{\Phi}^* [C] \mathbf{\Phi} = 2\xi\omega_n, \quad \mathbf{\Phi}^* [K] \mathbf{\Phi} = \omega_n^2 \tag{8.4.4}$$

where ω_n is the natural frequency.

Plugging (8.4.4) into (8.4.3), and collecting the imaginary parts together gives:

$$\xi = \Im \left(\frac{\mathbf{\Phi}^* \mathbf{F}_X}{2\omega\omega_n} \right) \tag{8.4.5}$$

The term $\mathbf{\Phi}^* \mathbf{F}_X$ in (8.4.5) represents the work done by the aerodynamic forces in the direction of the fluid during one cycle of vibration. Therefore, a positive value of ξ means that the moving blade is dissipating energy into the fluid, and thus the vibration is stable. However, when ξ is negative, then the moving blade is contributing additional energy to its motion. In this case, and when the mechanical damping is not strong enough to damp the vibration, the blade vibration is unstable and flutter occurs. Using harmonic linearised CFD methods, the aerodynamic damping is computed from an imposed fixed amplitude oscillation using (8.4.5). This is the method that is used in this chapter.

8.4.2 Nonlinear Method

Another convenient way to determine the damping of a blade-row is to measure the rate of decay of free oscillations. Large damping values mean large decay, and small damping values mean small decay.

The rate of decay of oscillation can also be measured by a parameter called "logdec", which is defined as the natural logarithm of the ratio of two successive amplitudes (Fig 8.7).

If a damped vibration is represented by the general equation:

$$\mathbf{X} = \mathbf{A} e^{-i\xi\omega_n t} sin \left(\sqrt{1-\xi^2}\omega_n t + \psi \right) \tag{8.4.6}$$

then the expression for the logarithmic decrement becomes:

$$\delta = ln \left(\frac{x_1}{x_2} \right) = ln \left(\frac{e^{-\xi\omega_n t_1}}{e^{-\xi\omega_n (t_1+\tau_d)}} \right) = ln e^{\xi\omega_n \tau_d} = \xi\omega_n\tau_d \tag{8.4.7}$$

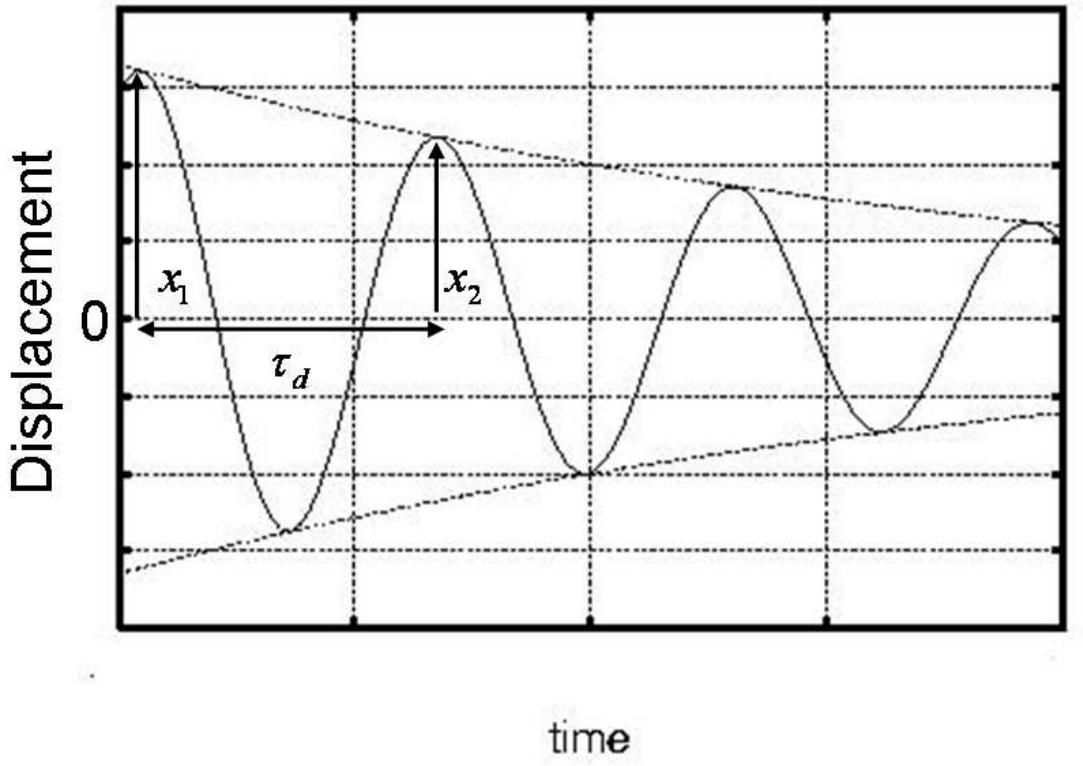

Figure 8.7: Logdec measuring the rate of decay of oscillation

Introducing the expression for a damped period, which is:

$$\tau_d = 2\pi/\omega_n\sqrt{1-\xi^2} \tag{8.4.8}$$

then the logarithm decrement can be expressed by:

$$\delta = \frac{2\pi\xi}{\sqrt{1-\xi^2}} \tag{8.4.9}$$

In the limit of small damping $\sqrt{1-\xi^2} \approx 1$, and an approximate expression is:

$$\delta \approx 2\pi\xi \tag{8.4.10}$$

Therefore, in nonlinear calculations, a process to determine the damping is to excite artificially the blades (using an initial kick for example) and to look at the evolution of the deflection amplitude against time. If the vibration amplitude grows in time, then the vibration is unstable, if it decays, then it is stable. This method was used by Sayma et al. [90] for the computation of the damping.

8.5 Sensitivity of Flutter Predictions to Operating Point and Numerical Modelling

In the first part of the present flutter analysis, the flow is computed by including Rotor 2 only in the computational domain. The far-field boundary conditions were provided by Rolls-Royce plc from a through flow analysis.

These conditions were assumed to be sufficiently representative of the "true" boundary conditions since the previous analysis of Sayma *et al.* correctly predicted flutter using these boundary conditions.

The steady-state code presented in Chapter 3 was used to compute the steady-state flow. A view of the pressure contours computed near the blade-midspan are shown in Fig. 8.8.

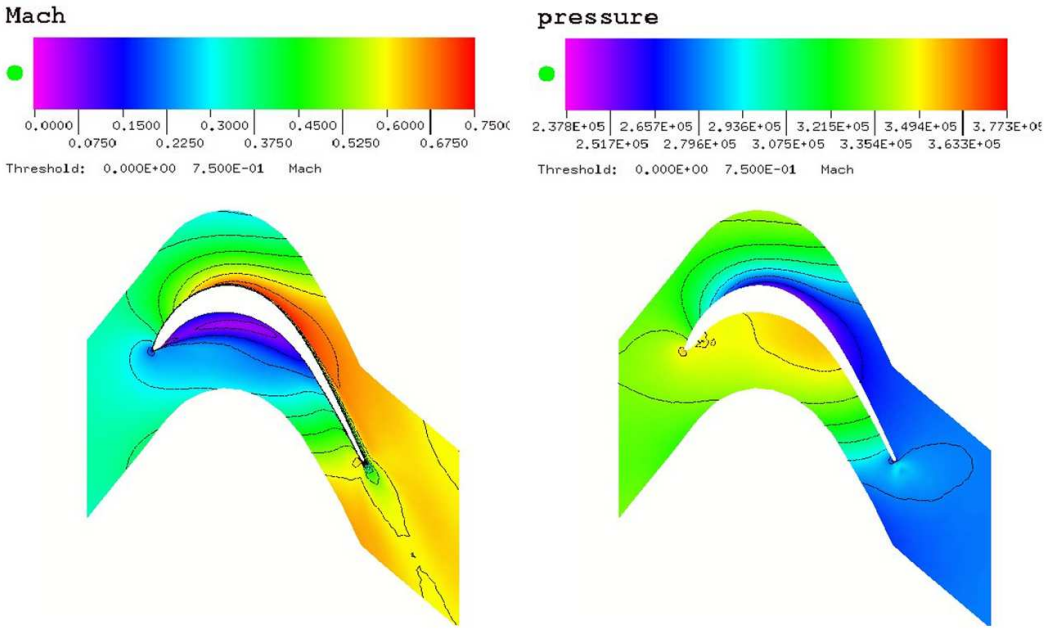

Figure 8.8: LPT Rotor 2 original steady-state flow solution; Mach number (left) and pressure (right) contours near the blade midspan

It can be seen that the flow passing through the turbine is subsonic. These flow conditions are for 94% speed, which puts the aerofoil slightly into positive incidence compared to 100 % speed. However, the pressure side diffusion is too strong for the flow to remain attached.

This solution was computed using the Spalart-Allmaras turbulence model of Chapter 3, which means that it was assumed that the flow is fully turbulent. However,

in reality, there is almost a laminar separation at the leading edge due to the operational Reynolds number. Therefore, it can be debated whether the "true" flow is adequately represented using this turbulence model. An attempt to answer this question will be given later in this chapter.

The harmonic linearised solver was then used for the determination of the logdec values for a series of nodal diameters ranging from -25 to +25 (Fig.8.9). It can be

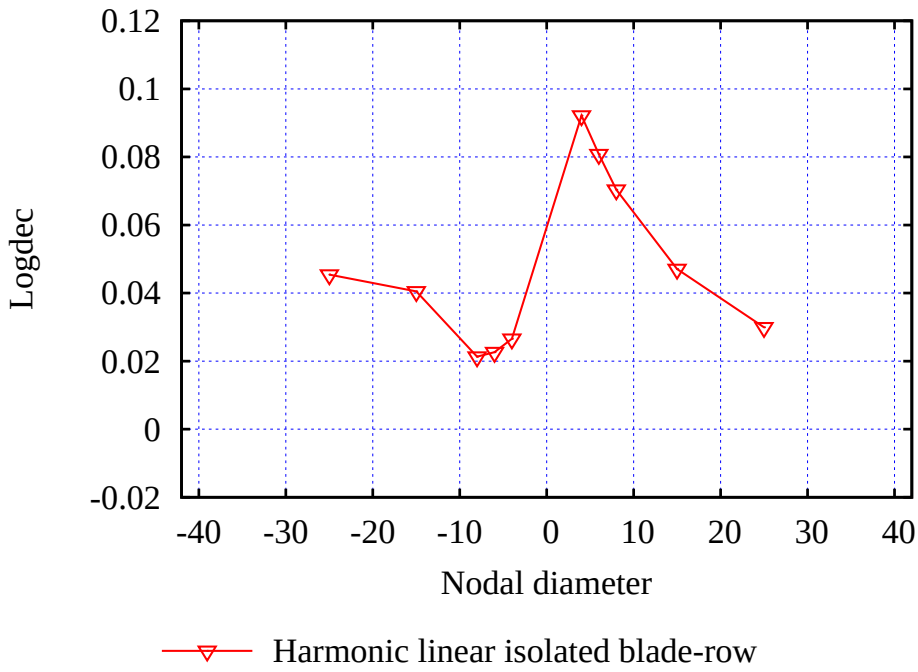

Figure 8.9: Logdec versus nodal diameter based on the original steady-state flow solution

observed that these results are not in line with the experimental measurements since no flutter instability is predicted for any of the computed nodal diameters.

The following sections aim to investigate why flutter is not predicted in this configuration. Experience on fan flutter tells us that flutter is correctly predicted only when the operating point is computed correctly. For instance, the position of the shock must be captured accurately for the steady-state flow. In the following analysis, the same path is followed and the effect of the steady-state flow solution on the flutter stability of this turbine is investigated.

8.5.1 Sensitivity to Turbulence Model

Two-dimensional semi-analytical theories used at Rolls-Royce suggest that the flow reattachment point in this LP turbine is almost at the same inviscid Mach number

location as where the separation starts. Therefore, it is essential to know the location of the separation point because the size of the separation bubble will depend on it. An alternative approach to use of a transitional model is to artificially influence the separation point by modifying the turbulence model. For that, a different flow solver to that presented in Chapter 3 was used for the computation of the steady-state flow. The second solver also uses the Spalart-Allmaras turbulence model. Using this solver, it is possible to modify the amount of numerical dissipation through a parameter called *omg*. This parameter is a second-order dissipation coefficient which can vary between 0 and 1. By lowering the value of *omg* down to zero we increase the numerical dissipation, while a value of $omg = 1$ means no numerical dissipation at all. We also computed the steady-state flow solution with and without destruction terms in (3.3.30). The results of these investigations are presented in Figs. 8.10 and 8.11, and the notation in these pictures is explained in Table. 8.2.

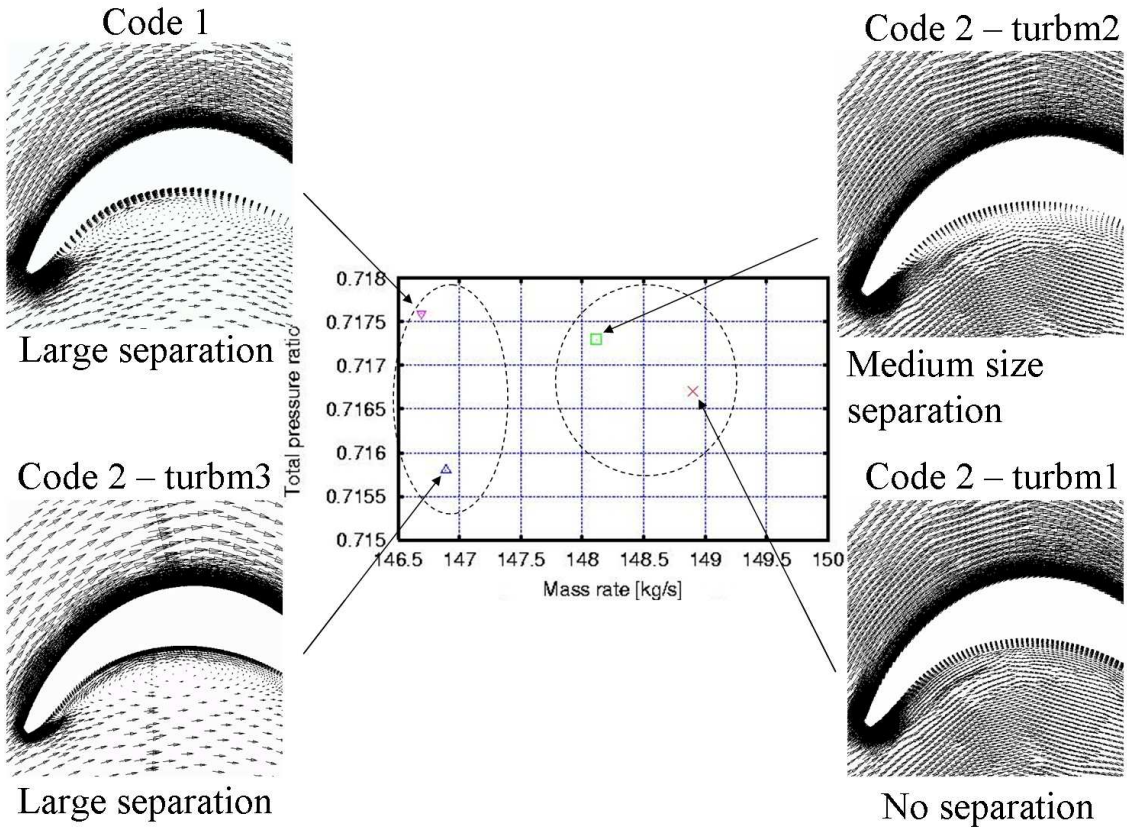

Figure 8.10: Pressure ratio versus mass rate. The effect of turbulence model on the steady-state solution

In Fig. 8.10 are plotted the velocity vectors near the blade midspan, and the effect of the separation on the turbine operating point. Two important results can be seen. First, by removing the destruction terms of the turbulence model and by also decreasing the amount of numerical dissipation, the flow viscosity increases such that

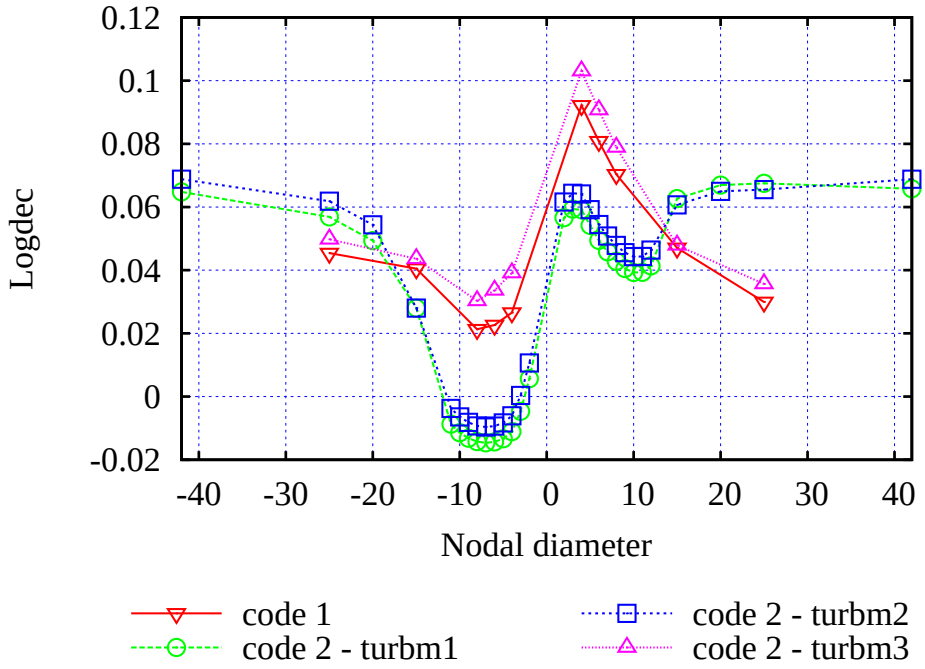

Figure 8.11: Logdec versus nodal diameter. The effect of turbulence model on the flutter stability

label	Description
code 1	Original solution with solver of Chapter 3
code 2 - turbm1	Destruction terms not included; omg = 0.01
code 2 - turbm2	Destruction terms not included; omg = 0.5
code 2 - turbm3	Destruction terms included; omg = 0.01

Table 8.2: Notation used in Figs. 8.10 and 8.11

the flow remains attached to the blade and there is no separation. However, when the numerical dissipation increases, the effect of removing the destruction terms is not enough to maintain the flow attached and a small separation occurs from near the blade leading edge on the pressure side. Secondly, when the destruction terms are included in the turbulence model, the flow separation increases, and the velocity vector profiles are similar to those obtained in the original solution. The size of the separation has a significant effect on the mass flow rate which goes through the turbine (about 2% change), and also a small effect on the pressure ratio (about 0.25 % change).

Figure 8.11 shows that flutter instability predictions are in line with the experiment for the solutions which present a mass flow rate greater than approximately 147.5 kg/s. Although the size of the separation can be seen as a controlling parameter for the mass rate, the separation itself cannot be attributed the role of triggering the

flutter instability since one of the numerical solutions showed flutter even with no separation.

Figure 8.12 shows that the lift vectors integrated over the blade surface at 80% height vary only slightly between the unstable and the stable flutter solutions, but perhaps sufficiently enough to favour the blade vibration instability.

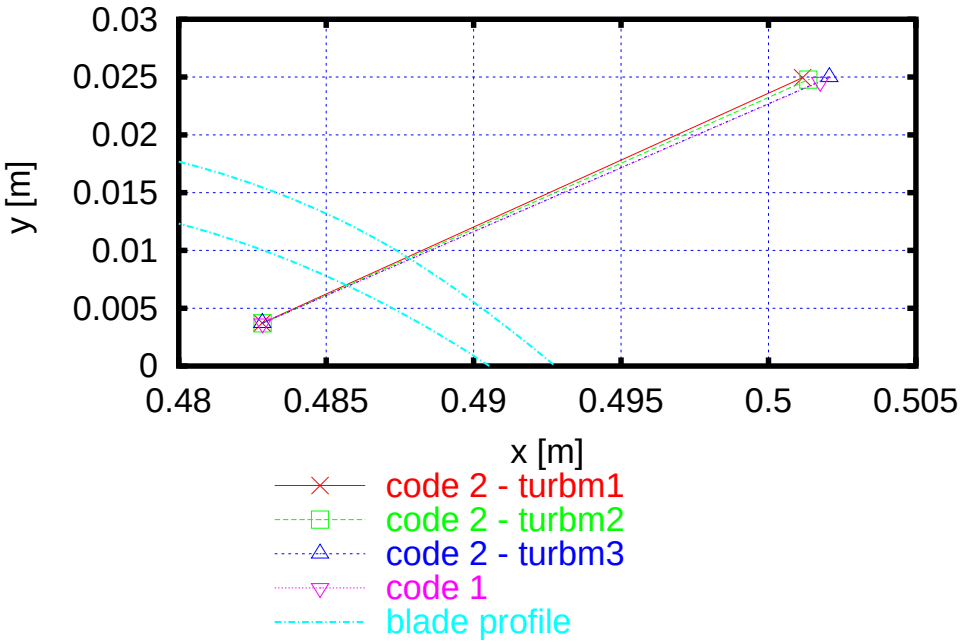

Figure 8.12: Comparison of integrated lift vectors at 80%; Normalised lift starting from the center of force

Finally, the local unsteady work (or worksum) on the blade surface integrated over a time-period can tell us which parts of the blade are unstable during the vibration. A global positive work on the blade causes the vibration to be unstable, which corresponds to a negative logdec. The local worksum is plotted on the blade surface for three of the above-computed steady-state flow solutions (Figs. 8.13, 8.14, 8.15). In these figures, the contour scale has been modified such that the contours on the left on the vertical line show only the unstable parts with minimum (red) equal zero to worksum, and the contours on the right show only the stable parts with maximum (pink) equal to zero worksum. These figures clearly show that, for all three solutions, the region near the blade trailing edge and on the pressure side is the most unstable. This unstable region starts from about 30% blade high and grows up to the tip. Other, but smaller, unstable patches can also be seen on the blade suction side. These results can be understood intuitively as the blade trailing edge is susceptible to travel a large distance during the mixed flap and twist vibration, and thus to produce a significant unsteady work. Due to the flap part of the vibration,

it was also expected that the upper part of the blade would produce or receive the largest amount of work. Importantly, what these plots also highlight is the fact that the flow separation seems to have a stabilising effect on the blade vibration. In fact, the most stable blade region is located on the blade pressure side and it can be seen that the stable region increases with increasing separation size. For steady flow solutions with no separation and small separation, the stable region on the pressure side is not big enough to counteract the unstable parts, and thus the blades vibrate. On the other hand, for flow solutions with large separation, the stable region is large enough to compensate the effect of the unstable parts.

The steady flow solution with a medium size separation seems to represent the best compromise between the expected aerodynamic features and the flutter instability predictions, therefore this solution will serve as a reference for the rest of the analysis.

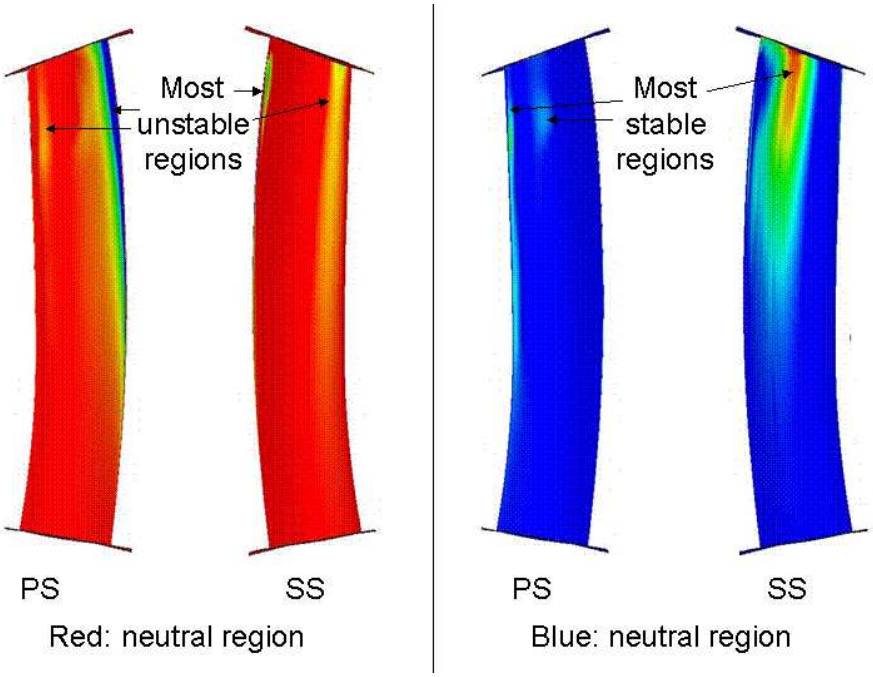

Figure 8.13: Worksum contours on Rotor 2 blade surface for ND = -8; based on steady-state solution from "Code 2 - turbm1"

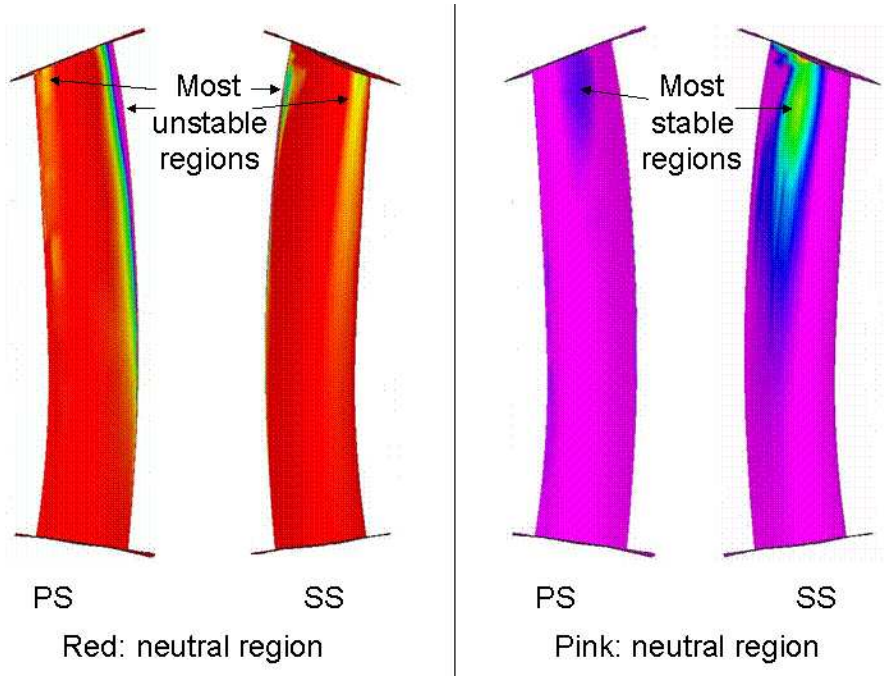

Figure 8.14: Worksum contours on rotor two blade surface for ND = -8; based on steady-state solution from "Code 2 - turbm2"

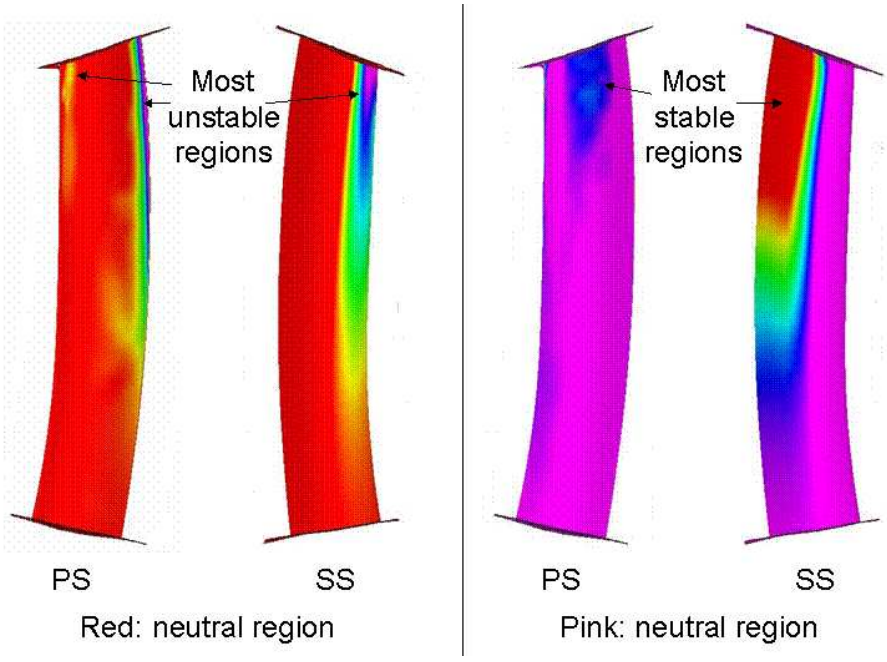

Figure 8.15: Worksum contours on rotor two blade surface for ND = -8; based on steady-state solution from "Code 1"

8.6 Nonlinear Flutter Analysis

Due to the flow separation forming on the pressure side the blade, it can be debated whether the flow is really linearisable in this case. One way to answer this question is to compare the present results against those from a nonlinear unsteady analysis. In this section, the whole-annulus nonlinear unsteady results of Sayma et al. [90] are used for comparison. In their analysis, they used an inviscid unsteady flow plus a loss model for viscous effects. The level of vibration was determined at each time step through the computation of the aerodynamic force, as follows:

$$\frac{d^2\eta_r}{dt^2} + \omega_r^2 \eta_r = \sum_{i=1}^{N} \mathbf{\Phi}_{i,r}.\mathbf{F}_i \tag{8.6.11}$$

where r is the mode index, i is the node number on the blade surface, N is the number of nodes on the blade surface, $\mathbf{\Phi}$ is the modeshapes matrix, η is the modal deflection, ω is the modal frequency, and $\mathbf{F}_i$ is the aerodynamic force given by $\mathbf{F}_i = p_i \delta A_i \mathbf{n}_i$, where p is the local static pressure, δA is the node corresponding area, and $\mathbf{n}$ is the unit normal vector. The comparison between their results and the those from the present analysis is shown in Fig. 8.16. These two results were obtained using 1-D non-reflecting boundary conditions at the far-field boundaries.

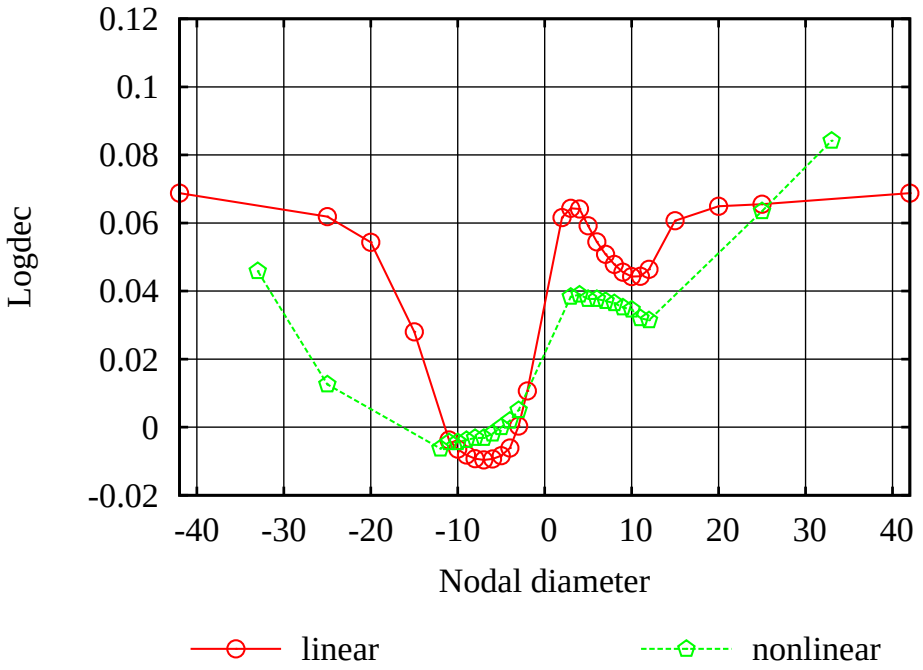

Figure 8.16: Logdec versus nodal diameter; Comparison between harmonic linearised (isolated) and fully nonlinear results

One can see a good trend agreement between the two curves for the unstable nodal diameters, but the agreement deteriorates for the high nodal diameter numbers. Sayma et al. [90] mentioned the uncertainty of their results for the high nodal diameters because they could not determine a well-defined lodgec from the deflection time history. This was later understood to be a too large time-step problem, and the meshes were also too coarse. Furthermore, some discrepencies between the two results were expected since the analysis of Sayma et al used a loss model. To conclude on these comparisons, the agreement between harmonic linearised and fully nonlinear results appears to be satisfactory, at least for the unstable nodal diameters.

8.7 Multi Blade-row Effects on Flutter Stability

The influence of the neighbouring blade-rows on flutter stability will now be investigated. The rotor instability was measured on the real engine in the presence of neighbouring blade-rows, therefore the numerical model must also include those. The following questions need to be answered: (i) What are the effects of the neighbouring blade-rows on the aerodynamic damping of Rotor 2? Is there a stabilising or else a destabilising contribution to flutter?; (ii) Which blade-rows interact the most with Rotor 2?

The number of blades in each blade-row is given in Table 8.3.

Stator 1	Rotor 1	Stator 2	Rotor 2	Stator 3	Rotor 3	Stator 4	Rotor 4
102	140	130	84	120	84	120	80

Table 8.3: Number of blades in the four stages of the LP turbine

A radial view of the steady-state solution near the midspan of each blade-row is shown in Fig. 8.17. Note that the pressure contours are not perfectly continuous in all the blade-rows. In fact, the solutions in all the blade-rows were computed without mixing-planes, but using through flow boundary conditions. This approach was selected for two good reasons: (i) the previously selected steady-state solution in Rotor 2 could be preserved for multi blade-row calculations and for later comparisons with isolated blade-row unsteady results; (ii) the through flow boundary conditions were calibrated using a loss model based on real engine loss data, so this removes the uncertainty of a pressure losses computed using a mixing-plane boundary condition.

For the following unsteady calculations, the harmonic linearised multi blade-row code developed in this thesis was used. Due to computational limitations, only the

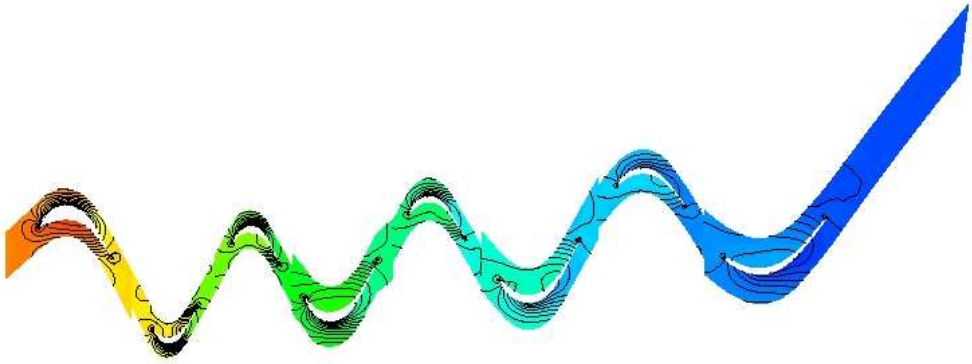

Figure 8.17: Pressure contours at the midspan of the entire LPT

fundamental spinning mode was allowed to propagate across the blade-rows for each assembly nodal diameter. For the same reason, only a few nodal diameter solutions were computed for each configuration. The unsteady solutions were computed for the nodal diameters which are known to be unstable, and for a few other nodal diameters outside this range to get a general trend. Note that for each nodal diameter, the fundamental acoustic mode is cut-off, but the blade-rows are sufficiently close to expect to see blade-row coupling effects.

The results of the unsteady multi blade-row calculation are presented in Fig. 8.18 in terms of the logarithmic decrement parameter. Please note that the isolated blade-row results are slightly different to those previously shown, because 3-D non-reflective boundary conditions were used for this analysis at the far-field boundaries.

These results are very interesting in that they show two important characteristics. First, neighbouring blade-row interactions have a stabilising effect on the flutter stability of Rotor 2. Although blade-row interaction effects do not remove flutter, they bring the aerodynamic damping coefficient closer to the stability region. This result is in accordance with experimental results since experimental measurements indicated that flutter occurred for nodal diameters ND = 7, 8 and 9 only, while the linearised isolated blade-row analysis showed that a wider range of nodal diameters were unstable. Note that a similar result was previously observed by Xuang and He [52] during the flutter analysis of a low-pressure steam turbine stage. In their work, Xuang and He demonstrated the stabilizing effect from a nozzle stator on the flutter of a low-pressure turbine rotor (30% change in logdec). Incidentally, their method (the time-domain Fourier shape correction method discussed in Section 2.2.3) also used the fundamental modes (rotor vibration with frequency shift and the rotor blade passing forcing) in the stator row. In their study of the present low-pressure turbine, Sayma et al. attributed the differences between their numerical results and

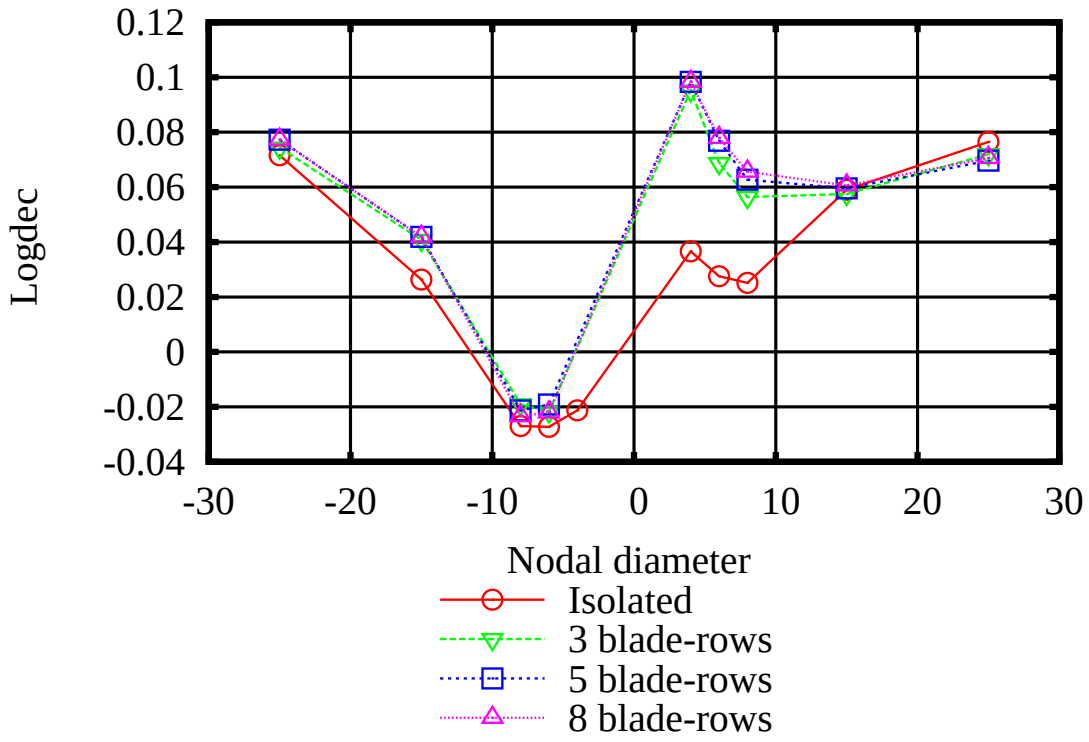

Figure 8.18: Logdec versus nodal diameter in rotor two computed under the influence 3,5, and 8 neighbouring blade-rows

experimental measurement to the fact that they assumed zero mechanical damping in their simulation. The present analysis additionally shows that neighbouring blade-rows provide a stabilising effect in the flutter stability of Rotor 2. Secondly, these results show that only the two immediate neighbouring blade-rows interact strongly with the flow in Rotor 2. The unsteady solutions which include 3, 5 and 8 blade-rows are virtually identical. This is a very important result from a design standpoint since it is currently virtually impossible to include more than two or three blade-rows in the aeroelasticity analyses due to computational limitations. The influence of other blade-rows are usually neglected, and it is shown here that it is not necessary to include more blade-rows in the Rotor 2 flutter analysis of this particular turbine.

Finally, note that it was not possible to validate these multi blade-row results against fully nonlinear methods. An equivalent fully nonlinear computation is currently almost practically impossible.

8.8 Computational Issues

The whole-turbine configuration could be run by using only 12×3.6 GHz Intel Xeon CPUs, on a 64-bit cluster. The computational time typically scaled with the number of blade-rows. In order to improve convergence rates, the following approach was used. The linearised solutions for one blade-row were computed first, then the computations with three blade-rows were started from the solutions with one blade-row, the computations with five blade-rows were started from the solutions with three blade-rows, and so on. Using this approach and due to slow convergence rates, it took about two weeks to obtain the unsteady solutions with 8 blade-rows for each nodal diameter. As shown in Table 8.4, it is estimated that the equivalent fully nonlinear unsteady viscous calculation, using the same quality mesh, would be currently almost practically impossible.

Type of Analysis	No. mesh points	CPU time
Harmonic linear isolated blade-row (1 blade-row)	666,600	1.5 day
Harmonic linear multi blade-row (8 blade-rows)	4,227,500	2 weeks ($\approx$ 168 CPU.day)
Whole-annulus nonlinear time-accurate (8 blade-rows)	450,000,000 (estimated)	$\approx$ 6300 CPU.day (estimated)

Table 8.4: Computational time comparisons between simulation methods

8.9 Conclusions for Chapter 8

The flutter stability of the Stage 2 rotor of a low-pressure turbine has been investigated in this chapter. The results of the present analysis were, as much as possible, validated against experimental measurements. The main findings are summarised below:

- The flutter instability of Rotor 2 is an isolated blade-row problem, and thus it can be, in principle, modelled using Rotor 2 only. It was found that the rotor vibration is mostly unstable through the blades TE, where the local worksum is positive and dominates the flutter behaviour. It was also found that, though the flow separates on the pressure side due to the large blade diffusion, the separation has a stabilising effect on the blade vibration, and it is not a source of excitation. It is thus important to determine the right separation point

accurately, which determines the size of the bubble. If the size of computed separation is too large, the flutter instability is no longer predicted correctly.

- Using the harmonic linearised multi blade-row method, it was found that the unsteady flow interactions between the blade-rows have a stabilising effect on the vibration of Rotor 2, though not enough to stop the rotor from reaching discernible vibration levels. The aerodynamic damping in Rotor 2 was significantly increased in several nodal diameter modes due to blade-row interaction effects. This result can be very important since the accurate prediction of the damping is essential for flutter predictions.

- Most of the unsteady blade-row coupling was captured by including the two nearest blade-rows only. The effects of further blade-rows were found to be negligible for this particular turbine.

- Due to time and computational limitations, only one spinning mode for each 1F vibration frequency was allowed to propagate across the blade-row. The effect of other spinning modes was not investigated and should be the subject of further analyses.

- It was possible to obtain an unsteady solution including the whole LP turbine (i.e. 8 blade-rows) by using the harmonic linearised multi blade-row method developed in this thesis. It is also shown that the equivalent fully nonlinear unsteady viscous calculation would be currently almost practically impossible.

Chapter 9

Conclusions and Further Work

A harmonic linearised multi blade-row solver for the computation of unsteady flows in turbomachinery is developed in this thesis. The blade-row coupling is represented using the theory of spinning modes, which provide a mechanism of communication between the blade-rows. The new method aims to provide efficient numerical solutions for the computation of turbomachinery aeroelasticity with enough engineering accuracy. The objective is to influence the early design stages of new blades by providing fast aeroelasticity predictions. The new method is tested and validated over several test cases against analytical, semi-analytical, reference solutions, and experimental data. Particular emphasis is put on studying the effects of multi blade-row interactions on turbomachinery aeroelasticity predictions. The main findings of this thesis are summarised below:

Multi blade-row effects Most previous research works, discussed in Chapter 2, had investigated unsteady blade-row interactions on flutter and forced response in both fans and compressors. Unsteady blade-row interactions in turbines are studied in this thesis. Chapter 6 analyses 2-D cascades of flat plates (stator/rotor/stator) for flutter. It is shown that blade-row interactions can modify the rotor lift coefficient by as much as 70 % for bending vibration. Results also suggest that the unsteady blade-row coupling may be good for the avoidance of acoustic resonances. Chapter 7 studies a real turbine stage (stator/rotor) in a 3-D transient flow for stator-rotor interaction. It is shown that blade-row interactions account for about 25% of the unsteady lift near the blade midspan. Chapter 8 analyses an industrial low-pressure turbine (8 blade-rows) for flutter occurring on the first flap mode of the stage two rotor. It is observed that blade-row interactions can change by more than 100 % the rotor aerodynamic damping associated with some nodal diameters, and that these interactions have an overall stabilizing effect on this rotor. This result can be very

important from a design standpoint as all corresponding flutter analyses, known to the author, have been made by modelling a blade-row in isolation. This result can also be important for mistuning analyses, as the latter rely on accurate aeroelasticity predictions.

Fundamental acoustic mode cut-on or cut-off It is shown in Chapter 6 that blade-row interactions can be larger when the fundamental acoustic mode is cut-off - as opposed to when it is cut-on - especially when the blade-rows are close to each other. It is also demonstrated that the blade-row interactions can increase with increasing axial gap when the fundamental acoustic mode is cut-on, whereas these interactions always decrease with increasing gap when the fundamental acoustic mode is cut-off. This is an important issue as a general trend adopted for design is to increase the axial gap between the blade-rows to decrease the forced response (or unsteady blade-row interactions).

Number of spinning modes retained in the analysis The present work suggests that most of the unsteady blade-row coupling can be represented using one spinning mode only, namely the fundamental spinning mode, which is that associated with the original disturbance. Chapter 7 also shows that the present code is quite sensitive to numerical reflections at the inter-row boundaries. The stator-rotor interaction analysis of this chapter had some numerical reflections at the inter-row boundary, which obscured the effects of spinning modes other than the fundamental one for this case.

Number of upstream/downstream blade-rows Chapter 8 suggests that most of the blade-row coupling can be captured by including only three blade-rows in the model.

Importance of steady-state solution Finally, it is shown in Chapters 7 and 8 that the present linear code is very sensitive to the steady-state solution. It is concluded that it is very important to get the steady-state flow (or operating point) right prior to running a harmonic multi blade-row calculation. In fact, the effect of the steady-state flow on the linear flutter and forced response results might be even greater than the effects of other blade-rows.

Computational issues As observed in Chapters 7 and 8, the computational time using the present code typically scales with the number of blade-rows and the num-

ber of spinning modes. The GMRES acceleration technique significantly improves convergence rate compared to conventional single-grid or multi-grid methods. However, as explained in Chapter 4, the iteration update of the inter-row boundary conditions does not make the GMRES algorithm unconditionally stable. This problem is avoided by restarting the GMRES calculation a sufficient number of times. A successful approach to stabilise the multi blade-row computation was to compute the linearised solution for one blade-row first, then the computation with the first upstream and downstream blade-rows were started from the solutions with one blade-row, and so on. As shown in Chapter 8, it took about two weeks to obtain the flutter unsteady solutions with 8 blade-rows for each nodal diameter using this approach. It is estimated that the equivalent fully nonlinear unsteady viscous calculation, using the same quality mesh, would be almost practically impossible.

Further Work

Below is a list of further research topics, which are recommended by the author to clarify some of the unresolved issues in this thesis, and to improve the general applicability of the present harmonic linearised multi blade-row solver:

- Investigate and identify for which applications, and for what range of flow conditions, the linearity assumption is valid for industrial configurations. There is already evidence that linearised codes can provide satisfactory results near design conditions, but not much work has been done to investigate their accuracy at off-design conditions, where most nonlinear effects exist. Such work would help to shed light on fundamental questions by designers: can linearised codes help to represent aeroelastic behaviour near stall of choke conditions? how far from the working line is the linearised assumption valid? or can low rotational speed unsteady flows be correctly represented by linearised codes?

Below is a list of further application areas which have not been tackled during this thesis. However, the present solver can, in principle, be used for such applications:

- The capability offered by the present code to propagate waves with discrete frequencies between blade-rows makes it invaluable in the analysis of tone-noise propagation. In particular, it is known that the fan tone-noise strongly interacts with both the downstream OGV and the ESS. It is today practically impossible to model such a configuration using a fully nonlinear method due to the very large mesh size required. However, such an analysis *is possible* using the present code since only a single-passage mesh is required per blade-row for each wave's frequency, reducing significantly the mesh size. This type of analysis is already scheduled at Rolls-Royce, which will use the present code.

- Distortion transfer analyses (in core compressors for example) require the propagation of distortions across many blade-rows. Current prediction methods are usually based on a fully nonlinear approach using very coarse meshes at the expense of accuracy. It is also often necessary to study many distortion levels for the assessment, for example, of stall margin variations caused by the distortions. Though the present code may not be suitable for the simulation of unsteady flows near stall, it is certainly advantageous in the study of distortion transfer across several blade-rows at a lower computational cost, and using finer meshes than those that can be afforded by current prediction methods. This type of analysis is also scheduled at Rolls-Royce, which will use the present code.

- During a personal discussion, Prof. M.B. Giles of Oxford University emphasised the possibility to develop further the present code to improve performance calculations at low computational cost. This idea is based on the observation that the unsteadiness may change the mean flow properties, such as mass flow rate and efficiency. The unsteady perturbations create deterministic stress terms in the time-averaged momentum and energy equations, which provide a time-mean correction to the steady-state solution in each blade-row. Therefore, multistage performance predictions can be significantly improved. Such code development would probably need to be based on either SLIQ or the nonlinear harmonic method discussed in Chapter 2.

Bibliography

[1] J.J. Adamczyk. Model equations for simulating flows in multistage turbomachinery. *ASME Paper 85-GT-226*, June 1985.

[2] AGARD. Multilingual aeronautical dictionary. *AGARD, ISBN 92-835-1666-7*, 1980.

[3] A. Arnone and R. Pacciani. Rotor-stator interaction analysis using the Navier-Stokes equations and a multigrid method. *ASME Journal of Turbomachinery*, 118:679–689, 1996.

[4] A. Brandt. Multi-level adaptive solutions to boundary value problems. *Mathematics of Computation*, 21:333–390, 1977.

[5] D.H. Buffum. Blade row interaction effects on flutter and forced response. *AIAA Paper 93-2084*, 1993.

[6] P. Calza. Investigation on different modelling of stator/rotor interaction in a turbine stage for aeroelastic purposes. *PhD thesis*, December 2005. Universita' degli Studi di Padova, Dipartamento Ingegneria Elettrica.

[7] W. Campbell. The protection of steam turbine disc wheels from axial vibrations. *Transactions of the ASME*, (23), 1924. New York, USA.

[8] W. Campbell. Tangential vibration of steam turbine buckets. *Transactions of the ASME*, (33), 1925. New York, USA.

[9] M.S. Campobasso and M.B. Giles. Effect of flow instabilities on the linear analysis of turbomachinery aeroelasticity. *AIAA Journal of Propulsion and Power*, 19(2), 2003. Springer-Verlag.

[10] M.S. Campobasso and M.B. Giles. Stabilization of a linearised Navier-Stokes solver for turbomachinery aeroelasticity. *in Computational Fluid Dynamics 2002*, 2003. Springer-Verlag.

[11] M.S. Campobasso and M.B. Giles. Stabilization of linear flow solver for turbomachinery aeroelasticity using recursive projection method. *AIAA Journal*, 42(9), September 2004.

[12] M.S. Campobasso and M.B. Giles. Computing linear harmonic unsteady flows in turbomachines with complex iterative solvers. *AIAA CFD Conference*, 2005.

[13] M.M. Cand. A 3D high-order aeroacoustics model for turbo machinery fan noise propagation. *PhD thesis*, 2005. Imperial College, London, United Kingdom.

[14] A.M. Cargill. Aspects of the generation of low engine order forced vibration due to non-uniform nozzle guide vanes. *Rolls-Royce plc, Report No. TSG0602*, 1992.

[15] J.E. Caruthers and W.N. Dalton. Unsteady aerodynamic response of a cascade to nonuniform inflow. *American Society of Mechanical Engineers, International Gas Turbine and Aeroengine Congree and Exposition, Paper 91-GT-174*, June 3-6 1991. Orlando.

[16] T. Chen and L. He. Analysis of unsteady blade row interaction using nonlinear harmonic approach. *Journal of Propulsion and Power*, 17(3), May-June 2001.

[17] T. Chen, P. Vasanthakumar, and L. He. Analysis of unsteady blade row interaction using nonlinear harmonic approach. *Journal of Propulsion And Power*, 17(3):651–658, 2001.

[18] G. Cicarelli and C.H. Sieverding. The effects of vortex shedding on the unsteady pressure distribution around the trailing edge of a turbine cascade. *ASME Paper 96-GT-356*.

[19] W.S. Clark and K.C. Hall. A time-linearized Navier-Stokes analysis of stall flutter. *Journal of Turbomachinery*, 122:467–476, July 2000.

[20] A.R. Collar. The expanding domain of aeroelasticity. *The Royal Aeronautical Society*, pages 613–636, 1946.

[21] S. Dewhurst and Li. He. Unsteady flow calculations through turbomachinery stages using single-passage domain with shape-correction method. *The 9th International Symposium on Unsteady Aerodynamics, Aeroacoustics and Aeroelasticity of Turbomachines*, pages 338–350, Septembre 2000. edited by Pascal Ferrand and Stephane Aubert.

[22] E.H. Dowel, H.C.Jr. Curtiss, R.H. Scanlan, and F. Sisto. A modern course on aeroelasticity (second ed.). *Kluwer Academic Publishers*.

[23] M.C. Duta. The use of the adjoint method for the minimization of forced response. *PhD Thesis*, 2001. University of Oxford, United Kingdom.

[24] J.A. Ekaterinaris and M.F. Platzer. Progress in the analysis of blade stall flutter. *Unsteady Aerodynamics and Aeroelasticity of Turbomachines*, pages 287–302, 1995. edited by Y.Tanida and M.Namba, Elsevier, Amsterdam.

[25] K. Ekici and K.C. Hall. Nonlinear analysis of unsteady flows in multistage turbomachines using the harmonic balance technique. *AIAA 2006-422, 44th AIAA Aerospace Sciences Meeting and exhibit*, 9-12 January 2006. Reno, Nevada.

[26] A.H. Epstein, M.B. Giles, T. Shang, and A.K. Sehra. Blade row interaction effects on compressor measurements. *AGARD 74th Specialists Meeting on Unsteady Aerodynamic Phenomena in Turbomachines*, August 1989.

[27] J.I. Erdos, E. Altzner, and W. McNally. Numerical solution of periodic transonic flow through a fan stage. *AIAA Journal*, 15:165–186, 1977.

[28] J.E. Ffowcs-Williams and D.L. Hawkings. Theory relating to the noise of rotating machinery. *Journal of Sound and Vibration*, 10(1), 1969.

[29] T.H. Fransson. Basic introduction to aeroelasticity. *VKI LS on Aeroelasticity in Axial-Flow Turbomachines*, May 1999.

[30] M.B. Giles. Calculation of unsteady wake/rotor interaction. *AIAA Journal of Propulsion and Power*, 4(4):356–362, July/August 1988.

[31] M.B. Giles. Non-reflecting boundary conditions for Euler equation calculations. *AIAA Journal*, 28(12):2050–2058, 1990.

[32] M.B. Giles. A framework for multi-stage unsteady flow calculations. *In Proceeding of the Sixth International Symposium on Unsteady Aerodynamics, Aeroacoustics and Aeroelasticity of Turbomachines and Propellers*, 1991. H.M. Atassi, editor. Springer-Verlag, 1993.

[33] M.B. Giles. SLIQ: A numerical method for the calculation of flow in multistage turbomachinery. *Rolls-Royce Internal Report*, 1991.

[34] M.B. Giles. An approach for multi-stage calculations incorporating unsteadiness. *ASME paper 92-GT-282*, 1992.

[35] C.K. Hall, J.P. Thomas, and W.S Clark. Computation of unsteady nonlinear flows in cascades using a harmonic balance technique. *AIAA Journal*, 40(5):879–886, May 2002.

[36] K.C. Hall and W.S. Clark. Linearised Euler predictions of unsteady aerodynamic loads in cascades. *AIAA Journal*, 31(3):540–550, March 1993.

[37] K.C. Hall, W.S. Clark, and C.B. Lorence. A linearized Euler analysis of unsteady transonic flows in turbomachinery. *Journal of Turbomachinery*, 116:447–488, July 1994.

[38] K.C. Hall and E.F. Crawley. Calculation of unsteady flows in turbomachinery using the linearized Euler equations. *AIAA Journal*, 27(6):777–787, 1989.

[39] K.C. Hall and K. Ekici. Multistage coupling for unsteady flows in turbomachinery. *AIAA Journal*, 43(3):624–632, March 2005.

[40] K.C. Hall and C.B. Lorence. Calculation of three-dimensional unsteady flows in turbomachinery using the linearized harmonic Euler equations. *Journal of Turbomachinery*, 115(4):800–809, October 1993.

[41] K.C. Hall, C.B. Lorence, and W.S. Clark. Non-reflecting boundary conditions for linearized unsteady aerodynamic calculations. *AIAA Paper*, (93-0882), 1993.

[42] K.C. Hall, J.P. Thomas, and W.S. Clark. Computation of unsteady nonlinear flows in cascades using a harmonic balance technique. *AIAA Journal*, 40(5):879–886, 2002.

[43] K.C. Hall and J.M. Verdon. Gust response of a cascade operating in a nonuniform mean flow. *AGARD Propulsion and Energetics Panel 74th Specialists Meetings on Unsteady Aerodynamic Phenomena in Turbomachines*, 28-Sept 1989. Kirchberg Plateau, Luxembourg.

[44] D.B. Hanson. Mode trapping in coupled 2D cascades-acoustic and aerodynamic results. *AIAA Paper 93-4417*, 1993.

[45] L. He, T. Chen, R. G. Wells, Y.S. Li, and W. Ning. Analysis of rotor-rotor and stator-stator interferences in multi-stage turbomachines. *Transactions of the ASME journal of turbomachinery*, 124(4):564–571, 2002.

[46] L. He and J.D. Denton. Three-dimensional time-marching inviscid and viscous solutions for unsteady flows around vibrating blades. *Transaction of the ASME journal of turbomachinery*, 116:469–476, 1994.

[47] L. He and W. Ning. Efficient approach for analysis of unsteady viscous flows in turbomachines. *AIAA Journal*, 36(11):2005–2010, 1998.

[48] L. He and W. Ning. Nonlinear harmonic aerodynamic modelling. *VKI Lecture Series, Aeroelasticity in Axial-Flow Turbomachines*, May 1999.

[49] C. Hirsch. Numerical computation of internal and external flows; volume 1: Fundamentals of numerical discretization. Editor: John Wiley and Sons.

[50] D.G. Holmes and H.A. Chuang. 2D linearised harmonic Euler flow analysis for flutter and forced response. *Presented at Sixth Symposium on Unsteady Aerodynamics and Aeroelasticity of Turbomachines and Propellers*, 1991. Notre Dame, IN.

[51] D.G. Holmes, B.E. Mitchell, and C.B. Lorence. Three-dimensional linearized Navier-Stokes calculations for flutter and forced response. *in Unsteady Aerodynamics and Aeroelasticity of Turbomachines: Proceedings of the 8th International Symposium held in Stockholm, Sweden 14-18 September 1997*, pages 211–224, 1998. T.H. Fransson, ed., Kluwer Academic Publishhers, Dordrecht.

[52] X. Huang, L. He, and D.L. Bell. Influence of upstream stator on rotor flutter stability in a low-pressure steam turbine stage. *Journal of Power and Energy*, 220(1):25–35, Feb 2006. Proc, IMech.E, Part-A.

[53] A.B. Johnson, M.J. Rigby, M.L.G. Oldfield, and M.B. Giles. Nozzle guide vane shock wave propagation and bifurcation in a transonic turbine rotor. *ASME Paper 90-GT-310*, June 1990.

[54] Green. J.S. and T.H. Fransson. Scaling of turbine blade unsteady pressures for rapid forced response assessment. *ASME paper GT2006-90613*, May 8-11 2006. Barcelona, Spain.

[55] E. Kivanc, D.M. Voytovych, and K.C. Hall. Time-linearized Navier-Stokes analysis of flutter in multistage turbomachines. *43rd AIAA Aerospace Sciences Meeting and Exhibit*, 10 -13 January 2005. Reno, Nevada.

[56] M. Koya and S. Kotake. Numerical analysis of fully three-dimensional periodic flows through a turbine stage. *Journal of Engineering for Gas Turbines and Power*, 107:945–952, 1985.

[57] F. Lane. System mode shapes in the flutter of compressor blade rows. *Journal of Aeronautical Sciences*, 23(1):54–66, 1956.

[58] H.D. Li and L. He. Single-passage analysis of unsteady flows around vibrating blades of a transonic fan under inlet distortion. *Transaction of the ASME journal of turbomachinery*, 124(2):285–292, 2002.

[59] H.D. Li and L. He. Blade count and clocking effects on three-bladerow interaction in a transonic turbine. *Transaction of the ASME journal of turbomachinery*, 125(4):632–640, 2003.

[60] H.D. Li and L. He. Blade aerodynamic damping variation with rotor-stator gap: A computational study using single-passage approach. *Journal of Turbomachinery-transactions of the Asme*, 127(3):573–579, 2005.

[61] H.D. Li and L. He. Toward intra-row gap optimization for one and half stage transonic compressor. *Journal of Turbomachinery-transactions of the Asme*, 127(3):589–598, 2005.

[62] J. Lighthill. Waves in fluids. *Cambridge University Press*, 1978. Cambridge.

[63] M.J. Lighthill. On sound generated aerodynamically. i - general theory. *Proc. Roy. Soc*, A 211, 1952.

[64] M.J. Lighthill. On sound generated aerodynamically.ii - turbulence as source of sound. *Proc. Roy. Soc*, A 211, 1954.

[65] D.R. Lindquist and M.B. Giles. On the validity of linearized Euler equations with shock capturing. *AIAA 10th Computational Fluid Dynamics Conference*, June 24-26 1991. Honolulu, Hawaii.

[66] D.R. Linquist and M.B. Giles. Generation and use of unstructured grids for turbomachinery. *Proceedings of Computational Fluid Dynamics Symposium on Aeropropulsion*, April 1990. NASA CP-10045.

[67] J.G. Marshall and M. Imregun. A review of aeroelasticity methods with emphasis on turbomachinery applications. *Journal of Fluids and Structures*, 10:237–267, 1996. ISSN: 0889-9746.

[68] L. Martinelli. Calculation of viscous flows with a multigrid method. *PhD Thesis*, 1987. Princeton University, Dept. of Mech. and Aerospace Eng.

[69] W.D. McNally. Review of experimental work on transonic flow in turbomachinery. *In Transonic Flow Problems in Turbomachinery*, 1977. Editor Adamson, T.C. Jr and Platzer, M.F. Hemisphere Publishing Corporation, London ISBN 0-9116-069-8.

[70] S. Moffatt and L. He. On decoupled and fully-coupled methods for blade forced response prediction. *Journal of fluids and structures*, 20(2):217–234, 2005.

[71] P. Moinier. Algorithm developments for an unstructured viscous flow solver. *PhD Thesis*, 1999. University of Oxford, United Kingdom.

[72] P. Moinier and M.B. Giles. Eigenmode analysis for turbomachinery applications. *AIAA Journal of Propulsion and Power*, 21(6):973–978, 2005.

[73] P. Moinier, M.B. Giles, and J. Coupland. Non-reflecting boundary conditions for 3D viscous flows in turbomachinery. *AIAA Journal of Propulsion and Power*, 23(5):981–986, 2007.

[74] R.W. Moss, R.W. Ainsworth, C.D. Sheldrake, and R. Miller. The unsteady pressure field over a turbine blade surface: Visualisation and interpretation of experimental data. *ASME Paper 97-GT-474*, 1997.

[75] M. Namba. Three dimensional flows. *AGARD Manual on Aeroelasticity in Axial-Flow Turbomachines, Unsteady Turbomachinery Aerodynamics*, 1, March 1987. edited by M.F. Platzer and F.O. Carta, AGARD-AG-298, Chap. IV.

[76] M. Namba and K. Nanba. Unsteady aerodynamic work on oscillating annular cascades in counter rotation (combination of subsonic and supersonic cascades). *Presented at the 10th International Symposium on Unsteady Aerodynamics, Aeroacoustics and Aeroelasticity of Turbomachines (ISUAAAT)*, Sept 2003.

[77] M. Namba, N. Yamasaki, and S. Nishimura. Unsteady aerodynamic force on oscillating blades of contra-rotating annular cascades. *Proceedings of the 9th International Symposium on Unsteady Aerodynamics, Aeroacoustics and Aeroelasticity of Turbomachines (ISUAAAT)*, pages 375–386, Sept 2000.

[78] R.H. Ni and F. Sisto. Numerical computation of nonstationary aerodynamics of flat plate cascades in compressible flow. *Journal of Engineering for Power*, 98:165–170, 1976.

[79] W. Ning. Computation of unsteady flows in turbomachinery. *PhD thesis*, 1998. School of Engineering, University of Durham.

[80] W. Ning and L. He. Computation of unsteady flows around oscillating blades using linear and nonlinear harmonic Euler methods. *Journal of Turbomachinery-transactions of The Asme*, 120(3):508–514, 1998.

[81] R. Parker. Resonance effects in wake shedding from compressor blading. *Journal of Sound and Vibration*, 6:302–309, 1967.

[82] A.B. Parry. Energy transport by cut-off sound waves. *Internal Rolls-Royce memorandum*, (ABP 186.DOC), 1998.

[83] M.M. Rai. Navier-Stokes simulations of rotor/stator interaction using patched and overlaid grids. *AIAA Journal of Propulsion and Power*, 3(5):387–396, 1985.

[84] M.M. Rai and R.P. Dring. Navier-Stokes analyses of the redistribution of the inlet temperature distorsions in a turbine. *AIAA Paper 87-2146*, 1987.

[85] M. Roger. The acoustic analogy some theoretical background. *Von Karman Institute for Fluid Dynamics, Lecture Series 2000-02*, February 2000.

[86] G. Samoylovich. Resonance phenomena in sub- and supersonic flow through an aerodynamic cascade. *Mekhanica Zhidkosti Gaza 2*, pages 143–144, 1967.

[87] A.I. Sayma. Low engine order excitation mechanisms in turbine blades. *VUTC/C/97023*, 1997.

[88] A.I. Sayma and L. Sbardella. ACE: Aeroelasticity computing environment - version 3.0 user manual. *IC Vibration UTC report*, (VUTC/C/97005), 1997.

[89] A.I. Sayma, M. Vahdati, and C. Breard. Flutter analysis of T800 fan using AU3D - intake duct effects. *VUTC/CB19/98007*, 1998.

[90] A.I. Sayma, M. Vahdati, J.S. Green, and M. Imregun. Whole-assembly flutter analysis of a low pressure turbine. *The Aeronautical Journal of the Royal Aeronautical society*, december 1998.

[91] A.I. Sayma, M. Vahdati, and M. Imregun. Whole-assembly flutter analysis of a low-pressure turbine blade. *AERONAUT J*, 102:459 – 463, 1998. ISSN: 0001-9240.

[92] A.I. Sayma, M. Vahdati, and M. Imregun. Multi-bladerow fan forced response predictions using an integrated three-dimensional time-domain aeroelasticity model. *Proc Instn Mech Engrs*, 214, 2000. Part C.

[93] A.I. Sayma, M. Vahdati, and M. Imregun. Multi-stage whole-annulus forced response predictions using an integrated non-linear analysis technique - part 1:numerical model. *Journal of Fluids and Structures*, 2000. ISSN: 0889-9746.

[94] A.I. Sayma, M. Vahdati, and M. Imregun. Turbine forced response prediction using an integrated non-linear analysis. *Proc Instn Mech Engrs*, 214, 2000. Part K.

[95] A.I. Sayma, M. Vahdati, L. Sbardella, and M. Imregun. Modeling of three-dimensional viscous compressible turbomachinery flows using unstructured hybrid grids. *AIAA Journal*, 38(6), June 2000.

[96] L. Sbardella. Levmap 2.0, a mesh generator for the cfd modelling of turbomachinery blades: User guide. *Technical Report VUTC/C/97022*, 1998. Imperial College.

[97] L. Sbardella. Time-domain simulation of sound attenuation in lined ducts. *VUTC/CB11/98006*, 1998.

[98] L. Sbardella. Simulation of unsteady turbomachineary flows for forced response predictions. *PhD thesis*, June 2000. Imperial College, London, England.

[99] L. Sbardella, A.I. Sayma, and M. Imregun. Semi-unstructured mesh generator for flow calculations in axial turbomachinery blading. *In 8th International Symposium on Unsteady Aerodynamics and Aeroelasticity of Turbomachines (ISUAAT)*, pages 541–554, 1997. Stockholm.

[100] L. Sbardella, A.I. Sayma, and M. Imregun. Semi-unstructured meshes for axial turbomachinery blades. *International Journal for Numerical Methods in Fluids*, (32):569–584, 2000.

[101] O.P. Sharma, G.F. Pickett, and R.H. Ni. Assessment of unsteady flows in turbines. *Journal of Turbomachinery*, 114:79–90, 1992.

[102] P.D. Silkowski. A coupled mode method for multistage aeroelastic and and aeroacoustic analysis of turbomachinery. 1996. PhD Thesis, Duke University, Durham, NC.

[103] P.D. Silkowski and K.C. Hall. A coupled mode analysis of unsteady multistage flows in turbomachinery. *Journal of Turbomachinery*, 120(3):410–421, 1998.

[104] S.N. Smith. Discrete frequency sound generation in axial flow turbomachines. *Report CUED/A-Turbo/TR 29*, 1971. University of Cambridge, Department of Engineering.

[105] P.R. Spalart and S.R. Allmaras. A one-equation turbulence model for aerodynamic flows. *La Recherche Aerospatiale*, 1:5–21, 1994.

[106] M.A. Spiker, J.P. Thomas, K.C. Hall, R.E. Kielb, and E.H. Dowell. Modelling cylinder flow vortex shedding with enforced motion using a harmonic balance approach. *AIAA 2006-1965, 47th AIAA/ASME/ASCE/AHS/ASC Structures, Structural Dynamics, and Materials Conference*, 1-4 May 2006. Newport, Rhode Island.

[107] A. Suddhoo, M.B. Giles, and P. Stow. Simulation of inviscid blade row interaction using a linear and a non-linear method. *ISABE Conference*, 1991.

[108] A. Suddhoo and P. Stow. Simulation of inviscid blade row interaction using a linearised potential method. *AIAA Paper 90-1916*, 1990.

[109] C.K.W. Tam. Advances in numerical boundary conditions for computational aeroacoustics. *AIAA Paper*, (97-1774), 1997.

[110] J.P. Thomas, E.H. Dowell, and C.K. Hall. Nonlinear inviscid aerodynamic effects on transonic divergence, flutter, and limit-cycle oscillations. *AIAA Journal*, 40(4):638–646, April 2002.

[111] J.P. Thomas, E.H. Dowell, and K.C. Hall. Modelling limit cycle oscillation behavior of the F-16 fighter using a harmonic balance approach. *AIAA 2004-1696, 45th AIAA/ASME/ASCE/AHS/ASC Structures, Structural Dynamics, and Materials Conference*, 19-22 April 2004. Palm Springs, California.

[112] J.P. Thomas, E.H. Dowell, and K.C. Hall. Further investigation of modelling limit cycle oscillation behavior of the f-16 fighter using a harmonic balance approach. *AIAA 2005-1917, 46th AIAA/ASME/ASCE/AHS/ASC Structures, Structural Dynamics, and Materials Conference*, 18-21 April 2005. Austin, Texas.

[113] J.P. Thomas, K.C. Hall, and E.H. Dowell. A harmonic balance approach for modelling nonlinear aeroelastic behavior of wings in transonic viscous flow. *AIAA 2002-1924, 44th AIAA/ASME/ASCE/AHS/ASC Structures, Structural Dynamics, and Materials Conference*, 7-10 April 2003. Norfolk, Virginia.

[114] M. Vahdati. Steady and unsteady flow predictions of rotor rt27a. *VUTC Report No. VUTC/C/98009*, 1998. Centre of Vibration Engineering. Department of Mechanical Engineering.

[115] M. Vahdati. A numerical strategy for modelling rotating stall in core compressors. *International Journal of Numerical Methods in Fluids*, 53(8):1381–1397, March 2007.

[116] M. Vahdati, A.I. Sayma, J.G. Marshall, and M. Imregun. Mechanism and prediction methods for fan blade stall flutter. *Journal of Propulsion and Power*, 17(5), September-October 2001.

[117] J.M. Verdon. Analysis of unsteady supersonic cascades - part 1. *ASME Paper 77-GT-44*, 1977.

[118] J.M. Verdon. Analysis of unsteady supersonic cascades - part 2. *ASME Paper 77-GT-44*, 1977.

[119] J.M. Verdon. Linearized unsteady aerodynamic theory. In M.F. Platzer and F.O. Carta, editors, *AGARD Manual on Aeroelasticity in Axial-Flow Turbomachines, Unsteady Turbomachinery Aerodynamics*, volume 1 of *AGARD-AG-298*. Neuilly sur Seine, France, March 1987.

[120] J.M. Verdon. Review of unsteady aerodynamic methods for turbomachinery aeroelastic and aeroacoustic applications. *AIAA Journal*, 31(2), February 1993.

[121] J.M. Verdon, J.J. Adamczyk, and J.R. Caspar. Subsonic flow past an oscillating cascade with steady blade loading - basic formulation. In R.B. Kinney, editor, *Unsteady Aerodynamics*, AZ, pages 827–851. Univ. of Arizona, Tucson, July 1975.

[122] J.M. Verdon and J.R. Caspar. Development of a linear unsteady aerodynamic analysis for finite-deflection subsonic cascades. *AIAA Journal*, 20(9):1259–1267, 1982.

[123] J.M. Verdon and J.R. Caspar. A linearized unsteady aerodynamic analysis for transonic cascades. *Journal of Fluid Mechanics*, 149(9):403–429, Dec 1984.

[124] D.S. Whitehead. Classical two-dimensional methods. *AGARD Manual on Aeroelasticity in Axial-Flow Turbomachines, Unsteady Turbomachinery Aerodynamics*, 1, March 1987. edited by M.F. Platzer and F.O. Carta, AGARD-AG-298, Chap. III.

[125] D.S. Whitehead and R.J. Grant. Force and moment coefficients of high deflection cascades. In *2nd International Symposium on Aeroelasticity in Turbomachines*, pages 85–127, Juris-verlag Zurich, 1981. edited by P. Suter.

Appendix A

Acoustic, Vortical and Entropic Modes for the 2-D Linearised Euler Equations

A.1 Eigenvalues

The *primitive* form of the 2-D linearised Euler equations, in cartesian coordinates, is given by:

$$\frac{\partial \tilde{\mathbf{U}}}{\partial t} + \mathbf{A}\frac{\partial \tilde{\mathbf{U}}}{\partial x} + \mathbf{B}\frac{\partial \tilde{\mathbf{U}}}{\partial y} = 0 \tag{A.1.1}$$

where

$$\tilde{\mathbf{U}} = \begin{pmatrix} \tilde{\rho} \\ \tilde{u} \\ \tilde{v} \\ \tilde{p} \end{pmatrix}, \mathbf{A} = \begin{pmatrix} u_0 & \rho_0 & 0 & 0 \\ 0 & u_0 & 0 & \frac{1}{\rho_0} \\ 0 & 0 & u_0 & 0 \\ 0 & \gamma p_0 & 0 & u_0 \end{pmatrix}, \mathbf{B} = \begin{pmatrix} v_0 & 0 & \rho_0 & 0 \\ 0 & v_0 & 0 & 0 \\ 0 & 0 & v_0 & \frac{1}{\rho_0} \\ 0 & 0 & \gamma p_0 & v_0 \end{pmatrix} \tag{A.1.2}$$

(ρ_0, u_0, v_0, p_0) are the steady-state primitive variables, and $(\tilde{\rho}, \tilde{u}, \tilde{v}, \tilde{p})$ are the corresponding unsteady perturbations. Under the linearity assumption, the unsteady perturbations must be small compared to their steady-state counterparts, so that: $\tilde{\rho} \ll \rho_0, \tilde{u} \ll u_0, \tilde{v} \ll v_0$, and $\tilde{p} \ll p_0$. Consider that the steady-state flow quantities are already known. Equation (A.1.1) is a partial differential equation with variable coefficients, in which the unknown parameters are the unsteady perturbations.

In turbomachinery applications, it is often preferable to work in cylindrical rather than cartesian coordinates. The 2-D Euler equations in cylindrical coordinates can

be written as follows:

$$\frac{\partial \tilde{\mathbf{U}}}{\partial t} + \mathbf{A}\frac{\partial \tilde{\mathbf{U}}}{\partial x} + \mathbf{B}\frac{1}{R}\frac{\partial \tilde{\mathbf{U}}}{\partial \theta} = 0 \tag{A.1.3}$$

where R is a constant radius, and v_0 and $\tilde{v}$ are the circumferential velocities.

The variable separation technique can be used to solve (A.1.3). It is assumed that the unsteady perturbations can be decomposed as follows:

$$\tilde{\mathbf{U}}\left(x,\theta,t\right) = X(x)\Theta(\theta)T(t) \tag{A.1.4}$$

This formulation allows to seek wave-like solutions of the form:

$$\tilde{\mathbf{U}}(x,\theta,t) = \hat{\mathbf{U}}e^{i(k_x x + k_\theta \theta + \omega t)} \tag{A.1.5}$$

where $\hat{\mathbf{U}}$ is the perturbation amplitude, k_x and k_θ are the axial and circumferential wave numbers respectively. Inserting (A.1.5) into (A.1.3) gives:

$$\left(\omega\mathbf{I} + k_x\mathbf{A} + \frac{k_\theta}{R}\mathbf{B}\right)\hat{\mathbf{U}} = 0 \tag{A.1.6}$$

where $\mathbf{I}$ is the identity matrix. Expanding (A.1.6), we obtain:

$$\begin{pmatrix} \omega + k_x u_0 + \frac{k_\theta}{R}v_0 & k_x\rho_0 & \frac{k_\theta}{R}\rho_0 & 0 \\ 0 & \omega + k_x u_0 + \frac{k_\theta}{R}v_0 & 0 & \frac{k_x}{\rho_0} \\ 0 & 0 & \omega + k_x u_0 + \frac{k_\theta}{R}v_0 & \frac{k_\theta}{R\rho_0} \\ 0 & k_x\gamma p_0 & \frac{k_\theta}{R}\gamma p_0 & \omega + k_x u_0 + \frac{k_\theta}{R}v_0 \end{pmatrix} \begin{pmatrix} \hat{\rho} \\ \hat{u} \\ \hat{v} \\ \hat{p} \end{pmatrix} = 0 \tag{A.1.7}$$

Pre-multiplying (A.1.6) by $\mathbf{A}^{-1}$ yields:

$$\left(\omega\mathbf{A}^{-1} + k_x\mathbf{I} + \frac{k_\theta}{R}\mathbf{A}^{-1}\mathbf{B}\right)\hat{\mathbf{U}} = 0, \tag{A.1.8}$$

In this form, it is clear that $\hat{\mathbf{U}}$ is the right eigenvector solution of the matrix $\left(\omega\mathbf{A}^{-1} + \frac{k_\theta}{R}\mathbf{A}^{-1}\mathbf{B}\right)$ with eigenvalue $-k_x$. Hence, (A.1.8) admits four distinct solutions. We will see that each of these solutions corresponds to a specific type of wave. Equation (A.1.8) also indicates that prior to finding the solutions for k_x, one must determine the values of k_θ. For this, one notes that the solution of (A.1.3) must be periodic in the circumferential direction, and thus:

$$\tilde{\mathbf{U}}\left(x,\theta+2\pi,t\right) = \tilde{\mathbf{U}}\left(x,\theta,t\right) \tag{A.1.9}$$

In turbomachinery applications, it is generally assumed that unsteady perturbations are periodic in the circumferential direction with a period smaller period than 2π.

Consider a circumferential section P and denote a phase shift between the ends of this section by σ, the circumferential periodicity becomes:

$$\tilde{\mathbf{U}}\left(x,\theta+P,t\right)=\tilde{\mathbf{U}}\left(x,\theta,t\right).e^{i\sigma} \tag{A.1.10}$$

Since the perturbation solution is periodic, it can be decomposed into a Fourier series:

$$\tilde{\mathbf{U}}(x,\theta,t)=\sum_{n=-\infty}^{+\infty}\hat{\mathbf{U}}_n(x,t)e^{ik_{\theta n}\theta} \tag{A.1.11}$$

where

$$\hat{\mathbf{U}}_n\left(x,t\right)=\frac{1}{P}\int_P\tilde{\mathbf{U}}\left(x,\theta,t\right)e^{-ik_{\theta n}\theta}d\theta \tag{A.1.12}$$

The combination of (A.1.10) and (A.1.11) yields:

$$\tilde{\mathbf{U}}(x,\theta+P,t)=\sum_{n=-\infty}^{+\infty}\hat{\mathbf{U}}_n\left(x,t\right)e^{ik_{\theta n}(\theta+P)}=\sum_{n=-\infty}^{+\infty}\hat{\mathbf{U}}_n\left(x,t\right)e^{i(k_{\theta n}\theta+\sigma+2\pi n)} \tag{A.1.13}$$

Therefore, it is shown that k_θ can take an infinite number of values, $k_{\theta n}$, given by:

$$k_{\theta n}=\frac{\sigma+2\pi n}{P},\forall n\in I\ (integer) \tag{A.1.14}$$

For each value of $k_{\theta n}$, (A.1.7) admits four roots $(k_{xn}^{(i)}, i=1,\ldots,4)$, which yield a non-trivial solution. The first two roots are identical:

$$k_{xn}^{(1)}=k_{xn}^{(2)}=-\frac{k+k_{\theta n}M_{\theta 0}/R}{M_{x0}} \tag{A.1.15}$$

where $k=\frac{\omega}{c_0}$ is the wave number, c_0 is the speed of sound, M_{x0} and $M_{\theta 0}$ are respectively the Mach numbers in the axial and circumferential directions respectively. Equation (A.1.15) indicates that if ω is *real* then k is also *real*, and $\frac{\partial k}{\partial k_x}=-M_{x0}<0$, provided that the flow is going in the positive axial direction. Therefore, these two roots correspond to downstream travelling waves.

The third and fourth roots are given by:

$$k_x^{(3)}=-\frac{(k+k_{\theta n}M_{\theta 0}/R)(-M_{x0}+S)}{(1-{M_{x0}}^2)} \tag{A.1.16}$$

$$k_x^{(4)}=-\frac{(k+k_{\theta n}M_{\theta 0}/R)(-M_{x0}-S)}{(1-{M_{x0}}^2)} \tag{A.1.17}$$

where

$$S=\sqrt{1-\frac{(1-{M_{x0}}^2){k_{\theta n}}^2/R^2}{\left(k+M_{\theta 0}k_{\theta n}/R\right)^2}} \tag{A.1.18}$$

For subsonic axial flows (i.e. $0 < M_{x0} < 1$), the *real branch* of S is comprised between zero and one ($0 < S < 1$). Hence, one obtains:

$$\frac{\partial k}{\partial k_x^{(3)}} = -\frac{1 - {M_{x0}}^2}{-M_{x0} + 1/S} < 0 \tag{A.1.19}$$

$$\frac{\partial k}{\partial k_x^{(4)}} = -\frac{1 - {M_{x0}}^2}{-M_{x0} - 1/S} > 0 \tag{A.1.20}$$

Therefore, the third root corresponds to a downstream propagating wave while the fourth root corresponds to an upstream propagating wave. For the downstream propagating wave, the relationships between density, velocities and pressure can easily be obtained by plugging the third root $k_x^{(3)}$ into (A.1.7), as follows:

$$\hat{\rho} = \frac{1}{{c_0}^2}\hat{p} \tag{A.1.21}$$

$$\hat{u} = \frac{-k_x^{(3)}}{\rho_0 c_0 (k + k_x^{(3)} M_{x0} + k_{\theta n} M_{\theta 0}/R)}\hat{p} \tag{A.1.22}$$

$$\hat{v} = \frac{-k_{\theta n}}{R\rho_0 c_0 (k + k_x^{(3)} M_{x0} + k_{\theta n} M_{\theta 0}/R)}\hat{p} \tag{A.1.23}$$

The same procedure can be applied to obtain the relationships between density, velocities and pressure for an upstream propagating wave by plugging the fourth root $k_x^{(4)}$ into (A.1.7).

Plugging the first and second roots $k_x^{(1)}$ and $k_x^{(2)}$ into (A.1.7) gives:

$$\hat{p} = 0 \tag{A.1.24}$$

$$\hat{u} = \frac{-k_{\theta n}}{R k_x^{(1)}}\hat{v} \tag{A.1.25}$$

From (A.1.24) and (A.1.25), it can be seen that density perturbations are not related to the pressure and velocities perturbations, and thus remain undetermined. Two cases can be differentiated:

- If $\hat{\rho} = 0$, (A.1.24) and (A.1.25) describe a vorticity wave. This can be verified by noticing that the wave carries some vorticity, but uniform entropy and pressure.

- If $\hat{\rho} \neq 0$, (A.1.24) and (A.1.25) describe an entropic wave. To verify this, note that pressure and velocities perturbation can also be set to zero ($\hat{u} = \hat{v} = \hat{p} = 0$). In this case, the only non-zero term is the density

perturbation, so that the wave carries a varying entropy and constant pressure but no vorticity.

A.2 Resonance Condition and Complex Eigenvalue

Acoustic resonance occurs when acoustic modes are neither *cut-on* nor *cut-off*, but at the transition between these two modes of propagation. Mathematically, this situation is found when the axial wave number is exactly at the transition between being *real* and *complex*. This happens when (A.1.18) is equal to zero, i.e:

$$\frac{(1-{M_{x0}}^2){k_{\theta n}}^2/R^2}{\left(k+M_{\theta 0}k_{\theta n}/R\right)^2}=1. \tag{A.2.26}$$

which yields a couple of inter-blade phase angle solutions:

$$\sigma=-\frac{\omega\times P\times R}{c_0}\times\frac{M_\theta\pm\sqrt{1-M_x^2}}{1-M^2} \tag{A.2.27}$$

When the flow conditions are such that:

$$\frac{(1-{M_{x0}}^2){k_{\theta n}}^2/R^2}{\left(k+M_{\theta 0}k_{\theta n}/R\right)^2}>1, \tag{A.2.28}$$

then S is no longer *real* but purely *imaginary*. Using (A.1.16) and (A.1.17), it can clearly be seen that when S is complex, so are the axial wave numbers $k_x^{(3)}$ and $k_x^{(4)}$:

$$\Re(k_x^{(3)})=-\frac{(k+k_{\theta n}M_{\theta 0}/R)(-M_{x0})}{(1-{M_{x0}}^2)},\ \Im(k_x^{(3)})=-\frac{(k+k_{\theta n}M_{\theta 0}/R)(\Im(S))}{(1-{M_{x0}}^2)}, \tag{A.2.29}$$

and,

$$\Re(k_x^{(4)})=-\frac{(k+k_{\theta n}M_{\theta 0}/R)(-M_{x0})}{(1-{M_{x0}}^2)},\ \Im(k_x^{(4)})=-\frac{(k+k_{\theta n}M_{\theta 0}/R)(-\Im(S))}{(1-{M_{x0}}^2)}, \tag{A.2.30}$$

In such case, (A.1.5) can be re-written as follows:

$$\tilde{\mathbf{U}}(x,\theta,t)=\hat{\mathbf{U}}e^{[i(\Re(k_x)x+k_\theta\theta+\omega t)-\Im(k_x)x]} \tag{A.2.31}$$

Noticing that $\Re(S)=0$, and $\Im(S)>0$, it is clear that the sign of $\Im(k_x^{(3)})$ and $\Im(k_x^{(4)})$ will depend on the sign of $k+k_{\theta n}M_{\theta 0}/R$. The root for which $\Im(k_x)>0$ corresponds to an acoustic downstream mode since it will decay exponentially in the positive x direction, while the root for which $\Im(k_x)<0$ corresponds to an acoustic upstream mode, which decays exponentially in the negative x direction. Finally, the roots

corresponding to vortical and entropic modes are always real indicating that they will never decay exponentially.

Appendix B

3-D Acoustic Waves for Non-Swirling Uniform Flows

B.1 Theory

The propagation of acoustic waves is governed by the balance between compressibility and inertia forces. Only the equations expressing the conservation of mass and momentum are sufficient to describe their motion. For 3-D inviscid gas, one can write:

$$\frac{\partial \rho}{\partial t} + \bigtriangledown.(\rho \mathbf{u}) = 0 \tag{B.1.1}$$

and

$$\frac{\partial \mathbf{u}}{\partial t} + \mathbf{u}.\bigtriangledown \mathbf{u} = -\frac{1}{\rho}\bigtriangledown p \tag{B.1.2}$$

where gravitational forces have been neglected, and $\mathbf{u}$ represents the gas velocity. Re-arranging (B.1.1) and (B.1.2) gives:

$$\frac{d\rho}{dt} + \rho \bigtriangledown .\mathbf{u} = 0 \tag{B.1.3}$$

$$\frac{d\mathbf{u}}{dt} + \frac{1}{\rho}\bigtriangledown p = 0 \tag{B.1.4}$$

where $d/dt \equiv \partial/\partial t + \mathbf{u}.\bigtriangledown$ is the convective derivative.

The following developments assume an ideal and inviscid gas. For such a gas, it can be demonstrated using the first and second laws of thermodynamics that the entropy s - which can be interpreted as the amount of thermal energy that is not available for conversion into mechanical energy - is advected with the flow, and thus is constant along the streamlines. This type of flow is said to be *isentropic*. When

the entropy is also spatially uniform (i.e when $s = s_0$ everywhere in the flow), the flow is said to be *homentropic*. For homentropic flows, density variations depend only on pressure (and not on temperature) variations ($\rho = \rho(p)$). More explicitly, the relation between density and pressure is given by:

$$p = k\rho^{\gamma}, \tag{B.1.5}$$

and

$$k = \kappa e^{s_0/c_v} \tag{B.1.6}$$

where κ is a constant, γ is the ratio of the specific heat ($\gamma = 1.4$ for diatomic ideal gas), and c_v is the specific heat at constant volume generally assumed to be constant.

For small amplitude perturbations, $\mid \tilde{p} \mid \ll p_0$, and thus it is possible to write that:

$$\rho_0 + \tilde{\rho} = \rho(p_0 + \tilde{p}) \tag{B.1.7}$$

One can use a Taylor series expansion to obtain:

$$\rho_0 + \tilde{\rho} = \rho(p_0) + \tilde{p}\frac{d\rho}{dp}(p_0) \tag{B.1.8}$$

Since $\rho_0 = \rho(p_0)$, one finds that:

$$\tilde{\rho} = \frac{d\rho}{dp}(p_0)\tilde{p} \tag{B.1.9}$$

Differentiating this with respect to t, and by noticing that the speed of sound is given by $c_0 = (\frac{d\rho}{dp}(p_0))^{-\frac{1}{2}}$, the isentropic relationship between density and pressure is obtained as:

$$\frac{\partial\tilde{\rho}}{\partial t} = \frac{1}{c_0^2}\frac{\partial\tilde{p}}{\partial t} \tag{B.1.10}$$

We now want to obtain the equations describing the propagation of 3-D acoustic waves for a specific geometry. Consider an annular duct of inner radius r_0 and outer radius r_1 with a uniform non-swirling flow going through it. The combination of (B.1.1) and (B.1.2) shows that the pressure perturbation satisfies the wave equation. If the mean flow has an axial Mach number M_{x0}, the wave equation is given by:

$$\left(\frac{1}{c_0}\frac{\partial}{\partial t} + M_{x0}\frac{\partial}{\partial x}\right)^2 \tilde{p} = \bigtriangledown^2\tilde{p}, \tag{B.1.11}$$

where the right hand side term, written in cylindrical coordinates, is given by:

$$\bigtriangledown^2\tilde{p} = \frac{\partial^2\tilde{p}}{\partial^2 x} + \frac{1}{r^2}\frac{\partial^2\tilde{p}}{\partial^2\theta} + \frac{1}{r}\frac{\partial}{\partial r}\left(r\frac{\partial\tilde{p}}{\partial r}\right) \tag{B.1.12}$$

At the inner and outer radius, the pressure perturbation must also satisfy the boundary condition:

$$\frac{\partial\tilde{p}}{\partial r} = 0 \; for \; r = r_0, r_1 \tag{B.1.13}$$

The variable separation technique can be used to obtain a solution for (B.1.11). Consider a general solution of the form:

$$\tilde{\mathbf{U}}(x,\theta,r,t) = \hat{\mathbf{U}}(r)e^{i(k_x x + k_\theta\theta + \omega t)} \tag{B.1.14}$$

Equation (B.1.11) becomes:

$$\frac{1}{\xi}\frac{d}{d\xi}(\xi\frac{d\hat{p}(\xi)}{d\xi}) - ({k_r}^2 - \frac{k_\theta^2}{\xi^2})\hat{p}(\xi) = 0 \tag{B.1.15}$$

where $\xi = \frac{r}{r_1}$, $\lambda < \xi < 1$ with $\lambda = \frac{r_0}{r_1}$, and:

$$k_r^2 = r_1^2((\frac{\omega}{c_0} + M_{x0} \times k_x)^2 - k_x^2) \tag{B.1.16}$$

where k_r denotes the number of zero crossing the radial direction (Fig.B.1). Using these notations, the boundary conditions (B.1.13) can then be re-written as:

$$\frac{d\hat{p}(\xi)}{d\xi} = 0 \; for \; \xi = \lambda, 1 \tag{B.1.17}$$

Equation (B.1.15) yields to a solution of the form:

$$\hat{p}(\xi) = aJ_{k_\theta}(k_r\xi) + bY_{k_\theta}(k_r\xi) \tag{B.1.18}$$

where J_{k_θ} and Y_{k_θ} are Bessel functions. The application of the boundary conditions (B.1.17) gives:

$$det\begin{vmatrix} J'_{k_\theta}(k_r\lambda) & Y'_{k_\theta}(k_r\lambda) \\ J'_{k_\theta}(k_r) & Y'_{k_\theta}(k_r) \end{vmatrix} = 0 \tag{B.1.19}$$

which yields to a set of real values for k_r, which in turn yields to a set of values for k_x by using (B.1.16). If k_x is *real*, the downstream going mode corresponds to the solution for which $k_x < 0$, and the upstream mode for $k_x > 0$. For complex k_x, it is explained in Appendix A how to differentiate between acoustic downstream and upstream modes. In cases where there is no inner annulus (i.e. $r_0 = 0$), the general

solution of (B.1.15) is given by:

$$\hat{p}(\xi) = aJ_{k_\theta}(k_r\xi) \tag{B.1.20}$$

and the boundary condition at the outer annulus gives:

$$J'_{k_\theta}(k_r) = 0 \tag{B.1.21}$$

which defines k_r and hence k_x. The relationships between primitive perturbation variables are then obtained by combining (B.1.1), (B.1.2) and (B.1.20):

$$\hat{u}_x(\xi) = \frac{-k_x}{\rho_0(\omega + k_x u_0)}\hat{p}(\xi) \tag{B.1.22}$$

$$\hat{u}_\theta(\xi) = \frac{-k_\theta}{\rho_0 r(\omega + k_x u_0)}\hat{p}(\xi) \tag{B.1.23}$$

$$\hat{u}_r(\xi) = \frac{i}{\rho_0 r_1(\omega + k_x u_0)}\frac{\partial\hat{p}(\xi)}{\partial\xi} \tag{B.1.24}$$

Then, the isentropic relationship in (B.1.10) is used to expression the relationship between density and pressure perturbations:

$$\hat{\rho}(\xi) = \frac{\hat{p}(\xi)}{c_0^2} \tag{B.1.25}$$

In turbomachinery applications, the computational domain does not usually include the whole annulus, but instead it uses a circumferential section P of the duct. In this case, it was shown in Appendix A that k_θ can take an infinite number of values $k_{\theta n}$ given by:

$$k_{\theta n} = \frac{\sigma + 2\pi n}{P}, \forall n \in I \tag{B.1.26}$$

where σ represents the perturbation phase differential between the plane at constant angles, $\theta = \theta$ and $\theta = \theta + P$.

B.2 Application

We will now consider half a duct for which θ varies between θ and π with a hub-casing ratio of $\frac{r_0}{r_1} = 0.5$. The flow is subsonic, inviscid, uniform and non-swirling. The mean flow axial Mach number $M_{x0} = 0.5$, and the speed of sound $c_0 = 345$ *m/s*. The acoustic wave frequency is imposed at $\omega = 20000$ *rad/s*. Several eigenmodes were computed using (B.1.15) and the results are presented in Fig.(B.1). Note that the eigenmode solutions for the acoustic downstream and upstream modes are

identical for a given set of values for k_θ and k_r.

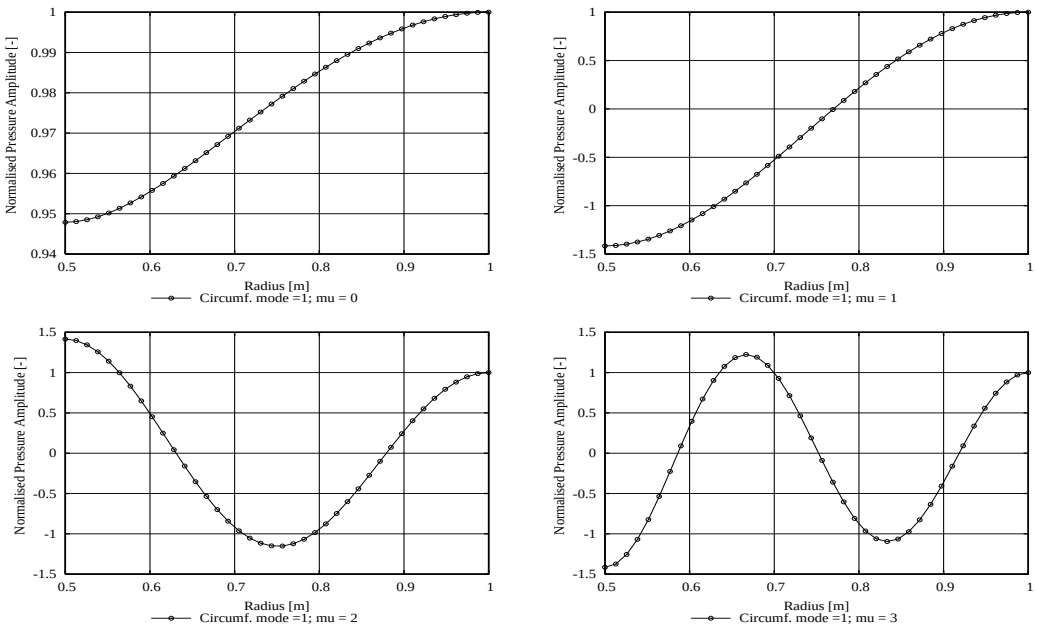

Figure B.1: Computed radial variation in pressure amplitude for half a cylindrical duct with hub-casing ratio 0.5. Top left: $(k_\theta = 1, k_r = 0)$; Top right $(k_\theta = 1, k_r = 1)$; bottom left: $(k_\theta = 1, k_r = 2)$; and bottom right: $(k_\theta = 1, k_r = 3)$